Development of Interfaces Containing Auxetic Constituents

A THESIS SUBMITTED IN PARTIAL FULFILMENT OF THE

REQUIREMENTS OF THE UNIVERSITY OF BOLTON

FOR THE DEGREE OF DOCTOR OF PHILOSOPHY

February 2013

By

Gleny Tambudzayi Chirima

Institute for Materials Research and Innovation

Dedication

In loving memory of my late father, Mr Donald Chirima

List of Publications

This work has already been accepted/published in the following:

Peer-reviewed journals:

1. **Gleny T. Chirima**, Khaled M. Zied, Naveen Ravirala, Kim L. Alderson, Andrew Alderson, Numerical and Analytical Modelling of Multi-layer Adhesive-Film Interface Systems, *Physica Status Solidi (b)*, 246, 2072-2082, 2009.

2. **G. Chirima**, N. Ravirala, A. Rawal, V.R. Simkins, A. Alderson and K.L. Alderson, The Effect of Processing Parameters on the Fabrication of Auxetic Extruded Polypropylene Films. *Physica Status Solidi (b)*, 245, 11, 2383-2390, 2008.

Conference proceedings and presentations:

1. G.T. Chirima, K. Zied, N. Ravirala, A. Burgess, P. Dooling, K.L. Alderson, A. Alderson, Modelling of Auxetic Particulate-Filled Polymeric Composites, 17th ICCM Conference, 27-31 July 2009, Edinburgh, UK.

2. **G.T. Chirima**, K. Zied, N. Ravirala, K.L. Alderson, A. Alderson, Modelling of Auxetic Filled Adhesive Systems, Euro Fillers 2009, 21-25 June, Alessandria, Italy.

3. **Chirima, G.T**., K.L. Alderson, A. Alderson, A.N. Burgess, P. Dooling, N. Ravirala, K. Zied, Auxetic Films and Interfaces Systems, 2nd International Conference on Auxetics and Related Systems, Bristol, UK, 14/09/2008.

4. **Chirima, G.T.**, K.L. Alderson, A. Alderson, A.N. Burgess, P. Dooling, N. Ravirala, K. Zied, Modelling of Auxetic Particulate Filled Adhesive Systems, Polymer Fibres Conference, Manchester, UK, 9/07/2008.

5. **Chirima, G.T**., REACTICS - Reactive Structural Materials with Auxetic Inclusions, Research and Innovation Conference, Bolton, 08/05/2008.

6. **Chirima, G.T.,** Ravirala, N., Alderson, K., Alderson, A.; The Effects of Processing on the Structure and Mechanical Properties of Auxetic Extruded Films, 1st International Conference on Auxetics and Related Systems, Exeter, UK, 03/09/06.

Patents

1. Andrew Alderson, Kim L. Alderson, **Gleny T. Chirima**. Multi-Layer Adhesive Interfaces: Application number GB 0816829.6

Awards

1. Best Young Researcher's Paper, 5th Annual Auxetnet Young Researchers Forum, Auxetics 2008, Bristol, UK, 14-17 Sept, 2008.

2. Best poster award, Research and Innovation Conference, Bolton, UK, 08/05/2008.

Declaration

No portion of the work referred to in this thesis has been submitted in support of an application for another degree or qualification of this or any other university or other institution of learning.

Copyright

Acknowledgements

I would like to express my sincere gratitude to the director of my doctoral studies, Prof Andrew Alderson and to my supervisors; Prof Kim Alderson and Dr Naveen Ravirala for their invaluable support and continuous guidance. I owe special thanks to Prof Andrew Alderson for painstakingly going through my thesis draft and subsequently providing helpful feedback.

I am thankful to Dr Khaled Zied for guidance on the modelling sections performed in this work. I am also thankful to partner companies in the consortium, namely AkzoNobel and Cytec. Special thanks to Dr Paul Dooling and Dr Andrew Burgess for their valuable input throughout my research.

I would also like to acknowledge the support received from the technical staff; Mrs Stella Peel, Mr Shahram Shafiee, Mr Akbar Zarei, Dr Gill Smart and the engineering workshop technicians. Thanks to Mrs Donna Zarei for her administrative support.

Special thanks are due to my dearest husband, Everson, for his invaluable support, understanding and encouragement throughout the whole research period and especially during the thesis write-up stages. Thanks for the sacrificial time spent in proof reading the thesis. I would also like to express special thanks to my family for their support, encouragement and prayers; my mother, Gladys, my brothers and sisters, Arther, Tawanda, Portia, Nyasha, Previledge and Patience.

Finally, I gratefully acknowledge the financial support obtained from Technology Stratergy Board (TSB).

Table of Contents

List of Figures

List of Tables

Abstract

Auxetic materials display a negative Poisson's ratio. Such materials have a host of potential benefits that could be exploited such as high shear resistance, fracture toughness, and high indentation resistance amongst others. The inclusion of auxetic materials within positive Poisson's ratio materials is investigated in an attempt to improve the effective mechanical properties. The project focuses on the modification of mechanical properties of an adhesive, or interface, system via the addition of either auxetic and/or conventional constituents. The objective is achieved via two main approaches: a multi-layer adhesive/film interface and auxetic particulate filled adhesives. Multi-layer film/adhesive interfaces are modelled for Constant Interface Thickness (CIT) and Constant Constituent Layer Thickness (CCLT) systems using Finite Element Modelling (FEM), analytical expressions from averaging techniques for the effective elastic properties of a composite (the Ramirez approach) and a modified (weighted) Rule of Mixtures approach developed by the author. High and low modulus adhesives relative to the films are considered. In the second approach, FEM of particulate filled systems is performed for high and low modulus auxetic fillers relative to the matrix. The results are compared to existing analytical theories such as the Self-Consistent Field theory, Hashin Shtrikman and the bounding techniques of elasticity. Auxetic materials are predicted by the models to give rise to improvements in the effective mechanical properties (Young's modulus and shear modulus) of both the multi-layer film/adhesive and particulate filled composite interfaces. Experimental work in support of the model predictions includes 3 and 4 point bending tests of multi-layer film adhesive interfaces comprising polypropylene films and polyolefin adhesive, and tensile testing of auxetic silica particulate (high modulus filler) and short chopped auxetic polypropylene fibre (low modulus filler) filled epoxy matrix composites. The multi-layer film adhesive approach requires an understanding of the production of

auxetic polypropylene films. A parametric study of the melt extrusion process for the production of auxetic and conventional films has, therefore, been undertaken and has included producing, for the first time, auxetic PP films at significantly higher processing temperatures than those previously established in the vicinity of the melt onset temperature.

CHAPTER 1: INTRODUCTION

Negative Poisson's ratio (auxetic) materials have theoretically been known to exist for approximately 150 years [1] although only a few examples of naturally occurring materials had been discovered. The existence of negative Poisson's ratio materials did not receive special attention until recently when the benefits of auxetic materials were realised and given serious consideration. The first man-made auxetic materials were synthetic foams which were manufactured in 1987 [2]. This discovery opened a vast amount of possibilities for everyday applications in which the auxetic behaviour could be exploited. The improved structural performance of engineering structures containing auxetic constitutive elements is a driver in seeking viable means via which these materials can be realised in the laboratory.

Further to the discovery of foams, there have been many developments in either fabrication or discovery of naturally-occurring auxetic materials. Materials with a high degree of anisotropy such as honeycomb structures[3-5], cubic metals, minerals and certain rocks [6-7] and living bone tissue [8] just to mention a few have been discovered. Despite the success demonstrated in the fabrication of auxetic materials, their potential use and exploitation in real-world application raises some challenging issues. The research programme undertaken by the author attempts to address practical issues involved in the design and development of interface materials containing auxetic constituents for joining of two distinct materials or components. Important properties of adhesive interface materials include enhanced Young's and shear moduli [9], and fracture toughness [10]. Independent of, but during the course of, this work, thick laminate structures containing auxetic layers have very recently been predicted using modelling methods to display enhanced Young's modulus [11, 12, 13].

The overall aim of the work reported in this thesis is to extend the previous work on

auxetic materials to their use as constituents in adhesive interfaces, and to investigate the potential of such systems to realise enhancement in some of the key properties required in adhesive systems. This objective is attempted via a two pronged approach; in the first case a multi-layered polymeric film/adhesive interface in which the through-thickness mechanical properties of a stacked interface consisting of auxetic and/or conventional film layers is investigated. Secondly, the mechanical properties of an auxetic particulate filled polymeric matrix are investigated.

This thesis describes the in-house fabrication of conventional and auxetic extruded polypropylene (PP) films which were subsequently incorporated into multi-layered film/adhesive interfaces for the first time. This includes the most comprehensive investigation to date into the effect of extrusion parameters on the properties of the extruded films. A parametric modelling study is conducted to provide fundamental insights into the effect of film mechanical properties such as Poisson's ratio and Young's modulus on the overall mechanical properties of the layered interface. The study into the layered film system is intended to be especially relevant to the future development of commercial tape adhesives containing auxetic constituents.

The second approach utilises a particulate-filled (polymeric resin/auxetic particulate fillers) adhesive. As for the layered system, auxetic particulate-filled systems have been fabricated and characterised for the first time and a parametric modelling study has been performed for the filled system to investigate the effect of constituent mechanical properties on the overall properties of the filled matrix. This approach leads to possibilities for eventually making filled adhesive in so-called 'squirt and squish' systems.

A review of literature with respect to the structure, mechanical properties and possible

application of auxetic materials is given in Chapter 2. Chapter 3 reports a processing parametric study of the production of conventional and auxetic polypropylene films. The study focuses on how the ultimate material behaviour (i.e. conventional or auxetic) of extruded polypropylene films is dependent on the processing parameters during extrusion. In Chapter 4 a Finite Element model of a multi-layer film/adhesive system is described. The chapter reports numerical (Finite Element Analysis) as well as analytical (modified Rule of Mixtures and the Ramirez approach) modelling of the multi-layer film/adhesive interfaces for the determination of the Young's and Shear moduli. Details of the numerical modelling of the three-point bending tests for the multi-layer interface are also reported. Chapter 5 reports the details of the FE and analytical models of the particulate filled composites. Theoretical (FE and analytical) results for the tensile and shear moduli model simulations of the multi-layer film/adhesive interfaces are presented in Chapter 6 and 7, respectively. Improvements in mechanical properties especially the shear modulus were anticipated for interfaces containing auxetic films. The availability of such a modelling tool allows the design of an experimental matrix concentrating on the lay-up arrangements (i.e. stacking patterns) of specific interface properties thus saving time and reducing costs. The feasibility of an auxetic particulate-filled resin-based adhesive is explored in Chapter 8. Numerical and analytical modelling techniques are used to investigate the effect of the inclusion of auxetic particles into a positive Poisson's ratio polymeric matrix. Chapter 9 reports the details of the experimental tests that were done in order to verify some aspects of the multi-layer systems (flexural modulus) and particulate filled models. The methodology employed in the fabrication of the multi-layer film/adhesive interfaces is presented together with results from mechanical testing in the first section of Chapter 9. The experimental trends in mechanical performance of the multi-layered interfaces are compared against theoretical predictions from the models. Fabrication and mechanical testing of a number of filled systems is also reported for the cases of a high modulus

auxetic filler (α-cristobalite) relative to the polymer (epoxy) resin as well as a low modulus auxetic filler (chopped auxetic fibres) relative to the polymer (epoxy) resin. Comparison is made between experimental and predicted mechanical properties of the filled system. Chapter 10 gives a summary of the conclusions drawn from this study together with suggestions for further work.

CHAPTER 2: LITERATURE REVIEW

2.0 Summary

The introductory part of this literature review focuses on the definition of an auxetic material. Examples of synthetic and naturally-occurring auxetic materials are given. A discussion on the possible applications as well as benefits of using auxetic materials follows the general introduction. A brief history of auxetic materials and mechanisms of deformation which lead to the realisation of auxetic behaviour in materials is highlighted. A melt extrusion process for the production of auxetic polymeric materials is discussed. An understanding of the extrusion process and how auxetic behaviour is achieved is a complex and on-going activity of the research group at the University of Bolton. Finally, particulate-filled polymer matrix systems are discussed. These composite materials present an opportunity to achieve auxetic behaviour in conventional matrices via the inclusion of micro-sized auxetic particles within the former.

2.1 Introduction

The word *auxetic* comes from the Greek word, "*auxetos*" meaning "that which grows" [14]. Materials with a negative Poisson's ratio, auxetics, have the fascinating property of becoming thicker when stretched [15] (refer to Fig 2.1). The schematic shown in Fig 2.1, illustrates the deformation behaviour of (i) positive and (ii) negative Poisson's ratio materials. In this illustration a uni-axial tensile force in the *X*-direction is applied to the original (un-deformed) material (left hand-side of Fig 2.1) resulting in a deformed material (right hand-side). The conventional material (positive Poisson's ratio) shows transverse contraction whilst negative Poisson's ratio (auxetic) materials expand laterally. The negative Poisson's ratios arise as a result of the particular geometry of the material microstructure and the way via which the material microstructure deforms when subjected

to a uni-axial force.

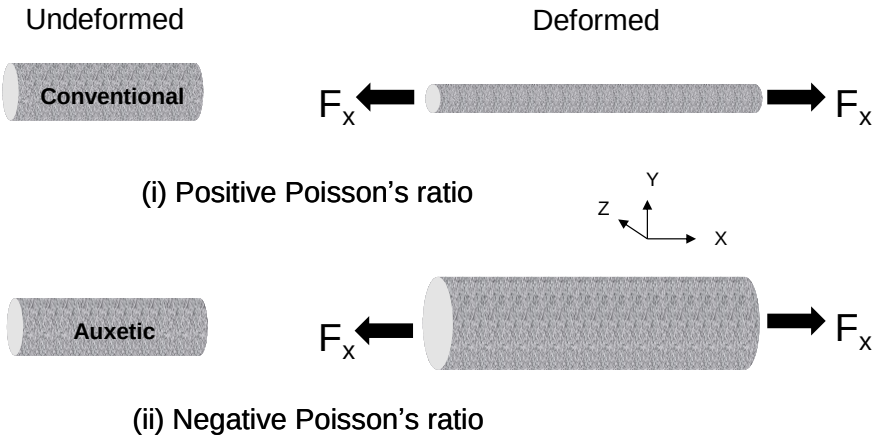

Fig 2.1 (i) Conventional and (ii) auxetic materials subjected to uni-axial tensile force, along the *X*-direction. F_X is the force applied in the *X*-direction.

Auxetic materials that occur naturally include single-crystal arsenic [6], cat skin, load-bearing cancellous bone from human shins [8] and silicate α-cristobalite (SiO_2) [7]. Extensive research has been performed since the late 1980's to develop man-made materials and structures giving rise to auxetic behaviour, [16, 17] including the fabrication of auxetic composites, [18], metallic and non- metallic foams, [2,19-23] and polymeric materials [23,24].

There are various everyday examples of applications where functional materials exhibiting negative Poisson's ratios can be exploited. These include packaging, filtration, piezo-electric composite sensors and acoustic/sound insulation [25]. Polymeric auxetic materials and structures have potential to be employed as smart filters with adjustable pore size and shape tuneability [26]. The pores of a conventional membrane filter undergoing uni-axial stretching tend to close up in the lateral direction (Fig. 2.2(a)). Applying a force in the same manner to an auxetic membrane, the pores open up thus making the possibility of particulate defouling achievable, Fig 2.2(b).

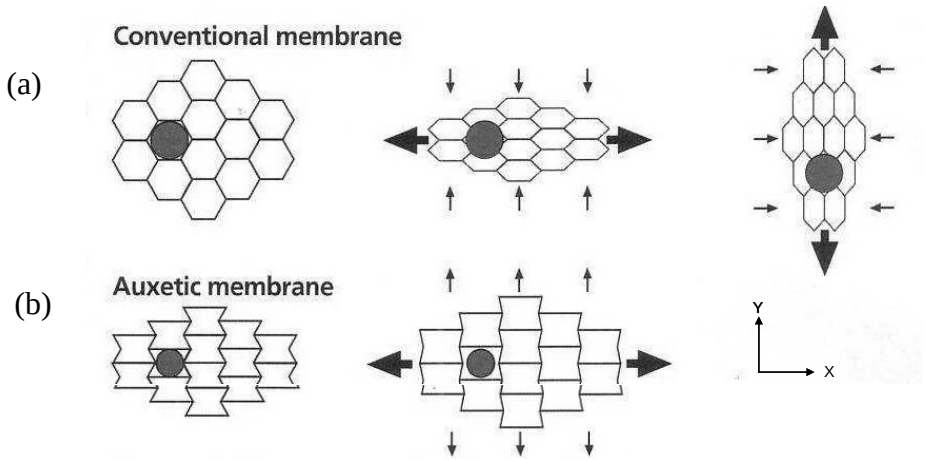

Fig 2.2 Illustrations of (a) conventional and (b) auxetic membrane filters [25].

Auxetic membranes undergo significant volumetric changes as a result of microstructural changes following application of a load. These large volumetric changes enable the entrapment or release of a guest material from within the auxetic membrane pores.

Auxetic polymer fibres can be woven into textiles, which in turn can be made into so-called "smart" bandages [26], capable of controlled release of chemical agents (anti-inflammatory, anti-odour or anti-bacterial) from within the pores of the filaments making up the structure. The smart bandage concept is shown in Fig 2.3.

Zeolites [27] are an important class of nano-structured materials commonly used as molecular sieves because of their availability and well-defined molecular-sized cavities and pathways. Zeolites are aluminosilicate framework structures containing molecular-sized cages and channels from an array of corner-sharing SiO_4^{4-} and AlO_4^{5-} networks. Auxetic behaviour has been predicted for a range of zeolites [28] and so the benefits in filtration materials at the macro- and micro- scales can be envisaged in these nano-scale sieve materials.

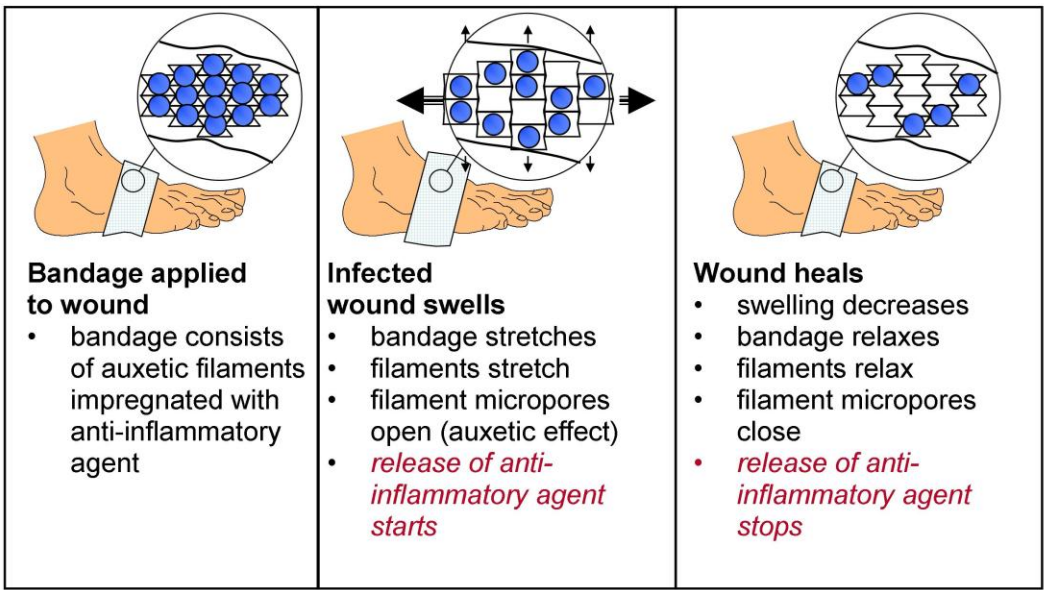

Fig 2.3 Characteristics of a "smart" bandage and how it works [26].

Initial research on auxetic zeolites reported that the mechanisms responsible for auxetic behaviour in zeolites include rotating squares (Fig 2.4) and triangles where the corners of the squares or triangles are oxygen atoms [28-30]. In an idealised structure where the squares are perfectly rigid and connected together through simple hinges, a Poisson's ratio of -1 can be achieved [29] for loading in any direction regardless of the size of the square or its orientation angle, θ. The deformation is restricted only to the co-operative rotation of the squares relative to each other. It is assumed that the stiffness of the structure is dominated by that of the hinges; precluding the idealised structure from shearing. The assumption of rigid units and deformation solely through cooperative rotation of the units may restrict the applications of simple analytical models for the accurate prediction of Poisson's ratio in real materials. Fig 2.4 shows schematically the rotating square mechanism acting in the *X*-*Y* plane of zeolite THO under tensile load along the *X*-direction.

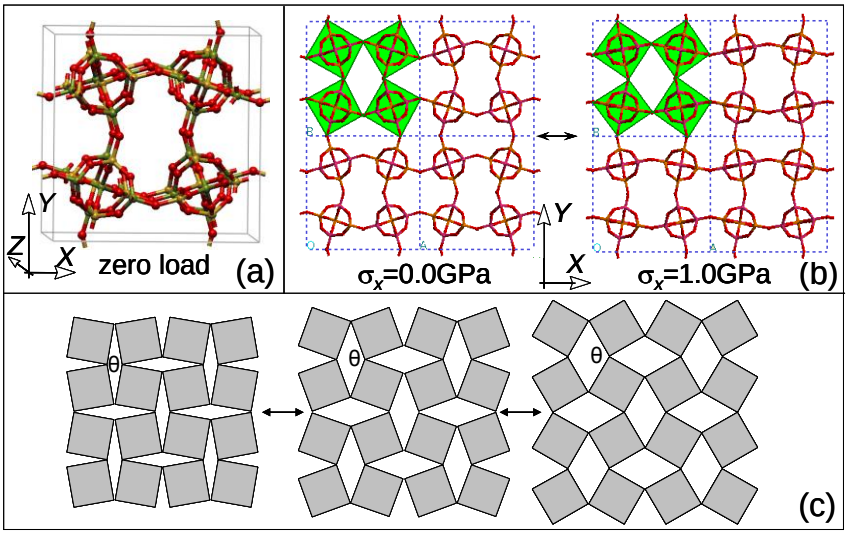

Fig 2.4 Auxetic 'rotating squares' (a) 3D THO framework, (b) minimum energy configurations of the (001) plane in THO at different uniaxial loads in the *X*-direction, and (c) the idealized rotating 'hinging squares' mechanism [28].

The initial studies on auxetic zeolites assumed that the presence of cations or interstitial water molecules have no effect on the deformation mechanism of the structures. Later, research work performed by Wood and co-workers [31] included modelling zeolites (namely NAT and EDI) structures via force-field based molecular mechanics simulations and software to investigate the effect of the presence of cations or water molecules. It was discovered that water molecules reduced the magnitude of negative Poisson's ratio although the overall auxetic behaviour was retained. The presence of nanostructured pores with controllable architecture makes auxetic zeolites ideal for molecular separation and ion exchange applications [32].

The use of auxetic materials as fastening devices has been shown in rivets and similar mechanical fasteners [34-35]. As an example, auxetic copper foam press fit fastener [35] contracts in a radial fashion as it is compressed into a hole, thereby easing the process of fastener insertion. When the fastener is pulled, it expands thereby having a locking effect leading to increased pull out resistance.

Auxetic materials have a large volumetric change when they deform and thus have potential in sensor and actuator applications. Highly anisotropic auxetic materials can be used as strain amplification devices where the transverse strain is much greater than the longitudinal strain being measured. Auxetic cubic elemental metals can be used as electrodes sandwiching a piezoelectric polymer and predictions show that this arrangement gives a two-fold increase in piezoelectric device sensitivity [36].

According to classical elasticity theory, the theoretical allowable range of Poisson's ratio for isotropic materials is $-1 \leq \upsilon \leq +0.5$ [1]. Most common materials have a Poisson's ratio close to +0.3; however, rubbery materials have values approaching +0.5. The relationship [37] between shear modulus (G), Young's modulus (E) and Poisson's ratio for isotropic materials is given by:

$$G = \frac{E}{2(1+\upsilon)}, \tag{2.1}$$

The relationship between shear modulus G, bulk modulus K, and Poisson's ratio for isotropic materials is given in equation 2.2.

$$G = \frac{(3K(1-2\upsilon))}{2(1+\upsilon)} \tag{2.2}$$

As the Poisson's ratio approaches a value of -1, the denominator in Eq. 2.1 approaches zero meaning that the shear modulus increases asymptotically. Similarly, in Eq. 2.2, G (shear modulus) becomes much greater than K (bulk modulus), hence it becomes difficult to shear but easy to deform with respect to material volume. This behaviour is in contrast to that exhibited by rubber; hence auxetic materials can be referred to as 'anti-rubber' [9].

Auxetic foams have better mechanical properties such as damping of vibrations and acoustic emissions or sound [38] compared to conventional ones. They also have better indentation resistance [39, 40].

The hardness, *H*, of a material is related to Poisson's ratio by the following equation:

$$H \propto \left(1-\upsilon^2\right)^{-x}, \tag{2.3}$$

where *x* is dictated by the shape of the indentor [41-43]. Equation (2.3) predicts enhanced indentation resistance as $\upsilon \to -1$. An auxetic material densifies under an indentor as shown schematically in Fig 2.5 [44], and recovers its original shape on removal of the indentor. Fig 2.5 illustrates that if an object impacts a conventional material, the material below the indenter 'flows' away in lateral directions, leading to a reduced density which then reduces the indentation resistance. On the other hand, if an auxetic material is impacted, the material experiences lateral contraction allowing material to 'flow' into the vicinity of the impact as shown by arrows converging at the point of impact in Fig 2.5. As a result auxetic materials densify under impact in both longitudinal and transverse directions leading to an increase in indentation resistance. This could be important in a range of applications including packaging, head and joints protection, car headrests and bumper systems. An auxetic mattress would fold itself around the human body [44], maximising support where it is needed.

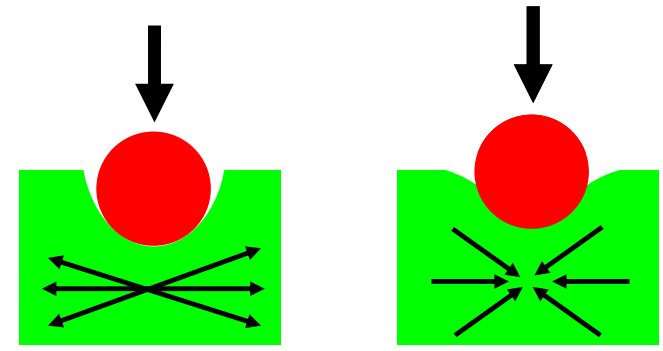

Fig 2.5 Schematic showing response of conventional and auxetic materials to indentations, with localised densification both axially and laterally under the indentor leading to enhanced indentation response for the auxetic material [44]. Arrows within the material indicate direction of material 'flow'.

Auxetic materials exhibit improved plane strain fracture toughness [10]. Tensile tests carried out on auxetic films containing a cut or tear aligned along the loading direction showed a decrease in the tear width (transverse to the loading direction) as opposed to conventional films where the tear width increased with deformation [45, 46]. Hence auxetic materials tend to both resist cracking and also close up any potential cracks before they start to grow [47]. Other examples of potential everyday applications identified include among other things wrestling mats, knee pads [48] and seat cushions [49, 50].

2.2 History of Auxetic Materials

Based on classical elasticity theory, the possibility of a negative Poisson's ratio material has been accepted for over 150 years [1]. The theory of elasticity is not scale dependent and so the negative Poisson's ratio effect in materials can be observed at both micro- and macroscopic levels. An example of a macro-scale structure is that of the graphite core found in nuclear reactors [44]. Most of these reactors constructed in the 1950s were designed in such a way as to withstand horizontal shear forces generated during earthquakes. The design also allowed free movement of the structure in response to thermal movements between the graphite and steel supporting structures. Consequently, the design was required to possess both high resistance to shear deformation and low resistance to changes in volume (i.e. $G >> K$). This is precisely the condition achieved when υ approaches -1 in equation 2.2.

Shown schematically in Fig 2.6, is the horizontal plane of the structure of a Magnox reactor which possesses a radially-keyed graphite moderator core. Auxetic behaviour occurs due to the radial movement of the free standing columns of graphite bricks. When subjected to a tensile load in the horizontal plane the Magnox structure expands in all radial directions through sliding of the bricks along the keyways. The structure also retains

the square lattice during deformation giving the structure a Poisson's ratio of -1 in the horizontal plane.

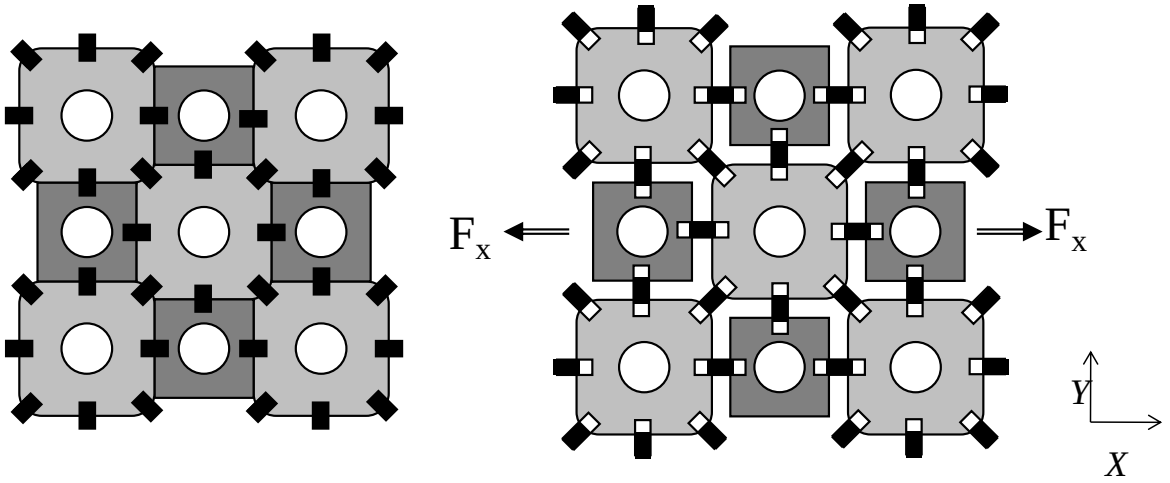

Fig 2.6 Schematic of horizontal plane of keyed-brick structures allowing radial movement of the free standing columns of graphite bricks in a Magnox nuclear reactor core: left side is the fully densified structure; right side is the expanded structure due to uni-axial force applied in the *X*-direction [44].

The earliest auxetic honeycombs consist of the tessellating re-entrant hexagon topology [3-5]. A simple example of how Poisson's ratio can be tailored by designing the structure of the material is illustrated in Fig 2.7 (and has already been compared to the conventional equivalent to demonstrate filter benefits in Fig 2.2). A two-dimensional conventional hexagonal honeycomb network deforming by hinging of the ribs, (Fig 2.2a) has a positive Poisson's ratio - that is, when the cells elongate along the *Y*-axis there is a closing of the cells along the *X*-axis and vice versa. By maintaining the same deformation mechanism (hinging of ribs) but modifying the honeycomb cell geometry to adopt a re-entrant structure, as shown in the Fig 2.7, the cell network undergoes elongation along both the *X* and *Y*-axes for a tensile load applied along either of these axes, and hence displays a negative Poisson's ratio. For the case of a tensile load applied along the *X* direction, the alignment of the diagonal ribs along the direction of applied load (shown by thick dark

arrows in Fig 2.7) causes the vertical ribs to move apart parallel and transverse to the loading direction to produce the auxetic effect (transverse expansion indicated by thin dark arrows in Fig 2.7).

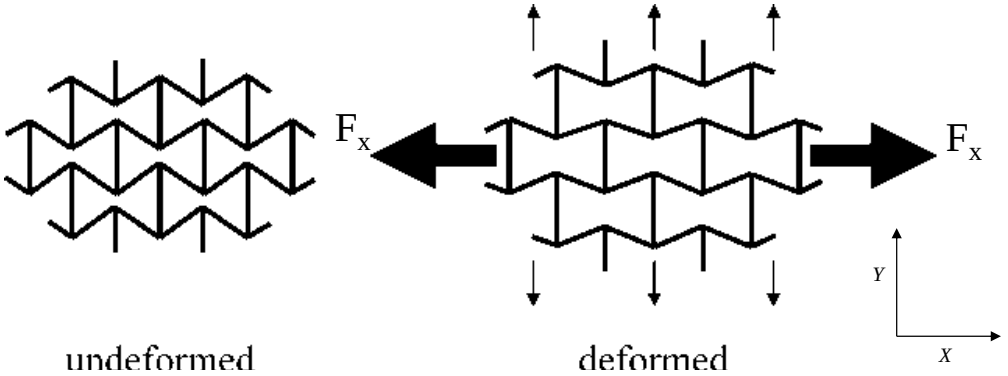

Fig 2.7 Re-entrant honeycomb in the un-deformed and deformed (due to uni-axial force along *X*) states [2, 9, 25].

Auxetic honeycombs have a potential use as the core material in curved parts such as the nose-cone of an aeroplane. They can easily adopt a curved shape without the need for machining or forcing into an unnatural shape. Auxetic sandwich panels containing re-entrant honeycomb core material have been successfully formed into doubly curved or domed shapes (synclastic behaviour) [9]. One disadvantage though, is the labour intensive manufacturing process for the re-entrant honeycomb. The usual method of gluing strips of material together at regular intervals and pulling to form conventional hexagonal honeycombs cannot be employed for the re-entrant honeycomb. Other methods like rapid prototype and moulding techniques could be used; however, a cost-benefit justification will be required to be satisfied before moving from the current methods used for manufacturing conventional hexagonal honeycombs to alternative fabrication processes for the re-entrant honeycombs. These limitations have given rise to alternative topologies such as star, [51] double arrowhead arrow [52] and chiral [53] systems which can lead to auxetic behaviour in honeycombs and may have a higher probability of commercial viability in some cases.

Of interest are the chiral honeycomb structures due to their features and how they affect the mechanical performance of the overall structure.

A structure which is not superimposable with its mirror image is defined as being chiral. A chiral honeycomb structure is composed of circular nodes joined by straight ligaments which are tangential to the nodes, Fig 2.8.

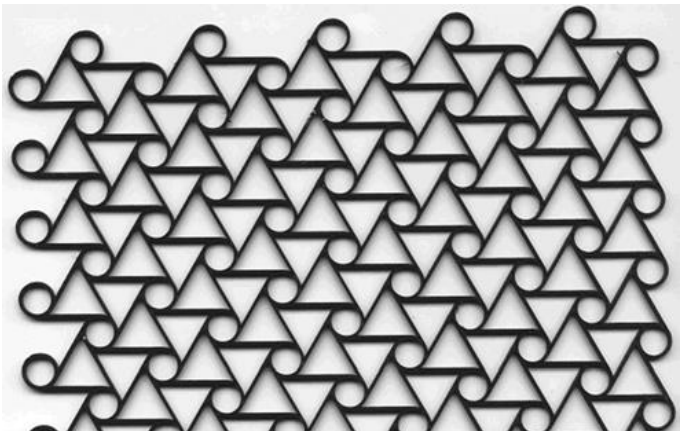

Fig 2.8 An illustration of a two-dimensional hexagonal chiral honeycomb [53].

A chiral honeycomb [53] that has a hexagonal symmetry has been shown to exhibit an in-plane Poisson's ratio of -1. The circular nodes rotate whilst the ligaments bend under uni-axial loading. The cylindrical components have been reported to lead to improved out-of-plane compressive strength under flat wise loading, [54, 55] and the ligaments provide resistance to the out-of-plane shear loading [56]. Work done by Prall and co-workers [53] showed that the Young's modulus of a chiral honeycomb depends on the ligament wall thickness and the cylinder radii, whilst the Poisson's ratio can reach -1 in both *X* and *Y* directions.

A method of fully converting open cell thermoplastic (polyurethane) foam displaying positive Poisson's ratio behaviour into auxetic foam was developed by Lakes in 1987 [2]. This was achieved by combined isotropic permanent volumetric compression and heat treatment of a conventional foam resulting in micro-buckling of cell ribs in the converted

foam. Other methods for the production of thermoset (silicone rubber) and metallic (copper) foam have also been reported [40]. Micrographs of polyurethane foam before and after conversion to auxetic foam are shown in Fig 2.9. The auxetic effect in foams is achieved by conversion of the convex polyhedral cell shape characteristic of conventional foams to re-entrant and more convoluted cell structures as shown by black arrows in Fig 2.9. Flexure of the cell ribs is the dominant deformation mechanism [57].

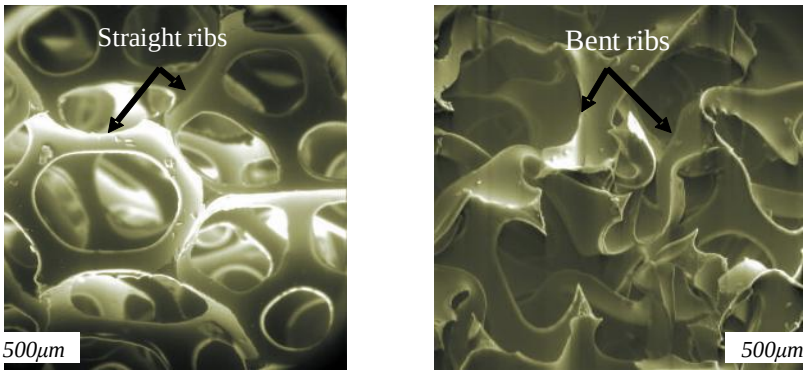

(a) (b)

Fig 2.9 Micrographs of (a) conventional and (b) auxetic polyurethane foams showing straight and bent ribs, respectively [44].

Auxetic foams display a synclastic curvature [9] and improved resilience. Fig 2.10 shows auxetic and conventional materials subject to pure bending. When a moment is applied to a conventional material, the free edges flip in an opposite direction; i.e. saddle formation (anticlastic curvature). Conversely, in the case of an auxetic material, the material forms a dome shape. This behaviour allows auxetic materials to be formed into complex structures such as the nose-cone of an aeroplane by the simple application of a moment.

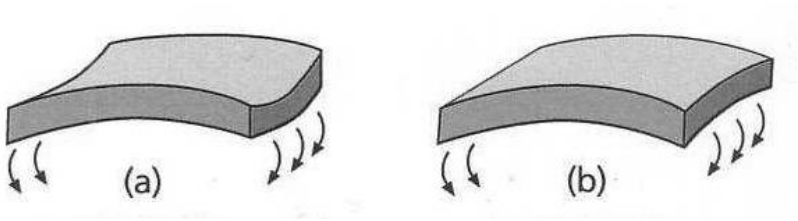

Fig 2.10 (a) Saddle shape (anticlastic) curvature in conventional plates and (b) dome shaped (synclastic) curvature in auxetic plates subject to a moment [9].

Since foams are not stiff enough to be used as structural materials by themselves, further development of auxetic materials to improve their stiffness for engineering applications is a subject receiving significant attention. Caddock and Evans [58, 59] discovered the auxetic behaviour exhibited by a form of expanded microporous polytetraflouroethylene (PTFE) was a result of its specific microstructure rather than an intrinsic property of PTFE itself. PTFE was found to be highly anisotropic, exhibiting a strain-dependent negative Poisson's ratio as low as -12. The negative Poisson's ratio was identified to arise as a result of a complex microstructure consisting of an array of nodules interconnected by fibrils as shown in Fig 2.11.

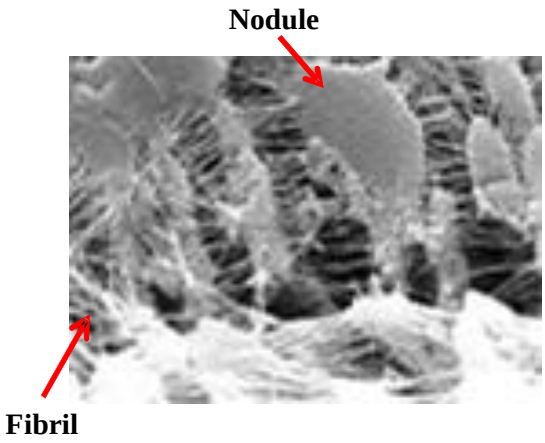

Fig 2.11 Nodule fibril microstructure possessed by auxetic PTFE [58].

A sample of compressed PTFE under the scanning electron microscope showed particles (nodules) lying flat and closely packed. As the PTFE was pulled the fibrils cause lateral

nodule translation resulting in a lateral expansion in the transverse direction. A simple analytical model based on translation of nodules due to rotation of interconnecting fibrils [59] explains the strain-dependent mechanical properties of auxetic microporous PTFE and is illustrated in Fig 2.12.

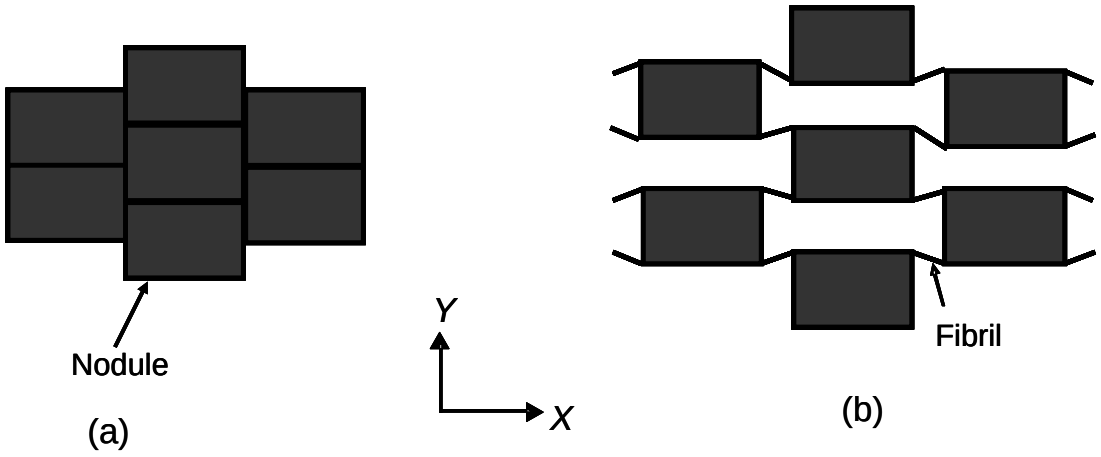

Fig 2.12 Schematic of nodule-fibril model microstructure of auxetic microporous polymers: (a) polymer at rest, (b) polymer under a tensile load [59, 60].

The observation of auxetic behaviour in PTFE was significant and revealed the possibility of producing different polymers with a similar microstructure. A process consisting of three distinct stages involving compaction, [23] sintering [24] and extrusion [61, 62] was developed which produced samples of auxetic microporous ultra high molecular weight polyethylene (UHMWPE). The auxetic UHMWPE samples were found to have a nodule-fibril microstructure (Fig 2.13) and to be stiffer (with a static Young's modulus of 0.2 GPa) than auxetic foams (Young's modulus of 72kPa).

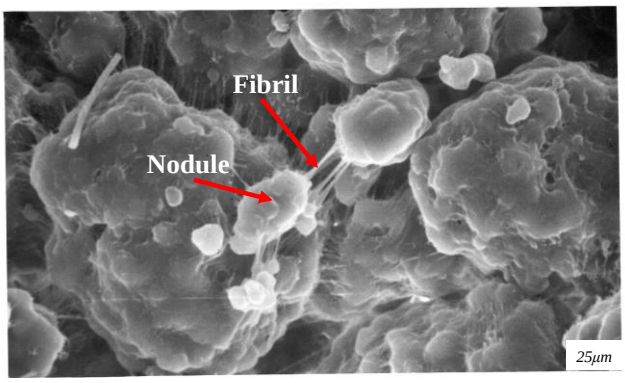

Fig 2.13 Micrograph of UHMWPE showing the nodule-fibril structure necessary for auxetic behaviour [63].

It was also discovered that omitting the compaction stage resulted in a highly fibrillated and auxetic extrudate with a lower flexural strength, Young's modulus and strain to failure [63, 64]. The ultrasonic attenuation co-efficient of auxetic UHMWPE was found to be 1.5 times higher than that of conventional UHMWPE [65]. Other polymers, which have subsequently been processed in order to exhibit auxetic behaviour, include polypropylene [66] and nylon [45]. The materials produced via this particular method were cylindrically shaped of typical dimensions 10 mm in diameter and a few tens of mm in length. Whilst these cylindrically shaped materials were important in assessing processing parameters and mechanical properties of auxetic materials, they were however difficult to machine and use in practical situations.

A more usable type of material, auxetic polypropylene (PP) fibre, was successfully fabricated [67] for the first time using a partial melt spinning technique on a conventional melt extruder. Through this method, nylon [45] and polyester [68] fibres were also produced. The fibres produced were continuous and of diameter typically in the range 0.018 cm to 0.1 cm. The production of auxetic fibres presented a host of practical applications such as in controlled delivery bandages as discussed in Section 2.1 and as

fibres in fibre-reinforced composites. Single fibre pull-out tests [69] on polypropylene fibres embedded in epoxy resin revealed that specimens with auxetic fibres displayed superior anchoring properties compared to those containing conventional reinforcement. Tests on several samples demonstrated that auxetic fibre specimens were able to withstand a maximum stress twice that of conventional fibre specimens and required three times the energy for complete extraction of the fibre. When an auxetic fibre embedded within a resin is pulled, it expands and locks into the matrix, thereby increasing the resistance to pull out. The pull-out concept is the same as that discussed earlier for auxetic fasteners.

The auxetic polypropylene (PP) fibres were extruded using an Emerson and Renwick Labline extruder at the following processing conditions: extrusion temperature of 159 ºC, screw speed of 1.05 rad s^{-1} and take-up speed of 0.03 ms^{-1}. Auxetic polypropylene films [70] were produced using similar processing parameters with an extruder die slit orifice geometry (63.5 mm × 14.2 mm × 0.38 mm). Initial work focused on the same processing window as that previously and successfully used for the production of auxetic polypropylene fibres, with slight variations in some key parameters; i.e. processing temperatures (158 - 162 ºC), screw speeds (0.525 - 1.575 $rads^{-1}$) and take-up speeds (0.015 - 0.06 m s^{-1}) were used. Processing the polypropylene powder at 230 °C was reported to produce no auxetic behaviour in the films regardless of variations in other processing parameters. In addition to the extruder processing parameters, the morphology and size distribution of the starting PP polymer powder were found to be important in the production of auxetic films and fibres [45].

Scanning electron microscopy on auxetic fibres and films has not revealed a nodule-fibril microstructure similar to that observed in the auxetic microporous cylinders. Rather the auxetic behaviour in the fibres and films appears to be based on a closely packed

particulate granular microstructure with low void content (Fig 2.14) [71].

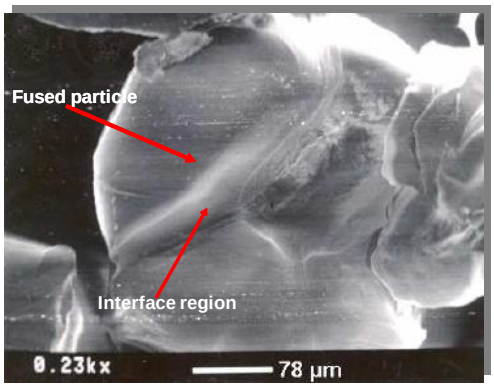

Fig 2.14 Micrograph of the cross-section of an auxetic fibre showing a fused particle microstructure [71].

Fig 2.15 shows a scanning electron microscope (SEM) image of the PP powder used as a starting material for the production of auxetic films and fibres. A rough morphology would appear to be necessary to enable sufficient contact points whilst a size distribution of particles (30-120 μm) enables efficient packing of particles during processing. When the polymer is extruded at a temperature of 159 ºC (the onset melting temperature for PP), the particles have been suggested to undergo surface melting, resulting in the formation of a network of connected interlocking rough particles which are thought to be responsible for the occurrence of auxetic behaviour in the films and fibres [45].

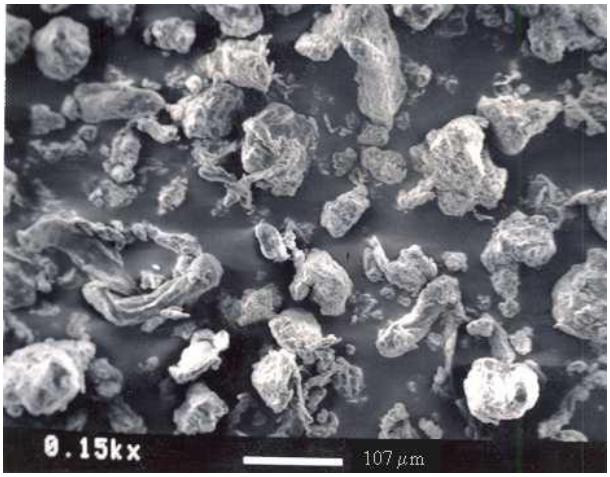

Fig 2.15 SEM micrograph of previously used PP (PB0580) powder [45].

The ratio of the thickness of the resolidified surface melt region to particle diameter is expected to affect the response of the micro-structure giving rise to auxetic behaviour. Larger particles undergo partial melting whilst smaller particles are fully melted. As the extrusion temperature is increased to 230 ºC, all particles become fully molten during the process and a conventional positive Poisson's ratio is observed.

Auxetic polymeric materials that have been fabricated so far have all shown some degree of variation in mechanical properties (Poisson's ratio varies along the fibre/film length). The non-uniform behaviour in mechanical properties was also observed in auxetic UHMWPE cylinders [63, 64]. The observed non-uniformity of mechanical properties along fibre/film length has been suggested to arise from the starting powder particle dimensions and the diameter/thickness of the extruded fibre/film [45]. Fig 2.16 (a) is a schematic of idealised polymer particles of the same size and shape uniformly distributed along the length of a partially-melt extruded fibre/film.

The grey regions represent the resolidified surface melt interfaces having positive Poisson's ratio characteristic of the intrinsic polymer connecting the polymer particles depicted as black hexagonal particles. These uniformly distributed particles of similar shape and size form a continuous array that has been shown to lead to auxetic behavior when the deformation mechanism is translation of the particles relative to each other along protruding interlocks [45, 72] (not shown), consistent with the rough morphology of the starting material. An infinite periodic array of such particles would have a uniform value of Poisson's ratio along its length. In a finite sized array where the thickness dimension of the array is of the order of a few particles (such as in the films and fibres produced to date) then the presence of variable amounts of resolidified (positive Poisson's ratio) material at

the edge of the array will modify the Poisson's ratio response of the system and lead to variable Poisson's ratio along the length.

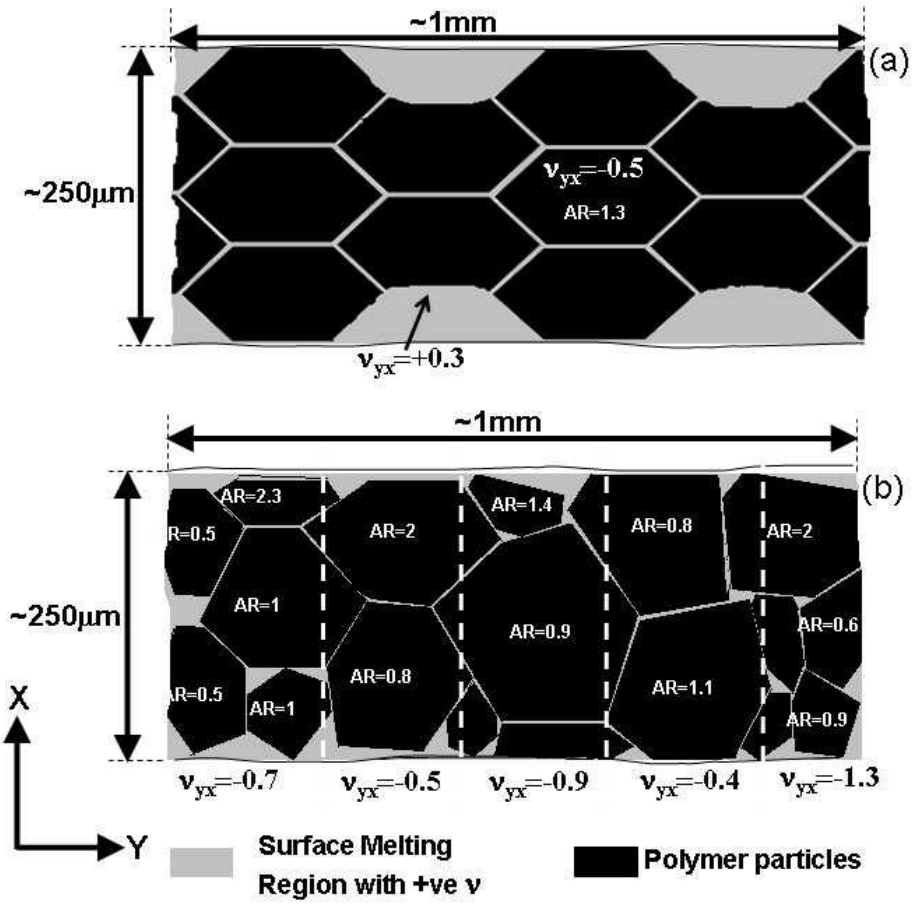

Fig 2.16 Schematic of polymer particle distribution in auxetic extruded polymer [45]. Abbreviation AR stands for 'Aspect Ratio'.

Fig 2.16 (b) shows a non-uniformly distributed array of polymer particles of varying sizes and shapes. The Poisson's ratio of the polymer will again be determined by the trade-off between the positive Poisson's ratio resolidified polymer and the negative Poisson's ratio of the connected particle network, resulting in a wide variation of mechanical properties along the length of the polymer. Further heterogeneity will be introduced through particle size, shape and orientation distribution. Previous studies have also shown that the overall auxetic behaviour of a polymer is dependent on the particle size, aspect ratio and alignment [45].

Fibre-reinforced polymer composites can be fabricated to exhibit auxetic response from conventional materials such as off-the-shelf pre-preg using established methods such as vacuum bagging techniques. The auxetic effect is achieved by selecting suitable stacking sequences of the unidirectional laminate layers [73]. Static indentation and low velocity impact tests performed on auxetic carbon fibre-reinforced epoxy laminates show a higher load to first failure with enhanced energy absorption [18] compared to conventional carbon fibre-reinforced epoxy laminates. The high load to failure and enhanced energy absorption combined with high impact resistance noted earlier for auxetic materials presents an advantage in engineering materials for aerospace applications.

2.3 Extrusion

Most auxetic fibres and films are obtained via hot/melt extrusion processes. Extrusion is widely used in continuous production of products that have a high viscosity in the fluid state. The process of extrusion involves the following sequential steps:

- heating and melting of the polymer,
- pumping the polymer into the shaping unit,
- forming the melt into the required shape and dimensions, and
- cooling and solidification.

The suitability of a material for a particular extrusion process depends on its melt flow index (MFI), which is the inverse measure of its viscosity. MFI is the output polymer flow rate collected through a standard die from a test apparatus in ten minutes. A high MFI polymer correlates to a low resin viscosity and low molecular weight, whilst a low MFI polymer has a high viscosity and molecular weight. A single screw extruder consists of a feed hopper, barrel, helical screw and a die at the end, Fig 2.17.

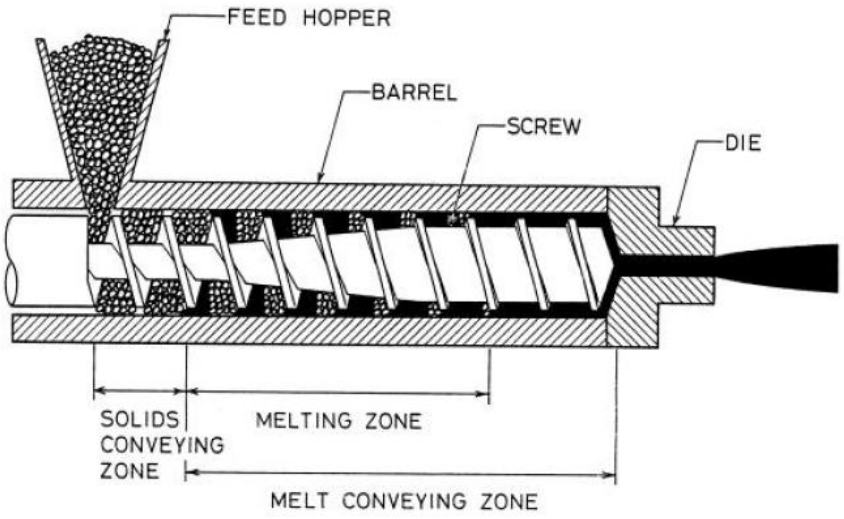

Fig 2.17 Schematic diagram of a single-screw extruder [74].

The extruder uses the Archimedean principle of a screw to perform the following:

- move un-melted polymer material from one zone to the next,
- compress and melt the polymer material, removing all air,
- generate enough pressure to push the molten polymer material through the die,
- homogenise molten polymer materials, and
- control the quantity of polymer material being pushed forward at any given moment along the length of the extruder.

The extruder consists of three distinct functional zones. In the first zone, solid polymer particles are compacted and conveyed by the action of a helical screw to form a solid bed of material (stage 1 in Fig 2.18). The compression zone (stage 2) is where the heat generated by the mechanical work due to screw rotation and the heat conducted from the heated barrel melts the polymer. In this zone the barrel heaters cause a thin film of molten polymer to form in the gap between the solid bed and the barrel wall. The melt film is subjected to intense shearing in the thin gap (stage 3), and due to the extremely high viscosities of molten polymers, high rates of viscous dissipation result (stage 4). The

generated heat melts the solid bed within a short distance of the commencement of melting. The last zone of the extruder; the metering section (sections 5 and 6); controls the extruder output and generates the pressure required at the die entry. A simple illustration by Vlachopoulos and Strutt [74] gives a visual representation of the processes occurring within different zones, Fig 2.18.

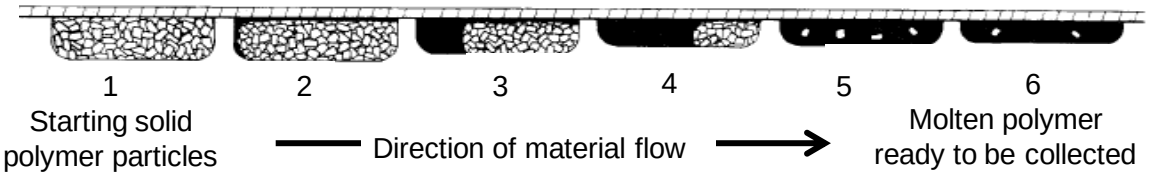

Fig 2.18 Illustration of how solid polymer melts in the screw channel of an extruder [74].

Parameters such as the screw speed, temperature and take-up speed do affect what goes on inside the extruder, and ultimately affect the quality and properties of the extruded product. Numerous models have been used by different researchers to predict the velocity, temperature, residence time, pressure and other variables of the polymer within the screw chamber [75-86]. One of the earliest pieces of research work on single-screw extruders was performed by Darnell and Mol [87]. The Darnell-Mol theory was based on solid to solid friction between the solid plug and the surrounding metal surfaces; that is the barrel, screw core, and the leading and trailing screw flight. The friction dependency theory on solid flow in the extruder makes optimisation a challenge since the co-efficient of friction is not constant and depends on temperature, pressure, velocity and many other parameters. According to Rauwendaal [88] it is preferred that the coefficient of friction between the solid particle and the barrel be greater than that between the particulate solids and the screw. It is possible that sometimes the solid precursor slips against the barrel and rotates with the screw resulting in that solid particle not advancing forward. Further mathematical simulations were performed by Karwe and Jaluria [80] on the behaviour of starch based

materials under high temperature environment. Chung, [79, 89] combined the theory based on friction coefficient with a theory based on viscosity to try and explain the mechanisms occurring inside an extruder. Most of the theories that have been developed are based on continuum mechanics, and therefore employ steady state or plug flow assumptions.

A discrete element method (DEM) was proposed by Moysey and Thompson [90] where each solid particle, in this case granular assembly, is modelled separately. The method takes into consideration the multiple contacts that each particle makes with neighbouring ones at a particular instance and a sum of all forces acting on a particle is determined. The resultant acceleration due to the sum of the forces is calculated from Newton's second law of motion. To visualise the flow behaviour of solid particles, a tracer was introduced and the movement of solid particles was monitored at different screw speeds. Similar work was also done by Janes and Winch [91] who used a tracer die to determine residence time and shear rate distribution. The effect of increasing screw speed reduces residence time but increases the shear rate. Despite efforts by different researchers to understand the processes and associated mechanisms within the extruder, this subject still remains complex and unresolved even for conventional extrusion processes, due to the many parameters involved, including the type of raw materials used. Clearly an improved understanding of the effect of the extrusion process parameters (temperature, screw speed, take-up speed) on the production of polymeric materials exhibiting auxetic behaviour is required and represents a very significant challenge in view of the difficulties encountered over many years of extrusion of conventional materials.

2.4 Filler Inclusions

Sometimes it is essential to add a proportion of fillers to conventional polymers in order to reduce costs and/or improve performance in some way. Research and development

activities have provided reasons for the inclusion of fillers which include improved processing, density control, optical effects, thermal conductivity, electrical properties [92], fire retardants [93], and improved mechanical properties such as elastic modulus [94] fracture toughness, hardness, and tear/wear resistance [95]. The main types of fillers that are used include carbon black, and natural and synthetic mineral materials.

Carbon black is an amorphous material that has a very high surface area to volume ratio. It is one of the first nanomaterials to find common use in the enhancement of mechanical properties of polymer-based products. A substantial proportion, about 70% of carbon black in the world is used as a pigment and reinforcing phase in automobile tyres [96]. Carbon black helps conduct heat away from the tread and belt area of the tyre, thus reducing thermal damage and prolonging tyre life. In fact, carbon black is used in rubber products where tensile and abrasion wear properties are crucial. Carbon black particles are also employed in some radar absorbent materials and in printer toner cartridges.

Calcium carbonate and talc are also widely used as mineral fillers in semi-crystalline polymers. Calcium carbonate can be used as a filler in elastomers, thermoplastics and thermosets [97]. A large percentage of the filler is used in polypropylene and poly(vinyl chloride) (PVC). The physical properties of the particulate fillers such as size, shape, and modulus can have a significant effect on the overall performance of the resultant composite [98, 99]. Envisaged interactions that include particle-particle and particle-polymer are important in the determination and prediction of mechanical properties of the filled systems. A homogeneous dispersion of particles, though difficult to achieve, is desirable [100, 101]. Fine particles have a tendency to agglomerate, hence making it difficult to achieve a homogenous particle distribution. Surface treatment or grafting can be used to modify the particle-matrix interactions giving the filler better dispersion and adhesion [102-104].

The study of micromechanics of heterogeneous materials is useful in order to assess the overall macroscopic properties of the hybrid materials. Since particle-filled materials are an important class of materials, a lot of researchers have focused their work on these [105-113]. Most of the work involves the statistical evaluation and modelling of the packing of particles with different shapes including cubic and spherical, for both random and ordered systems. Research work is also focused on nearest neighbour distances and the statistical entropy of the nearest neighbour distance [114,115].

The optimisation of mechanical properties of composites is based on the knowledge of the relationship between the microstructure and macrostructure. The early theories that were developed considered the matrix, reinforcement properties and their respective volume fractions. These theories include that proposed by Voigt [116] in the late 1920's in which he assumed an equal strain approximation in tensile deformation (a parallel connection between matrix and filler). During the same time, Reuss [117] (1929) developed an expression for an equal stress approximation; a series connection between matrix and fillers. Thus the combination of the two theories into what is now referred to as the Voigt-Reuss (Rule of Mixtures) model showed the existence of both an upper and a lower bound on material elastic properties. The Voigt-Reuss theory assumes a state of uniform strain or uniform stress in the individual phases of the filled system.

Further significant developments were made in the 1960's including Paul (*contained in ref* [118]) (1960), Hashin and Shtrikman [119, 120] (1962, 1963), Hashin and Rosen [121] (1964), and Hill [122] (1965) just to mention a few. The researchers developed variational methods, self-consistent methods and exact solutions. These solutions are based upon the assumption that the effective mechanical properties of a composite are dependent on the summation of the behaviour of the elementary particles contained therein. However, the

theories overlook the effect of physical properties such as shape, aspect ratio and distribution of particles [123].

A modification of the Voigt and Reuss theory which takes into account the parallel and series connection of particles was considered by Veldkamp [124]. Elastic properties of composites were determined by taking into account the particle arrangement, shape and volume fraction of fillers. Different particle distribution arrangements including cluster [125] or homogeneous arrangement [126] yield different effective mechanical properties of the composite. Statistical approaches are essential to apply to the two-phase materials in order to fully explain the effective properties of the composite. The statistical methods that have been used to evaluate the overall mechanical properties of the composite include the following:

- Representative volume element (RVE) [127]: RVE is used to predict the effective properties of random heterogeneous materials. In this method, a RVE size is defined for a given precision of the estimation of the required overall effective property. The challenge when using the RVE method is in defining the RVE size. Whilst one might want to reduce computational time, care should be taken such that the RVE size is not too small for the type of boundary conditions used. The computed apparent properties for each volume size are used to define the precision of the estimation.

- Nearest neighbour distances (NND) [128], nearest neighbour index (NNI) and statistical entropy of the nearest neighbour distance (SENND) [111]: This method determines the mean distance between neighbouring particles for multi-phase composites. The determination of the particle mean distances is important in the

evaluation of composite effective properties. A nearest neighbour index; predicting the clustering (or otherwise) of particles can be determined from the density of particles nearest neighbour mean distances.

- Random sequential addition/adsorption (RSA) [107-110]: This is a method used to pack particles (spheres) without overlapping. The particles are introduced on a surface in a random and sequential manner. The method assumes that once particles are inserted their position is clamped i.e maintains a fixed position.

- Average field theory/mean field models [126]: A complex system with a number of interacting particles can be simplified using the average field theory. The theory replaces all interactions with an average/effective interaction thereby reducing a multi-body problem into an effective one-body problem.

It should also be noted that the aspect ratios of the filler particles play an important role in predicting the mechanical properties of the composite materials [129, 130]. Aspect ratio is defined as the ratio of a particle's largest dimension to the smallest. Composite stiffness increases as a function of filler volume fraction and aspect ratio, whilst strength depends on particle size. The strength and stiffness of a composite can therefore be increased by a high aspect ratio filler of a very small particle size.

2.5 Hybrid Materials

The study of materials with positive and negative Poisson's ratio combined into hybrid materials is the subject of this work and has also been investigated during the course of this work independently elsewhere [11, 12, 13]. Hybrid materials can be defined as a combination of two or more materials, optimally serving a specific engineering purpose

[106]. Designing hybrid composites from already existing materials is cheaper when compared to the process of developing new alloys or polymer chemistries. The use of hybridisation techniques allows for the combination of different materials with unique physical properties in order to develop a new composite structure with improved properties compared to the starting materials. This concept has been utilised in this study where auxetic films have been used together with conventional films to develop multi-layer interface systems in an attempt to investigate the effect of hybridisation on the through-thickness Young's modulus.

The advantages of hybrid materials comprising of auxetic and conventional constituents have been postulated by some researchers [11, 12, 131]. For instance, when a unidirectional composite comprising of non-auxetic constituents is loaded in tension, both matrix and fibres undergo lateral contraction leading to fibre-matrix interfacial de-bonding. If auxetic fibres are used instead, the fibre-matrix interface can be maintained by matching the Poisson's ratio of the fibres to that of the matrix such that when the latter contracts, the fibres compensate the loss in matrix transverse dimension through lateral expansion of a similar magnitude. This phenomenon has been implicated as the driving force for the improvement observed in composite stiffness when auxetic fibres are bound together by a conventional matrix [131]. Nkansah et al [131] reported that the transverse modulus of a continuous fibre-reinforced composite can be increased by up to four fold by changing the Poisson's ratio of the matrix from +0.3 to −0.9.

In this work, the through-thickness Young's modulus of a multi-layered interface consisting of conventional and auxetic PP films held together by a polymeric adhesive are investigated. In a modeling study, thick multi-layered auxetic/conventional laminates have recently been investigated by Kocer and co-workers [12]. Kocer et al [12] reported a

predicted increase in the Young's modulus of a 10 mm thick multi-layer composite containing alternating auxetic and non-auxetic layers. An increase in the overall Young's modulus was observed when the Young's modulus of the auxetic material was equal to or greater than that of the non-auxetic material.

2.6 α-Cristobalite

Silica is an oxide of silicon, (SiO_2), and is the most abundant mineral in the earth's crust, existing in a number of distinct crystalline forms such as quartz, cristobalite and tridymite. All the crystalline polymorphs of SiO_2 form complex three-dimensional corner-linked networks of SiO_4 tetrahedral units linked together by shared vertices in different arrangements. Silicon-oxygen bond lengths and angles vary between the different crystal forms. Silica has a number of uses including glass manufacturing, abrasives, refractory products, semi-conductors, lenses for optical instruments and piezoelectric materials.

α-cristobalite has attracted a lot of attention because of its single-crystalline auxetic behaviour. From an experimental point of view, Yaganeh-Haeri [132] confirmed the presence of auxetic behaviour in α-cristobalite using laser Brillouin spectroscopy. The presence of auxetic behaviour in α-cristobalite was also reported by Keskar and Chelikowsky [133] who discovered the auxetic behaviour through *ab initio* modelling. The Poisson's ratio of α-cristobalite was reported to be direction dependent, and ranged from +0.08 to -0.5, with -0.5 occurring when the elastic compliance tensor is rotated about the crystallographic *a*-axis at approximately 42° from the *b*-axis [132]. The crystalline aggregate Poisson's ratio is auxetic with a value of -0.16. The Reuss and Voigt bounds of the single phase aggregate yielded a Poisson's ratio of -0.13 and -0.19 respectively. This result is significant since it implies particulate aggregates of α-cristobalite could represent a candidate auxetic filler material in filled composite systems.

Keskar and Chelikowsky [133] observed the inter-atomic O-O distances in α-cristobalite to have almost constant values under uni-axial force. By fixing the O-O distances in their simulations, the O-Si-O angles were also fixed, giving rigid SiO_4 tetrahedra. With this constraint Keskar and Chelikowsky [133] reported that cooperative rotation of rigid SiO_4 tetrahedral units can lead to the occurrence of auxetic behaviour in α-cristobalite. Alderson and Evans [134] showed that concurrent rotation and dilation of the tetrahedra predicts more accurately the occurrence of auxetic behaviour in α-cristobalite. However, it is difficult to pin-point the origin of the auxetic effect from calculations and simulations alone since different deformation mechanisms (e.g. distortion of the tetrahedra) operating at the molecular level cannot be ruled out.

Other researchers have argued that the observed negative Poisson's ratios in the silicate α-cristobalite is due to a two dimensional rotation of rigid units model involving rotating rectangles, analogous to that illustrated in Fig 2.4 [28]. The lattice positions occupied by oxygen and silicon atoms connect to form distinct square patterns.

The occurrence of auxetic behaviour at the molecular level in α-cristobalite presented a host of opportunities in the design of materials exhibiting intrinsic auxetic behaviour and more research is in progress [135-137].

CHAPTER 3: PARAMETRIC STUDY ON POLYPROPYLENE FILM PRODUCTION

3.0 Introduction

In the literature review section, Chapter 2, various forms of natural or synthetic auxetic materials were discussed. These include foams, fibres and films. Given the advantages identified for auxetic materials, interfaces containing auxetic constituents will be explored and compared with interfaces in the absence of auxetic constituents. The first approach uses auxetic films within a multi-layer film adhesive interface system. Consequently, a parametric study of the production of both auxetic and conventional films is required.

The parametric matrix was established based on previous work performed at Bolton [47, 67, 68, 69]. In the present work extrusion temperatures of 157, 159, 161, 163, 165, 170, 180, 190 and 230 °C were investigated alongside a systematic variation of other processing parameters such as the screw speed and take-up speeds. Films were extruded at screw speeds between 0.525 and 2.10 rad s^{-1} and take-up speeds in the range of 0.0225 to 0.15 m s^{-1}. The effects of varying these processing parameters (extrusion temperature, take-up speed and screw speed) on the characteristics of extruded films (auxetic behaviour and Young's modulus) were investigated. Mechanical characterisation of the extruded polypropylene films was carried out using video-extensometry in conjunction with a microtensile testing machine. A recently published study of the processing parameters for auxetic PP fibres [71] revealed that the key processing parameter was the processing temperature while the screw and take-up speeds also induced some degree of variation in the level of auxetic and other elastic behaviours.

3.1. Extrusion of Polypropylene Powder

Polypropylene films were produced via a specially adapted melt extrusion process with polypropylene powder used as the precursor. The polypropylene powder used was Coathylene PB0580, supplied by Univar plc, which is the same powder that was used in the previous production of auxetic polypropylene cylinders [60] and fibres [67].

The extruder used in this work is shown in Fig 3.1. The extruder has five temperature zones which can be independently set. A flat set temperature profile was used; i.e. the same temperature was set in each of the five zones. The powder is transferred to the die zone area by a single screw. By maintaining a constant feed rate, the powder is forced to move along the extruder barrel towards the slit die (63.5 mm ×14.2 mm × 0.38 mm) , Fig 3.2, for film production. As the film or tape emerges from the slit, it is directed to a set of take up rollers, and ultimately collected.

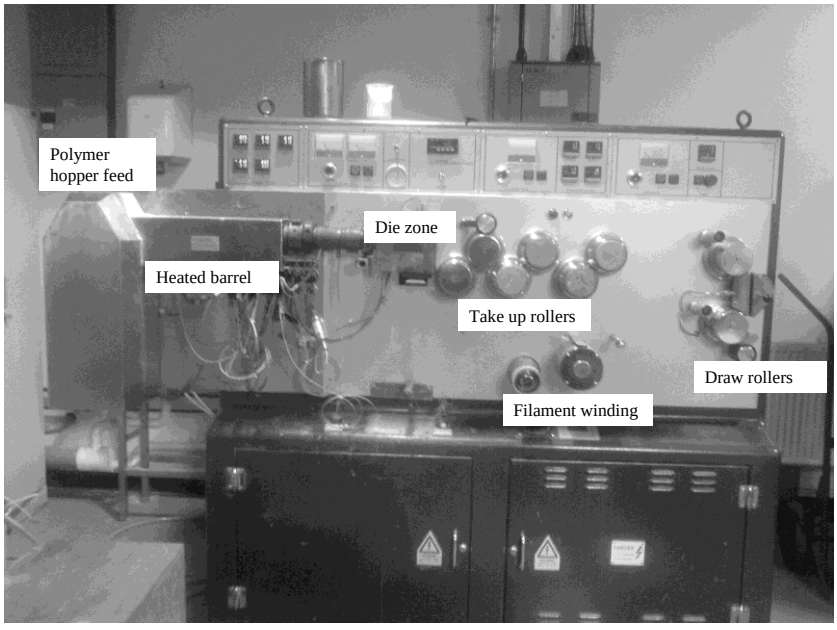

Fig 3.1 Melt extruder used in the production of polypropylene films.

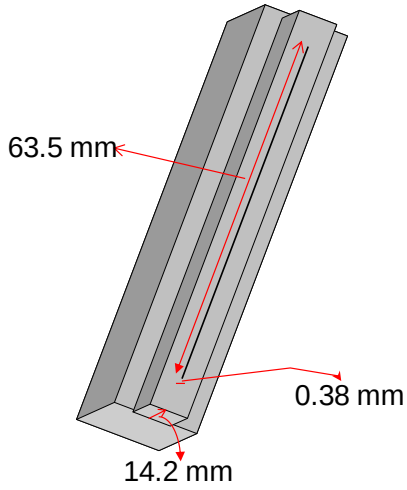

Fig 3.2 Schematic diagram of the slit die.

The processing parameters used for the production of films in this study are summarised in Table 3.1. In order to observe the effect of a specific parameter, it was systematically varied while the other parameters were kept constant. To investigate temperature effects in the range 157 to 190 ºC, the screw speed was maintained at 1.05 $rads^{-1}$ while a constant take-up speed of 0.0225 ms^{-1} was used. In another case, the effect of screw speed was investigated in the range of 0.53 to 2.1 $rads^{-1}$, with the temperature and the take-up speed held constant at 159 ºC and 0.0225 ms^{-1}, respectively. The effect of take-up speeds in the range of 0.0225 to 0.15 ms^{-1} were investigated at a processing temperature of 159 ºC and a constant screw speed of 1.05 rad s^{-1}. The temperature was controlled and monitored by manually measuring the heaters on the five zones of the extruder using a thermocouple. The measured temperature was compared to the target (set) temperature to ensure a steady state and avoid any significant variations. The range of parameters was chosen such that a fine grained approach around the previously established set temperature (159 °C) for auxetic fibres could be investigated. In addition, a course grained approach was also employed for temperatures greater than 170 °C. In addition, for comparison purposes with previous work on extruded fibres, a batch of films were produced at a processing temperature of 230 °C, screw speed of 1.05 rad s^{-1} and a take-up speed of 0.03 m s^{-1}.

Table 3.1: Extrusion parameters used in the production of conventional and auxetic polypropylene films.

Set Temperature (° C)	Measured Temperature (° C)					Screw Speed ($rads^{-1}$)	Take-up Speed (ms^{-1})
	Zone 1	Zone 2	Zone 3	Zone 4	Zone 5		
157	157	157	157	157	158	1.050	0.0225
159	160	160	159	160	160	0.525	0.0225
159	160	160	159	160	160	1.050	0.0225
159	160	160	159	160	160	1.050	0.0300
159	160	160	159	160	160	1.050	0.0450
159	160	160	159	160	160	1.050	0.0750
159	160	160	159	160	160	1.050	0.1500
159	160	160	159	160	160	2.100	0.0225
161	162	160	160	162	162	1.050	0.0225
163	164	164	163	164	164	1.050	0.0225
165	165	165	166	166	166	1.050	0.0225
170	169	168	172	170	172	1.050	0.0225
180	179	180	180	181	181	1.050	0.0225
180	179	180	180	181	181	2.100	0.0225
180	179	180	180	181	181	2.100	0.0675
190	191	190	188	191	192	1.050	0.0225
230	230	230	230	230	230	1.050	0.0300

Films that were extruded at a temperature of 230 °C, screw speed of 1.05 rad s^{-1} and a take-up speed of 0.03 m s^{-1} had a nominal thickness (measurements taken using a thickness tester and micrometer screw gauge) in the range 0.16 to 0.20 mm. Films that were extruded at a temperature of 159 °C, screw speed of 1.05 rad s^{-1} and a take-up speed of 0.03 m s^{-1} had a coarser texture with an average thickness of between 0.20 and 0.25 mm. The lengths of films produced were not restricted. All films were produced under atmospheric conditions (temperature 25 °C; atmospheric pressure).

3.2 Characterisation of Polypropylene Films

The edges of the films were trimmed using a razor blade prior to testing in order to remove the extra polymer on the edges. The average width of a test film after edge trimming was approximately 10 mm. The collected films were subjected to tensile testing along the

extrusion direction as shown by the red arrows in Fig 3.3. A Deben Microtensile testing machine was used together with a MESSPHYSIK ME 46 video-extensometer [138] to determine the Poisson's ratio and Young's modulus of the films. The Deben Microtest instrument allows for a range of materials to be deformed by uniaxial loads up to 300 N. Markers on the sample illustrated in Fig 3.3 applied using a black marker pen describe a square of dimensions 6 mm x 6 mm which provided the targets for the video-extensometer to track the expansion and contraction of the test specimen. The length and width of the film test specimens were 50 mm and 10 mm, respectively. A photograph of the marked film is shown in Fig 3.4.

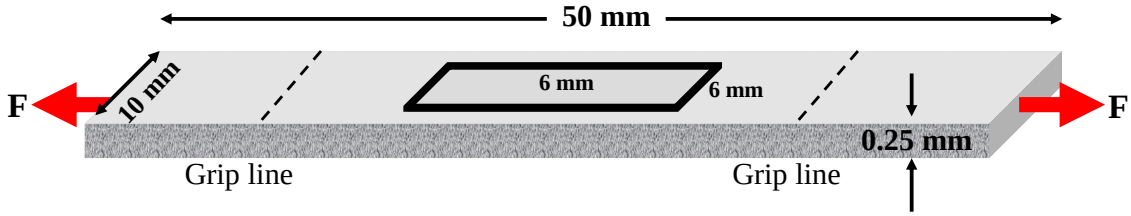

Fig 3.3 An illustration of a test specimen showing a marked target area (black box). Red arrows indicate the direction of applied force, F (i.e. tensile testing).

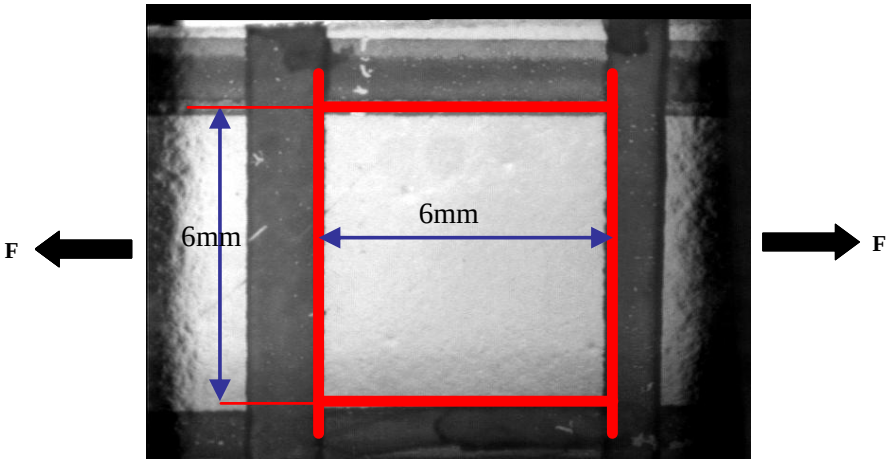

Fig 3.4 Photograph of a marked film (red square box showing marked edges) with arrows indicating testing direction.

Cyclic tests using travel limits maintained between 0.5 and 1% strain levels were performed at a loading strain rate of 0.1 mm min^{-1} for all specimens tested in this work. The travel limits were chosen such that developing strains would always be within the elastic region as pre-determined from previous research work [67, 70]. Force, time and displacement data were obtained and analysed using stress/strain equations described in later sections.

The video-extensometer is a commercially available software package developed by Messphysik GmbH [138] that measures strains and/or extensions. In the present work, video-extensometry was used to measure distances between fiducial markers during tensile loading in both axial and transverse directions. These measurements provided raw data that were subsequently analysed to obtain the Poisson's ratio of the films. The video-extensometry software works with a special measurement algorithm based on the evaluation of the black and white contrast between the specimen surface and the targets. A greater contrast ensures more accurate and consistent measured data. This technique is a non-contact strain measuring system that can determine the relative shift in the spacing between two markers or targets as a result of mechanical deformation of the specimen.

The camera was rigidly mounted onto a tripod and was positioned such that there was no obstruction between the lens and specimen during testing, Fig 3.5. During the tensile test, it was ensured that there was no movement of the specimen relative to the camera lens. Any such movements could lead to incorrect measurements. A schematic of the methodology is shown in Fig 3.6.

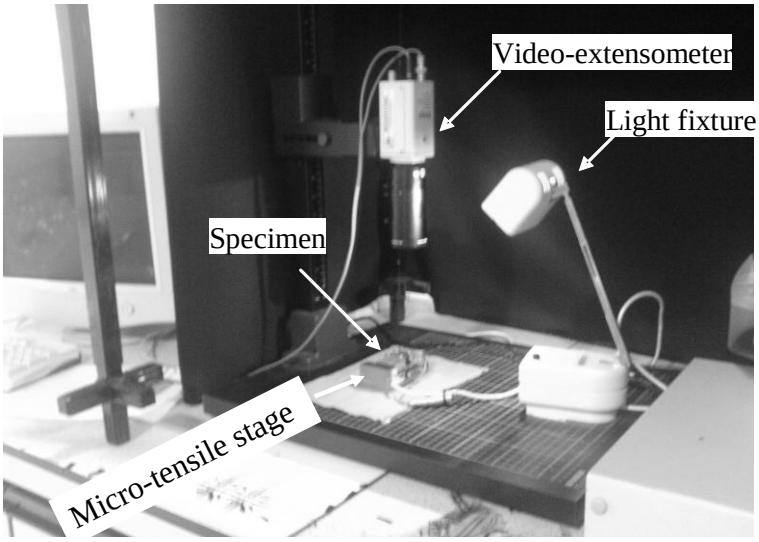

Fig 3.5 Photograph of the video-extensometer set up.

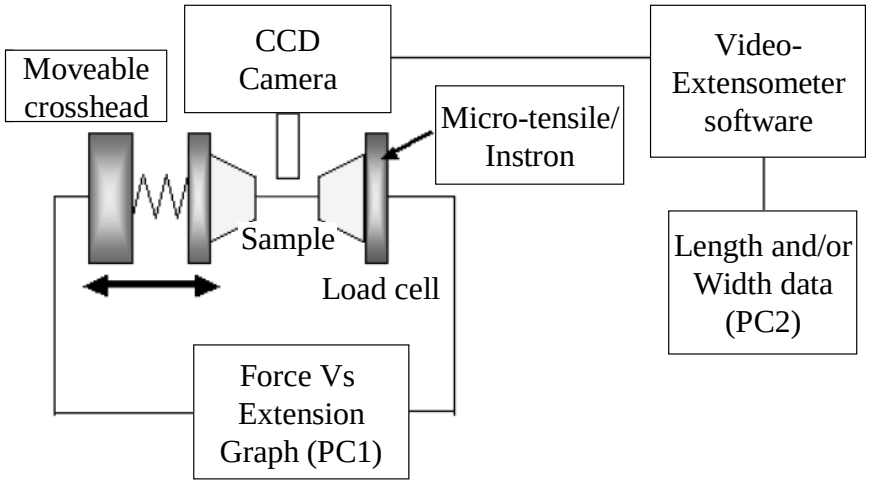

Fig 3.6 Schematic of the video-extensometer set-up [70].

It is essential to ensure adequate, even and constant intensified illumination of the sample to enable the changes in contrast to be defined accurately for the targets and specimen edges. To achieve the above prescribed lighting conditions, video-extensometry was performed in a black box with a lamp as a light source as shown in Fig 3.5. The camera lens was sharply focused and the diaphragm (aperture/iris) was adjusted to produce the required image. Transverse width data were collected for 10 sections along the length of the film, from which the average width section data could be calculated.

3.3 Data Analysis

Fig 3.7 shows the variation of length and the ten width sections on application of strain to a film produced at a temperature of 230 °C, screw speed of 1.05 rads^{-1} and a take-up speed of 0.03 ms^{-1}.

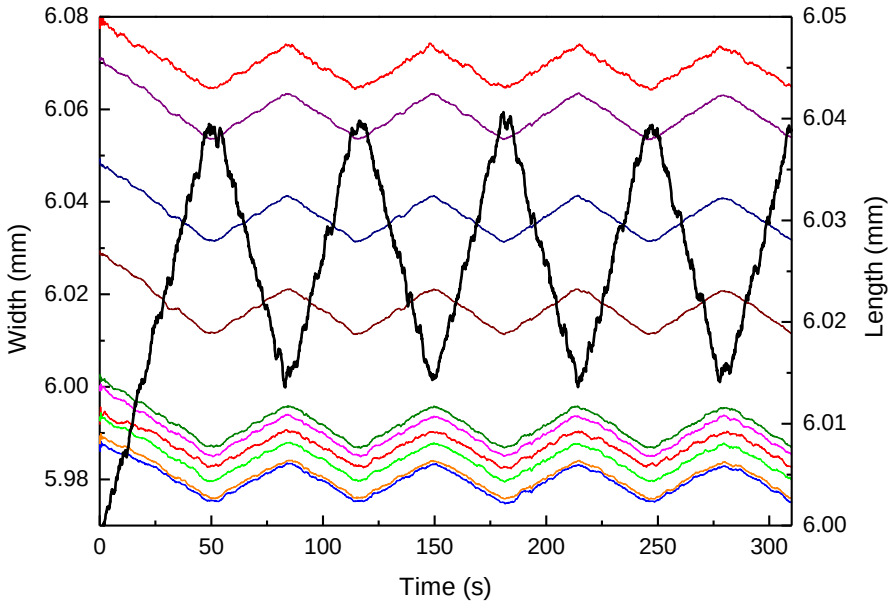

Fig 3.7 Video-extensometry displacement in length (bold black line) and width of ten sections (all other traces) as a function of time for a polypropylene film produced at a temperature of 230 °C, screw speed of 1.05 rads^{-1} and take-up speed of 0.03 m s^{-1}.

From these data, it can be seen that as the length increases, the width decreases, which is characteristic of a conventional material. The variations in length and width are repeatable over the number of cycles performed. In all test experiments, the extension phase of the third cycle of the graph was used to calculate the true strain. The approach follows that previously employed for analysing auxetic fibres and films [67, 68, 70]. By plotting the true strain in the *Y* direction (transverse) against the true strain in the *X* direction (longitudinal), the Poisson's ratio, υ_{XY}, was calculated. The formulae for the calculation of true strains along the *X* and *Y*- directions, respectively, are given by:

$$\varepsilon_X = \ln\left(\frac{l}{l_0}\right) \tag{3.1}$$

$$\varepsilon_Y = \ln\left(\frac{w}{w_0}\right) \tag{3.2}$$

where l_0 is the original length and l is the deformed length of the film, and w_0 is the original width and w is the deformed width of the film.

It should be noted that even though true strain was used for the determination of Poisson's ratio, the use of engineering strain would produce similar results because the strains considered herein are low such that the true strain and engineering strain definitions give very similar values.

A plot of the true strain in the *Y*-direction versus true strain in the *X*-direction is shown in Fig 3.8(a) for each of the ten width sections. From the slopes of the two extreme cases in Fig 3.8(a), the measured Poisson's ratio for this specimen ranges from υ = +0.33 to +0.38. Fig 3.8(b) shows the plot of average true strain in the *Y*-direction versus true strain in the *X*-direction for the film. The line of best fit indicating the average of data for each of the ten sections during the extension phase of the third cycle is shown as a solid line, Fig 3.8(b). Using these data, the average Poisson's ratio was calculated from the negative of the slope of the best fit line to be +0.35.

Engineering stress is plotted against engineering strain in the loading direction of the film in Fig 3.9. The slope of these data corresponds to the Young's modulus. The engineering stress and strains were obtained using equations 3.3 and 3.4.

$$\sigma = \frac{F}{A} \tag{3.3}$$

$$\varepsilon = \frac{\Delta l}{l} \qquad 3.4$$

where σ is the engineering stress, F is the force applied, A is the cross sectional area, ε is the engineering strain, Δl is the change in length and l is the original length in the longitudinal direction of the film.

A Young's modulus value of 0.37 GPa was determined from the slope of the best-fit straight line in Fig. 3.9. It should be noted that since the engineering strain and true strain values are similar within the strain levels considered in this work (≤ 1%) the use of true and engineering strains in the determination of Poisson's ratios and Young's modulus, respectively, is not an issue. The Poisson's ratio and the Young's modulus along the extrusion direction for all of the other films produced in this study were determined using the same methods as described above.

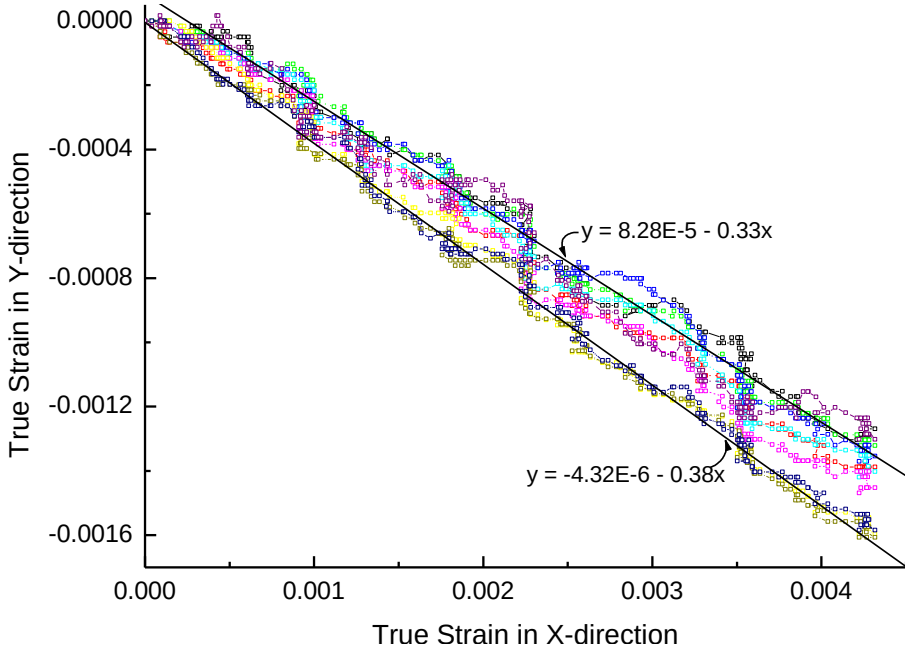

Fig 3.8(a) True strain in the *Y*-direction for each of the ten width sections plotted against the true strain in the *X*-direction for a film extruded at a temperature of 230 °C, screw speed of 1.05rads^{-1} and take-up speed of 0.03m s^{-1}.

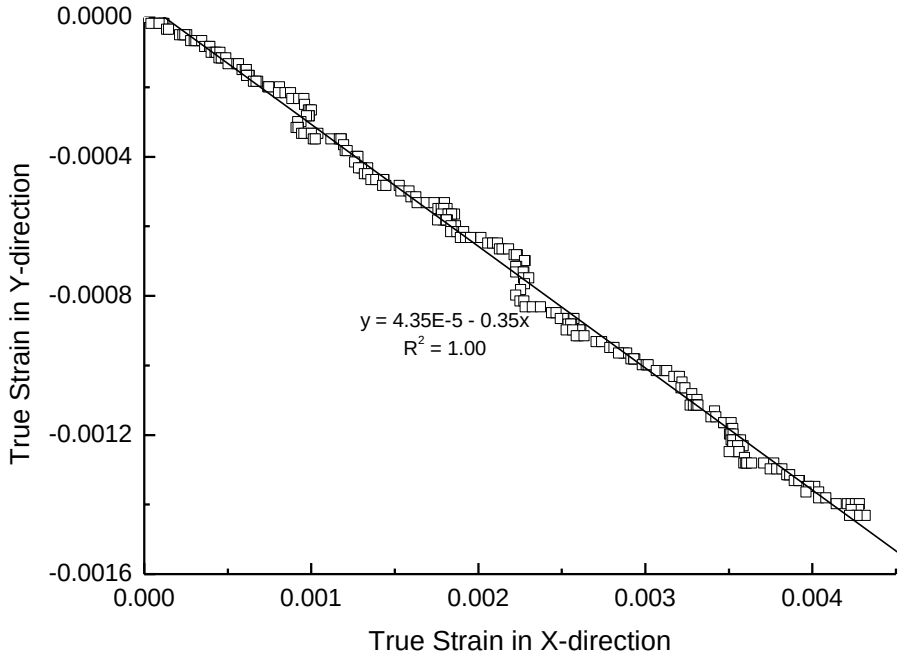

Fig 3.8(b) Average true strain in the *Y*-direction versus true strain in the *X*-direction for the film produced at a temperature of 230 °C, screw speed of 1.05 rads^{-1} and a take-up speed of 0.03 ms^{-1}.

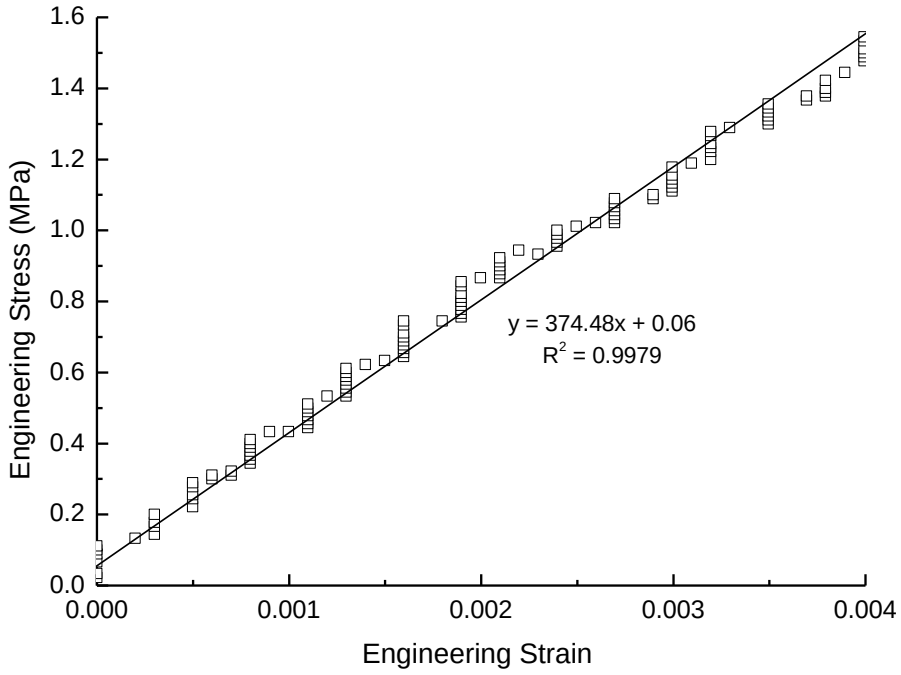

Fig 3.9 Engineering stress versus engineering strain in the extrusion direction for a polypropylene film extruded at a temperature of 230 °C, screw speed of 1.05 rads^{-1} and take-up speed of 0.03 m s^{-1}. The data are collected from the micro-tensile machine.

A video-extensometer data set for a film produced using processing parameters previously established [67,70] to lead to auxetic behaviour; i.e. a temperature of 159 °C, a screw speed of 1.05 rads^{-1} and a take-up speed of 0.03 ms^{-1}, is now considered. Fig 3.10 shows that the curves for width (ten sections) and length are in phase throughout all regions, indicating that this film is auxetic; i.e. the width increases with length.

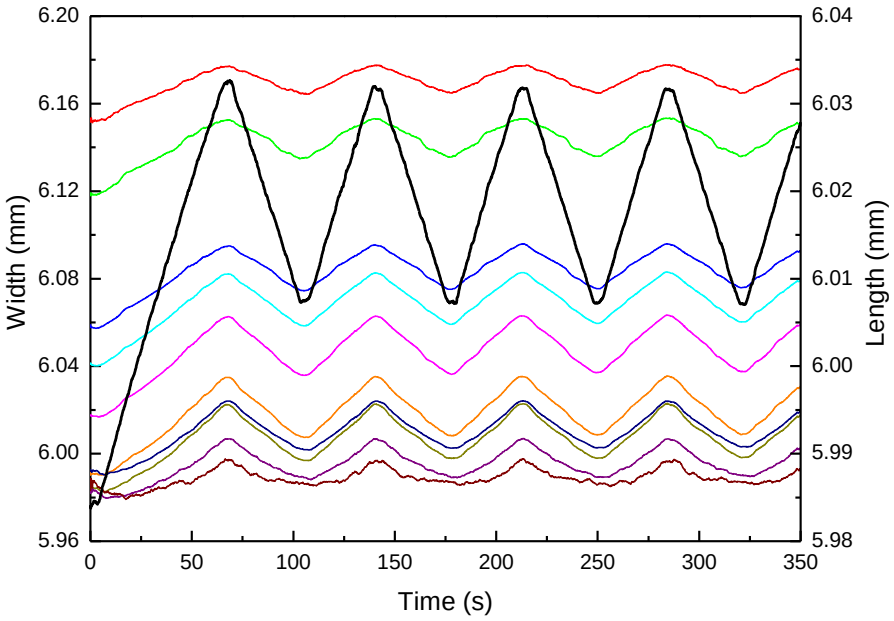

Fig 3.10 Video-extensometry displacement in length (bold line) and width of ten sections (all other traces) as a function of time for a polypropylene film produced at a temperature of 159 °C, screw speed of 1.05 rads^{-1} and take-up speed of 0.03 m s^{-1}.

From the plot of transverse strain for each individual section, Fig 3.11a, the range of Poisson's ratio determined for this sample is $\upsilon = -0.69$ to -1.07. Fig 3.11b shows the average transverse true strain versus longitudinal true strain constructed from the third cycle of Fig 3.10. An average Poisson's ratio of -0.82 was calculated for a PP film extruded at a temperature of 159 °C, screw speed of 1.05 rads^{-1} and take-up speed of 0.03 m s^{-1}.

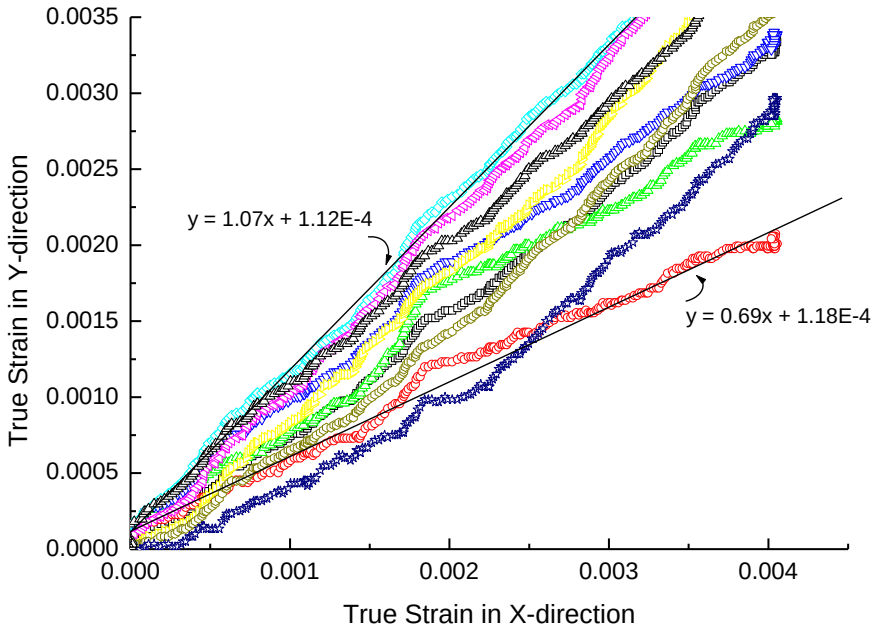

Fig 3.11(a) True strain in the *Y*-direction for each of the ten width sections plotted against the true strain in the *X*-direction for a film extruded at a temperature of 159 °C, screw speed of 1.05 rads^{-1} and take-up speed of 0.03m s^{-1}.

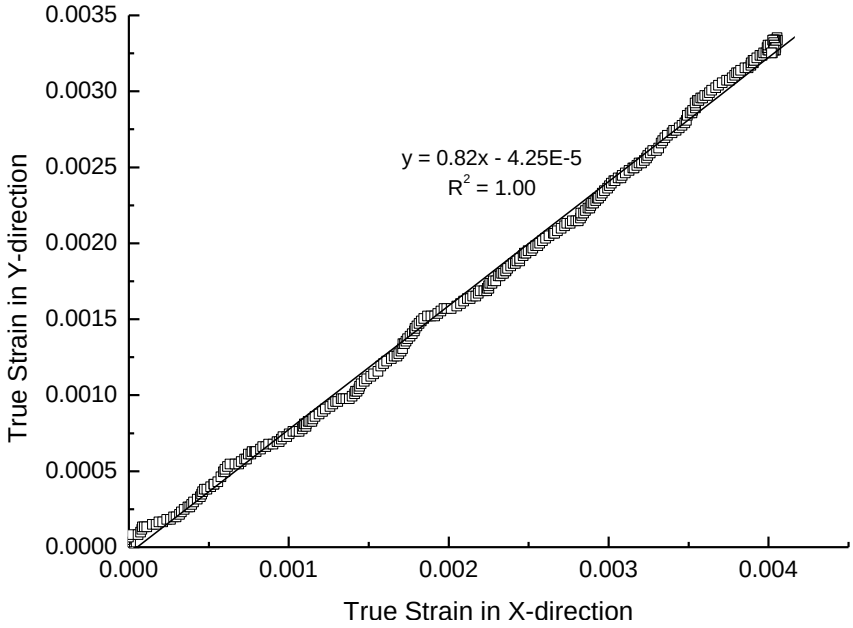

Fig 3.11(b) Average true strain in the *Y*-direction versus true strain in the *X*-direction for the film produced at a temperature of 159 °C, screw speed of 1.05 rads^{-1} and a take-up speed of 0.03 ms^{-1}.

The Young's modulus of this film was calculated from the gradient of the engineering stress versus engineering strain graph shown in Fig 3.12, giving a value of 0.39 GPa.

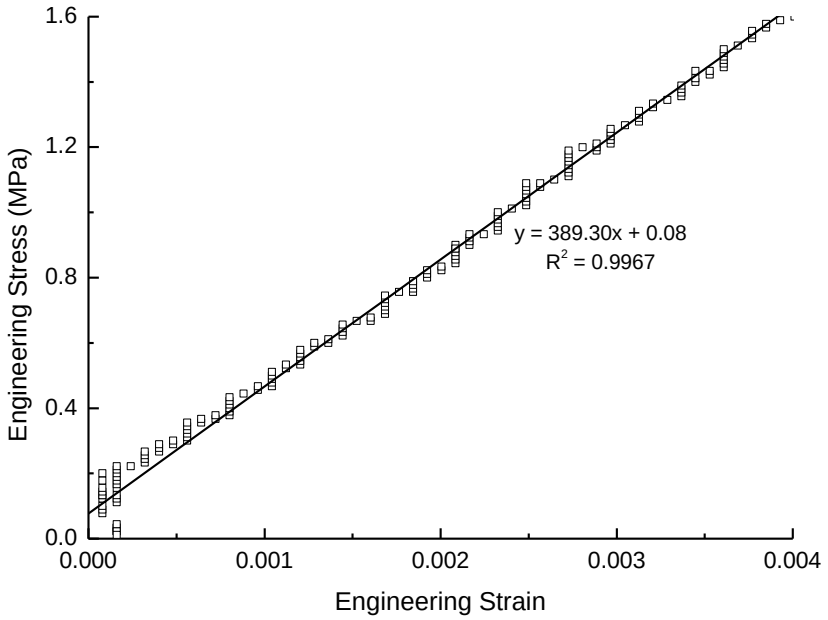

Fig 3.12 Engineering stress versus engineering strain in extrusion direction for a polypropylene film extruded at a temperature of 159 °C, screw speed of 1.05 rads^{-1} and take-up speed of 0.03 m s^{-1}.

3.4 Results

A summary of the Poisson's ratio and Young's modulus results obtained from the tested samples is shown in Table 3.2. Percentage auxeticity is also included in the table and was calculated as the fraction of specimens that gave auxetic behaviour (in all the ten width sections) of all test specimens which were cut out of the same PP film. At least 10 specimens were cut and tested from each sample. A discussion of the effect of the various parameters is considered in the following sections.

Table 3.2 Values of Poisson's ratio (range), percent auxeticity and Young's modulus for the polypropylene films tested.

Processing Temperature (° C)	Screw Speed ($rads^{-1}$)	Take-up Speed ($m\ s^{-1}$)	Poisson's Ratio	Percent Auxeticity (%)	Young's Modulus (GPa)
157	1.05	0.0225	-1.08 to +0.80	10	0.17±0.07
159	0.525	0.0225	+0.21 to +0.40	0	0.31±0.06
159	1.05	0.0225	-0.95 to -0.40	100	0.34±0.05
159	1.05	0.0300	-1.02 to +0.42	50	0.55±0.17
159	1.05	0.0450	-0.75 to +0.19	63	0.45±0.08
159	1.05	0.0750	-0.80 to +0.32	50	0.41±0.13
159	1.05	0.1500	-0.83 to -0.22	100	0.24±0.05
159	2.10	0.0225	-0.18 to +0.42	40	0.25±0.05
161	1.05	0.0225	-0.51 to 0.49	25	0.76±0.05
163	1.05	0.0225	-0.47 to 0.41	40	0.67±0.06
165	1.05	0.0225	-0.09 to +0.37	20	0.90±0.24
170	1.05	0.0225	+0.22 to +0.58	0	0.57±0.14
180	1.05	0.0225	+0.22 to +0.38	0	0.51±0.06
180	2.10	0.0225	-0.32 to +0.54	20	0.36±0.02
180	2.10	0.0675	-0.71 to -0.37	100	0.33±0.05
190	1.05	0.0225	-0.12 to +0.35	20	0.30±0.05
230	1.05	0.0300	+0.34 to +0.43	0	0.34±0.09

The films were found to display non-uniform mechanical properties along the extrusion direction. The non-uniformity of the films presents a challenge for their characterisation, and was most evident in films in which not all sections along the film length were auxetic, i.e. both auxetic and conventional sections were observed.

All extrusions were carried out when the extruder had equilibrated. Extruder parameters and ambient temperature were monitored during processing and no significant variations were found. The mechanical property variations along the extrusion direction have been suggested from previous studies on auxetic fibres and films under similar extrusion conditions to arise from the discrete nature of the granular microstructure and the proximity of the grain size and the extruded film/fibre thickness dimensions. A detailed discussion of factors that may cause non-uniformity along the extrusion direction is found

in the literature review, Section 2.2. In addition, it has also been observed that melt extrusion is challenging when extruding fine powder instead of pellets. The conveyance and flow of PP pellets is uniform since larger particles give rise to a desirable co-efficient of friction necessary to easily move the polymer forward within the extruder barrel. On the other hand, PP powder tends to stick together causing a non-uniform flow of the material.

3.4.1 Effect of Varying Extrusion Temperature

The variation in the Young's modulus as a function of extrusion temperature whilst maintaining screw and take-up speeds of 1.05 rad s^{-1} and 0.0225 m s^{-1}, respectively, is presented in Fig 3.13.

The Young's modulus is lowest at 157 ºC, rising steeply and peaking at 165 ºC after which there is a gradual reduction back to a value (at an extrusion temperature of 190 ºC) close to that of the specimens produced at 159 ºC.

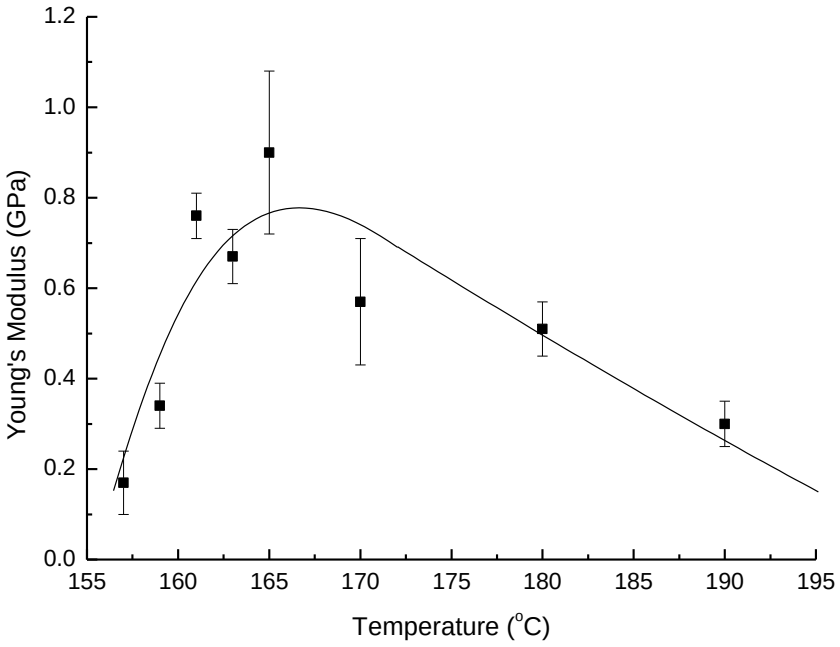

Fig 3.13 The Young's modulus plotted as a function of temperature for polypropylene films extruded at screw and take-up speeds of 1.05 rad s^{-1} and 0.0225 m s^{-1}, respectively.

The curve in the figure has been inserted in order to guide the eye through the trends.

The variation in the Poisson's ratio as a function of temperature is presented in Fig 3.14.

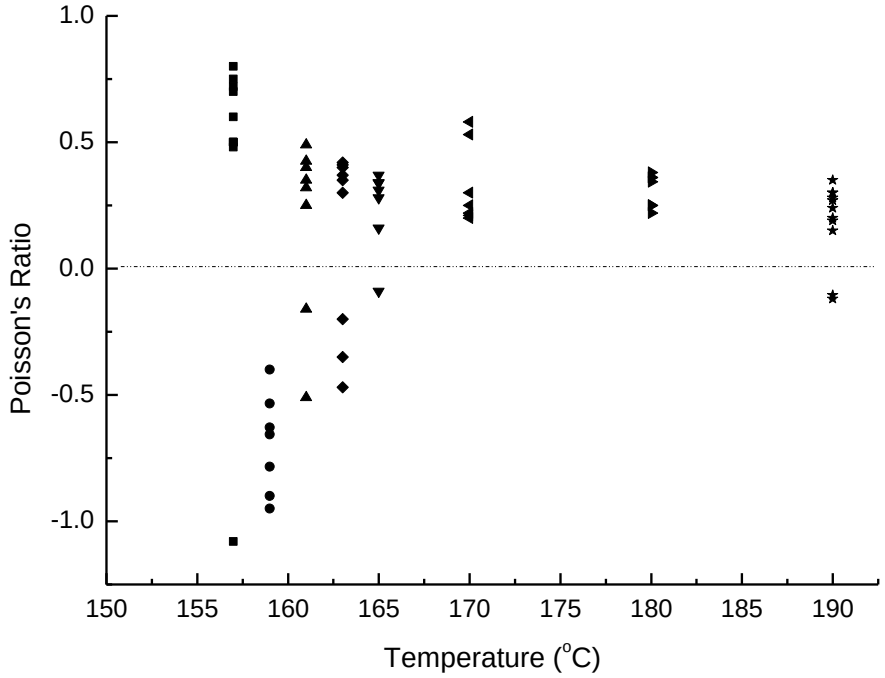

Fig 3.14 The Poisson's ratio plotted as a function of temperature for polypropylene films extruded at screw and take-up speeds of 1.05 rad s^{-1} and 0.0225 m s^{-1}, respectively.

The values of all samples tested are shown as discrete points in Fig 3.14 to clearly demonstrate the distribution in sign, magnitude and proportions of negative and positive Poisson's ratios.

These data show that melt extrusion at 159 ºC produced 100% auxetic films (negative Poisson's ratio) while that at 170 and 180 ºC produced films with 100% conventional (positive Poisson's ratio) characteristics with Poisson's ratio similar to textbook values of polypropylene (υ = +0.35). However, at the other processing temperatures, the films obtained show both auxetic and conventional characteristics; that is a combination of behaviours. The largest negative value, υ = -1.08, was observed for polypropylene films produced at a processing temperature of 157 ºC, which is below the 159 ºC processing

temperature previously established to produce auxetic films. It should be noted, though, that the auxetic behaviour for this processing condition was only observed in 1 of the 10 samples tested, giving the auxeticity probability value of 10% quoted in Table 3.2. The film produced at 157 °C also displayed the highest positive Poisson's ratio values.

Auxetic characteristics were also observed at 161 ºC, 163 ºC and 165 ºC and, surprisingly, at 190 ºC, with Poisson's ratio values in the range υ = -0.12 to υ = +0.35 for the latter extrusion temperature. For films processed at 161 ºC, 163 ºC and 165 ºC the magnitude of the negative Poisson's ratio regions tend to decrease as extrusion temperature increases. At 190 ºC, there is 20 % chance that any given section of the extruded film may show auxetic behaviour. The production of auxetic films at 190 ºC is significant as this is the first time that auxetic behaviour has been seen at such a high temperature in extruded polymeric films, i.e. 29 ºC above the peak melting temperature of 161 ºC defined by differential scanning calorimetry (DSC) [67].

3.4.2 Effect of Varying the Screw Speed

The effect of varying the screw speed on the Poisson's ratio for films with set extruder temperature of 159 °C and take-up speed of 0.0225ms^{-1} is presented in Fig 3.15. The films produced at 0.525 rads^{-1} and 159 °C are completely conventional, having a range of positive Poisson's ratios around the textbook value for polypropylene. As the extruder screw speed is increased to 1.05 rads^{-1}, the films become completely auxetic, i.e. probability of obtaining a film with all regions showing auxeticity is 100%. At this screw speed, the films display quite large negative values of Poisson's ratio (-0.40 to -0.95). The highest screw speed investigated here (2.1rads^{-1}) also shows some auxetic character, with 4 out of 10 tested films (40% probability) showing auxetic characteristics with Poisson's

ratio values as low as υ = -0.18.

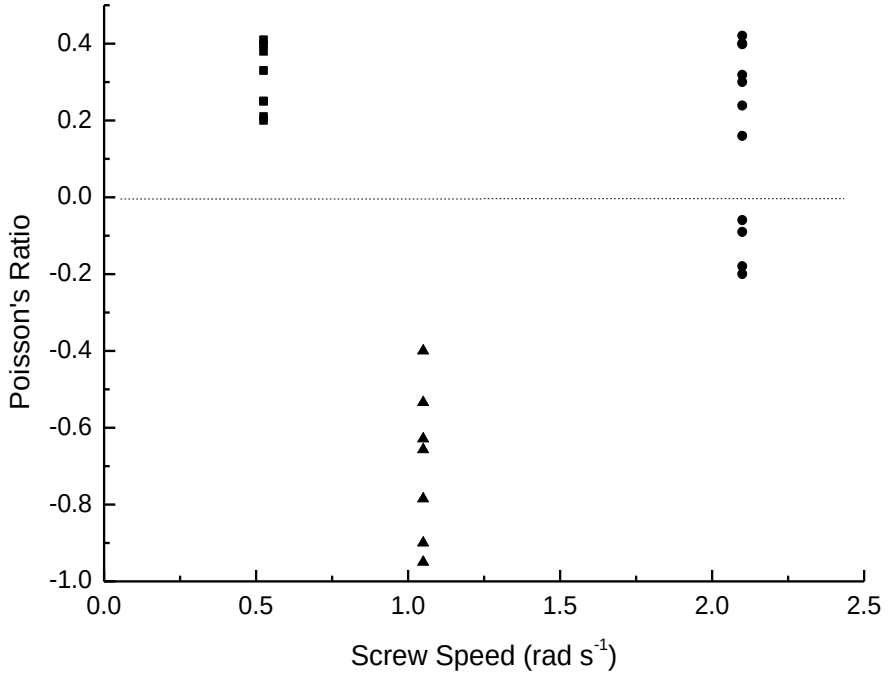

Fig 3.15 The variation of the Poisson's ratio as a function of the screw speed (rad s^{-1}) for polypropylene films extruded at 159 °C and a take-up speed of 0.0225 m s^{-1}.

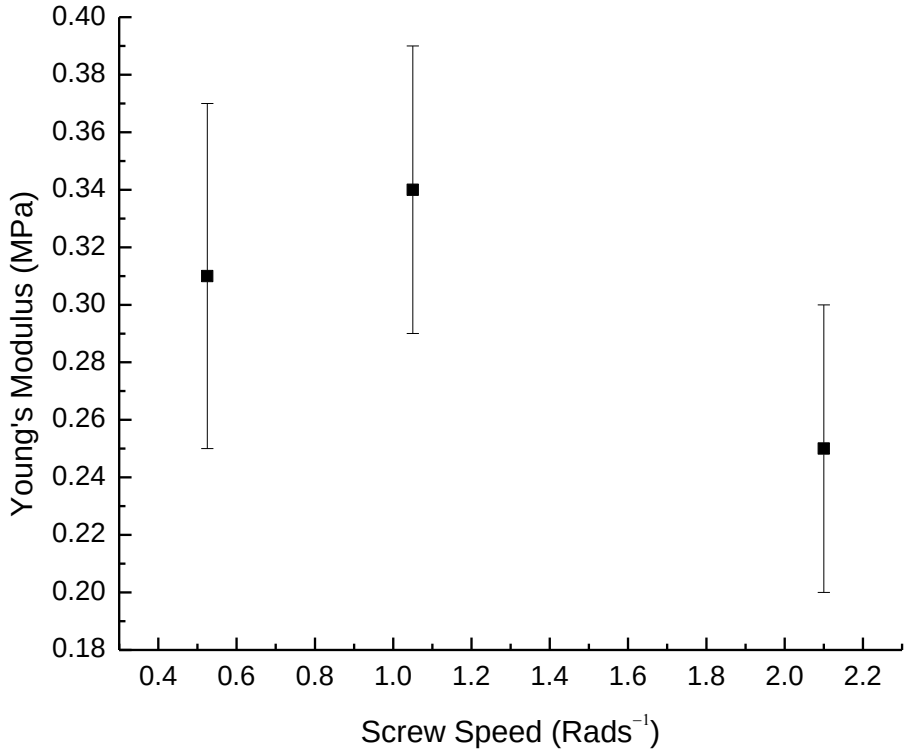

Fig 3.16 The variation of the Young's modulus as a function of the screw speed (rad s^{-1}) for polypropylene films extruded at 159 °C and a take-up speed of 0.0225 m s^{-1}.

At the screw speed of 1.05 rads^{-1} corresponding to the full auxetic behaviour, the highest Young's modulus of the films is observed (Fig. 3.16). This is interesting in that full auxetic films can attain a high Young's modulus by varying extruder parameters. The Young's modulus decreases with further increase in screw speed above 1.05 rads^{-1}.

3.4.3 Effect of Varying the Take-up Speed

The effect of varying the take-up speed on the Poisson's ratio of the films at set temperature of 159 ºC and screw speed of 1.05 rads^{-1} is shown in Fig 3.17.

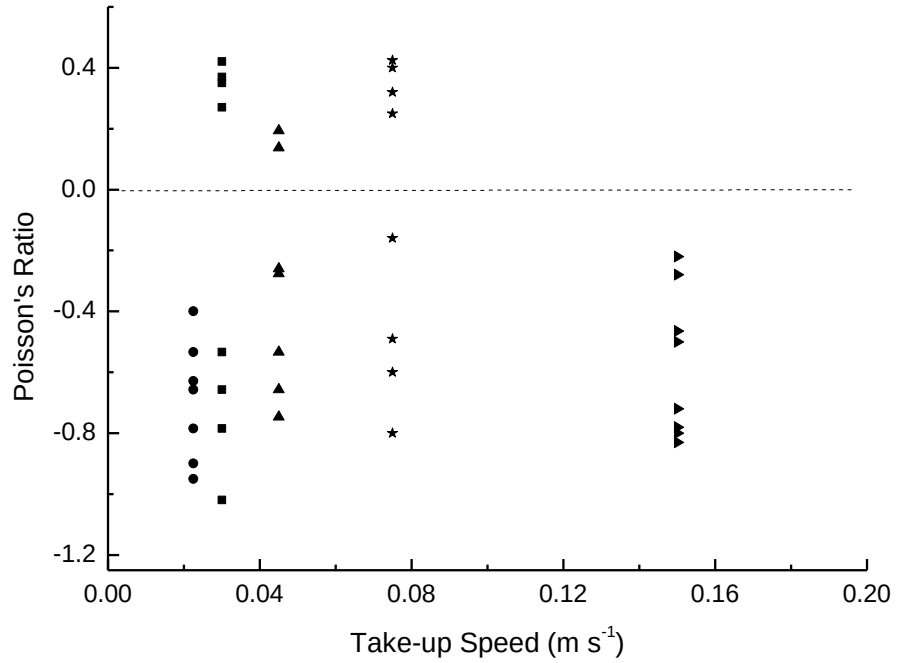

Fig 3.17 Variation of the Poisson's ratio as a function of take-up speed (m s^{-1}) for polypropylene films extruded at 159 °C with a screw speed of 1.05 rad s^{-1}.

Auxetic behaviour with varying percentage auxeticity was observed when the temperature and screw speed were kept constant at 159 °C and 1.05 rad s^{-1} respectively, while the take-up speed was varied from 0.0225 to 0.1500 ms^{-1} (Fig 3.17). Films with 100% auxetic behaviour were observed at take-up speeds of 0.0225 and 0.1500 ms^{-1}, whilst at least 50% auxetic behaviour was observed for take-up speeds between these two extremes.

Fig 3.18 shows the variation of Young's modulus with take-up speed for films processed at 159 °C and a screw speed of 1.05 rad s^{-1}.

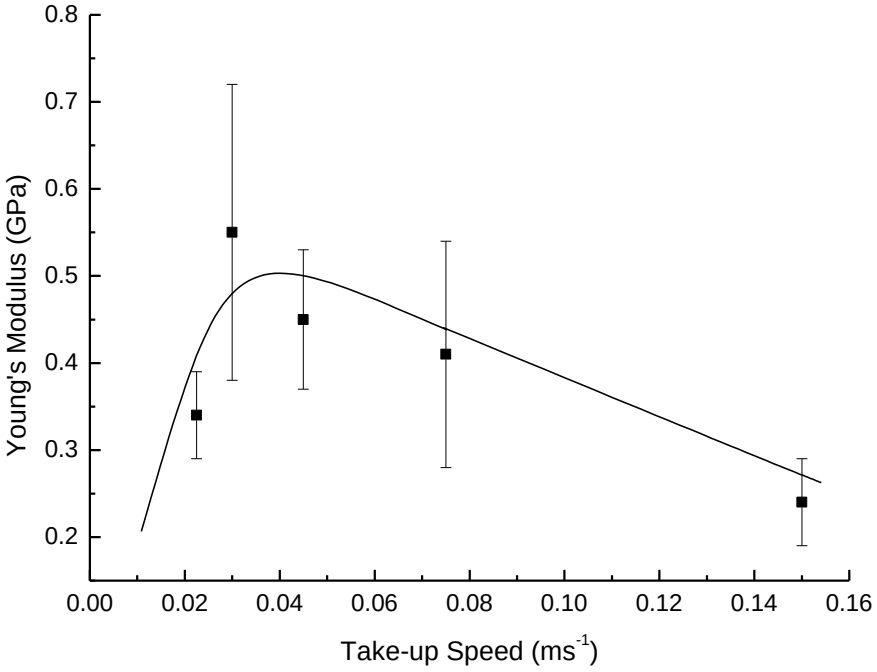

Fig 3.18 Variation of the Young's modulus as a function of take-up speed (m s^{-1}) for polypropylene films extruded at 159 °C and a screw speed of 1.05 rad s^{-1}.

The Young's modulus was also affected by varying take-up speed, with the lowest modulus values coinciding with parameters leading to 100% auxetic behaviour, Fig 3.18. The curve in the Fig 3.18 has been inserted in order to guide the eye.

Auxetic behaviour was also measured at the higher temperature of 180 °C and higher screw speed of 2.10 rad s^{-1}, for take-up speeds of 0.0225 and 0.0675 m s^{-1} (Table 3.2). The higher take-up speed of 0.0675 m s^{-1} resulted in 100% auxetic behaviour. High screw speeds reduce the residence time of the powder within the extruder, while high take-up speeds result in a faster collection of the material.

At the processing temperature of 180 ºC and a screw speed of 1.05 $rads^{-1}$, no auxetic

characteristics were observed (see Table 3.2). The occurrence of significant auxetic character at high temperatures (relative to the peak melting temperature), achieved through higher screw and/or take-up speeds than previously established at 159 ºC, is a significant discovery and may have implications for the commercial production of auxetic films and fibres.

3.5 Discussion

This study has shown that it is possible to produce polypropylene films with auxetic characteristics, not only in the vicinity of the previously established extruder temperature of 159 °C, but also at temperatures significantly higher than 159 º C by varying the screw speed and take-up speed. In order to understand the occurrence of auxetic behaviour at low (~159 °C) and high (~180 -190°C) extruder temperatures regimes, it is worthwhile to consider the evolution of the polymer microstructure during the extrusion process.

As already noted polymers exhibiting auxetic behaviour are known [5, 10, 14, 23, 25, 40, 58, 60, 67, 70]. In most cases the observation of a negative Poisson's ratio is believed to be a result of the microstructure of the material. However, unlike polymers produced in the form of rods, the extruded fibres/films are thought to be auxetic not because they exhibit a microporous nodule-fibril structure, but rather due to a reduced-porosity fused-particle microstructure [67, 70]. This microstructure has been suggested to form by the surface melting of the powder particles leading to the structure shown in Fig 3.19, which is a section through an auxetic polypropylene fibre. This fibre was processed at 159 °C, which is slightly below the peak melting temperature of 161 °C. The micrograph shows that the individual powder particles are still distinct, which would suggest that they did not become fully molten during the extrusion process. It is now necessary to consider the extent to

which particles are fully molten during the extrusion process employed in this work.

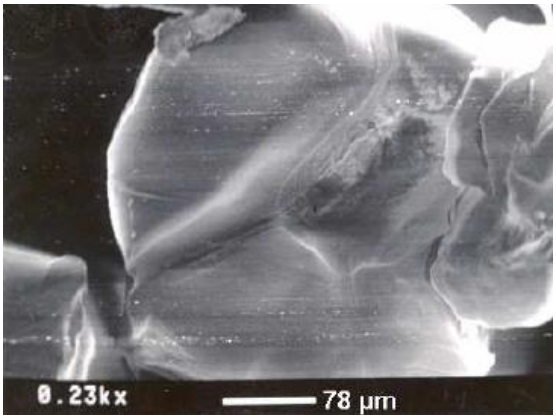

Fig 3.19 Micrograph of an auxetic fibre showing the fused particle microstructure [67].

As a first approximation, consider a powder particle likened to a sphere undergoing melting. The change in particle radius with time can then be calculated from [139]:

$$\frac{dR_\theta}{dt} = \frac{-h_\theta (T_b - T_o)}{\rho_s \Delta H} \tag{3.5}$$

where R_θ is the local radius of the particle, t is the dwell time in the extruder, h_θ is the local heat transfer coefficient (in this case 24.5 W/m^{2}K) [140], T_b is the bulk temperature (i.e. the set temperature of the extruder), T_o is the melting temperature, ρ_s is the density (in this case, 905 kg m^{-3}) [140] and ΔH is the latent heat (in this case, 134 kJ kg^{-1}) [140].

Integrating equation (3.5) with respect to time gives an equation that relates the local radius as a function of residence time, which is effectively the amount of radial melting of the particle, such that:

$$R_\theta = \frac{-h_\theta (T_b - T_o)t}{\rho_s \Delta H} + R_o \tag{3.6}$$

where R_o is the initial radius of the particle (at t=0). See appendix A for the plot of R_θ against $T_b - T_o$ when screw speed is 1.05 rad s^{-1}.

The average dwell time for the particles in the extruder [141] is given by:

$$t = \frac{2HD_s}{ND_b\delta_f} \tag{3.7}$$

where δ_f is the flight clearance of the screw (in this case 0.02 mm), H is the channel depth (in this case 2.5 mm), D_s is the screw diameter (in this case 25.4 mm), D_b is the inside diameter of the barrel and is given by $D_s + 2\delta_f$, so in this case is equal to 25.44 mm and N is the number of rotations of the screw. N was allowed to vary from 1 to 30 revolutions per minute and the dwell times associated with these values are given in Table 3.3.

Table 3.3 Dwell time of polymer associated with given screw rotations.

Screw Speed (rad s^{-1})	Screw Rotations, N (revs min^{-1})	Dwell Time (s)
0.105	1	15000
0.525	5	3000
1.050	10	1500
1.575	15	996
2.100	20	750
2.625	25	600
3.15	30	480

The average powder particle size used in this work was measured previously at 52 ± 13 μm in diameter. Once the calculated local radius exceeds 19.5 to 32.5μm, the powder is then presumed fully molten.

Very simple manipulations of equations (3.5-3.7) using the variables examined herein reveal that, for a screw speed of 1.05 rad s^{-1}, complete melting of the polypropylene powder will occur when $T_b - T_o$ ~0.1°C. In other words, the temperature window for processing is very tightly defined. It should be noted here, though, that the equations examined are very much a first approximation. The melting point of the polypropylene powder used is not as sharp as is assumed, with the DSC trace (Fig 3.20) [67] indicating a

20-30 ºC range of temperature from the onset of melting to the peak melting temperature of 161 ºC. The bulk temperature will also vary depending on particle location. Hence the calculated (see Fig.1 in Appendix A) relatively sharp window of 0.1°C above melting point will in practice be larger. In practice, as shown in Fig 3.14, there is a very small temperature range for producing 100% auxetic films (T = 159 ± 1°C), with partial auxetic behaviour seen in the range 157-165 ºC.

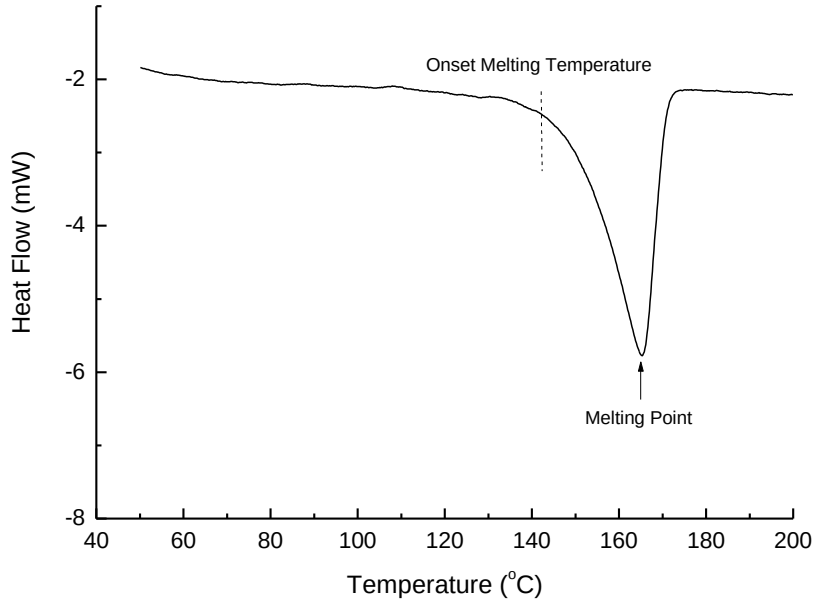

Fig 3.20 Differential scanning calorimetry profile for polypropylene powder in nitrogen flowing at 100 mL/min.

Interestingly, at processing temperatures of 190 °C (screw speed 1.05 rads^{-1} and take-up speed 0.0225 ms^{-1}) and 180 ºC (screw speed 2.10 rads^{-1} and take-up speeds of 0.0225 and 0.0675 ms^{-1}), well above the onset of melting and indeed the peak melting temperature, auxetic behaviour is also obtained.

It is unlikely, then, that a fused-particle microstructure exists in the extruded film at these processing temperatures, and so an alternative mechanism may give rise to the auxetic effect in these cases. It is possible that the auxetic behaviour in these high processing

temperature cases is due to random molecular chain arrangement i.e. a different mechanism (operating at a different microstructural length scale) may be occurring.

The simplified and basic particle melting model presented herein does not provide any insight into the effect of varying the take-up speed. However, it is interesting to note that changing this parameter (see Fig 3.17 and Table 3.2) still results in auxetic characteristics observed in the polypropylene films as was the case when this variable was considered for the auxetic fibres [67]. Therefore, it was concluded that increasing the take-up speed led to an introduction of slight tensional drawing of the fibres whilst still retaining their microstructure and this appears to be the case here. It is striking, however, that 100% auxetic behaviour was seen for films produced at a relatively high take-up speed of 0.15 m s^{-1} at a processing temperature of 159 ºC.

In this work we have seen that sometimes it is possible to produce films showing both conventional and auxetic behaviours; i.e. mixed behaviour. The non-uniformity of the properties of the films may arise from several factors including the type of raw materials and the extrusion process itself. Radial temperature gradients exist within the extruder barrel [84, 86]. The heat supplied by the barrel heaters has to be conducted through the entire thickness of the barrel through to the polymer. However the problems with this kind of energy transfer are the considerable heat losses by conduction, convection and radiation. In addition, the low thermal conductivity of the polymer presents yet more challenges. On the other hand, extra heat is contributed by the intense pressure and friction taking place inside the barrel. The mechanical energy of the screw is transformed into heat. The action of the screw adds to temperature gradients through localized shear heating. This results in the polymer within the extruder experiencing non-uniform temperature. The measurement of the actual temperature of the polymer may then be necessary in understanding the

processing temperature dependency of the films. The measurement of the polymer in the middle of the barrel is, however, challenging because of the rotating screw.

Equation 2.1 can give some insight into the scatter in the Young's modulus of the films. By rearranging Eq. 2.1, an expression (Eq. 3.8) is obtained;

$$E = 2G(1+\upsilon) \tag{3.8}$$

where E is Young's modulus, G is shear modulus and υ is the Poisson's ratio.

Eq. 3.8 suggests that as the Poisson's ratio of a material becomes negative, the Young's modulus is reduced if the shear modulus is kept constant. It is possible that purely auxetic films have lower Young's modulus values than purely conventional films. However, combining Eqs. 2.1 and 2.2, an expression for Young's modulus in terms of bulk modulus, K, and Poisson's ratio, υ, can also be obtained, Eq. 3.9:

$$E = 3K(1-2\upsilon) \tag{3.9}$$

Contrary to Eq 3.8, Eq. 3.9 suggests that if the Poisson's ratio of a material becomes negative, the Young's modulus will increase as long as the bulk modulus is kept constant. Hence regions which are shear modulus dominated may experience different Young's moduli to regions which are bulk modulus dominated, even if the Poisson's ratios are the same for both regions. In any case, for either scenario, the variation in Poisson's ratio observed in the films produced in this work could also explain the variations in the values of the Young's modulus. Although Equations 3.8 and 3.9 apply to isotropic materials, they are useful in giving an insight in understanding the data presented in Figs 3.13 and 3.16. Interestingly in Fig 3.16, the screw speed of 1.05 $rads^{-1}$ produces the highest modulus, coinciding with full auxetic behaviour. This is, then, an example of a material having

higher modulus as it becomes auxetic.

Previous works by different researchers show that subtle changes in structure can have dramatic effects on the sign and magnitude of Poisson's ratio [142, 143]. A classic example is that of a hexagonal honeycomb deforming by rotation (hinging) of the ribs, considered in detail by Masters and Evans [142]. For positive values of the angle θ the off-axis rib makes with the vertical (2) axis (defined in Fig. 3.21), the on-axis Poisson's ratios υ_{12} and υ_{21} are positive, and for negative values of θ (corresponding to the re-entrant hexagon geometry shown in the top left insert of Fig. 3.21) they are negative. When θ is zero (rectangular lattice geometry, middle top insert of Fig. 1), $\upsilon_{12} = 0$ and $\upsilon_{21} = \pm\infty$.

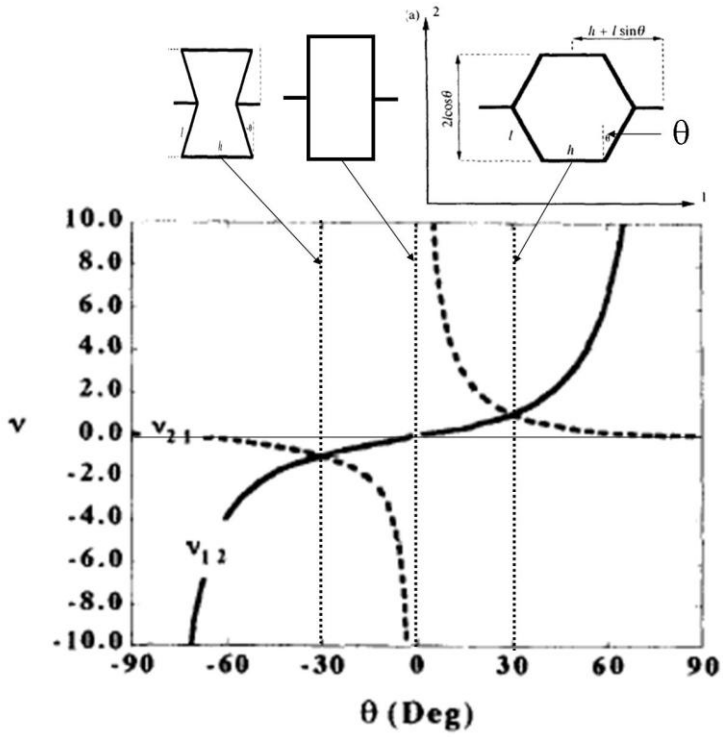

Fig 3.21 On-axis Poisson's ratios *vs* honeycomb angle θ for hexagonal honeycomb deforming by hinging of the honeycomb ribs (inserts at top of figure give schematic diagrams of cell geometry at different values of θ). Adapted from Masters and Evans 1996 [142].

It is clear from Fig 3.21 that small perturbations in θ about $\theta = 0$ lead to dramatic changes in Poisson's ratios. A small increase in θ, leads to positive Poisson's ratios, with υ_{21} having especially large magnitude. Conversely, a small decrease in θ, leads to negative Poisson's ratios, with υ_{21} again having especially large magnitude. Hence the two structures with honeycomb angles of $\theta + \Delta\theta$ and $\theta - \Delta\theta$ at ($\theta = 0$) are topologically very similar (almost rectangular grid) yet have markedly different Poisson's ratios associated with them.

Masters and Evans show this is not the case for the Young's moduli, which have similar values for both structures. Recent work by Horrigan et. al. [143] on simulated optimisation of disordered structures with negative Poisson's ratios also confirms that subtle changes in geometry (even though there might be no obvious visible changes) have a large effect on the magnitude and sign of the Poisson's ratio.

The subtle differences in the two structures may be achieved through adopting different process parameters. For example, one might consider the final honeycomb geometry is achieved through application of a tensile displacement in the horizontal (1) direction to an initially re-entrant geometry. The displacement rate and duration of the applied displacement will determine the final honeycomb geometry. Hence a honeycomb subjected to the same displacement rate but for a slightly longer duration may adopt the 'conventional' cell structure having $\theta > 0$, whereas the honeycomb to which the displacement was applied for a shorter period of time may have a final structure displaying $\theta < 0$. Alternatively, the final honeycomb geometry might conceivably be achieved through expansion of a gas within the cell structure of the honeycomb due to heating of the gas. Again processing parameters (in this case time and temperature of heating) might be controlled to achieve different final geometries having different structures and very different Poisson's ratio.

Turning now specifically to the PP films studied in this work. Previously an interlocked hexagonal particle model has been proposed [45] as a first approximation to the fused particulate structure believed to be present in the auxetic films. A negative-to-positive Poisson's ratio transition was predicted for subtle differences in particle shape (e.g. particle angle α~ 90° in Fig 3.22).

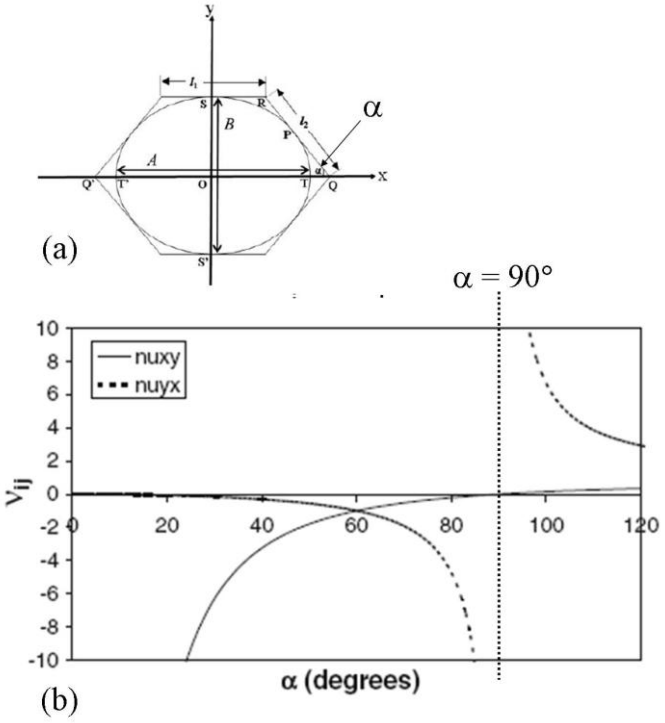

Fig 3.22 (a) Schematic of hexagonal particle showing particle angle α; (b) on-axis Poisson's ratios *vs* α for interlocked hexagonal particle array deforming by sliding of particles along particle interlocks. Adapted from Ravirala et. al. 2007 [72].

Films containing regions of film structure approximated by particles with α + Δα and α - Δα (about α = 90°) would then be topologically very similar yet have markedly different Poisson's ratios associated with them. This would be consistent with the measured Poisson's ratio data presented in Fig. 3.14. Subtle changes in film microstructure (e.g. particle size/shape) would be expected as processing parameters are varied (e.g. extrusion temperature), leading to changes in the measured Poisson's ratio, until the particulate microstructure disappears when the polymer becomes fully molten (at T > 165°C in Fig.

3.14).

Ravirala [45] also proposed a scheme showing the evolution of the film microstructure in terms of unmelted particles and resolidified melt interfaces, Fig 3.23. The network of unmelted particles was proposed to lead to the negative Poisson's ratio effect (around T_{onset}), whilst the resolidified melt interface regions provided positive Poisson's ratio material. The volume fraction of the interface region increases with extrusion temperature and so the proportion and magnitude of the auxetic effect decreases with increasing extrusion temperature (as found experimentally – Fig. 3.14) until the film microstructure consists of fully resolidified melt polymer (e.g. at T > 165 °C in Fig. 3.14). At $T < T_{onset}$ the volume fraction of the unmelted particles is higher than that of the resolidified melted polymer. Depending on the particle arrangement, it is possible to have a negative-to-positive Poisson's ratio transition, as was observed for the film produced at 157 °C, 1.05 rad s^{-1} and 0.0225 m s^{-1}, Fig. 3.14.

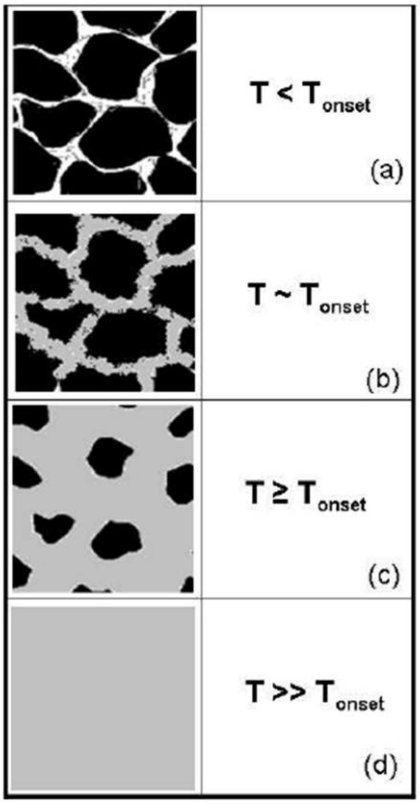

Fig 3.23 Schematic showing the effect of processing temperature in forming appropriate interconnected fused particulate structure. From Ravirala, 2006 [45].

It should be noted that the results obtained in this study also indicate that the process examined here is indeed complex. Further in-depth studies are necessary in order to gain a more complete understanding of the whole process. In addition, the study of the microstructure giving rise to auxetic films processed at temperatures higher than the onset of melting is imperative in understanding the auxetic mechanism in these films. If, as appears likely, the auxetic films produced at higher processing temperatures involve full melting of the polymer during the extrusion process, then the process is likely to be more viable in terms of commercial-scale production than the partial melt extrusion process of the prior art.

3.6 Summary

A parametric study of polypropylene films has been performed by varying the key processing parameters such as the extrusion temperature, the screw and the take-up speeds. The polypropylene films have been used in the development of multi-layered systems reported later in the thesis. It was found that auxetic behaviour was observed for the first time for processing polypropylene at temperatures well above the 159 ºC extrusion temperature previously established for that phenomenon [67,70,71], especially at 180 and 190 ºC. These observations suggest that there is a very complex interplay between the processing parameters (temperature and screw and take-up speeds) and film microstructure during the melt extrusion of polypropylene films. The occurrence of auxetic behaviour at processing temperatures higher than 159 ºC is of significant interest. The commercial production of auxetic films/fibres is difficult when the processing temperature is in the vicinity of the onset of melting temperature. This is because a commercial extruder is much larger than the laboratory extruder, and forcing partially-molten polymer through larger barrels introduces elevated risks such as pressure build-up and/or jamming of the extruder. Hence commercial melt extrusion of auxetic fibres/films at temperatures around

the onset temperature is likely to be difficult. The occurrence of auxetic behaviour well above the melt onset temperature provides a window of opportunity for commercial production of auxetic polymeric materials. The work reported here provides the impetus for further study to understand the microstructure responsible for auxetic behaviour at high extrusion temperatures.

CHAPTER 4: NUMERICAL AND ANALYTICAL MODELLING OF THE MULTI-LAYER SYSTEMS (YOUNG'S, SHEAR AND FLEXURAL MODULI)

4.0 Introduction

Polymer-based adhesives are commonly used in the joining of materials due to their large bonding surface area subsequently resulting in a reduction in stress concentrations within the joint. Adhesive-bonded joints are generally sensitive to shear and impact forces. As discussed in Chapter 2, auxetic materials can exhibit superior mechanical properties such as shear rigidity, impact resistance and fracture toughness. Consequently, their inclusion within interfacial bonding systems is envisaged to improve the overall mechanical performance of the interface. The objective of this study is to quantitatively evaluate the effect of the inclusion of auxetic films on the Young's, shear and flexural moduli of the hybrid material. The mechanical properties of multi-layered film-adhesive interfaces containing auxetic films are compared to interfaces containing conventional films.

This chapter describes a methodology used to model the through-thickness mechanical performance of multi-layered film(s)/adhesive interfaces. The Finite Element (FE) method was used to predict the through-thickness Young's and shear moduli of the interfaces. The predicted results were then verified against analytical solutions such as the modified Rule of Mixtures (RM) [144]. Two representative polymeric adhesives, one with a low (120 MPa) and another with a high (1700 MPa) Young's modulus value, relative to the film Young's modulus (340 MPa) were employed in the multi-layered interfaces and the effects of film Poisson's ratio on the effective mechanical properties of the multi-layered interfaces in the through-thickness dimension evaluated. Three types of multi-layered interfaces were modelled; those

which contained (i) conventional film only, (ii) auxetic film only or (iii) a combination of both. An illustration of multi-layer interfaces modelled in this study is shown in Fig 4.1.

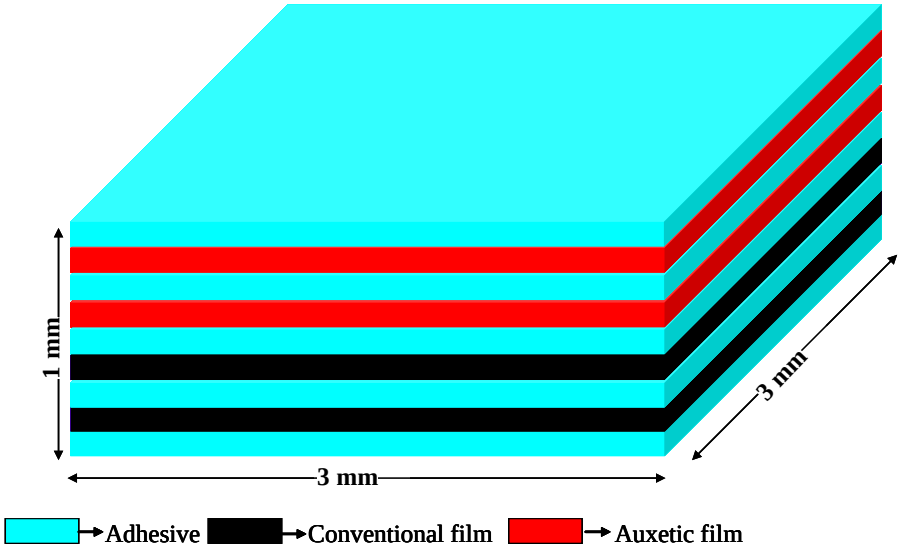

Fig 4.1 Illustration of a multi-layer interface used in the FE models.

The FE modelling method is discussed in terms of its origin and applicability in solving the problem at hand. The choice and number of elements used in the FE model was optimised using convergence methods which are also discussed in detail. A step-by-step discussion showing the FE model construction and the arrangement of films and adhesive layers is given in this chapter. This section precedes the discussion of analytical solutions used in this work including their derivation and modification for verification of the numerical modelling results.

4.1 Finite Element Modelling (FEM)

Finite Element modelling is a numerical technique that can be used to solve complex structural problems; e.g. the analysis of the mechanical behaviour of load-bearing structures. This may include structures that are subjected to uni-axial or multi-axial loads. The technique is also applicable to the assessment of material behaviour such as fatigue, vibration and heat transfer.

FEM is therefore an essential tool in the design optimisation of new products or performance improvements in existing products. While FEM has many potential applications, there is a need to validate results against experimental data in order to assess reliability. A great advantage of using modelling techniques to simulate real-life structural systems is the reduced costs to optimise parameters in an experimental test matrix without performing a large (often time-consuming and expensive) experimental test matrix in the laboratory.

In this work the ANSYS FE software (version 11.0) has been used. A general purpose FE model in ANSYS incorporates the following modules: pre-processor (geometry creation and meshing), solver and post-processor in a graphical user interface. The first step in developing the FE model requires the creation of a geometric representation of the structure in two or three-dimensions. Two-dimensional modelling geometries conserve structural simplicity and allow the analysis to be run using less advanced computing or operating systems. On the other hand, three-dimensional modelling geometries are more complex requiring larger and faster computer processing memory, but with a more realistic representation of real three-dimensional systems. Numerical modelling tools can be used to find solutions for linear or non-linear static and dynamic structural analysis, heat transfer, fluid mechanics, acoustic and electromagnetic problems.

FE modelling simulates the response of a physical system to structural loading, thermal and magnetic effects by using the underlying governing equations and the specific user-defined boundary conditions. Following the construction of a geometric structure, it is discretised; i.e. meshed to produce finite elements that are connected to adjacent neighbours at defined nodes. The mesh contains material and structural properties which define its reaction to specific loading conditions. The mesh can be refined; i.e. the number of elements or nodes can be

increased in order to improve the accuracy of the model. A major concern with FE modelling is the need to develop an alternative solution that can be used to provide assurance that the results are a reliable representation of the real structural behaviour. Where discrepancies are noted in relation to experimental data, it still can be a challenge to identify, quantify and correct errors introduced during the modelling process.

The determination of the through-thickness Young's and shear moduli of multi-layered film/adhesive interfaces is an important exercise that will lead to the gaining of fundamental insights into the role of auxetic constituents on the mechanical performance of the resultant interface. Classical Laminate Theory (CLT) can be been used to predict the mechanical performance of the interfaces, however the FE method provides extra information including the deformation patterns and the strain energy distribution during and after deformation. The FE method was thus chosen in order to the predict through-thickness Young's and shear moduli of three- and two-phase multi-layer interfaces.

4.2 FEM Methodology –Young's and Shear Moduli

Three-dimensional (3-D) multi-layered solid structures representing multi-component interfaces were constructed using the solid brick element, SOLID45. The SOLID45 element has eight nodes, each exhibiting three degrees of freedom, namely translations in the *X*, *Y*, and *Z*-axes. Different layers of a multi-component interface were connected using the gluing operation in ANSYS and the resultant structure subsequently meshed. In order to determine the Young's modulus in the through-thickness (*Z*-) direction of the multi-layer interface, a force (1 N) was applied (to a central node) normal to the top surface while the bottom surface was completely restrained from translational and rotational movements by fixing all nodal

degrees of freedom (DOF) to zero, as shown in Fig 4.2. The nodes on the loading surface were coupled in the *Z* direction to ensure a uniform distribution of displacement. The coupling ensures that all nodes translate by the same nodal displacement in the *Z* direction. The free edges of the multi-layer interface were left unconstrained to allow for transverse contraction and/or expansion under tensile loading.

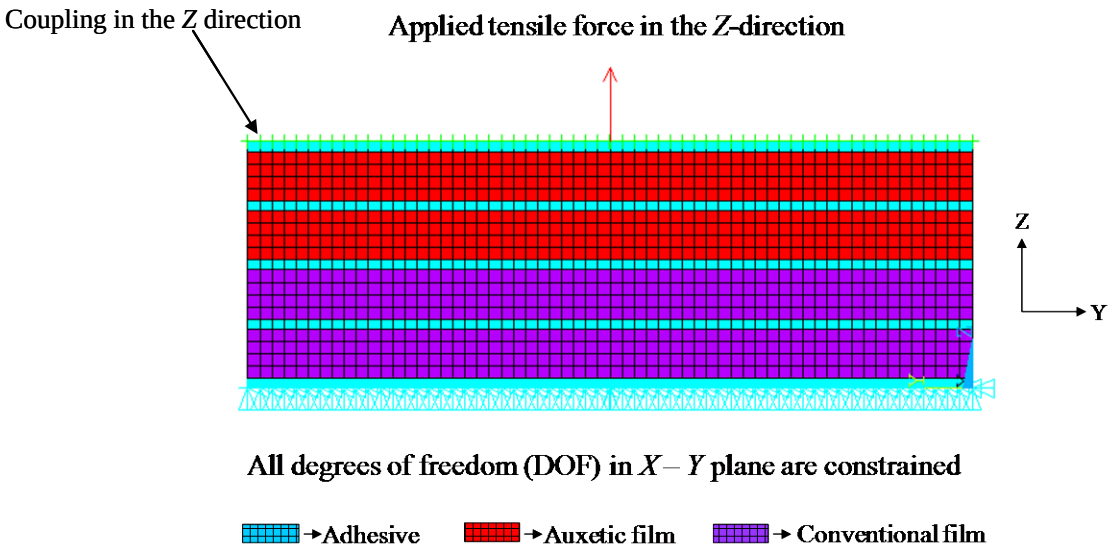

Fig 4.2 Illustration of a tensile test simulation in ANSYS. The red arrow represents the direction of applied tensile force in the *Z*-direction. All degrees of freedom in the $X - Y$ (bottom) plane are fixed to zero.

Following the acquisition of a numerical solution (post-processing), the nodal displacement of the top surface in the *Z*-direction was established from which strain values were calculated by dividing the displacement by the original height (thickness) of the interface. The stress is calculated by dividing the applied tensile force by the cross-sectional area of the surface to which the load was applied. The effective through-thickness Young's modulus, E_Z, was then calculated from the standard definition:

$$E_Z = \frac{\sigma_Z}{\varepsilon_Z}, \tag{4.1}$$

where σ_Z and ε_Z are the applied stress and resulting strain in the loading (Z) direction, respectively, as determined from the FE model.

The shear modulus was determined by applying a shear force along the X-direction on the top surface of the structure as shown in Fig 4.3. The nodes on the top surface were coupled in the X direction to ensure a uniform force distribution.

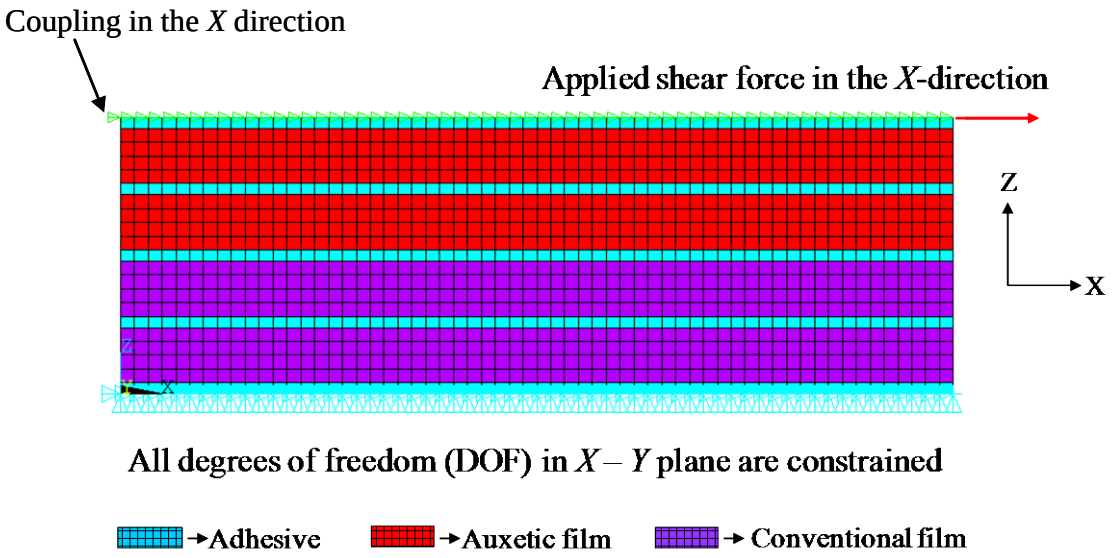

Fig 4.3 Illustration of a shear test simulation in ANSYS. The red arrow represents the direction of shear force. All degrees of freedom in the X – Y (bottom) plane are fixed.

The shear strain was determined by dividing the displacement of the top surface in the X-direction by the original height (in the Z- direction) of the multi-layer interface. The shear stress was determined by dividing the shear force by the cross-sectional area of the surface to which the force was applied. The shear modulus, G_{XZ}, was calculated by dividing the shear

stress by the shear strain:

$$G_{XZ} = \frac{\tau}{\gamma} \tag{4.2}$$

where τ and γ are shear stress and strain respectively determined from the model.

In modelling the multi-layer film/adhesive interface using ANSYS, the following assumptions were made: (i) all materials used are linear elastic and isotropic and (ii) a perfect bond exists between the films and the adhesive. The mechanical properties of the materials used in the simulations are given Table 4.1.

Table 4.1 Properties of materials used in the modelling of the multi-layer interfaces.

Material	Young's Modulus (GPa)	Poisson's Ratio
High modulus adhesive	1.70	+0.30
Low modulus adhesive	0.12	+0.30
Auxetic film	0.34	−0.90
Conventional film	0.34	+0.43

Conventional and auxetic films were assumed to have the same Young's modulus so that the effect of the Poisson's ratio on the mechanical properties of the multi-layered interface could be evaluated. The Young's modulus and Poisson's ratio values of the films were selected to be in the ballpark of typical experimental measured values determined for polypropylene (PP) films in Chapter 3 [140]. Typical polymeric adhesive systems with Young's modulus values relatively higher (1700 MPa) and lower (120 MPa) than the polypropylene films were chosen in order to evaluate the effect of the Young's modulus ratio of adhesive to film on the mechanical properties of the multi-layer interfaces. The adhesives were assumed to have a Poisson's ratio of +0.3 typical of many polymeric materials.

4.3 FEM Convergence Tests

The multi-layered film and adhesive structure was meshed in order to create the discrete building blocks known as finite elements. The accuracy of the FE model is dependent on the number of the discrete elements obtained via meshing. The accuracy of the model increases with the number of elements until a point after which increasing the number of elements has no significant effect on the modelling results. This value is obtained by performing convergence tests. In carrying out convergence tests, the mesh is refined by reducing the element size. Solutions are compared each time the mesh refinement is done and an element size which gives the most accurate predictions is determined. The use of a finer mesh requires a larger computer processing memory which slows down the modelling process leading to an increase in the clock time. Hence it is desired to find the minimum number of elements that gives a converged solution.

Convergence studies were performed for single layer interfaces of various layer thicknesses; i.e. 0.05 - 1.05 mm. The minimum and maximum thickness interfaces converged when the total number was elements was 7.1×10^4 and 1.5×10^5. An element length of 0.05 mm was used in the models. This element length was based on the convergence of the thinnest interface. Fig 4.4 shows an example of the variation between the through-thickness Young's moduli as function of number of elements for an interface model of 0.05 mm thickness.

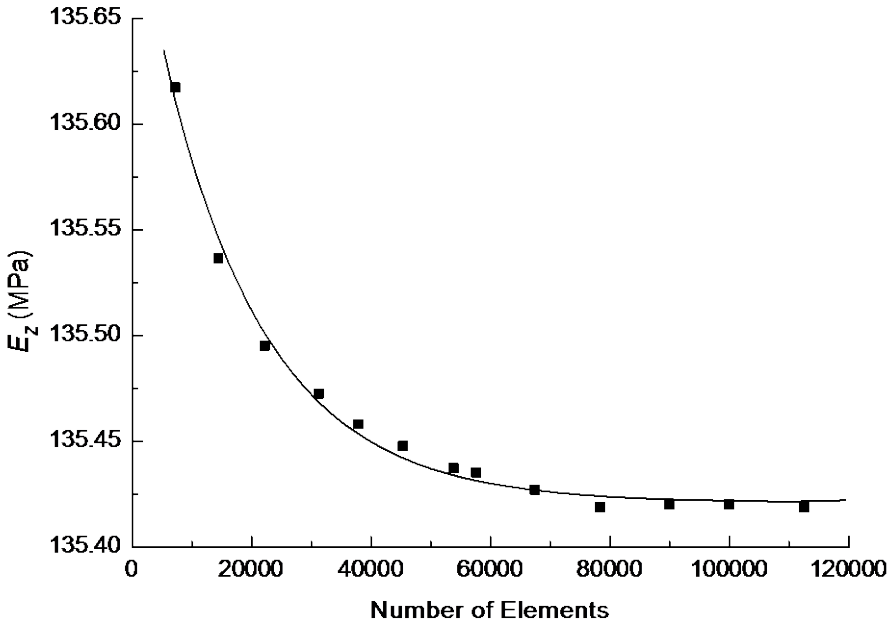

Fig 4.4 Variation in the through-thickness Young's modulus with number of elements for a single interface model of 0.05 mm thickness (low modulus (120MPa) adhesive).

The number of elements used for the interfaces of thicknesses 0.30, 0.55, 0.80, 1, and 1.05 mm are 8.8×10^4 , 9.0×10^4, 1.0×10^5, 1.2×10^5 , and 1.5×10^5, respectively.

4.4 Analytical Methods: The Rule of Mixtures

In order to validate the results obtained from the FE model, analytical solutions were also developed. The Rule of Mixtures (RM) is one of the analytical solutions against which numerical results obtained in this study were compared. The RM is a mathematical expression which can be used to estimate the effective mechanical properties of composite materials with respect to individual mechanical properties of the constituents, their quantity and arrangement.

For these mathematical expressions to be used for the multi-layer interfaces, the following assumptions are made:

(i) there exists perfect bonding between the films and the adhesive,

(ii) the matrix (adhesive) is void free,

(iii) the applied loads are either parallel or normal to the direction of the films,

(iv) the films and adhesive are linear elastic materials,

(v) the films and adhesive are isotropic materials and,

(vi) there are no residual stresses; i.e. the laminate is initially in a stress-free state.

The derivations of the modified RM expressions for multi-layer interfaces used in this study are presented in the following sections.

4.4.1 Determination of Transverse Modulus using RM

Fig 4.5 shows a schematic of the multi-layer interface where films are stacked upon each other and are bound together by a polymeric adhesive. In order to determine the transverse Young's modulus of the interface, the load is applied normal to the plane of the films.

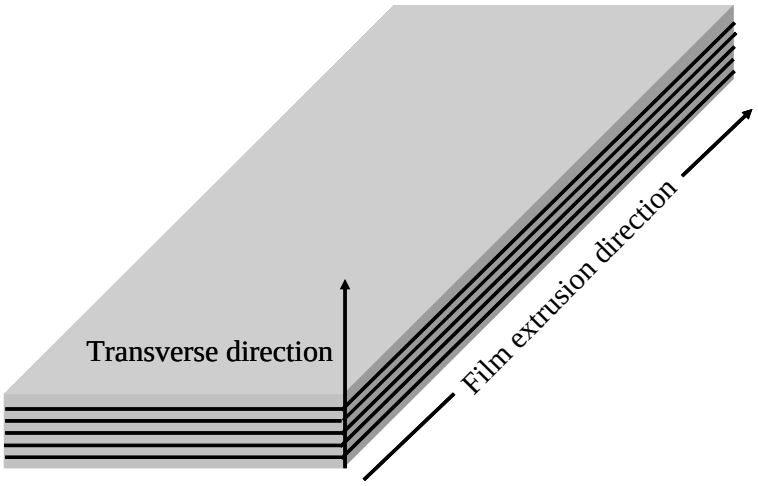

Fig. 4.5 Schematic of the multi-layer interface showing films (grey) held together by polymeric adhesive (black).

In order to compare the FE to analytical results, it was necessary to modify the Rule of Mixtures (RM) expression for fibre reinforced composites since the layered interface represented here consists of materials with similar Young moduli values. Unlike in fibre reinforced composites where the fibres are much stiffer compared to the resin (and hence the constraint of the resin constituent acting on the fibre constituent is negligible), the constraint of a film on an adhesive layer and vice versa is significant in the systems considered in this thesis since the Young's moduli are of similar order of magnitude. One approach developed in this thesis was to develop a 2-phase modified RM expression for the layered interface assuming continuity at the interface between adjacent layers. This was then used to determine the effective Young's modulus for a 3-phase layered system on weighted basis. A second approach was to adopt the Ramirez [145] approach for a similar layered system. The Ramirez approach used averaging techniques to the constitutive equations of the individual layers to develop the equations for the effective elastic properties of the composite. The results were compared to the results obtained from FE analysis.

4.4.1.1 Poisson's Correction in 2-phase System of Isotropic Material - Layers under Transverse Uni-axial loading

Consider 2 adjacent layers of isotropic material subject to a uni-axial stress applied along the *Z* direction $(\sigma_Z \neq 0)$:

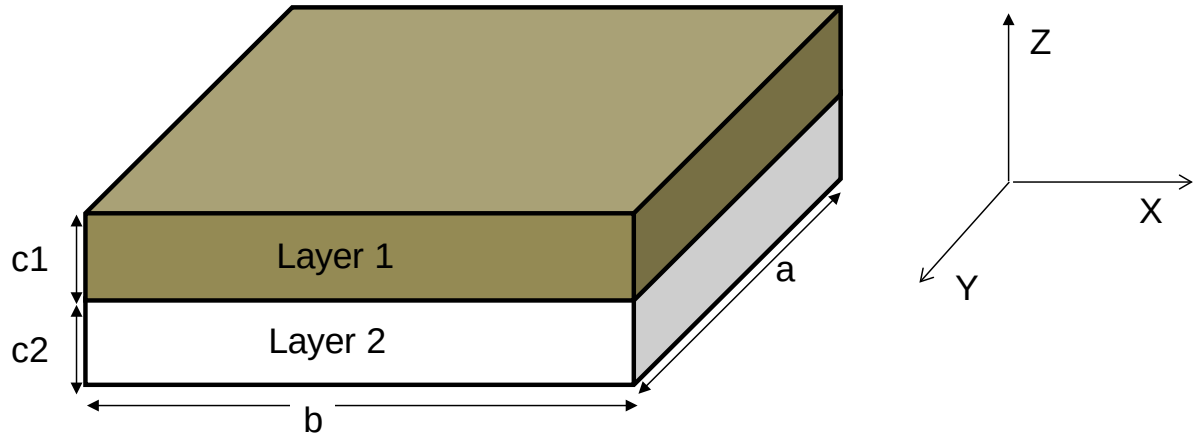

Fig 4.6 Schematic of the 2-phase layered interface.

Hooke's law for isotropic materials is represented in expression 4.3.

$$\begin{bmatrix} \varepsilon_X \\ \varepsilon_Y \\ \varepsilon_Z \\ \varepsilon_{YZ} \\ \varepsilon_{ZX} \\ \varepsilon_{XY} \end{bmatrix} = \frac{1}{E} \begin{bmatrix} 1 & -\nu & -\nu & 0 & 0 & 0 \\ -\nu & 1 & -\nu & 0 & 0 & 0 \\ -\nu & -\nu & 1 & 0 & 0 & 0 \\ 0 & 0 & 0 & 1+\nu & 0 & 0 \\ 0 & 0 & 0 & 0 & 1+\nu & 0 \\ 0 & 0 & 0 & 0 & 0 & 1+\nu \end{bmatrix} \begin{bmatrix} \sigma_X \\ \sigma_Y \\ \sigma_Z \\ \sigma_{YZ} \\ \sigma_{ZX} \\ \sigma_{XY} \end{bmatrix} \tag{4.3}$$

For a free standing layer subject to uni-axial stress in the *Z* direction (i.e. $\sigma_X = \sigma_Y = \sigma_{YZ} = \sigma_{ZX} = \sigma_{XY} = 0$) Eq. (4.3) gives:

$$\varepsilon_Z = \frac{1}{E}\sigma_Z \tag{4.4a}$$

This gives the standard definition of Young's modulus of

$$E = \frac{\sigma_Z}{\varepsilon_Z} \tag{4.4b}$$

For the case of adjacent layers then, in addition to the applied uni-axial stress, (with the exception of the special case of both layers having zero Poisson's ratio), the adjacent layers act upon each other so that stresses along the *X* and *Y* directions are also present (i.e. $(\sigma_X \neq 0)$ and $(\sigma_Y \neq 0)$). For static equilibrium the sign of the force acting along the *X* direction in one layer is opposite to that in the adjacent layer, and this is also true of the layer forces in the *Y* direction.

The strain in the loading (*Z*) direction of layer *i* (*i* = 1 or 2) is now given by:

$$\varepsilon_Z^{(i)} = \frac{1}{E_i}\left[-\nu_i\left(\sigma_X^{(i)} + \sigma_Y^{(i)}\right) + \sigma_Z\right] \tag{4.5a}$$

and in the transverse *X* and *Y* directions by:

$$\varepsilon_X^{(i)} = \frac{1}{E_i}\left[\sigma_X^{(i)} - \nu_i\left(\sigma_Y^{(i)} + \sigma_Z\right)\right] \tag{4.5b}$$

$$\varepsilon_Y^{(i)} = \frac{1}{E_i}\left[\sigma_Y^{(i)} - \nu_i\left(\sigma_X^{(i)} + \sigma_Z\right)\right] \tag{4.5c}$$

For isotropic materials:

$$\sigma_X^{(1)} = \sigma_Y^{(1)} = -\left(\frac{c2}{c1}\right)\sigma_X^{(2)} = -\left(\frac{c2}{c1}\right)\sigma_Y^{(2)} = \sigma_w \tag{4.6}$$

If we assume that each layer constrains the adjacent layer equally throughout the thickness of the layer, then:

$$\varepsilon_X^{(1)} = \varepsilon_X^{(2)} \tag{4.7}$$

From (4.5b), (4.5c), (4.6) and (4.7):

$$\sigma_w = \frac{\left(\frac{\nu_1}{E_1} - \frac{\nu_2}{E_2}\right)\sigma_Z}{\left[\frac{(1-\nu_1)}{E_1} + \left(\frac{c1}{c2}\right)\frac{(1-\nu_2)}{E_2}\right]} \tag{4.8}$$

Substituting (4.6) and (4.8) into (4.5a) for $i = 1$:

$$\varepsilon_Z^{(1)} = \left\{1 - \frac{2\nu_1\left(\frac{\nu_1}{E_1} - \frac{\nu_2}{E_2}\right)}{\left[\frac{(1-\nu_1)}{E_1} + \left(\frac{c1}{c2}\right)\frac{(1-\nu_2)}{E_2}\right]}\right\}\frac{\sigma_Z}{E_1} \tag{4.9}$$

Rearranging (4.9):

$$E_1^{'} = \frac{\sigma_Z}{\varepsilon_Z^{(1)}} = E_1 \left\{ 1 - \frac{2\nu_1 \left(\frac{\nu_1}{E_1} - \frac{\nu_2}{E_2} \right)}{\left[\frac{(1-\nu_1)}{E_1} + \left(\frac{c1}{c2} \right) \frac{(1-\nu_2)}{E_2} \right]} \right\}^{-1} \tag{4.10a}$$

Similarly,

$$E_2^{'} = \frac{\sigma_z}{\varepsilon_Z^{(2)}} = E_2 \left\{ 1 - \frac{2\nu_2 \left(\frac{\nu_2}{E_2} - \frac{\nu_1}{E_1} \right)}{\left[\left(\frac{c2}{c1} \right) \frac{(1-\nu_1)}{E_1} + \frac{(1-\nu_2)}{E_2} \right]} \right\}^{-1} \tag{4.10b}$$

Eqs (4.10a) and (4.10b) are the modified Young's moduli of the two layers taking into account Poisson's ratio constraints of the adjacent layers.

Consider now, a 2-phase layered system of alternating film and adhesive layers subject to a uni-axial stress applied along the transverse *Z* direction $(\sigma_Z \neq 0)$ (i.e. analogous to the 2-layer configuration shown in Fig. 4.6). The effective transverse Young's modulus (E_Z) of the layered interface is given by the well known formula for the lower (Reuss) bound [143]:

$$E_Z = \frac{E^{'}_{adh} E^{'}_{film}}{E^{'}_{film} V_{adh} + E^{'}_{adh} (1 - V_{adh})} \tag{4.11}$$

where $E^{'}_{film}$ and $E^{'}_{adh}$ are the modified Young's moduli of the film and adhesive layers, respectively, obtained from Equations 4.10a and 4.10b (i.e. subscripts 'film' = '1' and 'adh' = '2'); and V_{adh} is the volume fraction of adhesive. Equation 4.11 is, therefore, the modified

RM-Reuss expression for the effective Young's modulus of the 2-phase film-adhesive system capturing the Poisson's constraining effects of both film and adhesive layers.

4.4.1.2 Determination of 3-Phase Transverse Modulus using Weighted Approach

The use of the modified Young's moduli expressions such as (4.10a) and (4.10b) is not straightforward in 3-phase layered systems and hence a weighted approach was adopted for the 3-phase system. Consider the case of an adhesive layer sandwiched between auxetic and conventional film layers, Fig 4.7:

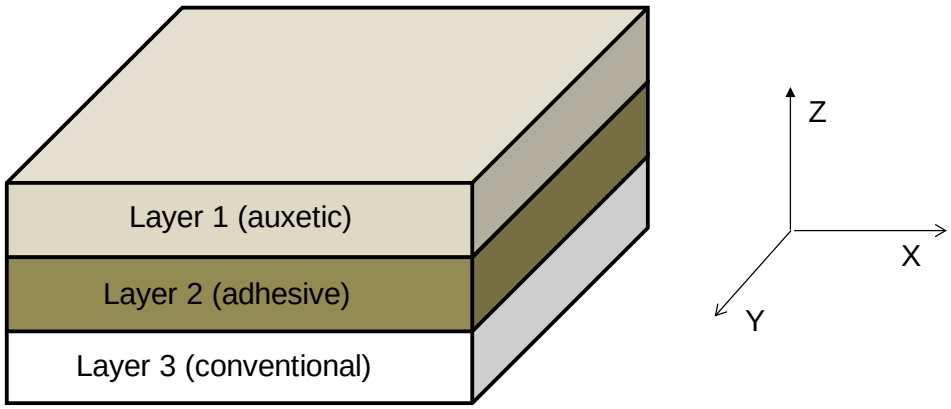

Fig 4.7 Schematic of the 3-phase layered interface.

In determining the modified Young's modulus of the adhesive (4.10b), the value calculated from the constraining effects of the auxetic layer will be different to that calculated from the influence of the conventional layer. One approach is to determine the modified adhesive Young's modulus for the 2-phase adhesive-auxetic film system and also for the 2-phase adhesive-conventional film system, and to then calculate the effective Young's modulus of the 3-phase system on a weighted basis according to Equation 4.12:

$$E_z^{(3-phase)} = \frac{V_{aux}}{(1-V_{adh})} E_z^{(aux-adh)} + \frac{V_{conv}}{(1-V_{adh})} E_z^{(conv-adh)} \tag{4.12}$$

where $E_z^{(aux-adh)}$ and $E_z^{(conv-adh)}$ are the 2-phase effective Young's modulus values for the adhesive-auxetic and adhesive-conventional systems, respectively, calculated from Eq. 4.11 with the modified constituent Young's moduli determined from Eqs. 4.10a and 4.10b in each case.

4.4.1.3 Determination of 2-Phase and 3-Phase Transverse Modulus using the Ramirez Approach

Recently, Ramirez *et al* [145] published expressions for the effective transverse Young's modulus of a composite laminate comprising *n* elastic isotropic phases. They applied averaging techniques to the constitutive equations of the individual layers to develop the equations for the effective elastic properties of the composite, from which the coefficients of the average stress components were used to determine the effective Young's moduli, Poisson's ratios and shear moduli.

Using this approach, the through thickness Young' modulus E_Z is given by:

$$\frac{1}{E_Z} = \sum_{i=1}^{n} \frac{V_i}{E_i} - 2\left[\sum_{i=1}^{n-1} \sum_{j=i+1}^{n} \frac{V_i V_j E_i E_j}{(1-\nu_i)(1-\nu_j)} \left(\frac{\nu_i}{E_i} - \frac{\nu_j}{E_j} \right)^2 \right] \left[\sum_{i=1}^{n} \frac{V_i E_i}{1-\nu_i} \right]^{-1} \tag{4.13}$$

(Note, there is an error in the respective Equation in [145], where the $\left(\frac{\nu_i}{E_i} - \frac{\nu_j}{E_j} \right)^2$ on the RHS

is incorrectly stated as $\left(\frac{\nu_i}{E_i} - \nu_j E_j\right)^2$, leading to an imbalance in the units of the LHS (Pa^{-1}) and those of the RHS in [145]).

For the 2-phase system (n = 2) then equation (4.13) becomes:

$$\frac{1}{E_z} = \frac{V_1}{E_1} + \frac{V_2}{E_2} - 2\left[\frac{V_1 V_2 E_1 E_2}{(1-\nu_1)(1-\nu_2)}\left(\frac{\nu_1}{E_1} - \frac{\nu_2}{E_2}\right)^2\right]\left[\frac{V_1 E_1}{1-\nu_1} + \frac{V_2 E_2}{1-\nu_2}\right]^{-1} \tag{4.14}$$

Expanding equation (4.13) to the 3-phase system (n = 3):

$$\frac{1}{E_z} = \frac{V_1}{E_1} + \frac{V_2}{E_2} + \frac{V_3}{E_3} - \frac{2\left[\frac{V_1 V_2 E_1 E_2}{(1-\nu_1)(1-\nu_2)}\left(\frac{\nu_1}{E_1} - \frac{\nu_2}{E_2}\right)^2 + \frac{V_2 V_3 E_2 E_3}{(1-\nu_2)(1-\nu_3)}\left(\frac{\nu_2}{E_2} - \frac{\nu_3}{E_3}\right)^2\right]}{\left[\frac{V_1 E_1}{1-\nu_1} + \frac{V_2 E_2}{1-\nu_2} + \frac{V_3 E_3}{1-\nu_3}\right]} \tag{4.15}$$

4.4.2 The RM Voigt Young's Modulus

The upper (Voigt) bound on the effective Young's modulus of a composite laminate can be estimated by use of Rule of Mixtures assuming that the load is applied in the plane of the laminate, i.e. along the extrusion direction in Fig 4.5. In this case the load applied is assumed to be shared between the film and the adhesive. The RM upper (Voigt) bound for a layered adhesive-film system is then represented by equation 4.16:

$$E = E_{adh} V_{adh} + E_{film} V_{film} \tag{4.16}$$

Evans and co-workers [131] have shown that Reuss and Voigt bound equations accurately represent the Young's modulus and Poisson's ratio for continuous fibre composite systems

incorporating a negative Poisson's ratio matrix when the Poisson's ratio of the matrix was varied in the range $-1 \leq \upsilon \leq -0.3$. The results obtained from the above equations; i.e. analytical solutions, will be used to validate and/or test the accuracy of the ANSYS-FE model.

4.4.3 Determination of Shear Modulus using RM

The shear modulus, G_{XZ}, of the multi-layer film-adhesive interfaces was calculated using the equation [143]:

$$G_{XZ} = \frac{G_{adh} G_{film}}{V_{adh} G_{film} + V_{film} G_{adh}} \tag{4.17}$$

where G_{adh} and G_{film} are the shear modulus values of the adhesive and film, respectively.

The RM expression given by Eq. (4.17) can be extended to a 3-phase system, such as the mixed multi-layered systems considered in the FEM interface models. In this case, the expression for shear modulus is:

$$G_{XZ} = \frac{G_{adh} G_{conv} G_{aux}}{V_{adh} G_{conv} G_{aux} + V_{conv} G_{adh} G_{aux} + V_{aux} G_{adh} G_{conv}} \tag{4.18a}$$

where G_{conv} and G_{aux} are the shear modulus values of the conventional film and auxetic film, respectively.

The change in interface shear modulus for a mixed 3-phase interface over the single-phase adhesive-only interface is calculated as follows:

$$\Delta G_{XZ} = \frac{G_{XZ} - G_{adh}}{G_{adh}} = \frac{G_{conv} G_{aux}}{V_{adh} G_{conv} G_{aux} + V_{conv} G_{adh} G_{aux} + V_{aux} G_{adh} G_{conv}} - 1 \quad (4.18b)$$

which can be expressed as

$$\Delta G_{XZ} = \frac{1}{V_{adh} + V_{conv} \frac{G_{adh}}{G_{conv}} + V_{aux} \frac{G_{adh}}{G_{aux}}} - 1 \quad (4.18c)$$

where $G_{adh} = \frac{E_{adh}}{2(1+\upsilon_{adh})}$, $G_{conv} = \frac{E_{conv}}{2(1+\upsilon_{conv})}$ and $G_{aux} = \frac{E_{aux}}{2(1+\upsilon_{aux})}$.

4.5 Types of Multi-Component Interface Lay-ups

4.5.1 Constant Interface Thickness (CIT) model

In this model, various lay-ups including films and/or adhesive, were constructed to give an interface with constant thickness of 1.0 mm. In all multi-layer lay-ups, the top and the bottom surfaces are adhesive layers, and adjacent layers alternate between film and adhesive through the thickness of the interface. Individual films used in all models have a fixed thickness of 0.2 mm, typical of the polypropylene films produced experimentally, (Chapter 3). The thickness of each layer of the adhesive varies from as high as 1.0 mm (adhesive only interface; one-layer system) to as low as 0.04 mm for the system which contains four film layers and five adhesive layers (referred to as the nine-layer system). The mechanical properties of the films, namely the Young's modulus and Poisson's ratio were the measured values of auxetic PP films produced at extrusion temperature of 159 °C, screw speed of 1.05 $rads^{-1}$, and take up speed of 0.0225 ms^{-1} and conventional films extruded at a temperature of 230 °C, screw speed of 1.05 $rads^{-1}$, and take up speed of 0.03 ms^{-1} (Chapter 3) [144]. Various lay-ups showing the

arrangement of auxetic and/or conventional films and the adhesive are illustrated in Fig 4.8 showing exemplar 1, 3, 5, 7 and 9 layer configurations and the resultant thickness for each case.

Lay-up arrangement					
Number of layers	1	3	5	7	9
Interface thickness (mm)	1.00	1.00	1.00	1.00	1.00
Adhesive thickness (mm)	1.00	0.40	0.20	0.10	0.04
Film thickness (mm)		0.20	0.20	0.20	0.20

Fig 4.8 Constant Interface Thickness (CIT) model representation of alternating adhesive and film layers.

4.5.2 Constant Constituent Layer Thickness (CCLT) model

In this model, shown in Fig. 4.9, the layer thicknesses of adhesive and films were kept constant at 0.05 mm and 0.2 mm, respectively.

Lay-up arrangement					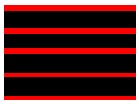
Number of layers	1	3	5	7	9
Interface thickness (mm)	0.05	0.30	0.55	0.80	1.05
Adhesive thickness (mm)	0.05	0.05	0.05	0.05	0.05
Film thickness (mm)		0.20	0.20	0.20	0.20

Fig 4.9 Constant Constituent Layer Thickness (CCLT) interface model representation of alternating adhesive and film layers.

The addition of adhesive and films in succession resulted in a progressively thicker interface. Fig. 4.9 is an illustration of the Constant Constituent Layer Thickness model, with the thickness varying from as little as 0.05 mm (adhesive only; 1 layer system) to 1.05 mm for the system containing four layers of films and five layers of adhesive (nine-layer system).

The elastic modulus of both conventional and auxetic films was kept constant at E = 340 MPa in order that the effect of different Poisson's ratios could be assessed. An adhesive with a positive Poisson's ratio (υ = +0.30) was employed. Results were obtained for interfaces containing a combination of conventional and auxetic films as well as interfaces with all conventional film/adhesive or all auxetic film/adhesive layers.

4.6 Finite Element Modelling of Three-Point Bending Tests

FE analyses were carried out using ANSYS to simulate and validate the three-point bending tests of the interfaces carried out experimentally in Chapter 9. When the layered interface was modelled to determine the Young's and Shear moduli, it was assumed that there was no change in the thickness of the adhesive and films during curing (refer to the lay-up arrangements in Figs 4.8 and 4.9). In practice (as observed during the fabrication of the multi-layer interfaces in Chapter 9) the films and adhesive become consolidated during curing and an interface thickness of about 0.5 mm was obtained instead of the 1.05 mm thickness previously assumed for a nine-layer interface. It was also assumed that films were perfectly flat. In practice this assumption may not be valid. The individual thicknesses of the film and adhesive layers used in the FE three-point bending test models were scaled so as to match the experimentally observed layer thicknesses in the fabricated systems, Chapter 9. The scaling procedures used are given in Eqs 4.19 and 4.20. The theoretical thickness of a single layer of film was determined according to Eq. 4.19:

$$T_{Theo}^{film} = \frac{T_{Exp}^{\text{int}}}{T_{Theo}^{\text{int}}} \times T_{Exp}^{film} \tag{4.19}$$

where T_{Exp} and T_{Theo} are the experimental and theoretical thicknesses, respectively. The superscripts *film* and *int* denote the film and interface, respectively.

Similarly, the thickness of the adhesive layer was determined using Eq. 4.20:

$$T_{Theo}^{adh} = \frac{T_{Exp}^{\text{int}}}{T_{Theo}^{\text{int}}} \times T_{Exp}^{adh} \tag{4.20}$$

where the superscripts *adh* denote the adhesive.

A polyolefin adhesive (Polyolefin 6218) which can bond to polypropylene films was supplied by Bemis Inc. [146], for the production of the multi-layer interface. The material properties obtained from the video extensometer tests, Table 4.2, were used in the three and four point bending FE models.

Table 4.2 Measured properties of the polyolefin adhesive and PP films.

Materials	Young's Modulus (MPa)	Poisson's Ratio	Average Thickness (mm)
Polyolefin 6218	50±5.5	+0.33	0.08±0.005
Conventional PP film	340±90	+0.34 to +0.43	0.17±0.05
Auxetic PP film	340±50	-0.95 to -0.40	0.20±0.06

The FE model of the interface was assembled as imitating the CCLT model, Fig 4.9. For clarity and simplicity, a block (layers not shown) is used to illustrate the boundary conditions in Fig 4.10. The laminate is simply supported, with one end constrained in all directions (i.e. displacements U_X, U_Y and U_Z in the X, Y and Z directions, respectively, set to zero). The displacements in Y and Z directions at the right hand side are constrained (i.e. $U_Y = 0$ and $U_Z =$

0). The constraints (which were adopted from Gupta *et al* [147]) are sufficient to prevent rigid body motion during the analysis. A force of 1 N was applied to the top surface of the specimen in the negative *Z*-direction, see Fig 4.10. The maximum displacements were determined from the ANSYS FE analysis.

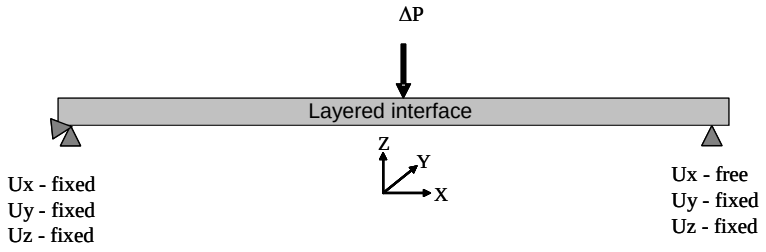

Fig 4.10 Schematic of FEM structural model for the three-point bending test.

Three-dimensional beams were constructed using SOLID-45 elements described in Section 4.2. The length, width and thickness of the interface model were taken to be 50 mm, 10 mm and 0.5 mm, respectively (dimensions obtained from experimental measurements, Chapter 9). Convergence tests similar to those discussed in Section 4.3 were performed in order to determine the optimum number of elements required for the solution to converge. The convergence test was performed on the C-C-C-C-C laminate and the system converged when approximately 40 000 elements were used. An element length of 0.2 mm (aligned along the length of the interface) was chosen to model the three-point bending model. The number of elements used to model the interfaces was 112,500, (see the convergence in Figure 4.11).

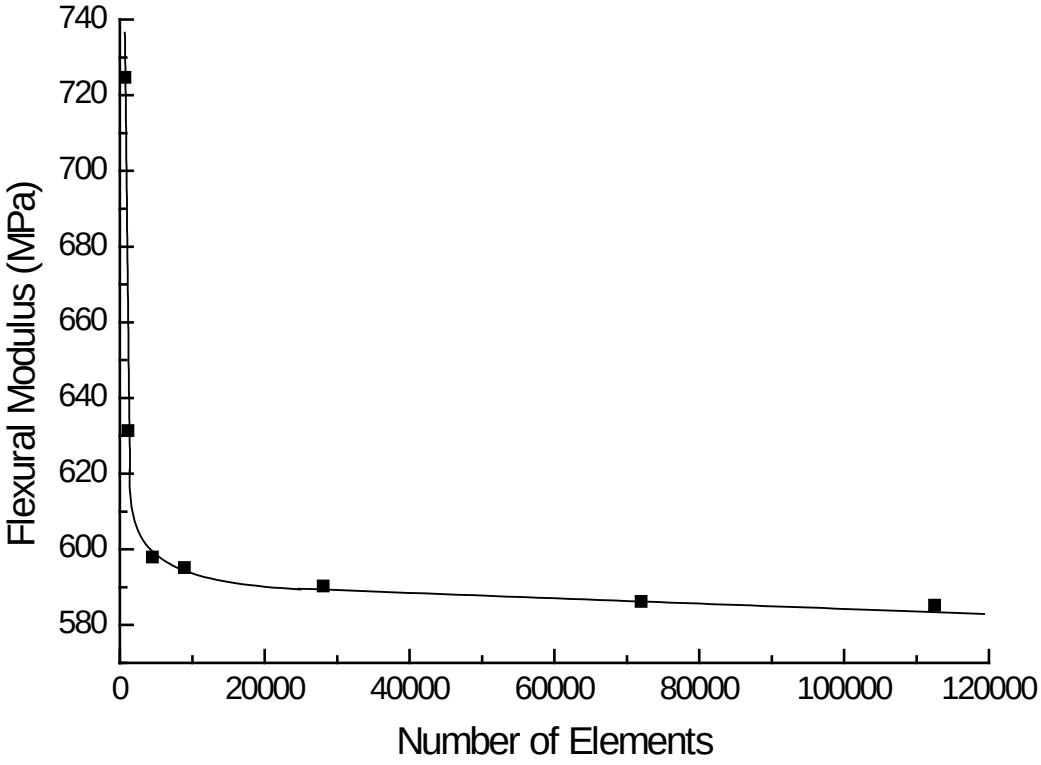

Fig 4.11 Variation in flexural modulus with number of elements for the C-C-C-C-C laminate.

CHAPTER 5: NUMERICAL AND ANALYTICAL MODELLING OF PARTICULATE FILLED POLYMERIC COMPOSITES

5.0 Introduction

This chapter describes a methodology used to model the effective Young's modulus and Poisson's ratio of particle-filled composites. A numerical model was developed using the ANSYS Finite Element Analysis package to simulate the material behaviour of particulate-filled composites under a tensile load. The numerical model was validated against experiments and existing analytical models including the Self-Consistent Field (SCF) theory and the Hashin-Shtrikman (H-S) theories.

5.1 Finite Element Modelling Methodology –Parametric Study

A simplified FE model constructed out of a polymeric matrix filled with conventional or auxetic fillers was used. A cubic block (1 mm × 1 mm × 1 mm) was generated using 8-noded SOLID 45 elements in ANSYS. A description of the SOLID 45 elements is found in Chapter 4, section 4.2. The cubic block was meshed using an element length on 0.05 mm, and a total of 8000 elements were obtained. A random generator was used to select elements for material property assignment. The random generator macro is in Appendix B. The numbers of filler elements were counted using ANSYS to enable the volume fractions of fillers to be calculated. The ANSYS representation of the cubic block with randomly selected cubes assigned with filler properties is shown in Figure 5.1.

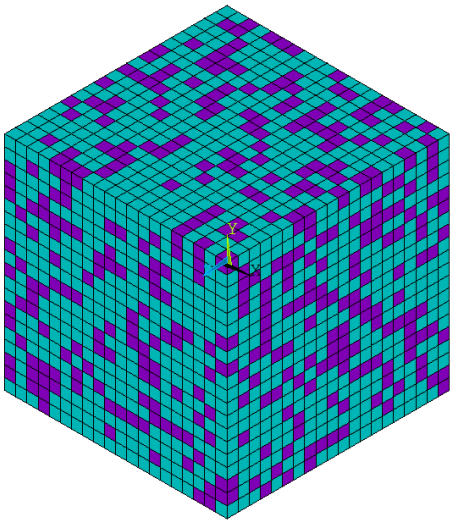

Fig. 5.1 ANSYS representation of the cubic block. Purple (dark) cubes represent fillers (32%) while green (light) cubes represent the matrix (68%).

The adhesive and filler elements were assigned material properties as shown in Table 5.1.

Table 5.1 Elastic materials properties used in the FE analyses.

Material type	Young's Modulus (MPa)	Poisson's Ratio	Shear Modulus (MPa)
Adhesive (matrix)	1600	+0.30	615
Filler (auxetic)	340	-0.90	1700
Filler (conventional)	340	+0.43	119

The following assumptions were made: (i) the filler and matrix were perfectly bonded and (ii) both filler and matrix were considered to be linear, isotropic elastic materials. While the shape of fillers was simplified to be of a cubic form, in practice the shape of filler particulates is more complex. Results from the numerical analysis are expected to be overestimates since the numerical models do not take into account imperfect interfaces between the matrix and the fillers.

Boundary conditions were applied as follows. The plane normal to the *X*-axis and located at $X = 0$ was constrained from movement in the *X* direction, and the plane normal to the *Y*-

axis (located at Y= 0) was constrained from movement in the Y direction as shown in Fig 5.2. The nodes on the constrained surfaces were allowed to translate and rotate in the plane of the surface. A strain of 1% was applied to each node on the unconstrained surface normal to the X direction. Nodal reaction loads were calculated on the surface to which the strain was applied and converted to stress by dividing the summed nodal reaction force by the cross-sectional area of the face to which the strain was applied. The effective Young's modulus was calculated using Eq. (4.1).

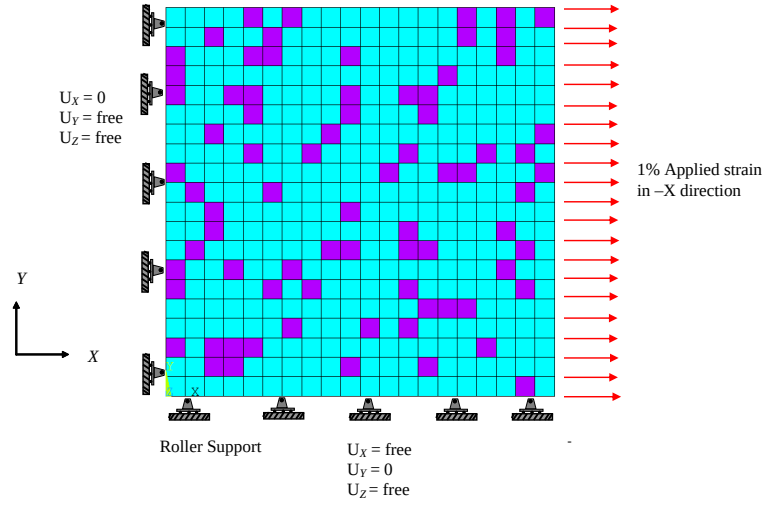

Fig 5.2 An illustration of the boundary conditions used in the FE analyses. Purple cubes represent fillers while green cubes represent the matrix. U_X, U_Y, and U_Z are the displacements in the X, Y and Z directions.

5.1.1 FE modelling of α-cristobalite composites

A 3-D block of length 30 mm, width 3 mm and thickness 1 mm representing the proportional geometric dimensions of the test specimens (fabricated in Chapter 9) was constructed using SOLID 45 elements in the ANSYS FE package (Fig 5.3). As discussed in the FE methodology in section 5.1, the block was meshed producing over 11, 000 elements and a known fraction of elements were randomly selected and assigned filler (α-

cristobalite) properties. A 1% strain was applied in the *X*-direction (along the length) and the tensile behaviour was numerically determined. The Young's modulus was calculated by dividing the applied stress by the axial strain, while Poisson's ratios were determined by dividing the strain in the transverse *Y* direction by the strain the *X* direction for filler volume fractions used in the specimens in the experiments.

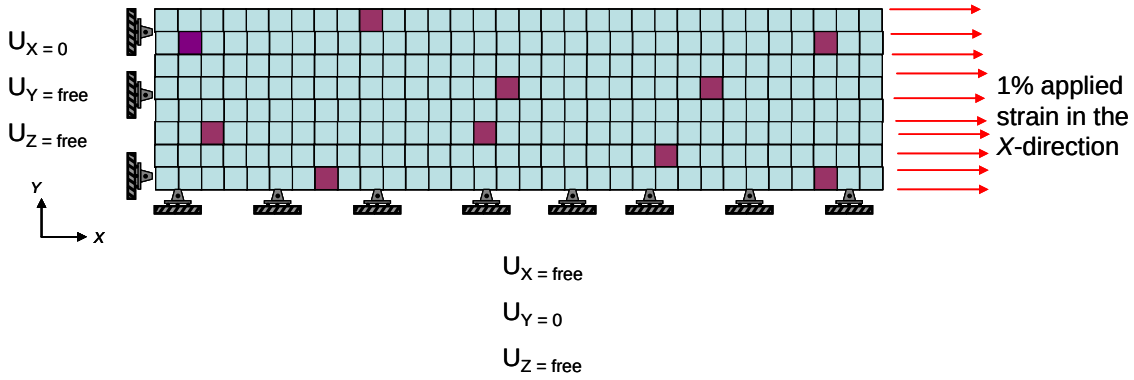

Fig 5.3 Projection of the 3D FE model in the *X*-*Y* plane of the α-cristobalite-filled epoxy resin composites. Purple cubes represent the α-cristobalite filler while green cubes represent the epoxy matrix. U_X, U_Y and U_Z are strains in the *X*, *Y* and Z directions respectively.

5.2 Analytical Modelling

5.2.1 Upper and Lower Bounds

The FE analysis results were compared to upper and lower bounds [118], Hashin-Shtrikman (H-S) bounds [119, 120] and the Self-Consistent Field Theory [122]. The upper and lower bounds are based on the principles of Minimum Potential Energy and Complementary Energy, respectively. The theory assumes that the composite is made up of different isotropic constituents (matrix and filler) which are uniformly dispersed without a preferred orientation.

In the derivation of the upper and lower bounds, the matrix Young's modulus, Poisson's ratio and volume fraction are represented by E_m, υ_m and V_m, respectively. Similarly, the Young's modulus, Poisson's ratio and volume fraction of dispersed material is represented by E_f , υ_f and V_f, respectively. When stress is plotted against strain, the strain energy density is determined by integrating the area under the curve and the strain energy is then given by:

$$U = \frac{1}{2}\sigma\varepsilon V \tag{5.1}$$

where σ is the stress, ε is the strain and V is the volume of the material.

The basis for the determination of the upper bound utilises the Principle of Minimum Potential Energy. If the displacements are specified over the surface of a body such that the strain; ε^*_X, ε^*_Y, ε^*_Z, and the shear strain; γ^*_{XY}, γ^*_{YZ}, γ^*_{ZX} satisfy specified boundary conditions then the strain energy that satisfies this strain state is U^*. The stress-strain relations from which strain energy is determined are given in Eqs. (5.2(a)) – (5.2(f)) [118]:

$$\sigma_X = \frac{\upsilon E}{(1+\upsilon)(1-2\upsilon)}(\varepsilon_X + \varepsilon_Y + \varepsilon_Z) + \frac{E}{(1+\upsilon)}\varepsilon_X \tag{5.2(a)}$$

$$\sigma_Y = \frac{\upsilon E}{(1+\upsilon)(1-2\upsilon)}(\varepsilon_X + \varepsilon_Y + \varepsilon_Z) + \frac{E}{(1+\upsilon)}\varepsilon_Y \tag{5.2(b)}$$

$$\sigma_Z = \frac{\upsilon E}{(1+\upsilon)(1-2\upsilon)}(\varepsilon_X + \varepsilon_Y + \varepsilon_Z) + \frac{E}{(1+\upsilon)}\varepsilon_Z \tag{5.2(c)}$$

$$\tau_{XY} = G\gamma_{XY} = \frac{E}{2(1+\upsilon)}\gamma_{XY} \tag{5.2(d)}$$

$$\tau_{XZ} = G\gamma_{XZ} = \frac{E}{2(1+\upsilon)}\gamma_{XZ} \qquad (5.2(e))$$

$$\tau_{YZ} = G\gamma_{YZ} = \frac{E}{2(1+\upsilon)}\gamma_{YZ} \qquad (5.2(f))$$

where σ_X, σ_Y, and σ_Z are the stresses acting in the *X*, *Y* and *Z* directions, respectively, υ is the Poisson's ratio, *E* is the Young's modulus, *G* is the shear modulus and τ_{XY}, τ_{XZ} and τ_{YZ} are the shear stress values in the *XY*, *XZ* and *YZ* planes, respectively. ε_X, ε_Y and ε_Z are the strains in the *X*, *Y*, and *Z* directions, respectively, and γ_{XY}, γ_{XZ} and γ_{YZ} are the shear strains in the *XY*, *XZ* and *YZ* planes.

Expanding Eq. (5.1) to include *X*, *Y* and *Z* dimensional quantities leads to the strain energy being defined by:

$$U = \frac{1}{2}\int_V (\sigma_X\varepsilon_X + \sigma_Y\varepsilon_Y + \sigma_Z\varepsilon_Z + \tau_{XY}\gamma_{XY} + \tau_{YZ}\gamma_{YZ} + \tau_{ZX}\gamma_{ZX})dV \qquad (5.3)$$

The actual strain energy *U* in the body due to specified displacements cannot exceed U^*; i.e. $U \leq U^*$. In order to determine the upper bound on Young's modulus, a specimen subjected to a uniaxial force has an elongation of εL, where ε is the average strain and *L* is the specimen length. The internal strain field that corresponds to the average strain at the boundaries due to a uniaxial force applied in the *X* direction is given by the expressions:

$$\varepsilon^*_X = \varepsilon, \qquad \varepsilon^*_Y = \varepsilon^*_Z = -\upsilon\varepsilon, \qquad \gamma^*_{XY} = \gamma^*_{YZ} = \gamma^*_{ZX} = 0 \qquad (5.4)$$

where υ is the apparent Poisson's ratio of the composite (matrix plus filler). Substituting the expressions contained in Eq. (5.4) into the strain-stress expressions of Eq. (5.2), the following equations are obtained for the matrix:

$$\sigma^{*}{}_{X_m} = \frac{1-\upsilon_m - 2\upsilon_m\upsilon}{1-\upsilon_m - 2\upsilon_m{}^2} E_m\varepsilon \tag{5.5(a)}$$

$$\sigma^{*}{}_{Y_m} = \sigma^{*}{}_{Z_m} = \frac{\upsilon_m - \upsilon}{1-\upsilon_m - 2\upsilon_m{}^2} E_m\varepsilon \tag{5.5(b)}$$

$$\tau^{*}{}_{XY_m} = \tau^{*}{}_{YZ_m} = \tau^{*}{}_{ZX_m} = 0 \tag{5.5(c)}$$

Similar expressions for the dispersed particles within the matrix can also be obtained.

The strain energy of the composite can be obtained by substituting the strain and stress expressions for the matrix (Eqs. (5.4) and (5.5)), and the equivalent expressions for the dispersed particles, into the strain energy equation, (Eq. (5.3)):

$$U^{*} = \frac{\varepsilon^2}{2}\int_{V_m} \frac{1-\upsilon_m - 4\upsilon_m\upsilon + 2\upsilon^2}{1-\upsilon_m - 2\upsilon_m{}^2} E_m dV + \frac{\varepsilon^2}{2}\int_{V_f} \frac{1-\upsilon_f - 4\upsilon_f\upsilon + 2\upsilon^2}{1-\upsilon_f - 2\upsilon_f{}^2} E_f dV \tag{5.6}$$

Using the inequality; $U \leq U^{*}$, the following expression is obtained from Eqs. (5.1) and (5.6):

$$\frac{1}{2}E_c\varepsilon^2 V \leq \frac{\varepsilon^2}{2}\left[\frac{1-\upsilon_m - 4\upsilon_m\upsilon + 2\upsilon^2}{1-\upsilon_m - 2\upsilon_m{}^2} E_m V_m + \frac{1-\upsilon_f - 4\upsilon_f\upsilon + 2\upsilon^2}{1-\upsilon_f - 2\upsilon_f{}^2} E_f V_f\right] V \tag{5.7}$$

The upper bound on Young's modulus is then obtained from expression (5.7) giving:

$$E_c = \frac{1-\upsilon_m - 4\upsilon_m\upsilon + 2\upsilon^2}{1-\upsilon_m - 2\upsilon_m^2} E_m V_m + \frac{1-\upsilon_f - 4\upsilon_f\upsilon + 2\upsilon^2}{1-\upsilon_f - 2\upsilon_f^2} E_f V_f \tag{5.8}$$

where E_c is the Young's modulus of the composite.

The Poisson's ratio of the composite can be determined by differentiating Eq. (5.7) and equating the resultant solution to zero as shown in Eq. (5.9):

$$\frac{\partial U^*}{\partial \upsilon} = 0 \tag{5.9}$$

The first derivative (Eq. (5.9)) is zero when:

$$\upsilon = \frac{(1-\upsilon_m - 2\upsilon_m^2)\upsilon_f E_f V_f + (1-\upsilon_f - 2\upsilon_f^2)\upsilon_m E_m V_m}{(1-\upsilon_m - 2\upsilon_m^2)E_f V_f + (1-\upsilon_f - 2\upsilon_f^2)E_m V_m} \tag{5.10}$$

The value of Poisson's ratio obtained in Eq. (5.10) may be substituted into expression (5.8) to give the upper bound on Young's modulus of the composite.

The lower bound is based on the Principle of Complementary Energy. The same stress-strain relations given in Eq. (5.2) and the expression for the strain energy, Eq. (5.3), are also used in this case. By letting σ^0_X, σ^0_Y, σ^0_Z, τ^0_{XY}, τ^0_{YZ}, τ^0_{ZX} satisfy the stress equations at equilibrium for specified boundary conditions, U^0 can be defined as the strain energy for the stress state σ^0_X, σ^0_Y, σ^0_Z, τ^0_{XY}, τ^0_{YZ}, τ^0_{ZX}. The strain energy, U, is determined using Eq. (5.3). However, the actual strain in the body due to specific boundary conditions cannot exceed U^0; i.e. $U \leq U^0$.

For the lower bound, the internal stress field that satisfies uniaxial loading along the X direction and the stress equations at equilibrium are:

$$\sigma^0_X = \sigma; \qquad \sigma^0_Y = \sigma^0_Z = \tau^0_{XY} = \tau^0_{YZ} = \tau^0_{ZX} = 0 \tag{5.11}$$

The strain energy equation is then represented by Eq. (5.12):

$$U^o = \frac{1}{2}\int_V \frac{(\sigma^o{}_x)^2}{E}\partial V = \frac{\sigma^2}{2}\int_V \frac{\partial V}{E} \tag{5.12}$$

Since the matrix E_m spans over volume, V_m and the dispersed particles E_f spans over V_f then:

$$\int_V \frac{\partial V}{E} = \int_{V_m} \frac{\partial V}{E_m} + \int_{Vf} \frac{\partial V}{E_f} = \frac{V_m}{E_m} + \frac{V_f}{E_f} \tag{5.13}$$

Therefore Eq. (5.12) becomes:

$$U^o = \frac{1}{2}\int_V \frac{(\sigma^o{}_x)^2}{E}\partial V = \frac{\sigma^2}{2}\left[\frac{V_m}{E_m} + \frac{V_f}{E_f}\right] \tag{5.14}$$

Since $U \le U^O$, then:

$$\frac{1}{2}\frac{\sigma^2}{E}V \le \frac{\sigma^2}{2}\left[\frac{V_m}{E_m} + \frac{V_f}{E_f}\right] \tag{5.15}$$

Thus the lower bound is then given by:

$$E = \frac{E_m E_f}{V_m E_f + V_f E_m} \tag{5.16}$$

5.2.2 Self-Consistent Field Theory

The Self-Consistent Field (SCF) theory is a refinement of the Rule of Mixtures for Young's modulus and Poisson's ratio. The SCF uses strain-displacement and constitutive relations. It assumes uniform strain in the constituents of the composite and continuity at the filler/matrix interface. The SCF expressions for the Young's modulus and Poisson's ratio of the composite are given in Eqs. (5.17) − (5.18) [122].

$$E_c = V_f E_f + V_m E_m + \frac{4(\upsilon_m - \upsilon_f)^2 K_f K_m G_m V_m V_f}{K_f K_m + G_m (V_f K_f + V_m K_m)} \tag{5.17}$$

$$\upsilon = V_f \upsilon_f + V_m \upsilon_m + \frac{(\upsilon_m - \upsilon_f)(K_m - K_f) G_m V_m V_f}{K_f K_m + G_m (V_f K_f + V_m K_m)} \tag{5.18}$$

where $K_i = \dfrac{E_i}{2(1+\upsilon_i)(1-2\upsilon_i)}$, $G_i = \dfrac{E_i}{2(1+\upsilon_i)}$ and *i* represents the matrix (*m*) or particle (*f*).

5.2.3 Hashin-Shtrikman Bounds

Other existing bounds for two-phase materials were obtained from the Hashin- Shtrikman (H-S) model [120, 123]. This model assumes that the composite is isotropic and linearly elastic. The H-S lower bound on Young's modulus is given in Eq. (5.19) [123]:

$$E_c = \frac{9\left(K_m + \dfrac{V_f}{\dfrac{1}{K_f - K_m} + \dfrac{3V_m}{3K_m + 4G_m}}\right)\left(G_m + \dfrac{V_f}{\dfrac{1}{G_f - G_m} + \dfrac{6(K_m + 2G_m)V_m}{5(3K_m + 4G_m)G_m}}\right)}{3\left(K_m + \dfrac{V_f}{\dfrac{1}{K_f - K_m} + \dfrac{3V_m}{3K_m + 4G_m}}\right) + \left(G_m + \dfrac{V_f}{\dfrac{1}{G_f - G_m} + \dfrac{6(K_m + 2G_m)V_m}{5(3K_m + 4G_m)G_m}}\right)} \tag{5.19}$$

where K_f, K_m, and G_f, G_m are the bulk and shear moduli of the particle and matrix, respectively.

The H-S upper bound on Young's modulus is given in Eq. (5.20) [123]:

$$E_c = \frac{9\left(K_f + \dfrac{V_m}{\dfrac{1}{K_m - K_f} + \dfrac{3V_f}{3K_f + 4G_f}}\right)\left(G_f + \dfrac{V_m}{\dfrac{1}{G_m - G_f} + \dfrac{6(K_f + 2G_f)V_f}{5(3K_f + 4G_f)G_f}}\right)}{3\left(K_f + \dfrac{V_m}{\dfrac{1}{K_m - K_f} + \dfrac{3V_f}{3K_f + 4G_f}}\right) + \left(G_f + \dfrac{V_m}{\dfrac{1}{G_m - G_f} + \dfrac{6(K_f + 2G_f)V_f}{5(3K_f + 4G_f)G_f}}\right)} \tag{5.20}$$

CHAPTER 6: RESULTS OF THROUGH THICKNESS YOUNG'S MODULI OF MULTI-LAYER MODELS

6.0 Introduction

This chapter reports the through-thickness Young's modulus values obtained from numerical modelling of thin multi-layer film/adhesive interfaces containing auxetic and/or conventional films and adhesive layers. The thickness of these multi-layer film/adhesive interfaces ranged from 0.05 mm to 1.05 mm.

6.1 Through-Thickness Tensile Properties: Low Modulus Adhesive

The effect of adhesive thickness on the effective Young's modulus in the through-thickness direction is shown in Fig 6.1 for the adhesive-only interface with adhesive Young's modulus of 120 MPa. A decrease in the effective through-thickness Young's modulus values converging towards 120 MPa is observed with increase in the thickness of the interface. The solid curve in Fig 6.1 represents a line of best fit through the data points.

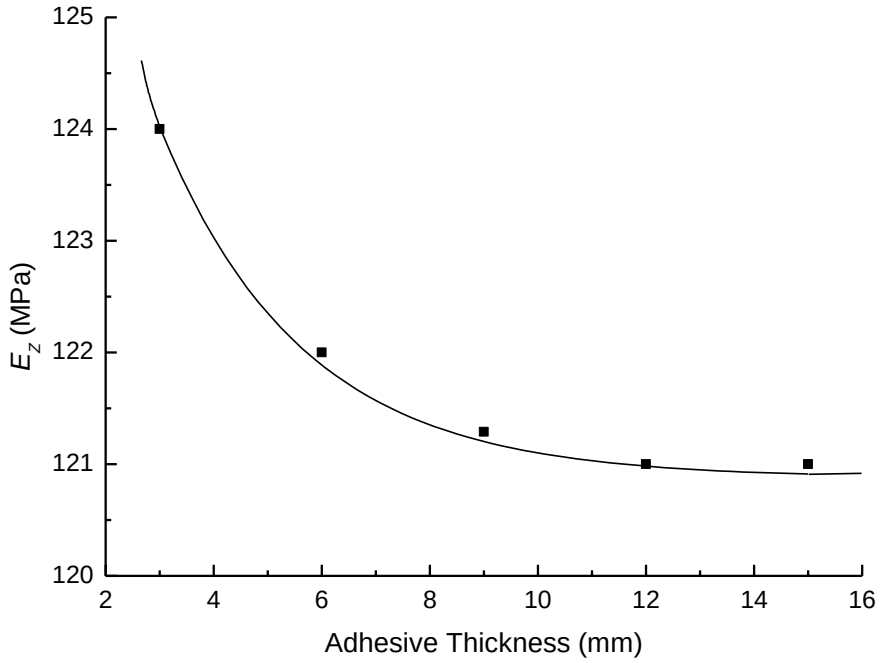

Fig 6.1 Variation in the through-thickness Young's modulus as function of adhesive thickness as modelled using FE employing a low modulus (120 MPa) adhesive.

6.1.1 CIT Model - Young's Modulus Predictions - FE

As described in Chapter 4, Section 4.5, a thickness of 1 mm was maintained for all models of the multi-layer interfaces in the Constant Interface Thickness (CIT) model. The continual addition of conventional and/or auxetic films (film thickness = 0.2 mm) into the interface leads to a reduction in the volume fraction of the adhesive. The three-layer film/adhesive interface containing one film has an adhesive layer thickness of 0.4 mm (adhesive volume fraction of 0.8) while on the other hand the nine-layer film/adhesive interface containing four films has an adhesive layer thickness of only 0.04 mm (adhesive volume fraction of 0.20). In the CIT model the change in the through-thickness Young's modulus, E_Z, was evaluated against the Young's modulus of the control interface (1 mm thick adhesive-only interface).

The Young's modulus values obtained from the FE modelling for interfaces containing auxetic and conventional films within a low modulus (120 MPa) adhesive for the CIT model are presented in Table 6.1. The lay-up sequences, adhesive volume fractions and the percentage changes in the through-thickness Young's modulus are also shown in the table.

Table 6.1 Lay-up sequences, layer thicknesses, volume fractions of adhesive, FE model calculated values of, and percentage changes in, E_Z for the CIT model incorporating a low modulus (120 MPa) adhesive, film layers of thickness 0.2 mm and a total interface thickness of 1 mm.

Sample	Number of Layers	Adhesive Layer Thickness (mm)	Adhesive Volume Fraction	E_Z (MPa)	ΔE_Z (%)
Adhesive only	1	1.00	1.0	132	-
F—C—L	3	0.40	0.8	154	16
F—A—L	3	0.40	0.8	180	36
F—C—C—L	5	0.20	0.6	183	38
F—C—A—L	5	0.20	0.6	221	67
F—A—A—L	5	0.20	0.6	248	88
F—C—C—C—L	7	0.10	0.4	226	71
F—C—C—A—L	7	0.10	0.4	260	97
F—C—A—C—L	7	0.10	0.4	278	110
F—A—C—A—L	7	0.10	0.4	325	146
F—A—A—C—L	7	0.10	0.4	326	147
F—A—A—A—L	7	0.10	0.4	346	163
F—C—C—C—C—L	9	0.04	0.2	294	123
F—C—C—C—A—L	9	0.04	0.2	345	161
F—C—C—A—C—L	9	0.04	0.2	375	184
F—A—A—C—C—L	9	0.04	0.2	421	219
F—A—C—A—C—L	9	0.04	0.2	462	250
F—A—C—C—A—L	9	0.04	0.2	466	252
F—C—A—A—C—L	9	0.04	0.2	478	262
F—A—A—A—C—L	9	0.04	0.2	498	276
F—A—A—A—A—L	9	0.04	0.2	509	285

Key: — - adhesive layer; **A** - Auxetic film; **C** - Conventional film
F— and —L represent the fixed and loading surfaces, respectively

From Table 6.1, generally there is a significant increase in E_Z as the number of films (both conventional and auxetic) in the interface increases. However, the increase in the through-thickness Young's modulus is more pronounced for interfaces containing auxetic films. For example, all-auxetic film/adhesive interfaces (—A—, —A—A—, —A—A—A— and —A—A—A—A—) showed remarkable increases of 36, 88, 163 and 285% in E_Z, respectively. On the other hand, the percentage increase in E_Z for all-conventional film/adhesive interfaces (—C—, —C—C—, —C—C—C— and —C—C—C—C—) were less pronounced; showing changes of 16, 38, 71 and 123%, respectively.

The general increases in through thickness Young's modulus with the addition of films regardless of their Poisson's ratio is primarily due to the fact that the films have a higher Young's modulus (340 MPa) when compared to the adhesive (120 MPa). The additional enhancement due to incorporating auxetic films compared to conventional films can be explained by considering the constraining effects of adjacent layers having different magnitudes and/or signs of Poisson's ratio. The adhesive and conventional film layers contract laterally when a tensile force is applied in the through thickness direction of the interface. On the other hand, the auxetic film layers expand laterally in opposition to the adhesive layers. The auxetic film layers thus constrain the deformation of the adhesive layers to a far greater extend that the conventional film layers, and vice versa, leading to a reduced overall elastic deformation. Thus, the stiffness of a multi-layer interface containing auxetic films is higher than that of an interface containing conventional films.

The FE data also indicate a slight dependency on the ordering of layers for systems having the same constituent volume fractions. For example, in the 9-layer system, four different lay-up sequences were investigated for the case of two auxetic films, two conventional films and five

adhesive layers. The effective interface Young's modulus was found to increase in the sequence: ▬A▬A▬C▬C▬ → ▬A▬C▬A▬C▬ → ▬A▬C▬C▬A▬ → ▬C▬A▬A▬C▬.

6.1.2 Comparison of the FE CIT Model with Analytical Models

The through-thickness Young's moduli of the two-phase interfaces obtained from FE predictions are compared to analytical solutions calculated from the 2-phase modified Rule of Mixtures (Eqs. (4.10a,b and 4.11) and the Ramirez approach [145] (Eq. 4.14) in Fig 6.2. The RM Voigt Eq. (4.16) bounds) are also plotted in Fig 6.2 for the CIT model. The through-thickness Young's moduli values obtained from FE modelling are generally in good agreement with those obtained from the modified RM expression and the Ramirez approach. However the 9-layer interface FE results are higher compared to the analytical models. This may be explained by the fact that the adhesive thickness within the 9-layer CIT interface is only 0.04 mm thick, possibly leading to edge effects that are accounted for in FE and not in the analytical models. The RM-Voigt is independent of variation in the Poisson's ratio; hence the Young's moduli values calculated are the same for both auxetic and conventional film interfaces. The effective in-plane Young's moduli (RM-Voigt bound) are higher than the modified through thickness RM values for the all-conventional film/adhesive (▬C▬, ▬C▬C▬, ▬C▬C▬C▬ and ▬C▬C▬C▬C▬) interfaces in the CIT model. However, the effective through-thickness Young's moduli obtained from modified RM exceed the in-plane RM-Voigt bound predictions for the all-auxetic film/adhesive interfaces in the CIT models. In other words, incorporating auxetic materials within the multi-layer system leads to a large stiffening effect in the RM-Reuss configuration such that it is possible to exceed the RM-Voigt 'upper' bound on E_Z.

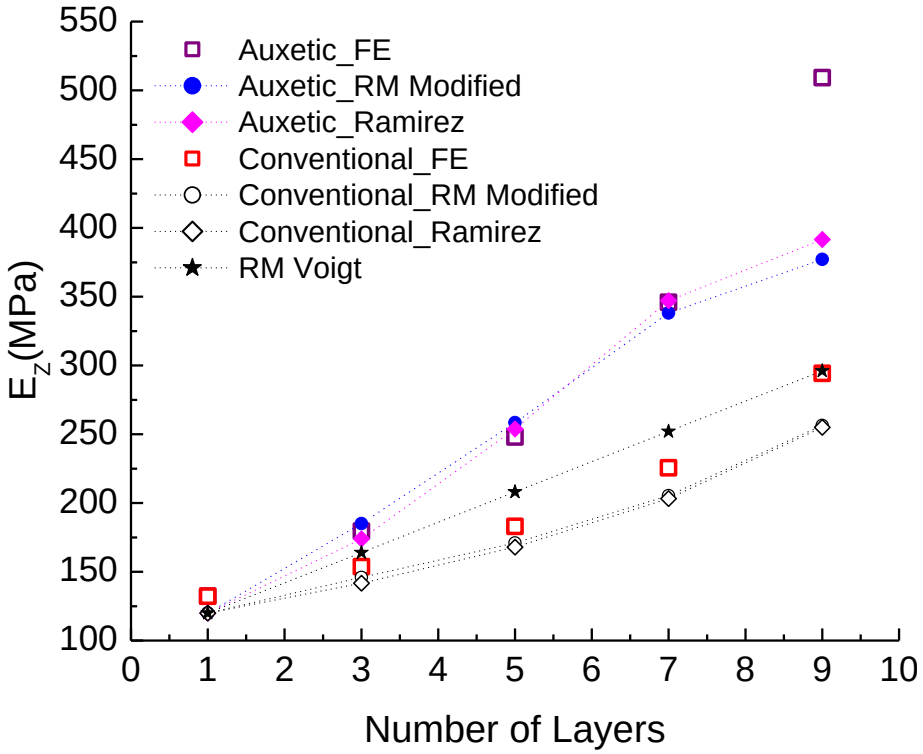

Fig 6.2 FE and analytical predictions of E_Z as a function of number of layers of films and low modulus adhesive (120 MPa) for the CIT 2-phase model.

The two analytical approaches give very similar predictions for the Reuss configuration.

The FE data are generally in reasonable agreement with the analytical predictions for the Reuss configuration. The notable exception is for the case of the auxetic 9-layer system (V_{film} = 0.8) where the FE model prediction is significantly higher than the analytical predictions. There is also a small offset for the adhesive-only 1-layer case (V_{film} = 0), where the FE prediction is 10% higher than the analytical predictions. The offset is maintained, and increases slightly, with film volume fraction in the conventional system. The FE and analytical predictions are in good agreement at intermediate film volume fractions for the auxetic system.

It is likely that the FE model accounts for edge affects not accommodated in the analytical predictions. Note that in the FE models, periodic boundary conditions have deliberately not been employed so as to model the properties of interfaces having through-thickness dimension considerably lower than the in-plane dimensions. In this case, the boundary conditions applied at the surfaces will place significant constraint on the interface material closest to the surfaces.

As a first approximation, consider that each outer region of interface material is fully constrained by the applied boundary conditions in the FE model (i.e. having a Young's modulus $E = \infty$), with the remaining material in the interior of the interface having properties expected of the bulk (i.e. $E = E_{bulk}$). Assume a total interface thickness of T, the thicknesses of the inner and outer regions being t_{int} and t_{out}:

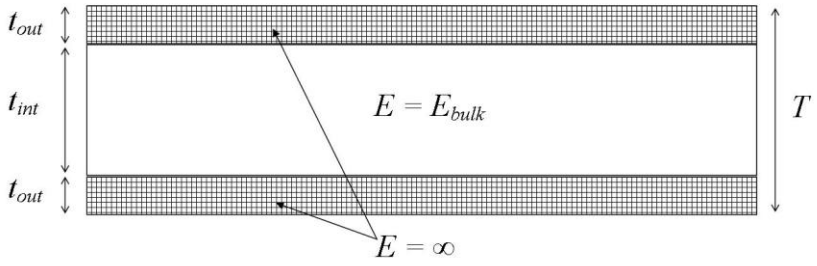

Fig 6.3 Schematic representing a film layer embedded between two outer adhesive layers.

A tension applied through the thickness will increase T by ΔT which will be entirely due to the increase in t_{int} of Δt_{int}, i.e.

$$\Delta T = \Delta t_{\text{int}} \tag{6.1}$$

Now

$$\Delta T = \varepsilon_T T \tag{6.2}$$

and

$$\Delta t_{\text{int}} = \varepsilon_{t\,\text{int}} t_{\text{int}} \tag{6.3}$$

where ε_T and ε_{tint} are the strains through the thickness of the interface and the inner region, respectively.

Substituting (6.2) and (6.3) into (6.1)

$$\varepsilon_T = \frac{\varepsilon_{t\,\text{int}} t_{\text{int}}}{T} \tag{6.4}$$

Recalling the definition of Young's modulus (= σ/ε) and noting that the same stress acts on the overall interface and the inner region, then (6.4) becomes:

$$\frac{\sigma}{E_z} = \frac{t_{\text{int}}}{T}\frac{\sigma}{E_{bulk}} \tag{6.5}$$

Rearranging (6.5) we now have the expression for the effective Young's modulus of the interface taking into account edge effect constraints to modify the bulk modulus:

$$E_z = E_{bulk}\frac{T}{t_{\text{int}}} = E_{bulk}\frac{T}{T - 2t_{out}} \tag{6.6}$$

Considering the adhesive-only system in Fig 6. 2, (V_{film} = 0), then a value of t_{out} = 0.048mm corresponds to T/t_{int}. ~ 1.1 for a 1mm thick interface and, from Eq. (6.6), E_Z = 132.7 MPa,

which agrees with the FE model prediction of 132 MPa. Therefore the thickness of the outer region of the interface that would appear to be affected by edge effects is ~ 0.05mm.

Interestingly, the variation of the through-thickness Young's modulus as a function of adhesive thickness, shown for the FE predictions shown in Fig 6.1 can be reproduced using Eq. 6.6 employing adhesive Young's modulus of 120 MPa and outer layer thicknesses of 0.048 mm (Fig. 6.4).

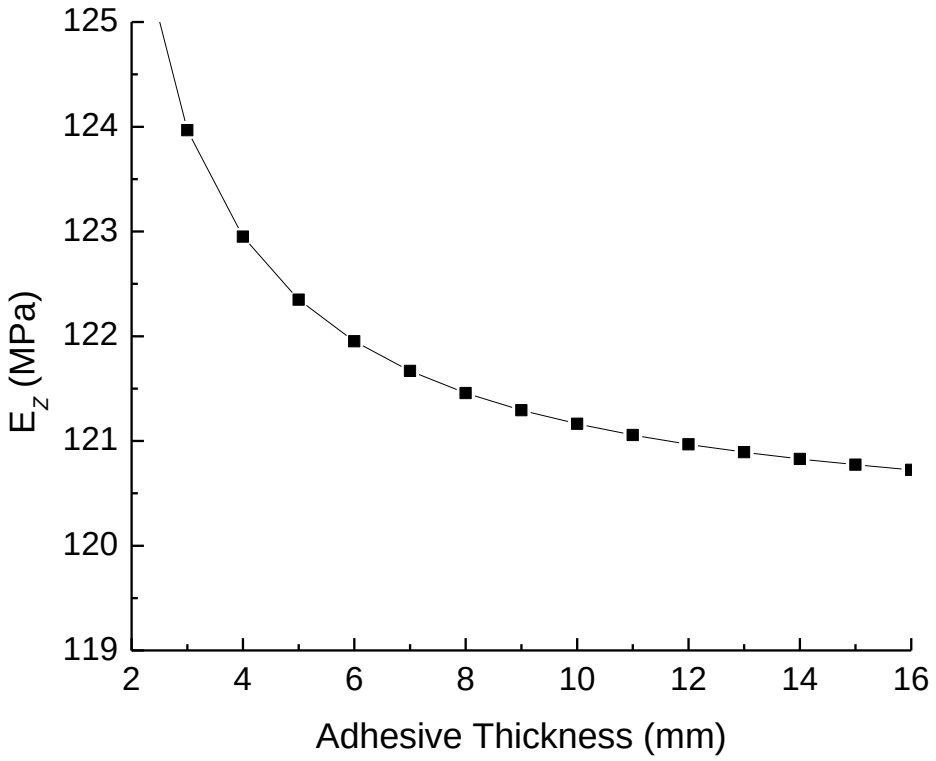

Fig 6.4 Variation in the through-thickness Young's modulus as function of adhesive thickness reproduced using Eq. 6.6 employing a low modulus (120 MPa) adhesive.

Note that for the CIT models, the edge effects are confined to the outermost adhesive layers for all systems except the 9-layer systems. In the 9-layer systems, the adhesive layers have a thickness of 0.04 mm and so the edge effect constraint effectively means that the outermost

adhesive layer is rigid (i.e. has a modulus tending to larger values than employed in the analytical model calculations). A stiff outer adhesive layer would then provide an enhanced stiffening effect on the adjacent film layer (Equation 4.10a in Chapter 4), leading to the current analytical model predictions underestimating the effective Young's modulus of the interface.

This enhanced stiffening would be more pronounced for the auxetic system relative to the conventional system, explaining the large discrepancy between the FE and analytical models in the 9-layer all-auxetic system.

The significance of the edge effect in the 9-layer system is also in evidence when considering the 3-phase interface systems (Fig. 6.5). A comparison of the FE and analytical models of the effective Young's modulus for the 3, 5, 7 and 9-layer interface with volume fraction of auxetic constituents is shown in Fig 6.5. For the 3-, 5- and 7-layer systems the FE data are in reasonable agreement with the analytical model data, but show dramatic increase over the analytical model predictions for the 9-layer systems. The RM predictions are in closest agreement with the FE data for the 3-, 5- and 7-layer systems. The Ramirez prediction trends show increasing slopes with increasing auxetic film volume fraction, whereas the FE data trends show decreasing slopes as the volume fraction of auxetic film increases. The presence of a 'hump' in the FE data may indicate next-nearest neighbour (i.e. film-film) interactions are providing additional constraint not accounted for in the analytical models.

The Ramirez approach, modified RM and FE analysis are in good agreement and all show increase in effective through thickness Young's modulus of the interfaces with increase in auxetic volume fraction.

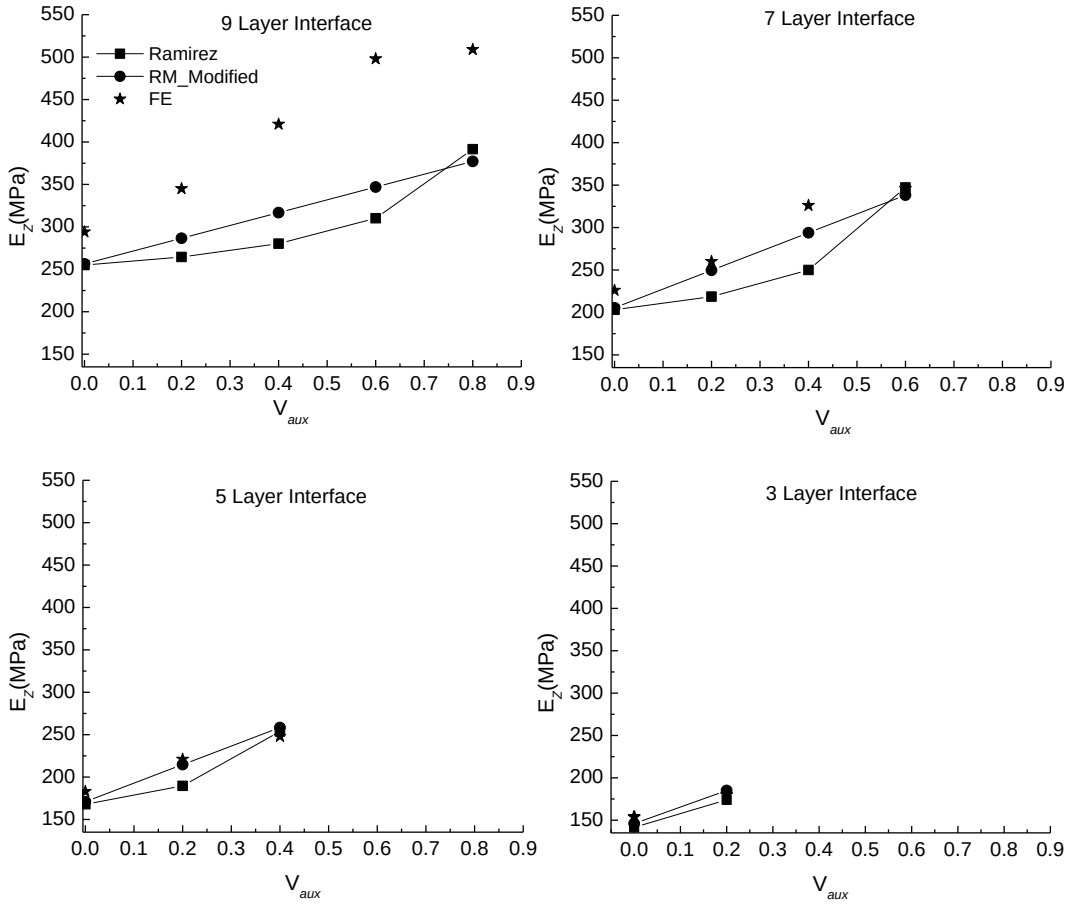

Fig 6.5 Effective through thickness Young's modulus predictions for the CIT model as a function of volume fraction of auxetic films (low modulus adhesive system). Data shown for modified RM, Ramirez approach and FE predictions.

6.1.3 CCLT Model - Young's Modulus Predictions

In the Constant Constituent Layer Thickness (CCLT) model the adhesive layer and film thicknesses are kept constant at 0.05 mm and 0.2 mm, respectively. The variation in E_Z was determined by comparing the Young's modulus values of the multi-layered interfaces (adhesive and the films) to that of an adhesive only interface of the same thickness. This comparison was necessitated by the fact that the Young's modulus values calculated for adhesive interfaces of different thicknesses varied for the interface thickness investigated in

this work (0.05 mm −1.05 mm) and is due to the influence of edge effects associated with the loading surfaces being significant for the interface thicknesses considered.

The Young's modulus values obtained from FE modelling for interfaces containing auxetic and conventional films within a low modulus (120 MPa) adhesive are presented in Table 6.2 for the CCLT model. The lay-up sequences, adhesive volume fractions and the percentage changes in the through-thickness Young's modulus are also shown in the table.

The all-conventional film/adhesive CCLT interfaces (**—C—**, **—C—C—**, **—C—C—C—** and **—C—C—C—C—**) showed significant increases in the through-thickness Young's modulus of 102, 108, 109 and 110%, respectively. The all-auxetic film/adhesive CCLT thickness interfaces (**—A—**, **—A—A—**, **—A—A—A—** and **—A—A—A—A—**) showed relatively higher increases in E_Z of between 175 and 253%.

Table 6.2 Lay-up sequences, layer thicknesses, volume fractions of adhesive, FE model calculated values of, and percent changes in, E_Z for the CCLT model incorporating a low modulus (120 MPa) adhesive and film layers of thickness 0.2 mm.

Sample	Number of Layers	Adhesive Layer Thickness (mm)	Adhesive Volume Fraction	E_Z (MPa)	ΔE_Z (%)
Adhesive only	1	0.30	1	150	-
^{F}—C—^{L}	3	0.05	0.33	302	102
^{F}—A—^{L}	3	0.05	0.33	411	175
Adhesive only	1	0.55	1	141	-
^{F}—C—C—^{L}	5	0.05	0.27	296	108
^{F}—C—A—^{L}	5	0.05	0.27	414	193
^{F}—A—A—^{L}	5	0.05	0.27	462	227
Adhesive only	1	0.80	1	135	-
^{F}—C—C—C—^{L}	7	0.05	0.25	284	109
^{F}—C—C—A—^{L}	7	0.0.5	0.25	380	181
^{F}—C—A—C—^{L}	7	0.05	0.25	345	155
^{F}—A—C—A—^{L}	7	0.05	0.25	461	241
^{F}—A—A—C—^{L}	7	0.05	0.25	449	231
^{F}—A—A—A—^{L}	7	0.05	0.25	469	246
Adhesive only	1	1.05	1	132	-
^{F}—C—C—C—C—^{L}	9	0.05	0.23	276	110
^{F}—C—C—C—A—^{L}	9	0.05	0.23	319	143
^{F}—C—C—A—C—^{L}	9	0.05	0.23	344	162
^{F}—A—A—C—C—^{L}	9	0.05	0.23	445	238
^{F}—A—C—A—C—^{L}	9	0.05	0.23	430	227
^{F}—A—C—C—A—^{L}	9	0.05	0.23	424	222
^{F}—C—A—A—C—^{L}	9	0.05	0.23	419	219
^{F}—A—A—A—C—^{L}	9	0.05	0.23	455	246
^{F}—A—A—A—A—^{L}	9	0.05	0.23	465	253

Key: — - adhesive layer; **A** - Auxetic film; **C** - Conventional film
^{F}— and —^{L} represent the fixed and loading surfaces, respectively

As with the CIT models, the CCLT model through-thickness Young's modulus generally increases with the addition of films regardless of their Poisson's ratio, due to the higher film Young's modulus (340 MPa) compared to the adhesive Young's modulus (120 MPa). The stiffness of a multi-layer interface containing auxetic films is higher than that of an interface containing conventional films due to the constraining effects of adjacent layers having differing Poison's ratios being more pronounced for the systems containing auxetic films.

6.1.4 Comparison of the FE CCLT Model with Analytical Models

The through-thickness Young's moduli of the two-phase interfaces obtained from FE predictions are compared to analytical models, Fig 6.6. Interestingly, the FE data is consistently higher than the Ramirez and the modified RM. In the CCLT model, the adhesive layer has a constant thickness of 0.05 mm, hence the edge effects are bound to be more significant for all layer systems. Similar to the observations made in the CIT model, the modified through thickness model exceeds the RM Voigt bounds for the auxetic interfaces.

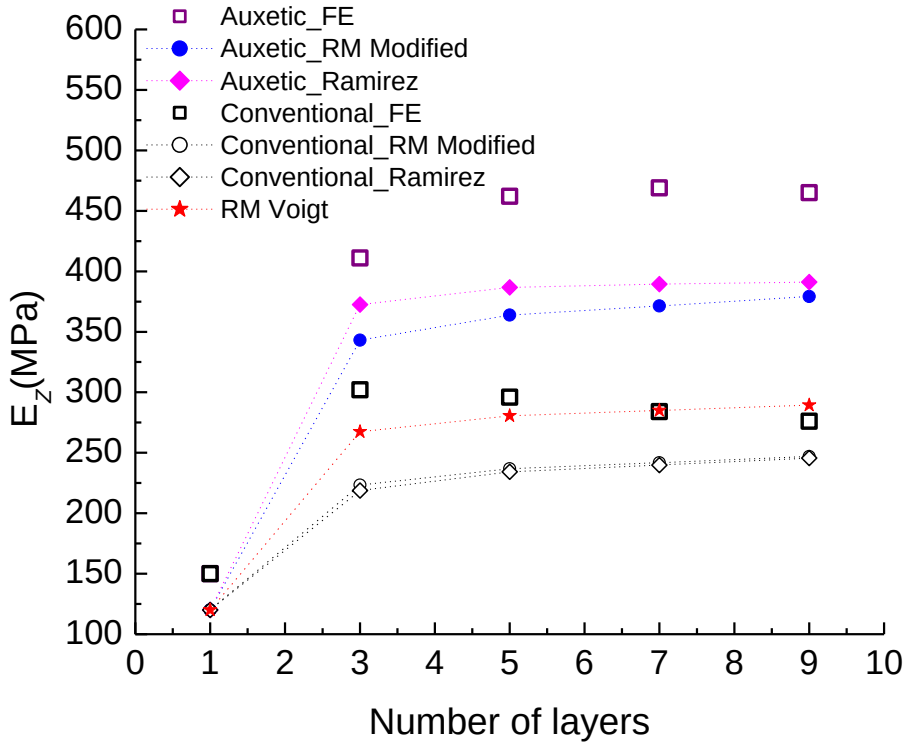

Fig 6.6 FE and analytical predictions of E_Z as a function of total number of layers of films and low modulus adhesive (120 MPa) for the CCLT model 2-phase model.

The predicted Ramirez and modified RM Young's moduli data for the 3, 5, 7 and 9-layer 3-phase interface systems are compared with the FE predictions in Fig 6.7. All models show an increase in effective Young's modulus with increase in auxetic volume fraction. The FE

predictions are consistently higher than the analytical models. The Ramirez and modified RM are in reasonable agreement.

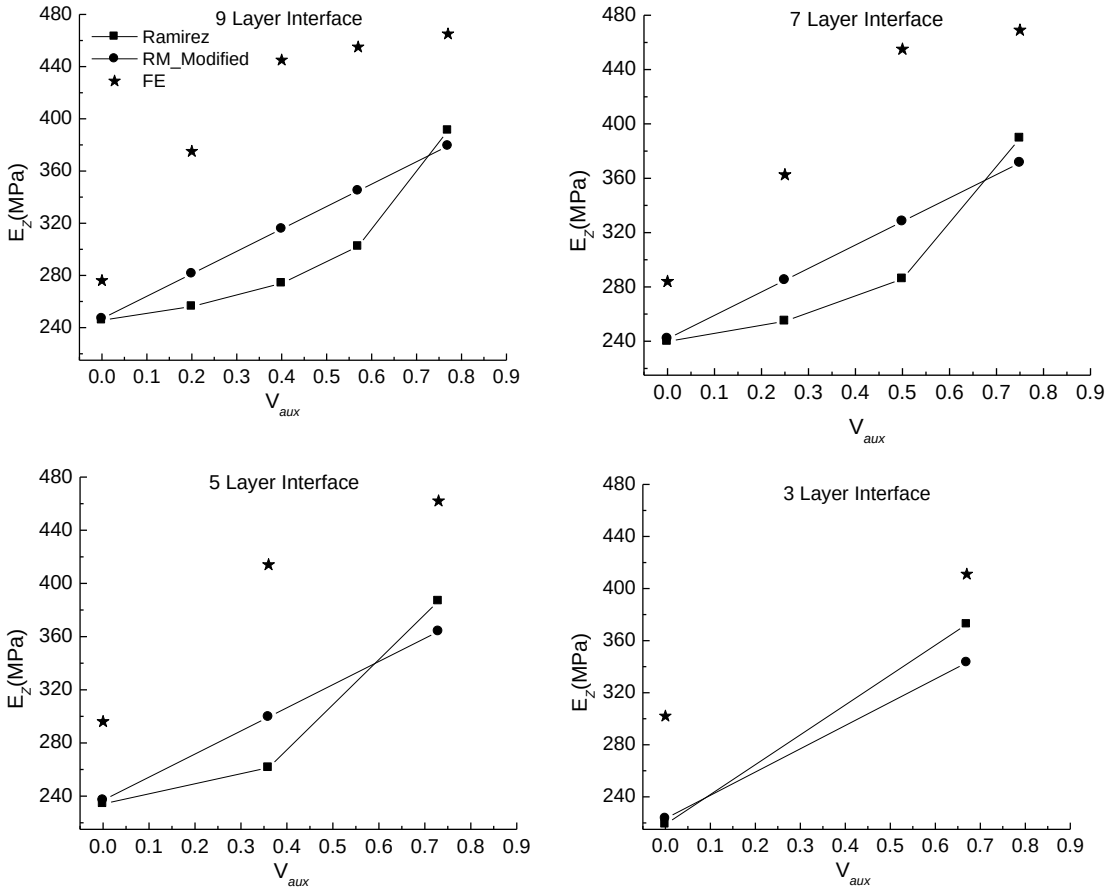

Fig 6.7 Effective through thickness Young's modulus predictions for the CCLT interface model as a function of volume fraction of auxetic films (low modulus adhesive system). Data shown for the Ramirez approach, modified RM and FE analysis.

Increases in E_Z for the 3, 5, 7 and 9 layer interfaces seem to level off for each system. The reason for similar effective E_Z values is the little variation in the adhesive volume fraction i.e. 0.33, 0.27, 0.25, 0.23 adhesive volume fractions for the 3, 5, 7 and 9 layer interfaces respectively. This is different from the CIT model where there is significant variation in

adhesive volume fraction for the layer systems i.e. 0.8, 0.6, 0.4 and 0.2 for the 3, 5 ,7,and 9 layers respectively.

6.1.5 Deformation Patterns: Low Modulus Adhesive Models

The conventional and auxetic films used in the models described in this chapter have the same Young's modulus but different Poisson's ratios of +0.43 and −0.90, respectively. The Poisson's ratio of the polymeric adhesive is +0.30. Lateral expansion or contraction of the films and the adhesive were analysed in order to understand the changes in the through-thickness Young's modulus of the interfaces with composition. Non-auxetic materials such as the adhesive and conventional films contract laterally when a tensile load is applied along the *Z*-axis of the multi-layer interface. In contrast, auxetic materials show a lateral expansion under similar loading conditions. The auxetic films therefore tend to resist the lateral deformation of the adhesive, thus providing a stiffening mechanism such that the overall displacement (strain) in the axial (*Z*-direction) is reduced and therefore higher E_Z values are obtained.

Fig 6.8 shows the deformation patterns of single layers of the adhesive, conventional and auxetic films, subject to an applied stress of 0.11Pa in the Z direction. The adhesive and conventional films contract transversely whilst the auxetic film expands. The auxetic layer has the least maximum displacement in the through thickness direction compared to the conventional film (even though they are of the same modulus), clearly showing the stiffness effect brought about by the negative Poisson's ratio. Fig 6.9 shows the FE deformation patterns of an all-auxetic 9-layer (combination of the adhesive and auxetic film) interface (**—**A**—**A**—**A**—**A**—**) subjected to tensile loading in the through-thickness direction. Auxetic

films (red layers) expand outward. The adhesive layers also expand transversely, despite having a positive Poisson's ratio, due to the constraining effects of the adjacent higher modulus auxetic layers.

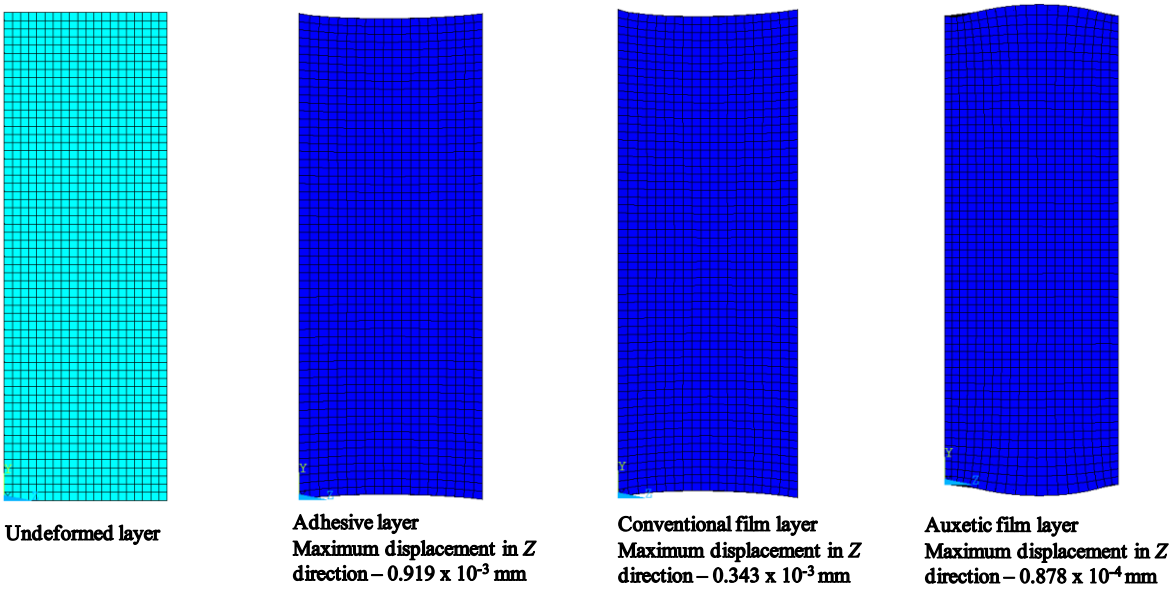

Fig 6.8 Deformation patterns of single layers of low adhesive, conventional and auxetic film.

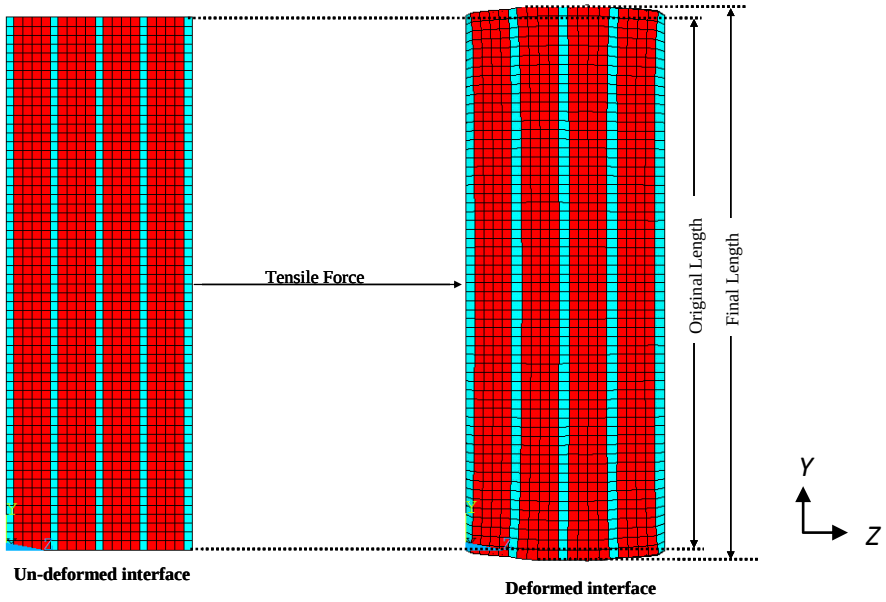

Fig 6.9 Deformation patterns of the all-auxetic nine-layer interface (—A—A—A—A—). Maximum displacement in the through thickness direction is 0.218 x 10^{-3} mm.

The deformation pattern for an all-conventional film interface (combination of the adhesive and conventional film) is shown in Fig 6.10. In this case both the films and adhesive laterally contract when a tension force is applied in the through-thickness direction. The FE models therefore support the considerations above regarding the opposing lateral deformations of auxetic and conventional materials to lead to stiffness effects for alternative layers of negative and positive Poisson's ratio materials.

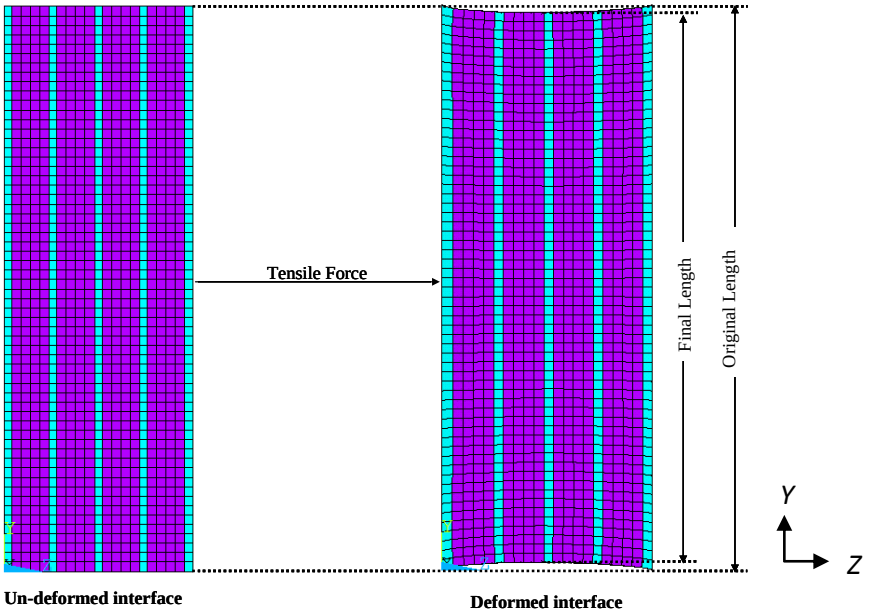

Fig 6.10 Deformation patterns of the all-conventional nine-layer interface (—C—C—C—C—). Maximum displacement in the through thickness direction is 0.378 x10 $^{-3}$ mm.

6.2 Through-Thickness Tensile Moduli: High Modulus Adhesive

The effect of using an adhesive with a higher modulus (1700 MPa) than the films on the through-thickness Young's modulus of the multi-layer interface was investigated using the FE and analytical methods described earlier. The CIT and CCLT models were considered and the modelling results are discussed herein. As with the low modulus adhesive models, the

through-thickness Young's modulus of the adhesive varied with interface thicknesses, Fig 6.11. The through-thickness Young's modulus values for the adhesive interfaces decreased with the increase in interface thickness approaching a value of about 1700 MPa.

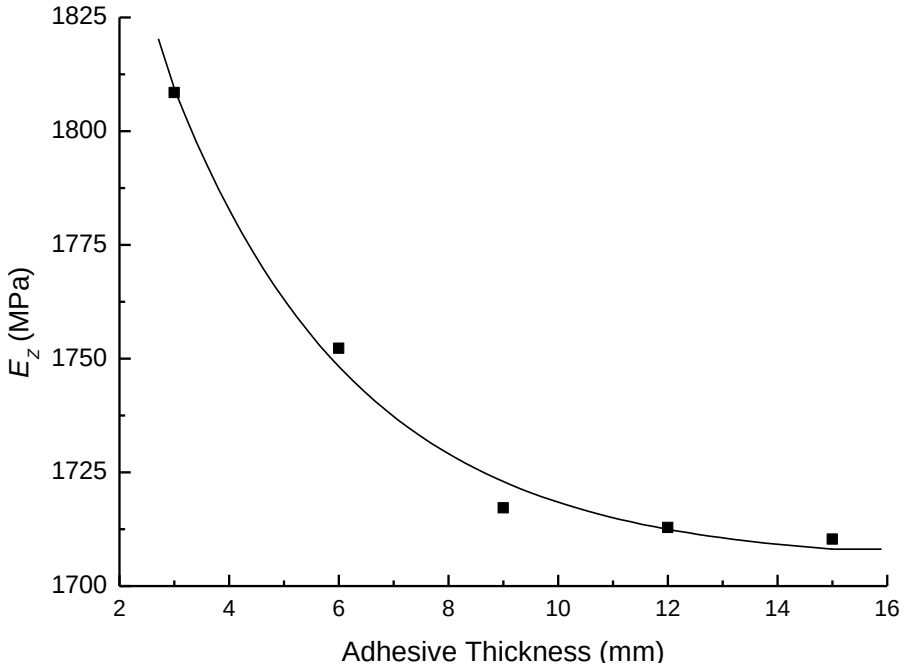

Fig 6.11 Variation in the effective through-thickness Young's modulus of an adhesive-only interface as a function of adhesive thickness, modelled using FEM employing a high modulus (1700 MPa) adhesive.

6.2.1 CIT Model - Young's Modulus Predictions - FE

The Young's modulus values and their change relative to the adhesive-only interface of equivalent thickness, obtained from FEM for interfaces containing auxetic and conventional films within a high modulus (1700 MPa) adhesive, CIT model are presented in Table 6.3. The lay-up sequences, adhesive layer thicknesses, and adhesive volume fractions are also given.

Table 6.3 Lay-up sequences, adhesive layer thicknesses, volume fractions of adhesive, FE model calculated values of, and percentage changes in, E_Z for the CIT model incorporating a high modulus (1700 MPa) adhesive, film layers of thickness 0.2 mm and a total interface thickness of 1 mm.

Sample	Number of Layers	Adhesive Layer Thickness (mm)	Adhesive Volume Fraction	E_Z (MPa)	ΔE_Z (%)
Adhesive only	1	1.00	1.0	1873	-
F—C—L	3	0.40	0.8	1351	-28
F—A—L	3	0.40	0.8	2082	11
F—C—C—L	5	0.20	0.6	1026	-45
F—C—A—L	5	0.20	0.6	1462	-22
F—A—A—L	5	0.20	0.6	2035	9
F—C—C—C—L	7	0.10	0.4	793	-58
F—C—C—A—L	7	0.10	0.4	1099	-41
F—C—A—C—L	7	0.10	0.4	1154	-38
F—A—C—A—L	7	0.10	0.4	1512	-19
F—A—A—C—L	7	0.10	0.4	1507	-20
F—A—A—A—L	7	0.10	0.4	1966	5
F—C—C—C—C—L	9	0.04	0.2	604	-68
F—C—C—C—A—L	9	0.04	0.2	856	-54
F—C—C—A—C—L	9	0.04	0.2	853	-55
F—A—A—C—C—L	9	0.04	0.2	1158	-38
F—A—C—A—C—L	9	0.04	0.2	1191	-36
F—A—C—C—A—L	9	0.04	0.2	1145	-39
F—C—A—A—C—L	9	0.04	0.2	1220	-35
F—A—A—A—C—L	9	0.04	0.2	1422	-24
F—A—A—A—A—L	9	0.04	0.2	1787	-5

Key: — - adhesive layer; **A** - Auxetic film; **C** - Conventional film
F— and —L represent the fixed and loading surfaces, respectively

A decrease in E_Z is observed in the CIT model as conventional films with a Young's modulus of 340 MPa are added to the higher modulus adhesive. The reduction varies from 28% for the three-layer interface (—C—) to 68% for the nine-layer interface (—C—C—C—C—). However, it is observed that the addition of auxetic films with a Young's modulus of 340 MPa to the higher modulus adhesive within the CIT model actually led to a slight increase in the through-thickness Young's modulus for the all-auxetic film three-layer (11% increase), five-

layer (9%) and seven-layer (5%) interfaces. The nine-layer all-auxetic film interface (—A—A—A—A—) consisting of an adhesive volume fraction of 0.2 had a reduction in the effective through-thickness Young's modulus of 5 %.

6.2.2 Comparison of the FE CIT Model with Analytical Models

Fig 6.12 is a plot of the comparison between the Ramirez approach, modified RM and FE data for the 2-phase (all auxetic and all conventional) interfaces. The FE data and the analytical models show a reasonable agreement in the effective Young's modulus trend of the interfaces with increase in layer numbers. The auxetic interfaces show an enhancement in the effective Youngs modulus for the 3, 5 and 7 layer interfaces regardless of the fact that the auxetic layer has a lower Young's modulus (340 MPa) compared to the high modulus adhesive (1700 MPa). A decrease in the Young's modulus is observed for the nine layer all-auxetic interface in which the volume fraction of the high modulus adhesive is only 0.2. The Ramirez and the modified RM model predictions tend to exceed the FE data for 5 and 7 layer interfaces.

On the other hand, the addition of conventional films to the high modulus adhesive shows a reduction on the effective Young's modulus of the interfaces. Similar to previous observations, the modified RM exceeds the RM-Voigt bounds for the auxetic interfaces, but not for the conventional interfaces.

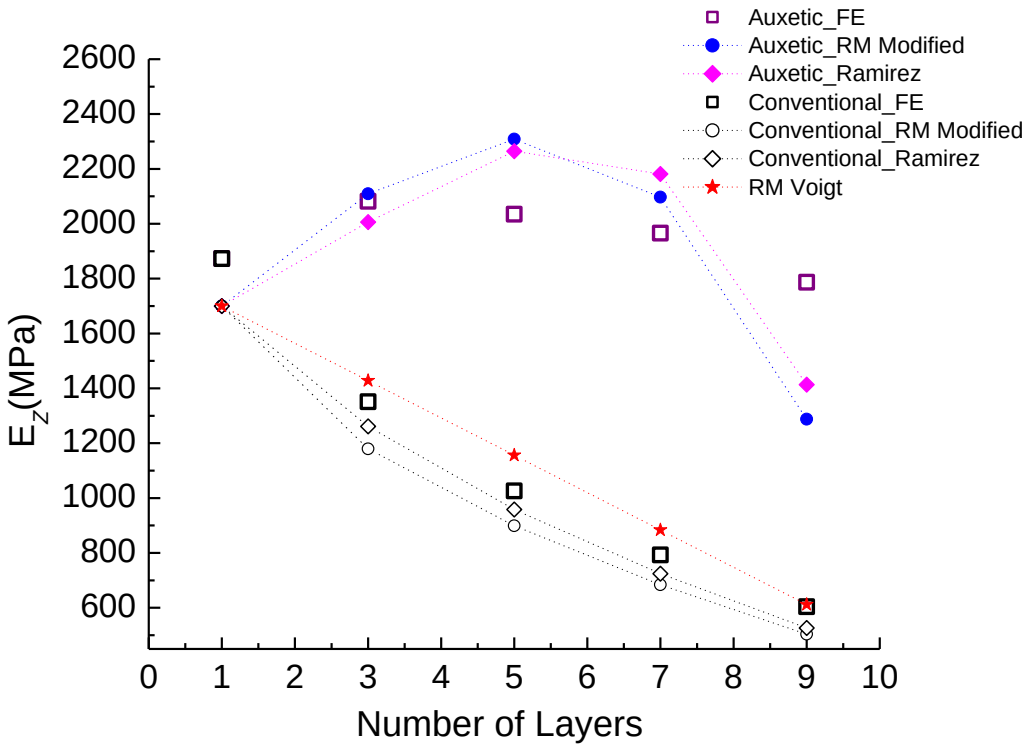

Fig 6.12 FE and analytical predictions of E_Z as a function of total number of layers of films and high modulus adhesive (1700 MPa) for the CIT model.

The predicted Ramirez and modified RM Young's moduli data for the 3, 5, 7 and 9-layer 2-phase and 3-phase interface systems are compared with the FE predictions in Fig 6.13. All models show an increase in effective Young's modulus with increase in auxetic volume fraction. The Ramirez and modified RM are in reasonable agreement with the FE data, with the largest discrepancy being observed for the 9-layer systems due to edge effects as also observed for the low modulus adhesive systems. The modified RM model best reproduces the linear increase in effective Young's modulus with auxetic film volume fraction predicted by the FE models. The Ramirez model predicts an increasing slope, as also observed in the low modulus adhesive CIT models.

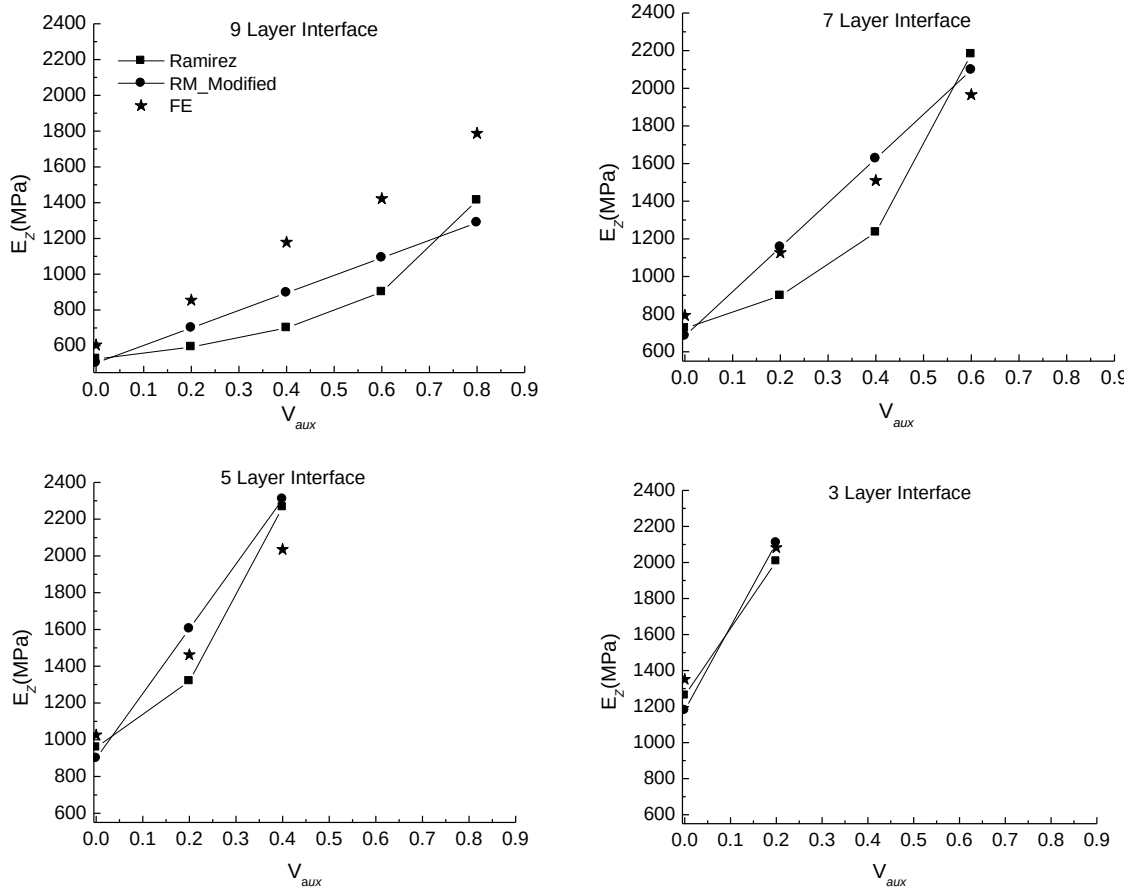

Fig 6.13 Effective through thickness Young's modulus predictions for the CIT model as a function of volume fraction of auxetic films (high modulus adhesive system). Data shown for modified RM, Ramirez approach and FE predictions.

6.2.3 CCLT Model - Young's Modulus Predictions - FE

The Young's modulus values and their change relative to the adhesive-only interface of equivalent thickness, obtained from FEM for interfaces containing auxetic and conventional films within a high modulus (1700 MPa) adhesive, CCLT model are presented in Table 6.4. The lay-up sequences, adhesive layer thicknesses, and adhesive volume fractions are also given.

Table 6.4 Lay-up sequences, adhesive layer thicknesses, volume fractions of adhesive, FE model calculated values of, and percentage changes in, E_Z for the CCLT model incorporating a high modulus (1700 MPa) adhesive, and film layers of thickness 0.2 mm.

Sample	Number of Layers	Adhesive Layer Thickness (mm)	Adhesive Volume Fraction	E_Z (MPa)	ΔE_Z (%)
Adhesive only	1	0.30	1.00	2118	-
F—C—L	3	0.05	0.33	942	-56
F—A—L	3	0.05	0.33	1828	-14
Adhesive only	1	0.55	1.00	2001	-
F—C—C—L	5	0.05	0.27	761	-62
F—C—A—L	5	0.05	0.27	1246	-38
F—A—A—L	5	0.05	0.27	1868	-7
Adhesive only	1	0.80	1.00	1918	-
F—C—C—C—L	7	0.05	0.25	677	-65
F—C—C—A—L	7	0.0.5	0.25	1070	-44
F—C—A—C—L	7	0.05	0.25	933	-51
F—A—C—A—L	7	0.05	0.25	1458	-24
F—A—A—C—L	7	0.05	0.25	1413	-26
F—A—A—A—L	7	0.05	0.25	1862	-3
Adhesive only	1	1.05	1.00	1864	-
F—C—C—C—C—L	9	0.05	0.23	633	-66
F—C—C—C—A—L	9	0.05	0.23	794	-57
F—C—C—A—C—L	9	0.05	0.23	879	-53
F—A—A—C—C—L	9	0.05	0.23	1267	-32
F—A—C—A—C—L	9	0.05	0.23	1261	-32
F—A—C—C—A—L	9	0.05	0.23	1177	-37
F—C—A—A—C—L	9	0.05	0.23	1158	-38
F—A—A—A—C—L	9	0.05	0.23	1471	-21
F—A—A—A—A—L	9	0.05	0.23	1824	-2

Key: — - adhesive layer; **A** - Auxetic film; **C** - Conventional film
F— and —L represent the fixed and loading surfaces, respectively

The CCLT model showed a decrease in E_Z when either auxetic or conventional films were added to the high modulus adhesive. As with the CIT model, the addition of conventional films showed a more profound decrease in the through-thickness Young's modulus of the interfaces compared to the addition of auxetic films. The addition of conventional films showed decreases of 56% and 66% for the three-layer (—C—) and nine-layer interfaces (—C—C—C—C—), respectively. The addition of auxetic films showed a decrease of 14% and 2% for the three-layer (—A—) and nine-layer (—A—A—A—A—) interfaces,

respectively, corresponding to respective increases in auxetic film volume fraction as the adhesive volume fraction changes from 0.33 to 0.23.

6.2.4 Comparison of the FE CCLT model with analytical models

FE, Ramirez and modified RM predictions of the 2-phase through-thickness Young's modulus for the CCLT model are shown in Fig 6.14.

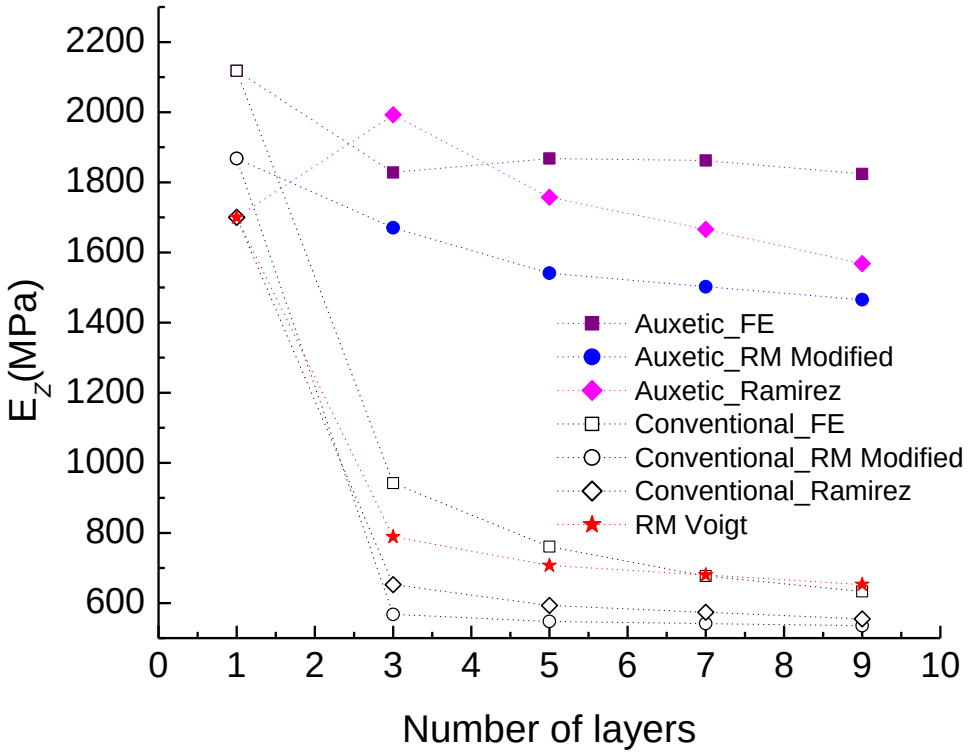

Fig 6.14 FE and analytical predictions of E_Z as a function of total number of layers of films and high modulus adhesive (1700 MPa) for the CCLT model.

Whilst the absolute values obtained from numerical and analytical methods are different, their trends as a function of number of interface layers are similar. For the all-conventional film/adhesive interfaces, RM-Voigt (in-plane) predictions are higher than their modified through thickness RM counterparts. However, the opposite is true when the all-auxetic

film/adhesive interfaces are considered. A similar ability to exceed the upper Voigt bound when incorporating auxetic film in the Reuss configuration was observed for the low modulus adhesive interfaces.

The predicted Ramirez and modified RM Young's moduli data for the 3, 5, 7 and 9-layer interface systems are compared with the FE predictions in Fig 6.15.

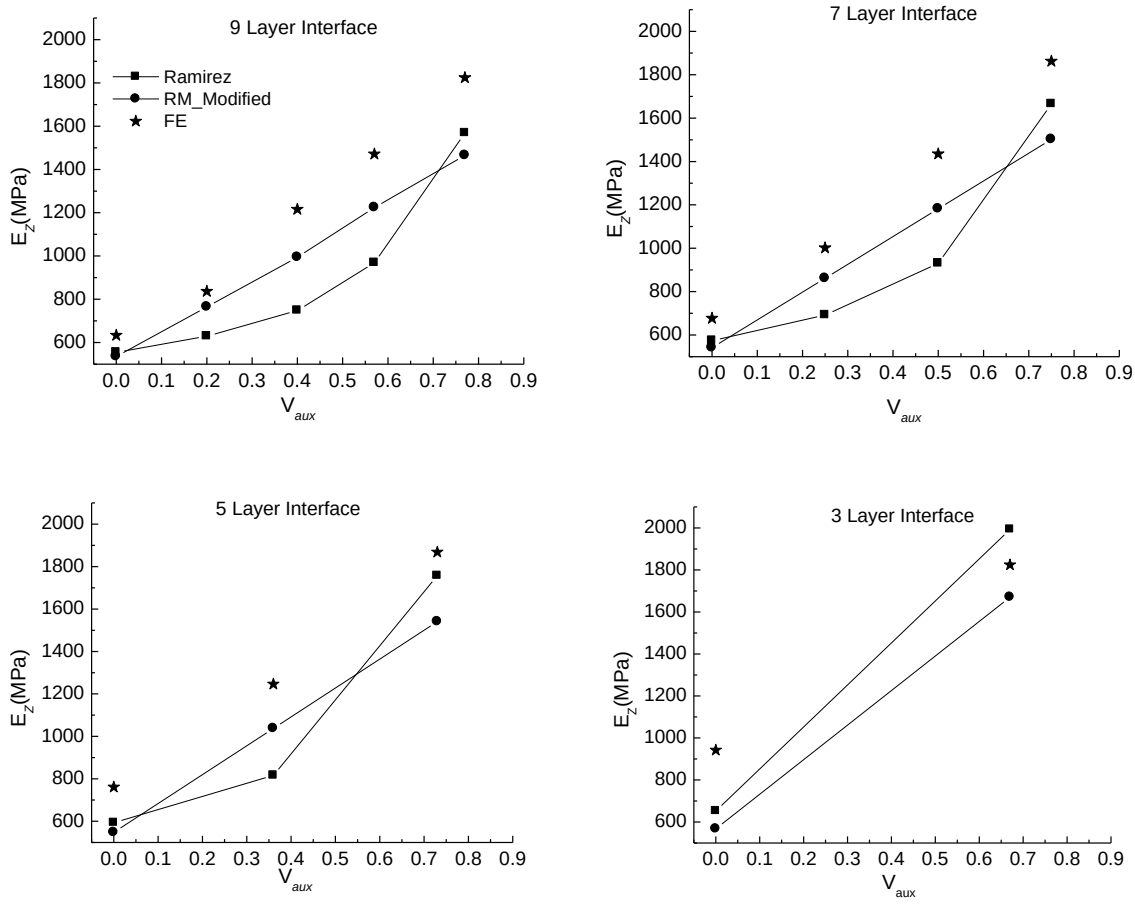

Fig 6.15 Effective through thickness Young's modulus predictions for the CCLT model as a function of volume fraction of auxetic films (high modulus adhesive system). Data shown for modified RM, Ramirez approach and FE predictions.

All models show an increase in effective Young's modulus with increase in auxetic volume fraction. The Ramirez, modified RM and FE data are in reasonable agreement with the FE showing slightly higher trends.

6.2.5 Deformation Patterns: High Modulus Adhesive Models

Fig 6.16 shows the deformation patterns of single layers of the high modulus adhesive, conventional and auxetic films, subject to a stress of 0.11Pa. In this case, since the adhesive has a high Young's modulus, the interface tends to contract much less compared to the low adhesive interface. FE deformation patterns of an all-auxetic nine-layer high modulus adhesive interface (—A—A—A—A—) subjected to a tensile load in the through-thickness direction are shown in Fig 6.15. The auxetic films expand laterally due to the negative Poisson's ratio; similar to the observation made for the low modulus adhesive case, Fig 6.8, 6.9. However in Fig 6.16, the adhesive Young's modulus is higher than in the low modulus adhesive interface, and hence pulls in more, resisting the lateral expansion of the auxetic films. Fig 6.17 does not have a smooth curvature at the top and bottom surfaces due to the more resistant adhesive. As a consequence of the high modulus adhesive, the interfacial expansion is reduced compared to the deformed low modulus interface. The deformation pattern for an all-conventional nine-layer high modulus adhesive interface is shown in Fig 6.18. Both the conventional films and adhesive contract laterally since they have positive Poisson's ratios, as was observed for the low modulus adhesive case, Fig 6.10. The overall transverse contraction of the interface in Fig 6.17 is less pronounced compared to the low modulus deformed interface, Fig 6.9.

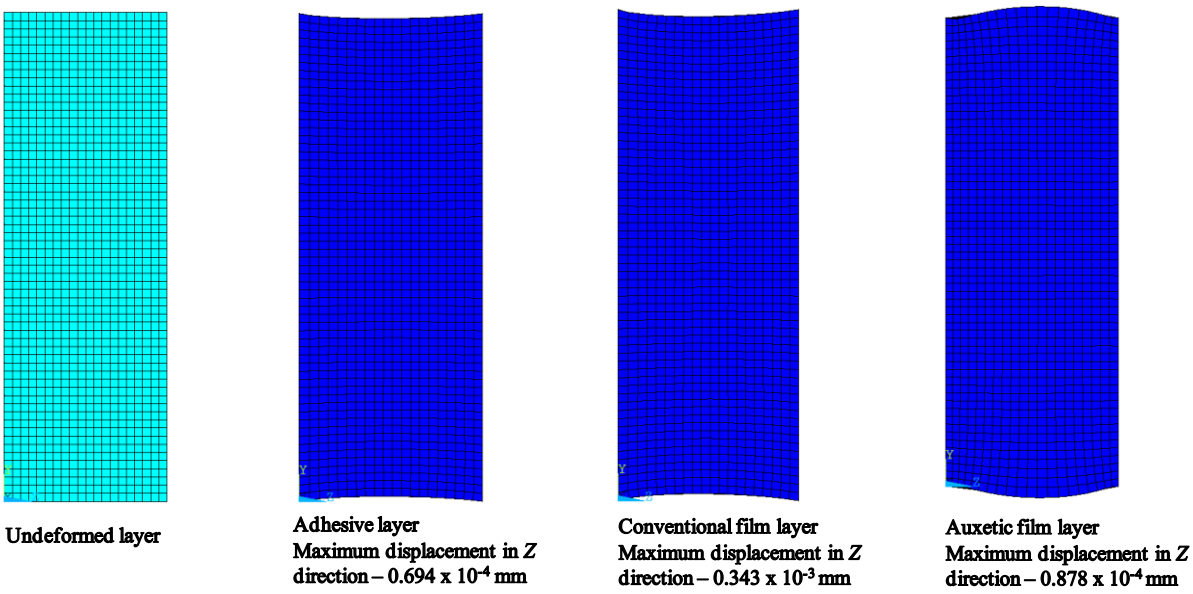

Fig 6.16 Deformation patterns of single layers of high adhesive, conventional and auxetic film.

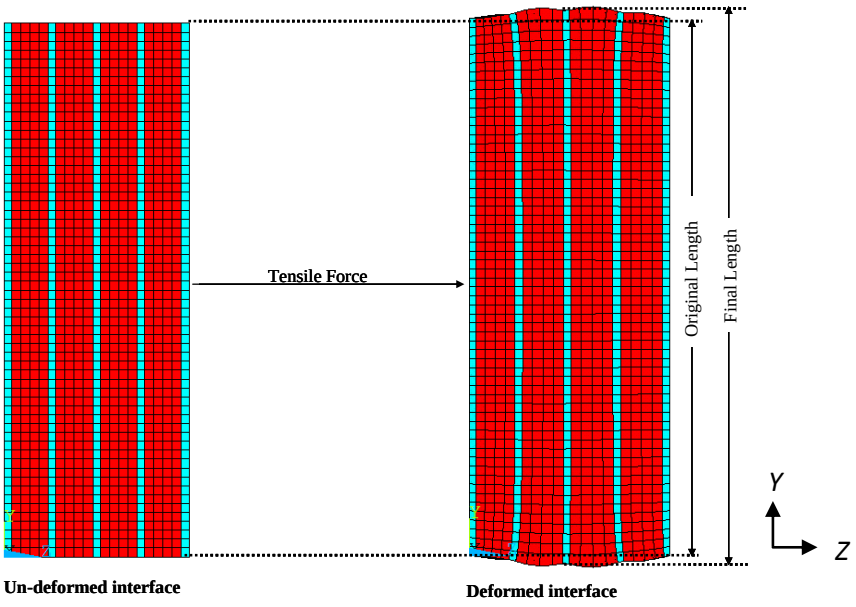

Fig 6.17 Deformation patterns of the all-auxetic nine-layer interface (▬A▬A▬A▬A▬).

Maximum displacement in the through thickness direction is 0.622 x 10^{-4} mm.

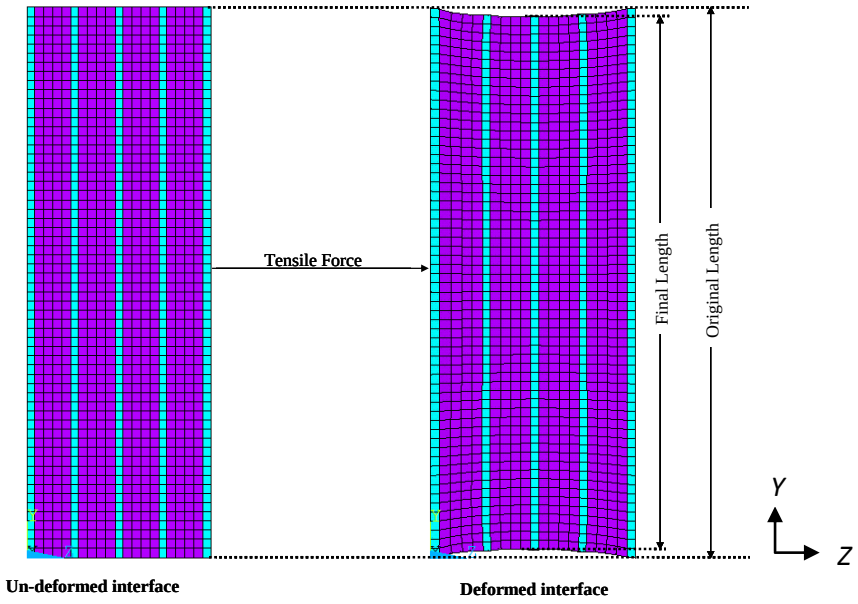

Fig 6.18 Deformation patterns of the all-conventional nine-layer interface (—C—C—C—C—). Maximum displacement in the through thickness direction is 0.184 x 10^{-3} mm.

6.3 Summary

Multi-layer film/adhesive interfaces were modelled using FE and analytical solutions in order to investigate the effect of the constituent material properties such as the Poisson's ratio and Young's moduli on the overall transverse tensile modulus. Two types of multi-layer interfaces, the CIT and CCLT models were considered. It has been shown that the overall Young's modulus of the interface is dependent on the inherent mechanical properties of the films as well as the adhesive. The following conclusions were drawn from predictive modelling performed during this study;

(i) Combining a 340 MPa Young's modulus material with a lower Young's modulus (120 MPa) adhesive increases the effective through-thickness Young's modulus of the interface.

(ii) The effective through-thickness Young's modulus increase due to incorporating higher Young's modulus films within a low modulus adhesive is enhanced when using auxetic films compared to conventional films of the same Young's modulus.

(iii) When a 340 MPa Young's modulus conventional film is combined with a higher Young's modulus (1700 MPa) adhesive in the multi-layer interface, significant decreases in overall through-thickness effective Young's modulus of the interfaces were observed.

(iv) However, the addition of 340 MPa Young's modulus auxetic films within a 1700 MPa Young's modulus adhesive led to an increase in the overall effective Young's modulus for the 3-, 5- and 7-layer CIT interfaces. The improvements in the overall Young's moduli for the CIT model when auxetic films and high modulus adhesive were used were less than 15%.

(v) The effective Young's modulus in the CCLT model when a high modulus adhesive used was lower than the adhesive-only counterpart for all the interfaces studied. However, the addition of auxetic films showed a higher through-thickness effective Young's modulus of the interface relative to the addition of conventional films.

(vi) The 3-phase through thickness modified RM model and the Ramirez approach show reasonable agreement with the FE data for all interfaces studied. The modified RM model generally reproduces the linear Young's modulus vs. auxetic film volume fraction trend predicted from the FE models better than the Ramirez approach.

(vii) In all cases the through-thickness Young's moduli obtained from the modified RM-Voigt were higher than those determined using modified RM for the Reuss configuration for the all-conventional film interface. In the case of all-auxetic films, the RM-Voigt 'upper' bound is exceeded by the RM-Reuss predictions.

(viii) The effective Young's modulus of the multi-layer film/adhesive interfaces is not only dependent on the Young's modulus, Poisson's ratio and volume fractions of the individual constituents, but also on interface thicknesses.

(ix) Future work can include a more detailed modified RM expression which takes into consideration the nearest film neighbour interactions which may be significant in interfaces with low adhesive layer thickness.

(x) FE models take into account the edge effects which are not considered by the analytical models. The thin outer adhesive layers experience edge effects such that the layers are effectively rigid. This further enhances the stiffening effect on the adjacent film layer leading to high effective Young's modulus of the interface. The analytical models thus under estimate the effective Young's modulus of the interfaces. This is observed for the 9 layer CIT model (with adhesive layer thicknesses of 0.04 mm) and all the CCLT models (adhesive thickness 0.05 mm).

CHAPTER 7: SHEAR MODULUS RESULTS OF THE MULTI-LAYER FILM/ADHESIVE INTERFACES

7.0 Introduction

This chapter reports the through-thickness shear properties of the multi-layer film/adhesive interfaces for the two models introduced in Chapter 4; i.e. the CIT and CCLT interfaces. Low modulus (120 MPa) and high modulus adhesives (1700 MPa) were used in the models. Interfaces with high shear resistance are useful in joints where significant shearing forces may be applied. Auxetic materials have a higher shear resistance than their conventional counterparts having the same Young's modulus: consider, for example, negative and positive values of Poisson's ratio in Equation (2-1). Consequently, it expected that incorporating auxetic layers within a multi-layer system should enhance the effective through-thickness shear modulus of the system. The effects of incorporating auxetic and non-auxetic films with a non-auxetic adhesive in a multi-layer interface system were, thus, investigated using FEM and analytical methods.

7.1 Through-Thickness Shear Properties: Low Modulus Adhesive

Numerical modelling of the multi-layer interfaces was performed in the same manner and using the same material properties used in the prediction of the through-thickness Young's modulus in Chapter 6. The Constant Interface Thickness (CIT) and Constant Constituent Layer Thickness (CCLT) models were considered for the cases of low and high Young's modulus adhesives relative to the film Young's modulus.

7.1.1 Comparison of FE and RM Shear Modulus data for the CIT Model

The shear modulus values obtained from the FE modelling for interfaces containing auxetic and conventional films incorporated in a low modulus (120 MPa) adhesive are presented in Table 7.1 for the CIT interface.

Table 7.1 Lay-up sequences, layer thicknesses, volume fractions of adhesive, FE model calculated values of, and percentage changes in, G_{XZ} for the CIT model incorporating a low Young's modulus (120 MPa) adhesive, film layers of thicknesses 0.2 mm and a total interface thickness of 1 mm.

Sample	Number of Layers	Adhesive Layer Thickness (mm)	Adhesive Volume Fraction	G_{XZ} (MPa)	ΔG_{XZ} (%)
Adhesive only	1	1.00	1.0	41	-
^{F}—C—^{L}	3	0.40	0.8	47	14
^{F}—A—^{L}	3	0.40	0.8	51	25
^{F}—C—C—^{L}	5	0.20	0.6	55	33
^{F}—C—A—^{L}	5	0.20	0.6	61	47
^{F}—A—A—^{L}	5	0.20	0.6	68	64
^{F}—C—C—C—^{L}	7	0.10	0.4	65	59
^{F}—C—C—A—^{L}	7	0.10	0.4	74	79
^{F}—C—A—C—^{L}	7	0.10	0.4	74	79
^{F}—A—C—A—^{L}	7	0.10	0.4	85	106
^{F}—A—A—C—^{L}	7	0.10	0.4	85	106
^{F}—A—A—A—^{L}	7	0.10	0.4	99	140
^{F}—C—C—C—C^{L}	9	0.04	0.2	81	97
^{F}—C—C—C—A^{L}	9	0.04	0.2	95	129
^{F}—C—C—A—C^{L}	9	0.04	0.2	95	130
^{F}—A—A—C—C^{L}	9	0.04	0.2	114	178
^{F}—A—C—A—C^{L}	9	0.04	0.2	114	178
^{F}—A—C—C—A^{L}	9	0.04	0.2	114	178
^{F}—C—A—A—C^{L}	9	0.04	0.2	113	176
^{F}—A—A—A—C^{L}	9	0.04	0.2	141	241
^{F}—A—A—A—A^{L}	9	0.04	0.2	180	344

Key: — - adhesive layer; **A** - Auxetic film; **C** - Conventional film
^{F}— and —^{L} represent the fixed and loading surfaces, respectively

An increase in the shear modulus of the CIT interface was observed with the addition of either conventional or auxetic films to the lower Young's modulus adhesive. Increases in shear modulus of 14, 33, 59 and 97% were observed for interfaces containing one (—C—), two (—C—C—), three (—C— C—C—) and four (—C—C—C—C—) conventional films, respectively. However, when auxetic films replaced conventional films in the same lay-ups, the increases in shear modulus were greater. Increases in shear modulus of 25, 64, 140 and 344% were observed for interfaces containing one (—A—), two (—A—A—), three (—A—A—A—) and four (—A—A—A—A—) auxetic films, respectively.

The shear modulus, *G*, is proportional to the Young's modulus, *E*, for linearly elastic isotropic materials (see Eq. 2.1). Eq. 2.1 also shows that *G* is inversely proportional to (1 + υ). Hence as the Poisson's ratio changes from +0.43 (conventional film) to −0.90 (auxetic film) a 14-fold increase in *G* is expected for the auxetic film. For this reason auxetic films have a greater effect on the increase in overall shear modulus of the multi-layer interfaces than conventional films of comparable Young's modulus.

The shear moduli obtained from the FEM predictions for the 2-phase interfaces are compared to analytical solutions calculated from the Rule of Mixtures (RM) (Eq. (4.13)) in Fig 7.1 for the CIT model. The FEM and RM G_{XZ} values are in good agreement, with the latter tending to slightly higher values.

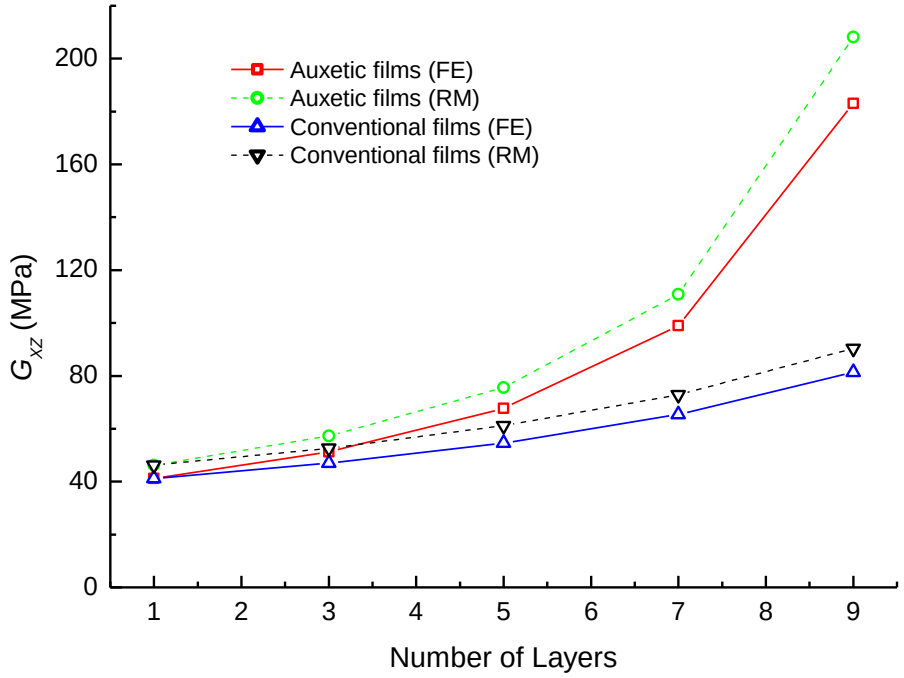

Fig 7.1 FE and RM values of G_{XZ} versus number of layers of films and low modulus adhesive (120 MPa) for the CIT all-auxetic and all-conventional interfaces.

The RM shear moduli increases for the 3-phase, 3, 5, 7 and 9-layer interface systems (Eq. 4.14c) are compared with the FEM predictions in Figure 7.2. Excellent agreement is achieved, indicating the FE analyses produce shear moduli predictions that can be represented by the 3-phase RM to a degree not achieved for the E_Z predictions.

It appears that shear response of the multi-layer interfaces is adequately represented by the RM approach and so modifications for constraining effects of adjacent layers are not required (i.e. adjacent layers do not constrain the deformation of each other for through-thickness shear loading). In the case of Young's modulus, adjacent layers do constrain each other and, whilst significant improvements can be achieved when accounting for Poisson's ratio and layer thickness effects, it appears a more detailed consideration of nearest neighbour interactions

will need to be undertaken before the same level of agreement can be achieved between the FE and RM approaches for E_Z as for G_{XZ}.

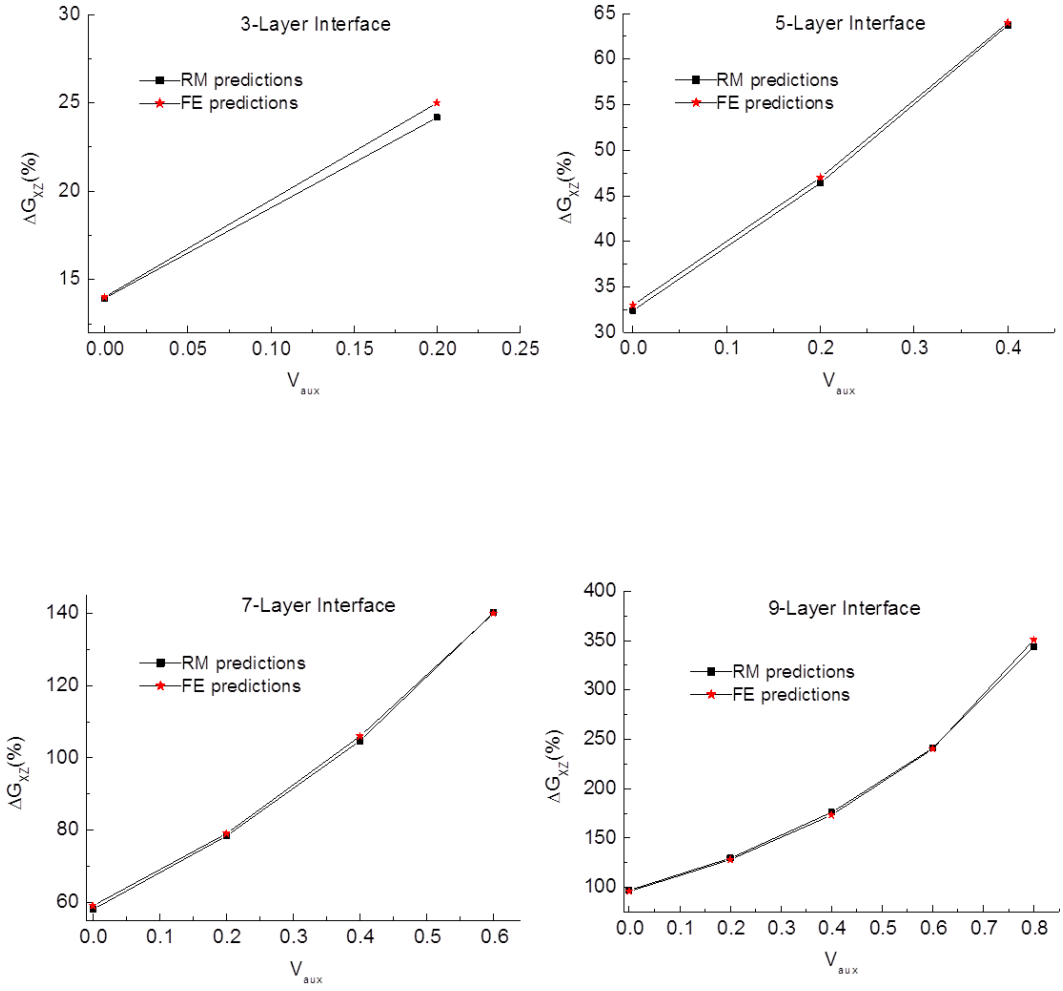

Fig 7.2 Comparison of FEM and 3-phase RM predictions for change in effective through-thickness shear modulus of the 9-layer CIT model as a function of volume fraction of auxetic films (low modulus adhesive system).

7.1.2 Comparison of FE and RM Shear Modulus data for the CCLT Model

The shear modulus values obtained from the FE modelling for interfaces containing auxetic and conventional films incorporated in a low modulus (120 MPa) adhesive are presented in Table 7.2 for the CCLT interface.

Table 7.2 Lay-up sequences, layer thicknesses, volume fractions of adhesive, FE model calculated values of, and percentage changes in, G_{XZ} for the CCLT model incorporating a low Young's modulus (120 MPa) adhesive and film layers of thicknesses 0.2 mm.

Sample	Number of Layers	Adhesive Layer Thickness (mm)	Adhesive Volume Fraction	G_{XZ} (MPa)	ΔG_{XZ} (%)
Adhesive only	1	0.30	1.00	45	-
F—C—L	3	0.05	0.33	76	69
F—A—L	3	0.05	0.33	127	185
Adhesive only	1	0.55	1.00	44	-
F—C—C—L	5	0.05	0.27	79	81
F—C—A—L	5	0.05	0.27	103	136
F—A—A—L	5	0.05	0.27	148	241
Adhesive only	1	0.80	1.00	42	-
F—C—C—C—L	7	0.05	0.25	78	86
F—C—C—A—L	7	0.05	0.25	94	123
F—C—A—C—L	7	0.05	0.25	102	141
F—A—C—A—L	7	0.05	0.25	118	179
F—A—A—C—L	7	0.05	0.25	119	179
F—A—A—A—L	7	0.05	0.25	155	267
Adhesive only	1	1.05	1.00	41	-
F—C—C—C—C—L	9	0.05	0.23	77	89
F—C—C—C—A—L	9	0.05	0.23	89	117
F—C—C—A—C—L	9	0.05	0.23	89	117
F—A—A—C—C—L	9	0.05	0.23	105	155
F—A—C—A—C—L	9	0.05	0.23	104	154
F—A—C—C—A—L	9	0.05	0.23	105	155
F—C—A—A—C—L	9	0.05	0.23	104	154
F—A—A—A—C—L	9	0.05	0.23	125	206
F—A—A—A—A—L	9	0.05	0.23	157	282

Key: — - adhesive layer; **A** - Auxetic film; **C** - Conventional film
F— and —L represent the fixed and loading surfaces, respectively

From Table 7.2, all-auxetic film/adhesive CCLT interfaces gave higher increases in shear modulus when compared to their conventional counterparts, as was observed for the CIT interfaces. The all-conventional film/adhesive CCLT interfaces (—C—, —C—C—, —C—C—C— and —C—C—C—C—) showed significant increases in the shear modulus of 69, 81, 86 and 89%, respectively. The all-auxetic film/adhesive CCLT interfaces (—A—, —A—A—, —A—A—A— and —A—A—A—A—) showed relatively higher increases in G_{XZ} of between 185 and 282%. It is noted, however, that the variations in the predictions for different lay ups at the same auxetic film volume fraction were much smaller for G_{XZ} for both the CIT and CCLT interfaces than reported in Tables 6.1 and 6.2 for E_Z, indicating that layer ordering has much less significance for through-thickness shear modulus than for through-thickness Young's modulus.

The FE predictions are compared to the shear moduli calculated from analytical expressions (RM) for the CCLT all-auxetic and all-conventional interfaces in Fig 7.3.

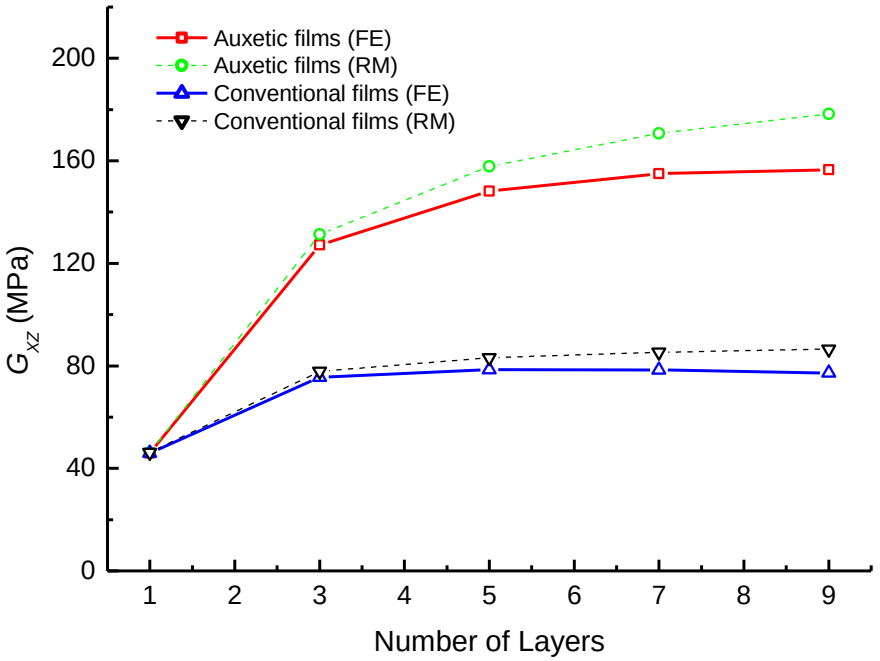

Fig 7.3 FEM and analytical predictions of G_{XZ} as a function of total number of layers of films and low modulus adhesive (120 MPa) for the CCLT model (2-phase interfaces).

Generally, there is good agreement between the FEM and RM values, with the latter slightly higher.

In the case of the more general 3 phase 3 ,5 ,7 and 9-layer CCLT interfaces, the 3 phase RM predictions (using Eq. (4.14c)) and the FEM predictions are in excellent agreement for all volume fractions (see Fig 7.4). Again, this is in contrast with the trends observed for the Young's modulus predictions for the same system, where the FEM, Ramirez and modified RM predictions do not show similar excellent agreement , Fig 6.5.

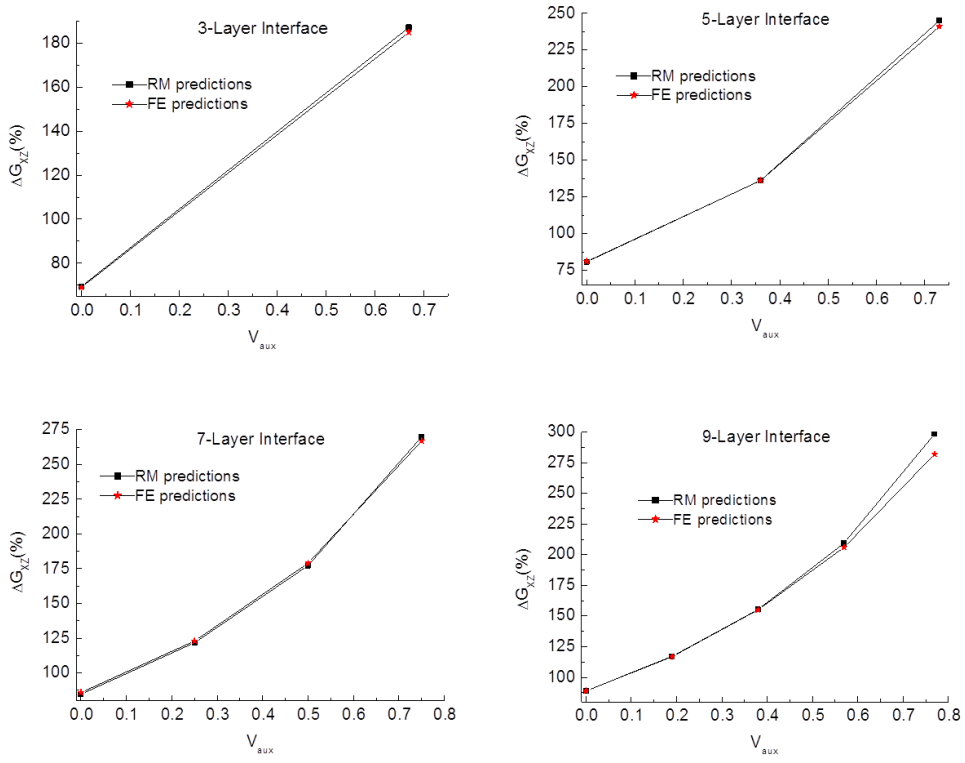

Fig 7.4 Comparison of FEM and 3-phase RM predictions for change in effective through-thickness shear modulus of the 3, 5, 7 and 9-layer CCLT model as a function of volume fraction of auxetic films (low modulus adhesive system).

The normalised values of all-auxetic to all-conventional shear moduli versus adhesive volume fraction for the CIT and CCLT interfaces are presented in Fig 7.5. Shear modulus ratios predicted by the FE and RM analyses lie on the same trendline. The FE trends compare very well to the RM trends for both the CIT and the CCLT models.

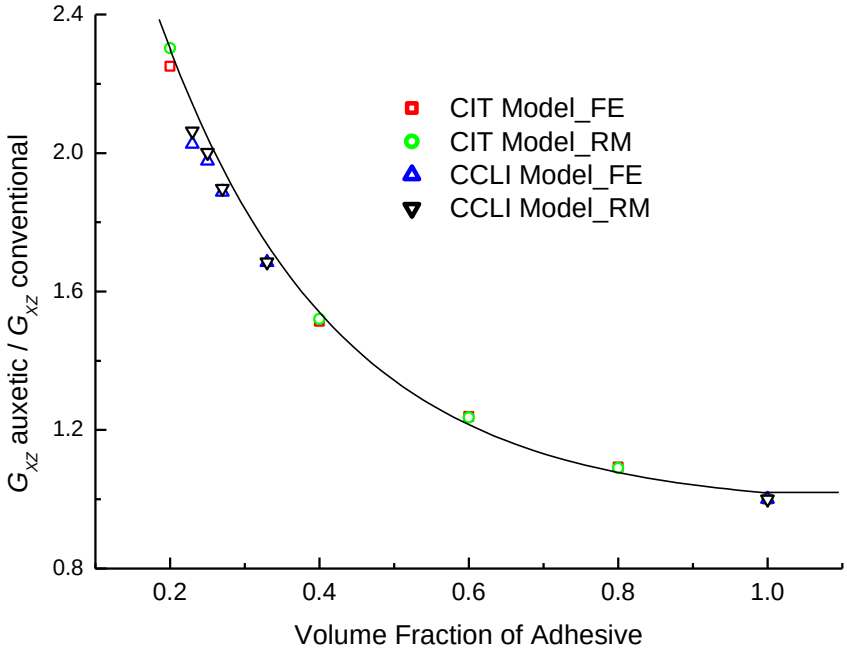

Fig 7.5 Ratio of the shear modulus of the all-auxetic to all-conventional interfaces for the CCLT and the CIT interfaces versus adhesive volume fraction (low modulus adhesive).

As already noted for the CIT interfaces, the increase in shear modulus is dependent on the relative proportions of conventional and auxetic films, but not significantly on the ordering of the films in the CCLT model. For example, in the nine-layer interface, samples with three auxetic and one conventional film ((—A—A—A—C—) and (—A—A—C—A—)) have a greater increase in G_{XZ} than interfaces with two auxetic and two conventional films ((—A—C—A—C—) and (—A—C—C—A—)). However, the shear modulus improvement for (—A—A—A—C—) is the similar to that of (—A—A—C—A—), while that of (—A—C—A—C—) is similar to that of (—A—C—C—A—), see Table 7.2.

7.1.3 Deformation Patterns: Low Modulus Adhesive Models

Shear deformation patterns for conventional and auxetic films contained in a multi-layer interface (—A—C—A—C—) are shown in Fig 7.6.

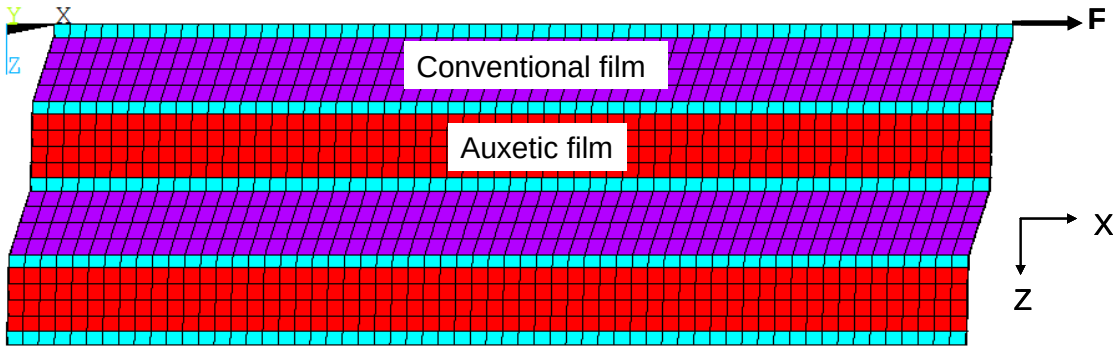

Fig 7.6 Deformation patterns of (—A—C—A—C—) interface subjected to a shear force applied to the top surface in the *X*-direction. Auxetic and conventional layers are represented in red and purple respectively.

Auxetic films represented in red, show a higher resistance to the shear force applied in the *X*-direction as shown by the auxetic layers retaining an almost perfect rectangular cross-section in the *X*-*Z* plane. Conventional films (purple colour) show a reduced resistance to shear force as evidenced by the conventional layers adopting a non rectangular cross-section in the *X*-*Z* plane after application of the shear load. It is clear from Fig 7.6 that the overall shear of the interface is essentially a summation of the shearing of the constituent layers, explaining the close agreement between the FEM and RM predictions of G_{XZ}.

7.2 Through-Thickness Shear Properties: High Modulus Adhesive

Analytical and numerical calculations of shear modulus were undertaken for both CIT and CCLT models in which a high Young's modulus (1700 MPa) adhesive, relative to the film Young's modulus, was used.

7.2.1 Comparison of FE and RM Shear Modulus data for the CIT Model

The layer arrangements and shear modulus predictions from the FE analysis for the CIT model interfaces are shown in Table 7.3.

Using Eq. 2.1 the shear moduli of the high modulus adhesive, and conventional and auxetic films were calculated to be 654, 119 and 1700 MPa, respectively. Hence, addition of auxetic films to the high modulus adhesive tends to increase the overall shear modulus of the interface; whilst addition of conventional films of the same Young's modulus as the auxetic films tends to reduce the overall shear modulus of the interface. An all-auxetic 9-layer film interface (**—**A**—**A**—**A**—**A**—**) produced the highest increase (85%) while the all-conventional 9-layer film interface (**—**C**—**C**—**C**—**C**—**) showed the highest reduction in G_{XZ} (-78%), Table 7.3.

Table 7.3 Lay-up sequences, layer thicknesses, volume fractions of adhesive, FE model calculated values of, and percentage changes in, G_{XZ} for the CIT model incorporating a high Young's modulus (1700 MPa) adhesive, film layers of thicknesses 0.2 mm and a total interface thickness of 1 mm.

Sample	Number of layers	Adhesive layer thickness (mm)	Adhesive volume fraction	G_{XZ} (MPa)	G_{XZ} (%)
Adhesive only	1	1.00	1	584	
F—C—L	3	0.4	0.8	314	-46
F—A—L	3	0.4	0.8	612	13
F—C—C—L	5	0.2	0.6	214	-63
F—C—A—L	5	0.2	0.6	337	-42
F—A—A—L	5	0.2	0.6	762	31
F—C—C—C—L	7	0.1	0.4	162	-72
F—C—C—A—L	7	0.1	0.4	223	-62
F—C—A—C—L	7	0.1	0.4	224	-62
F—A—C—A—L	7	0.1	0.4	360	-38
F—A—A—C—L	7	0.1	0.4	361	-38
F—A—A—A—L	7	0.1	0.4	895	53
F—C—C—C—C—L	9	0.04	0.2	130	-78
F—C—C—C—A—L	9	0.04	0.2	167	-71
F—C—C—A—C—L	9	0.04	0.2	167	-71
F—A—A—C—C—L	9	0.04	0.2	236	-60
F—A—C—A—C—L	9	0.04	0.2	235	-60
F—A—C—C—A—L	9	0.04	0.2	235	-60
F—C—A—A—C—L	9	0.04	0.2	234	-60
F—A—A—A—C—L	9	0.04	0.2	389	-33
F—A—A—A—A—L	9	0.04	0.2	1079	85

Key: — - adhesive layer; **A** - Auxetic film; **C** - Conventional film
F— and —L represent the fixed and loading surfaces, respectively

The FE predictions are compared to the shear moduli calculated from the analytical expressions (RM) for the 2-phase CIT model in Fig 7.7. Generally, there is good agreement between the FE and RM values, with the latter giving slightly higher predictions.

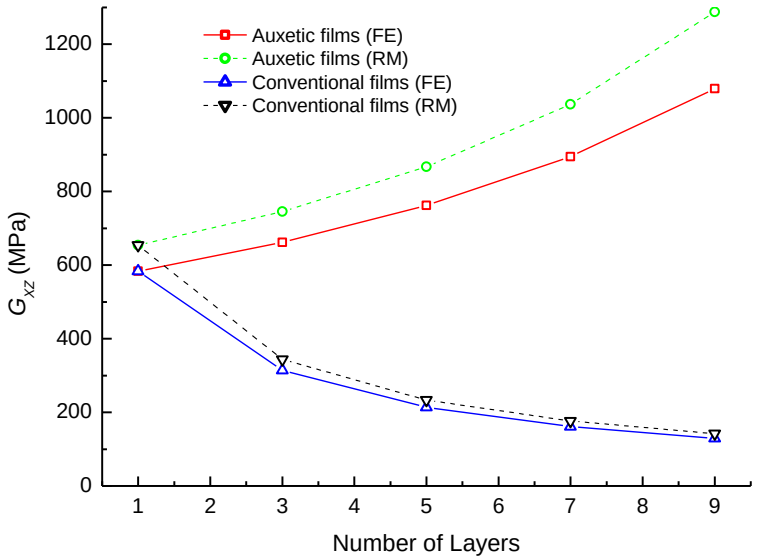

Fig 7.7 FEM and RM values of G_{XZ} versus number of layers of films and high modulus adhesive (1700 MPa) for the CIT (all-auxetic and all-conventional) interfaces.

For the high modulus adhesive system, an increase in G_{XZ} is only predicted for the all-auxetic film case. For the all-conventional and mixed conventional/auxetic film interfaces, a decrease in G_{XZ} is predicted. This is in contrast to the low modulus adhesive system where an increase in G_{XZ} was predicted in all interfaces. The contrast between the low and high modulus adhesive cases can be understood by examining Eq. (4.18c).

The denominator of the first term of the right hand side of Eq. (4.18c) contains two terms which depend on the shear modulus of the adhesive with respect to each of the film phases; $V_{conv}\frac{G_{adh}}{G_{conv}}$ and $V_{aux}\frac{G_{adh}}{G_{aux}}$. For the low modulus adhesive system, $\frac{G_{adh}}{G_{conv}} = 0.388$ and $\frac{G_{adh}}{G_{aux}} = 0.027$. Hence, since V_{conv} and V_{aux} are both less than unity, Eq. (4.18c) always leads to an increase in G_{XZ} for the values of $\frac{G_{adh}}{G_{conv}}$ and $\frac{G_{adh}}{G_{aux}}$ that exist in the low modulus adhesive

case. On the other hand, when a high modulus adhesive is used, $\frac{G_{adh}}{G_{conv}} = 5.5$ and $\frac{G_{adh}}{G_{aux}} = 0.385$.

The high value of $\frac{G_{adh}}{G_{conv}}$ (>>1) now leads to the denominator in the first term of the right hand side of Eq. (4.18c) being greater than unity except when V_{conv} = 0 (i.e. V_{aux} = 0.8 for the 9-layer system), and so a decrease in G_{XZ} is observed for interfaces containing at least one conventional film.

Figure 7.8 shows the comparison between FE and RM ΔG_{XZ} (%) values for the high modulus 3, 5, 7 and 9-layer CIT model.

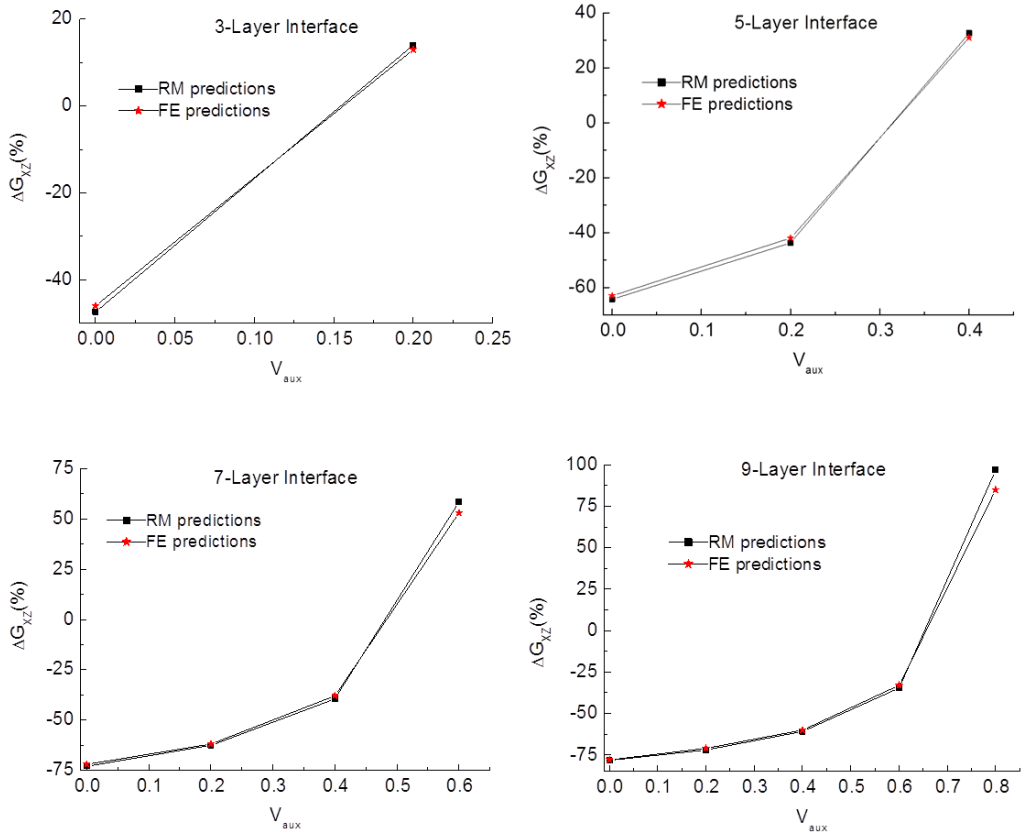

Fig 7.8 Comparison of FEM and 3-phase RM predictions for the change in effective through-thickness shear modulus of the 3, 5, 7 and 9-layer CIT model as a function of volume fraction of auxetic films (high modulus adhesive system).

Excellent agreement between the FE and RM predictions is achieved in the high modulus adhesive systems.

7.2.2 Comparison of FE and RM Shear Modulus data for the CCLI Model

The changes in the shear modulus of the CCLT model interfaces predicted from the FE analysis when a high modulus adhesive is used are given in Table 7.4.

Adhesive-only single layer interfaces of varying thicknesses equivalent to the 3, 5, 7 and 9-layer adhesive-film interfaces were modelled to provide base values to which calculated shear modulus values obtained for multi-layer interfaces containing films were compared. A reduction in shear modulus is observed for all-conventional film/adhesive CCLT interfaces ((—C—) (-75%); (—C—C—) (-76%); (—C—C—C—) (-77%); (—C—C—C—C—) (-77%)), whereas an increase in the overall shear modulus is observed for all-auxetic film/adhesive interfaces ((—A—) (67%); (—A—A—) (76%); (—A—A—A—) (77%); (—A—A—A—A—) (78%)).

Table 7.4 Lay-up sequences, layer thicknesses, volume fractions of adhesive, FE model calculated values of, and percent changes in, G_{XZ} for the CCLT model incorporating a high modulus (1700 MPa) adhesive and film layers of thickness 0.2 mm.

Sample	Number of Layers	Adhesive Layer Thickness (mm)	Adhesive Volume Fraction	G_{XZ} (MPa)	ΔG_{XZ} (%)
Adhesive only	1	0.30	1.00	633	-
F—C—L	3	0.05	0.33	159	-75
F—A—L	3	0.05	0.33	1061	67
Adhesive only	1	0.55	1.00	616	-
F—C—C—L	5	0.05	0.27	146	-76
F—C—A—L	5	0.05	0.27	258	-58
F—A—A—L	5	0.05	0.27	1085	76
Adhesive only	1	0.80	1.00	598	-
F—C—C—C—L	7	0.05	0.25	139	-77
F—C—C—A—L	7	0.05	0.25	197	-67
F—C—A—C—L	7	0.05	0.25	197	-67
F—A—C—A—L	7	0.05	0.25	334	-44
F—A—A—C—L	7	0.05	0.25	336	-44
F—A—A—A—L	7	0.05	0.25	1064	77
Adhesive only	1	1.05	1.00	580	-
F—C—C—C—C—L	9	0.05	0.23	134	-77
F—C—C—C—A—L	9	0.05	0.23	172	-70
F—C—C—A—C—L	9	0.05	0.23	172	-70
F—A—A—C—C—L	9	0.05	0.23	241	-58
F—A—C—A—C—L	9	0.05	0.23	240	-59
F—A—C—C—A—L	9	0.05	0.23	242	-58
F—C—A—A—C—L	9	0.05	0.23	240	-59
F—A—A—A—C—L	9	0.05	0.23	393	-32
F—A—A—A—A—L	9	0.05	0.23	1029	78

Key: — - adhesive layer; **A** - Auxetic film; **C** - Conventional film
F— and —L represent the fixed and loading surfaces, respectively

The changes in G_{XZ} for interfaces when a high modulus adhesive is used are consistently lower than those observed when a low modulus adhesive is used. This is a consequence of the film Young's modulus leading to an increase in the shear modulus for the low modulus adhesive systems. The percent increase in shear modulus for the 3, 5 and 7-layer all-auxetic film

interfaces were higher for the CCLT model interfaces than for the CIT model interfaces when a high modulus adhesive was used. This can be explained by the higher volume fraction of the high shear modulus material (auxetic films) present within the CCLT interfaces compared to the CIT interfaces for the 3, 5 and 7-layer interfaces, Table 7.4. Similarly, the higher volume fraction of conventional films (low shear modulus constituent) in the 3, 5 and 7-layer systems showed larger decreases in the CCLT interfaces than the CIT model interfaces for the high modulus adhesive systems.

FEM and Rule of Mixtures predictions for the 2-phase interface shear modulus values are compared in Fig 7.9 for CCLT model interfaces. Significant decreases and increases in shear modulus are predicted for all-conventional and all-auxetic film/high modulus adhesive systems, respectively.

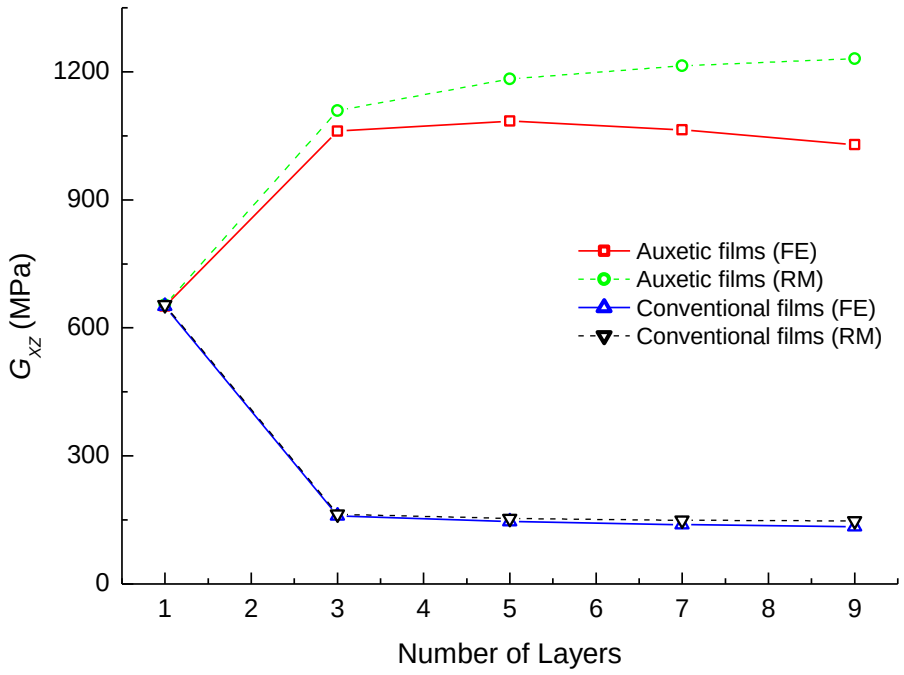

Fig 7.9 FEM and analytical predictions of G_{XZ} as a function of total number of layers of films and high modulus adhesive (1700 MPa) for the CCLT model.

The FEM predictions for auxetic films are slightly different from those calculated using the RM at low volume fractions of the adhesive (corresponding to higher number of layers). For all-conventional interfaces, there is negligible difference in the values calculated using FE and RM methods.

The changes in the shear modulus for the 3-phase, 3, 5, 7 and 9-layer interface systems predicted using the RM (Eq. 4.18c) are compared with the FEM predictions in Fig.7.10. Similar to the CIT model discussed earlier, the shear response of the CCLT model is adequately represented by the RM.

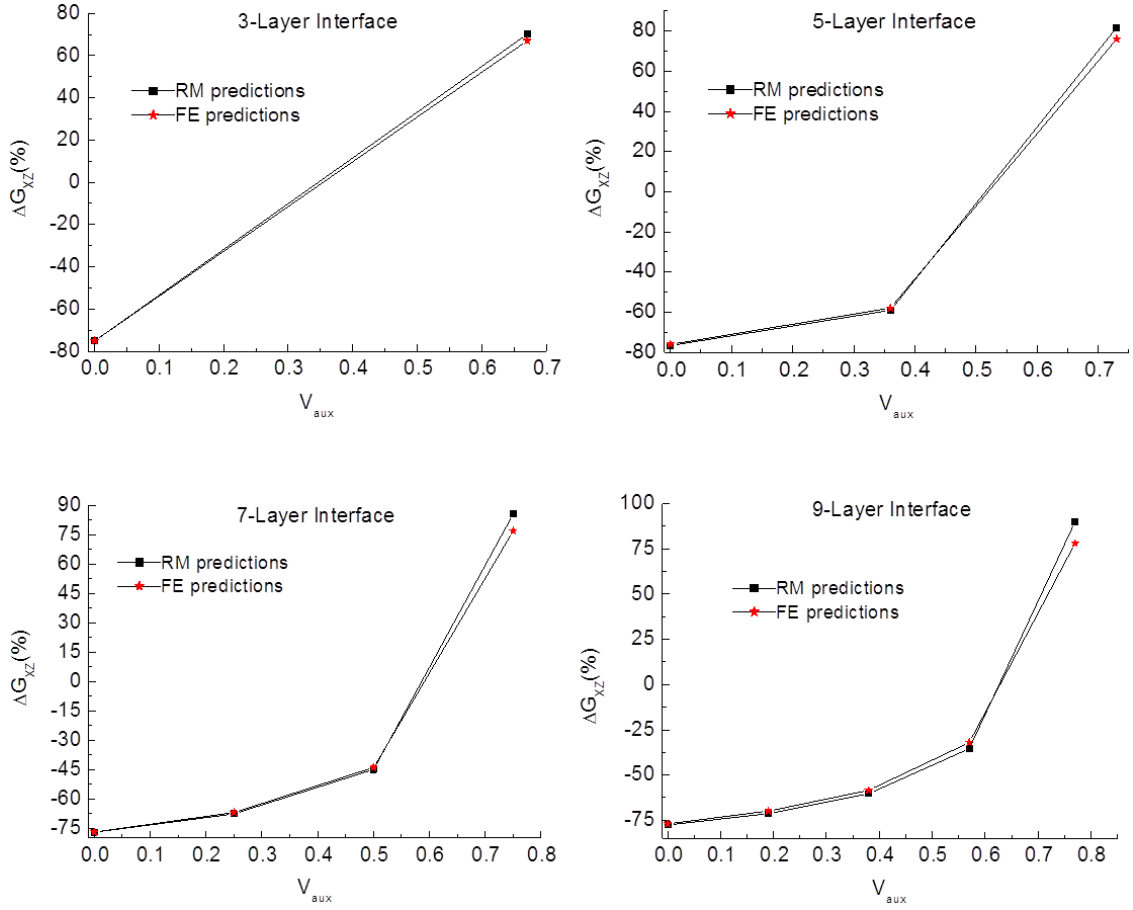

Fig 7.10 Comparison of FEM and 3-phase RM predictions for the change in effective through-thickness shear modulus of the 3, 5, 7 and 9-layer CCLT model as a function of volume fraction of auxetic films (high modulus adhesive system).

The normalised values of all-auxetic to all-conventional shear moduli versus adhesive volume fraction for the CIT and CCLT model interfaces are presented in Fig 7.11. There is good agreement between the shear modulus predicted by the FEM and RM.

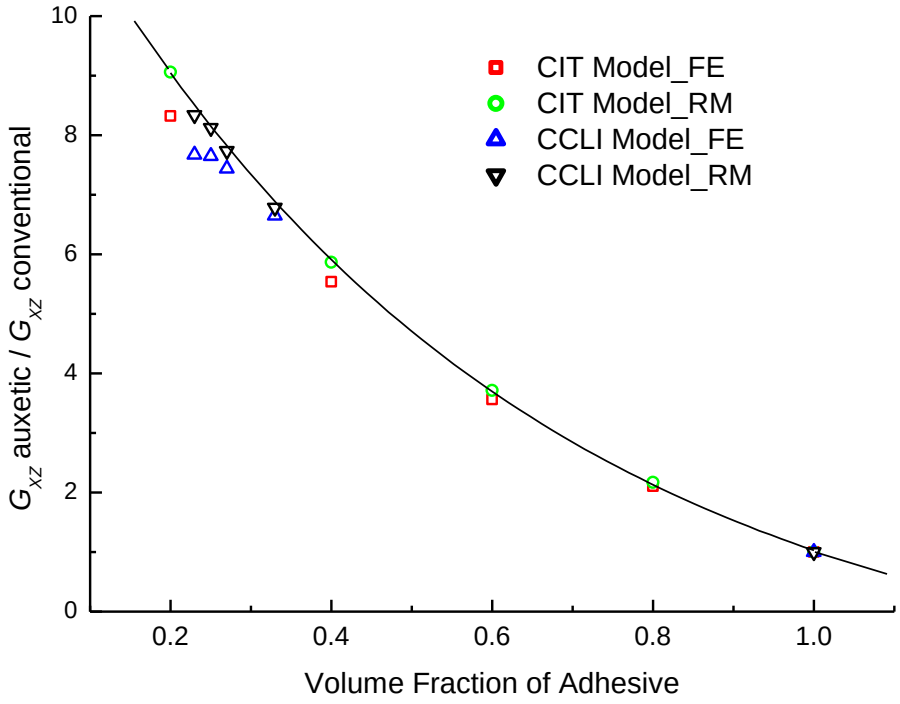

Fig 7.11 Ratio of the shear modulus of the all-auxetic to the all-conventional interfaces for the CCLT and the CIT model interfaces versus adhesive volume fraction (high modulus adhesive).

7.3 Summary (Shear Modulus Prediction)

Film/adhesive interfaces have been modelled to investigate the effect of the Young's moduli and Poisson's ratios of the constituent materials on the interface effective through-thickness shear modulus. It has been shown that the addition of auxetic and/or conventional films to the low and high modulus adhesives may either reduce or increase the overall shear modulus. In all models each adhesive and film layer has been assumed to comprise of isotropic material. In

such cases films having Young's modulus higher than the adhesive will tend to increase the shear modulus due to the relationship between Poisson's ratio, shear modulus and Young's modulus for isotropic materials (Eq. 2.1) The increase will be enhanced for negative Poisson's ratio films combined with a positive Poisson's ratio adhesive. Additionally, the use of adhesives with different Young's moduli also affects the overall interface shear modulus. Combining high modulus films with low modulus adhesive tends to increase the interface shear modulus with respect to adhesive shear modulus and vice versa. The extent of shear modulus variation is dependent on the volume fractions of the adhesive and film layers within the interface. Based on this work the following conclusions can be drawn;

(i) Combining stiffer material (film) with a low modulus adhesive increases the overall shear modulus of the interface, with auxetic films showing very significant increases,

(ii) All-auxetic film/high modulus adhesive interfaces showed increased shear modulus of the interfaces relative to the adhesive even though the auxetic films have a lower Young's modulus compared to the high modulus adhesive (340 versus 1700 MPa). Incorporating conventional films with the same Young's modulus as that of the auxetic films within the high modulus adhesive system led to the reduction in the overall shear modulus of the interface. The negative Poisson's ratio exhibited by auxetic films has been identified as responsible for the increase in the shear modulus of the all-auxetic high modulus adhesive interface systems,

(iii) The overall shear modulus values predicted using FE analysis have been shown to be in good agreement with those obtained from the Rule of Mixtures formulation,

(iv) The superior shear modulus characteristics of negative Poisson's ratio materials can be utilised in joints in order to improve the load bearing capacity.

7.4 Comparison of FE and RM Predictions of Through-Thickness Shear and Young's Moduli of Multi-Layered Interfaces.

The modelling results presented in the thesis show excellent agreement between FEM and RM for the through-thickness shear response of the multi-layer system. This agreement is achieved for a RM approach without any modification to the established RM in the literature, with the exception of the extension to a 3-phase system presented in the thesis. Essentially, the shear response of the multi-layer system is a summation of the shear response of each layer, and there appear to be no significant constraining effects between adjacent layers for shear loading considered in this study. In terms of ease of calculation, the RM provides a quick prediction of the shear modulus of the layered system with the same accuracy as the more time-consuming FE approach.

In the case of through-thickness Young's modulus, adjacent layers do appear to constrain each other and, whilst significant improvements in agreement between the RM and FE approaches can be achieved when accounting for Poisson's ratio effects in each layer in the RM expressions, it appears further modifications are required before the same level of agreement between the FEM and RM approaches can be achieved for Young's modulus as for shear modulus.

The modified RM was developed in recognition that the multi-layer systems considered in this work have phases in which the Young's moduli are much closer to each other than in the fibre-reinforced composite systems. Hence, the modified RM expressions developed in this work assumed each layer (film and adhesive) is constrained by adjacent layers and so Poisson's correction was applied to both film and adhesive layers. This provided good

agreement between the FE and RM approaches, but not to the same level as for the shear modulus predictions. The analytical methods developed by Ramirez and the author take into account the transverse deformations and constraints that each layer undergoes. However, even when these factors have been incorporated into the equations, the analytical predictions for Young's modulus are not as close to the FE data as the shear modulus predictions. The larger differences between FE and analytical data observed in the Young's modulus predictions may be as a result of next-nearest neighbour constraint effects (which have not been considered by the analytical methods presented in the thesis). The FE approach captures edge effects and layer thicknesses as well as any next-nearest neighbour effects that may be present. The FE approach is, therefore, considered likely to give the best predictions of the through- thickness Young's modulus since it inherently accounts for edge effects, adjacent layer constraining effects and Poisson's ratio contractions in a more sophisticated manner than currently considered in the modified RM and Ramirez approaches.

CHAPTER 8: MODELLING RESULTS OF PARTICLE FILLED MODELS (PARAMETRIC STUDY)

8.0 Introduction

In this chapter the modelling results of particulate-filled epoxy composites (both auxetic and conventional filled particulate composites) are presented. The FE models are compared to existing analytical models including Self Consistent Field (SCF) model and the Hashin Shtrikman (H-S) theories, Chapter 5. In addition, parametric studies to investigate the effect of conventional and auxetic fillers on the effective Young's modulus and Poisson's ratio of the filled composite were performed using the SCF theory. Limitations of the theoretical methods are considered.

8.1 FE and Analytical Results and Discussion

8.1.1 Young's Modulus Plots: Auxetic Inclusions

The Young's modulus plots as a function of filler volume fraction are shown in Fig 8.1. The FE analysis predicts an increase in modulus of the filled adhesive up to a peak at approximately 40% volume fraction of the filler, above which it starts to fall. The filler has a negative Poisson's ratio which, by analogy with the findings from the multi-layer film/adhesive interface, will influence the effective Young's modulus of the filled composite. When a tensile strain is applied to the composite, the positive Poisson's ratio matrix contracts laterally whilst the auxetic filler expands, thus providing a restraining effect on the matrix lateral contraction and vice versa. The reduction in lateral displacement of the matrix is resisted by the auxetic inclusions, resulting in a reduction of the overall axial strain on the composite and, therefore, an increase in the effective Young's modulus.

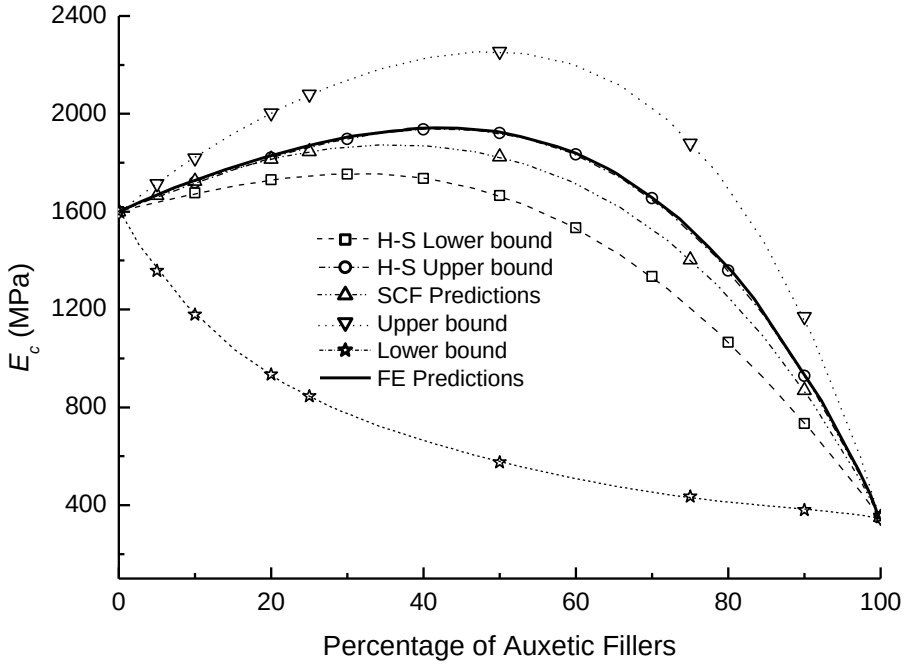

Fig 8.1 Comparison of FE results, H-S upper and lower bounds, Upper and Lower bounds and SCF model for auxetic fillers within a conventional matrix.

The restraining effects between auxetic and conventional particles are maximised at 50% filler content when the ratio of auxetic material to conventional material is 1:1. However, the auxetic filler in these models has a lower modulus than the matrix and so the actual peak effective Young's modulus of the composite is a trade off between maximal filler-particle restraint (50% filler content) and higher content of high modulus matrix material (filler content <50%). Hence the maximum effective Young's modulus occurs at lower filler content (i.e in this case ~40% filler content) than the 50% filler content that would otherwise be expected from consideration of maximal filler-matrix restraint effects alone.

With the exception of the lower bound, the FE trend is consistent with the trends predicted by the analytical models, see Fig 8.1. The FE analysis results coincide with the H-S upper bound prediction. The SCF lies in-between the H-S lower and upper bounds. The upper and lower bounds are more widely separated than the H-S bounds. Note that the lower bound expression (Equation 5.16) does not include the Poisson's ratios of the constituent

materials and so filler-matrix restraint due to constituent Poisson's ratio effects is not accounted for in the lower bound model.

8.1.2 Young's Modulus Plots: Conventional Inclusions

The inclusion of a low modulus positive Poisson's ratio filler resulted in a reduction of the overall Young's modulus of the composite predicted by all analytical and FE models, see Fig 8.2. Whilst there is some slight filler-matrix particle restraint due to the different values of constituent positive Poisson's ratios, the effects are much smaller than the auxetic filler-conventional matrix case due to the much closer values of the two positive Poisson's ratios in the conventional filler-conventional matrix system. Hence the effective Young's modulus response with filler content is dominated by the Young's modulus of the constituents in the conventional-conventional system modelled here, i.e. the effective Young's modulus decreases as the volume fraction of the lower Young's modulus filler constituent increases. The auxetic filler curve (FE analysis) is also included in Fig. 8.2 for comparison and can be clearly distinguished from those for conventional fillers.

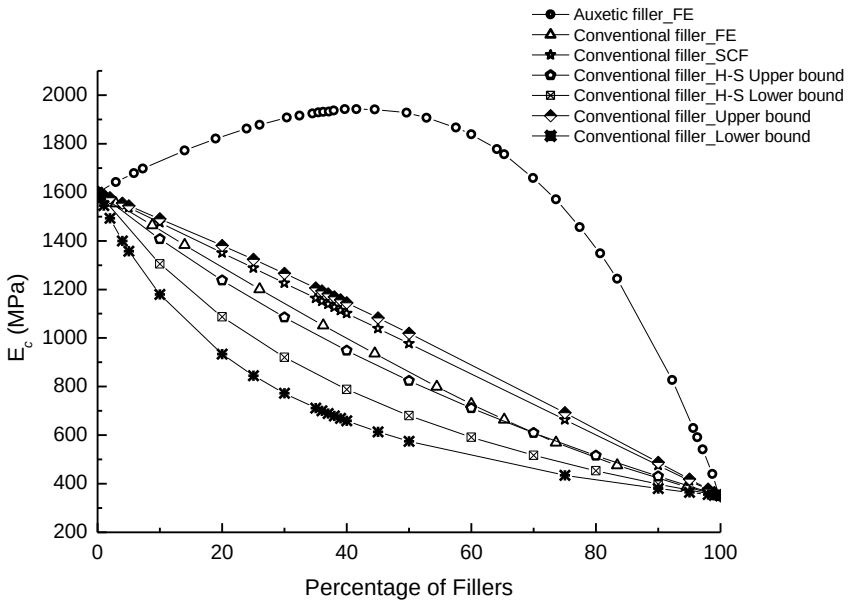

Fig 8.2 Young's modulus versus percentage of conventional filler-comparison of FE and analytical results. FEM data for the auxetic filler system are also included for comparison.

The FEM results for the conventional filler are within the Upper and Lower bounds but are slightly higher than the H-S upper bound for low and intermediate filler content. The H-S upper bound, nevertheless, gives the closest agreement with the FEM data. The analytical theories, however, give reasonable to good agreement with the FE predictions of the Young's modulus for conventional fillers in a conventional matrix.

8.2 SCF Young's Modulus Predictions: Parametric Studies

The SCF theory was used to predict mechanical properties in composites where the matrix and filler properties were varied, i.e. the ratio of filler to matrix Young's modulus ratios(E_f/E_m) ranging from 0.1 to 20 and the Poisson's ratio of the filler and matrix components ranging from υ = +0.45 to -0.9. Fig 8.3 is a plot of the Young's modulus as a function of the volume fraction of conventional fillers (large positive Poisson's ratio, υ_f = +0.45) in a conventional matrix (υ_m = +0.225) as E_f/E_m is varied. By contrast, Fig 8.4 shows the predicted Young's moduli when auxetic fillers (large negative Poisson's ratio, υ_f = -0.9) are added to the same conventional matrix.

Fig 8.3 shows that increases in Young's moduli are only observed for E_f/E_m ratios greater than 1 i.e. adding stiffer fillers into a lower Young's modulus matrix. For E_f/E_m less than 1, there is a reduction in Young's modulus of the composite as the fraction of conventional fillers increases. The stiffening effect due to filler-matrix Poisson's restraint is negligible for two systems having positive (albeit different) Poisson's ratios.

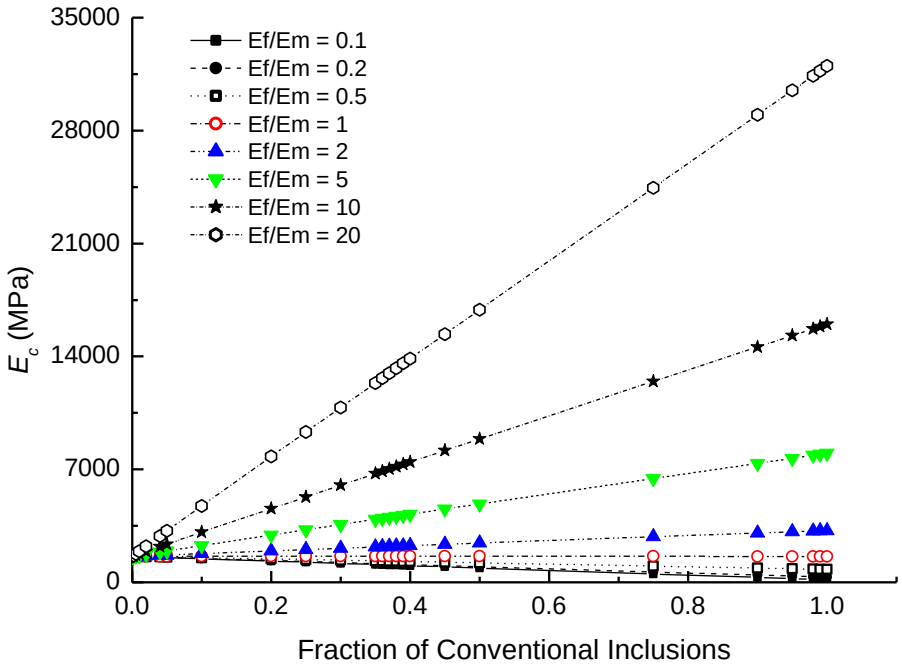

Fig 8.3 Young's modulus versus fraction of conventional inclusions for E_f/E_m = 0.1 − 20 in a conventional matrix; [υ_m= +0.225 and υ_f = +0.45].

Fig 8.4 shows that further increases in Young's modulus are achieved when auxetic fillers are added to the conventional matrix.

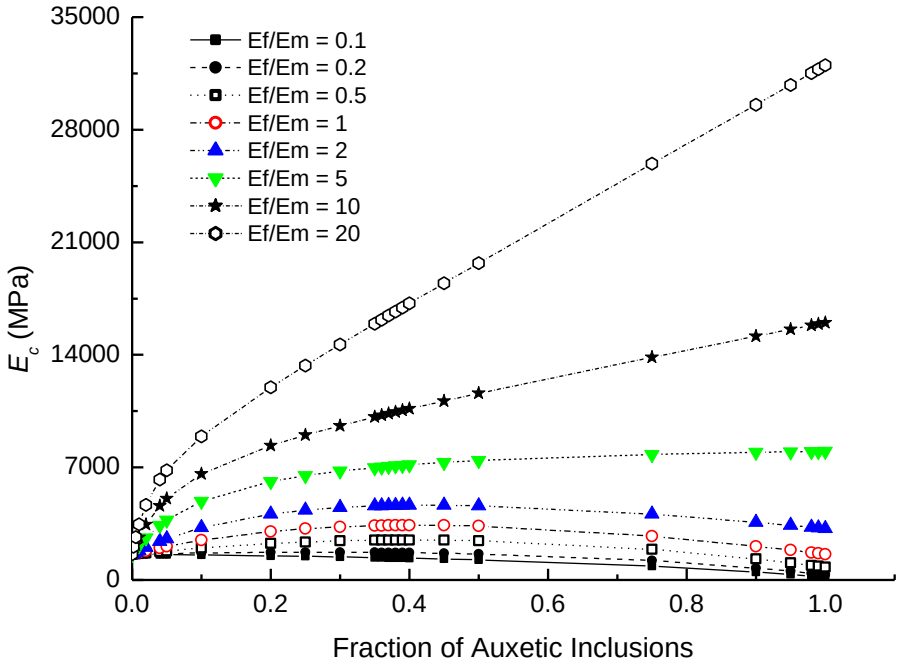

Fig 8.4 Young's modulus versus fraction of auxetic inclusions for E_f/E_m = 0.1−20 in a conventional matrix; [υ_m= +0.225 and υ_f = −0.9].

Increases in the composite Young's modulus due to auxetic fillers (relative to those due to conventional fillers) are especially evident for filler fractions less than 50% (compare Figs. 8.3 and 8.4). When auxetic materials are used as fillers, the Young's modulus of the composite can be increased even though auxetic fillers have a Young's modulus lower than that of the matrix i.e. $E_f/E_m < 1$.

The advantage of using auxetic fillers instead of conventional fillers is shown in Fig 8.5. The plot was obtained by dividing the data in Fig 8.4 by the data in Fig 8.3 ($E_{(auxetic\ inclusions)}/E_{(conventional\ inclusions)}$ vs. filler volume fraction), hence obtaining an enhancement factor of the auxetic fillers.

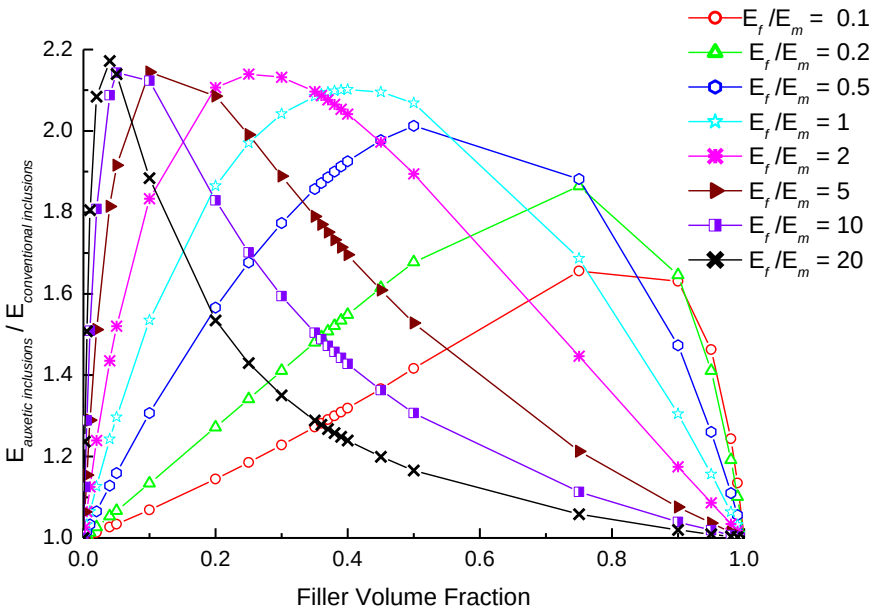

Fig 8.5 Enhancement factor of auxetic fillers for E_f/E_m = 0.1−20; [υ_m= +0.225, and υ_f = −0.9 and +0.45].

The graph shows that there is an advantage in using auxetic fillers compared to conventional ones when seeking to increase the effective modulus of the filled system. This is especially significant for high E_f/E_m ratios (E_f/E_m ratios greater than 1) since the maximum enhancement can be achieved at low filler volume fractions (less than approx

20%). The curves shift to the right with a decrease in the E_f/E_m ratios, which means that the maximum advantage of using auxetic fillers is not only lower than at high E_f/E_m ratios, but is observed at high filler volume fractions (which may be difficult to achieve in practice) for low modulus fillers.

Fig 8.6 shows the Young's modulus predictions when auxetic inclusions are added to an auxetic matrix (large negative Poisson's ratio filler, υ_f = -0.90) in a lower negative Poisson's ratio matrix (υ_m = -0.45).

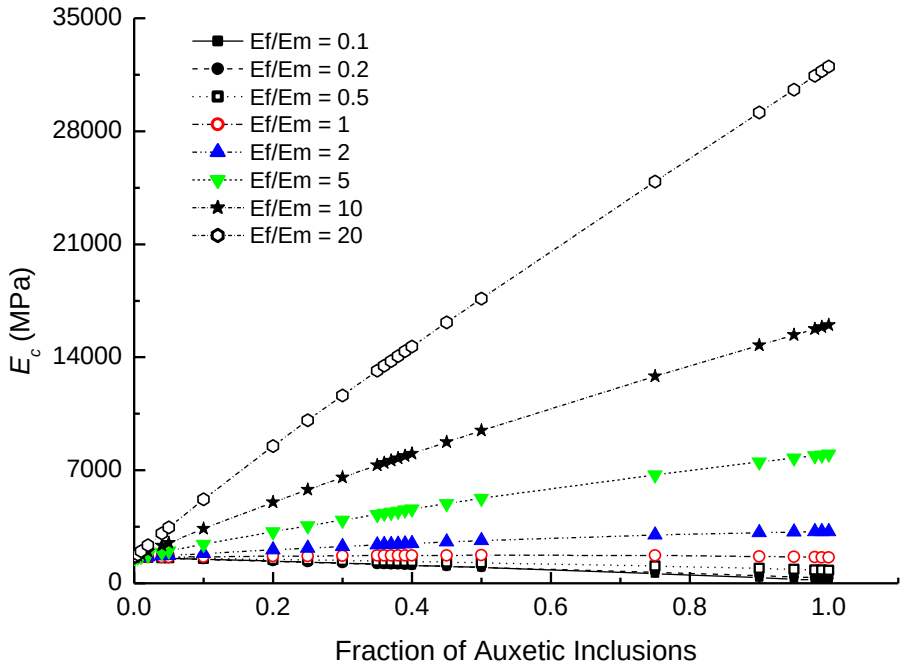

Fig 8.6 Young's modulus versus fraction of auxetic inclusions for E_f/E_m = 0.1−20 in an auxetic matrix; [υ_m= −0.45 and υ_f = −0.9].

Interestingly, Fig 8.6 is very similar to Fig 8.3 even though auxetic fillers were used. The auxetic filler/auxetic matrix combination results in similar increases in Young's modulus predictions as the conventional filler/conventional matrix combination for all E_f/E_m ratios. This confirms that in order to achieve larger increases in Young's modulus, the Poisson's ratios of the two materials should preferably have different signs.

For completeness, an auxetic matrix in which conventional inclusions are added was considered. The filler and matrix were assigned Poisson's ratio values of +0.45 and -0.45, respectively. The predicted increases in the Young's modulus for conventional fillers in an auxetic matrix are shown in Fig 8.7 and the trends are similar to those for auxetic fillers in a conventional matrix, see Fig 8.4.

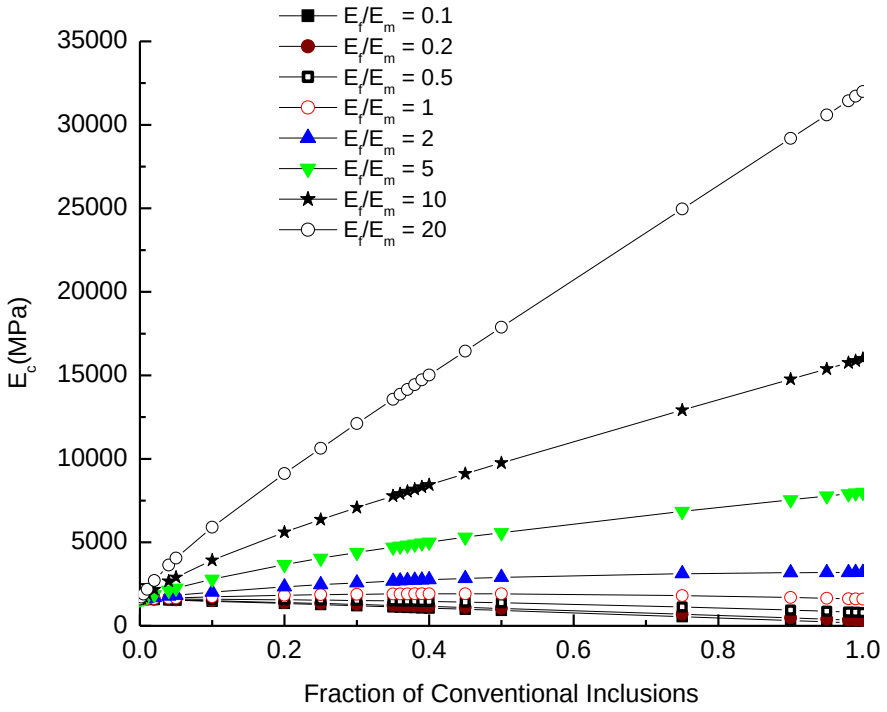

Fig 8.7 Young's modulus versus fraction of conventional inclusions for E_f/E_m = 0.1−20 in an auxetic matrix; [υ_m= −0.45 and υ_f = +0.45].

In all cases the E_f/E_m ratio of 20 gives the highest improvement in the Young's modulus of the composite. The effect of varying the Poisson's ratio of the filler material on the resultant composite Young's modulus was calculated for E_f/E_m = 20, υ_m= +0.225 and υ_f = −0.9 to +0.45. The results are shown in Fig 8.8. The data for $\upsilon_f \geq -0.25$ closely overlap, showing little effect due to changing Poisson's ratio of the filler in this case. When $\upsilon_f \leq -0.5$ a discernible increase in effective Young's modulus is predicted, with the largest increase in modulus shown for the highest negative Poisson's ratio filler; in this case −0.9.

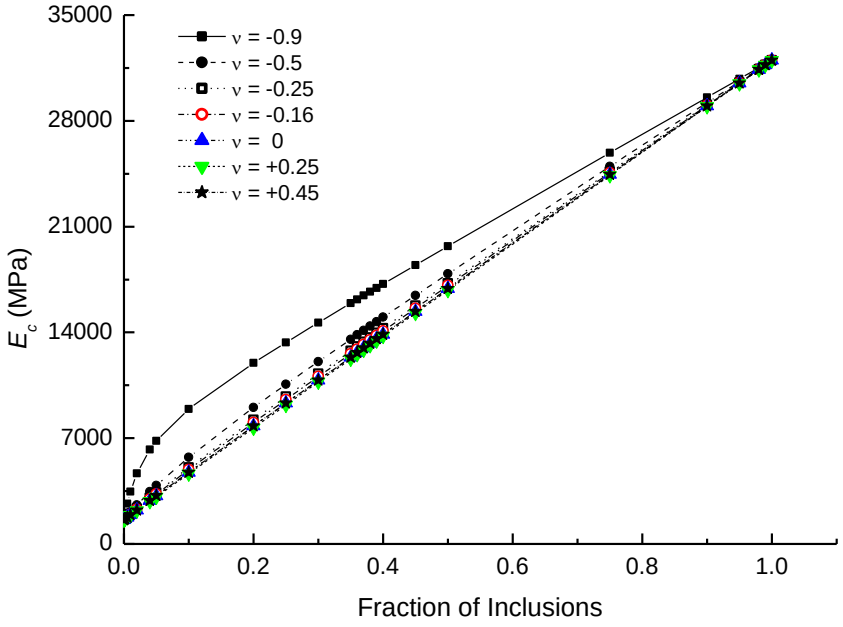

Fig 8.8 Young's modulus versus fraction of inclusions with υ_f = −0.9 to +0.45 in a conventional matrix; [E_f/E_m = 20, υ_m= +0.225].

Fig 8.9 represents the inclusion of low modulus fillers (E_f/E_m = 0.2) of varying Poisson's ratios, υ_f = −0.9 to +0.45 in a matrix having υ_m= +0.225.

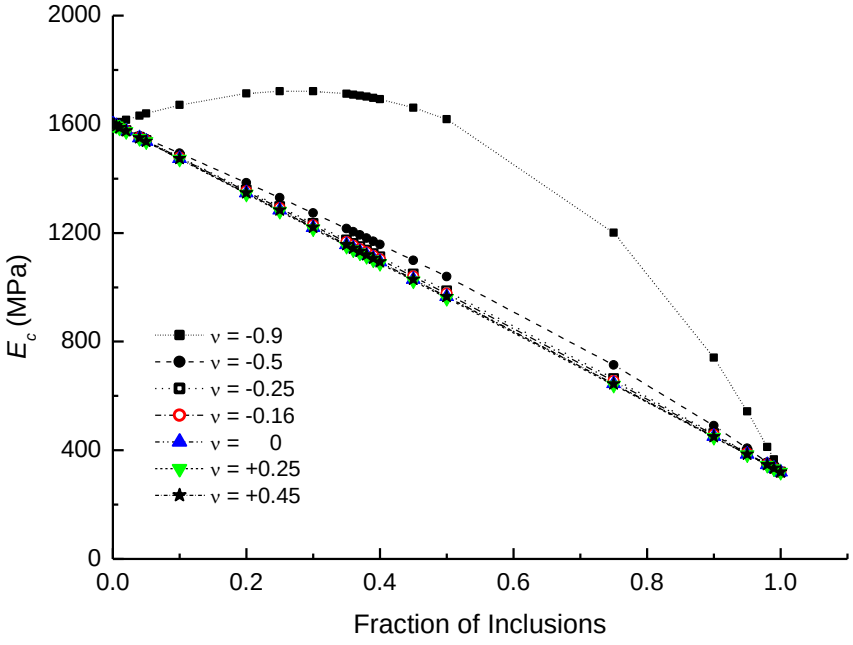

Fig 8.9 Young's modulus versus fraction of inclusions with υ_f = −0.9 to +0.45 in a conventional matrix; [E_f/E_m = 0.2, υ_m= +0.225].

For the filler having highest magnitude of negative Poisson's ratio (υ_f = −0.9) an increase in modulus is observed for volume fractions up to approximately 50% filler content. For all other fillers ($\upsilon_f \geq$ -0.5) the composite Young's modulus decreases with filler volume fraction.

8.3 SCF Predictions for Shear Modulus of the Composite

Auxetic materials can be used in structural applications where high shear resistant materials are required. Fig 8.10 shows a plot of predicted shear modulus versus volume fraction of conventional fillers for a range of filler to matrix Young's modulus ratios. Poisson's ratios of +0.225 and +0.45 were used for the matrix and filler, respectively.

The inserted plot in Fig 8.10 shows the shear modulus trends at lower filler content (0 % - 20 %) more clearly. Improvements in shear modulus are predicted for E_f/E_m ratios of 2 or higher. Hence the fillers with a higher Young's modulus compared to the matrix result in an improvement in the overall shear modulus of the composite system.

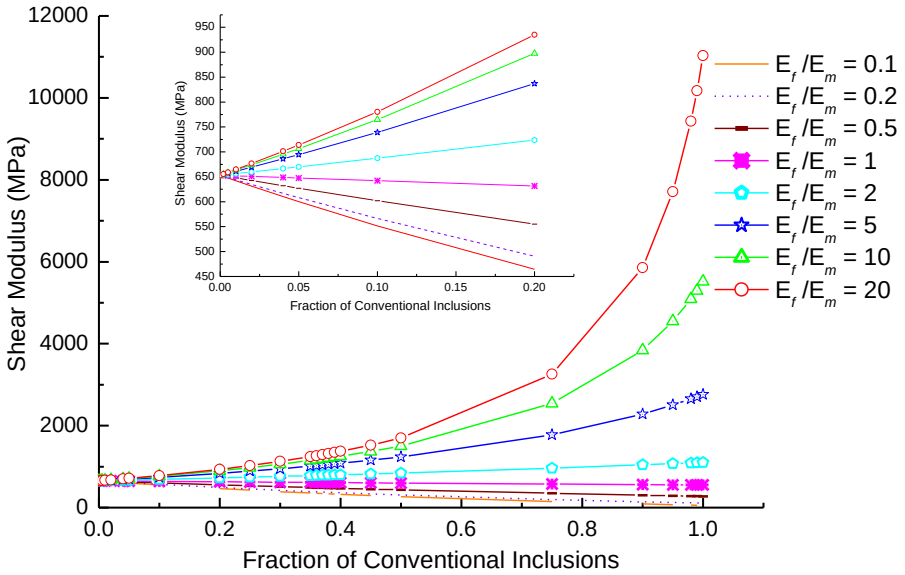

Fig 8.10 Predicted shear modulus vs. volume fraction of conventional inclusions for E_f/E_m = 0.1 to 20 within a conventional matrix. (Poisson's ratio of matrix is +0.225 and filler is +0.45).

A plot of the shear modulus prediction when auxetic fillers are added is shown in Fig 8.11 for Poisson's ratios of +0.225 and −0.9 for the matrix and filler, respectively. The inserted plot in Fig 8.11 clearly shows the trends in properties occurring up to 2% filler volume fraction. Unlike conventional fillers, auxetic fillers show improvements in shear modulus at E_f/E_m ratios as low as 0.1 when auxetic fillers are used.

The high shear modulus improvements in the composite systems when auxetic fillers are used have been demonstrated for low volume fractions. The complete set of shear modulus predictions are included in Appendix B.

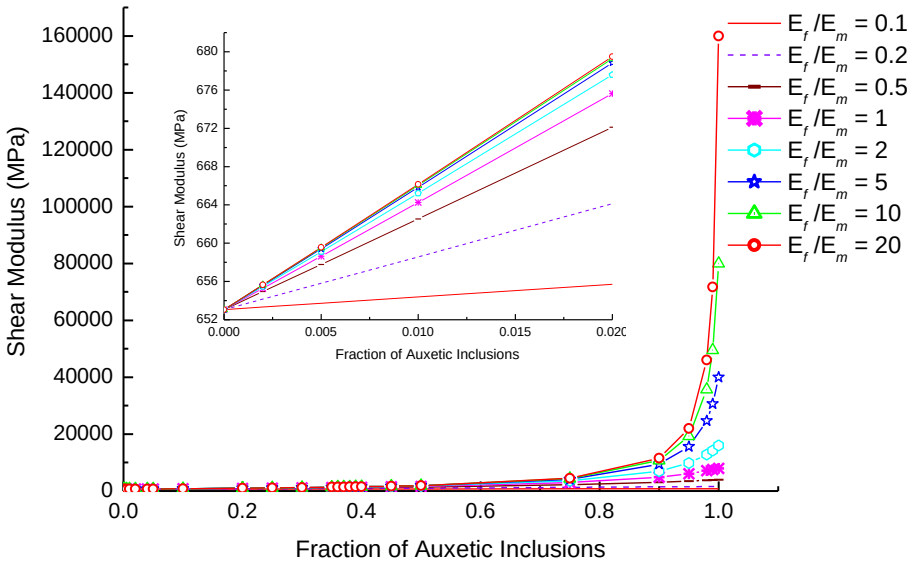

Fig 8.11 Predicted shear modulus vs. volume fraction of auxetic inclusions for E_f/E_m = 0.1 to 20 within a conventional matrix. (Poisson's ratio of matrix is +0.225 and filler is −0.9).

8.4 SCF Predictions for Poisson's Ratio of the Composite System

Fig 8.12 shows the predicted trends in Poisson's ratio of the composite when conventional fillers are added to a conventional matrix (υ_m= +0.225 and υ_f = +0.45). The addition of higher positive Poisson's ratio fillers leads to an increase in the effective positive Poisson's ratio of the composite. Increases in the Poisson's ratios are realised at lower filler volume

fractions as the E_f/E_m increases.

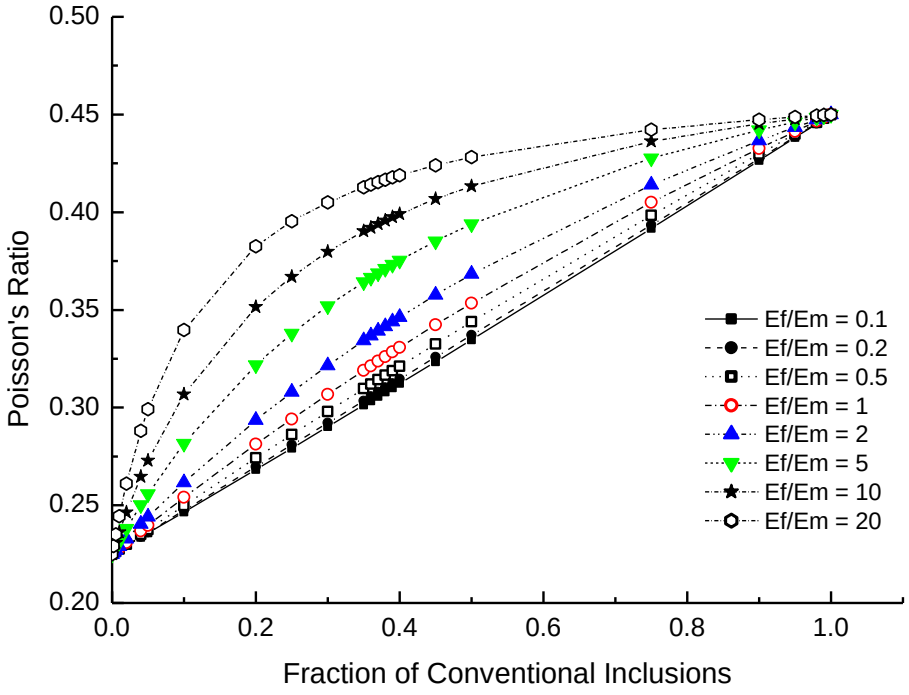

Fig 8.12 Predicted Poisson's ratio of the filled system versus volume fraction of conventional inclusions for E_f/E_m = 0.1 − 20 in a conventional matrix; [υ_m= +0.225 and υ_f = +0.45].

Fig 8.13 shows the trends in Poisson's ratio for composites produced when auxetic fillers are added to a conventional matrix (υ_m= +0.225 and υ_f = −0.9). A change of Poisson's ratio from positive to negative values is predicted for all E_f/E_m ratios. The higher the stiffness of the auxetic filler, the lower the volume fraction of filler required to achieve the change from positive to negative effective Poisson's ratio of the composite system.

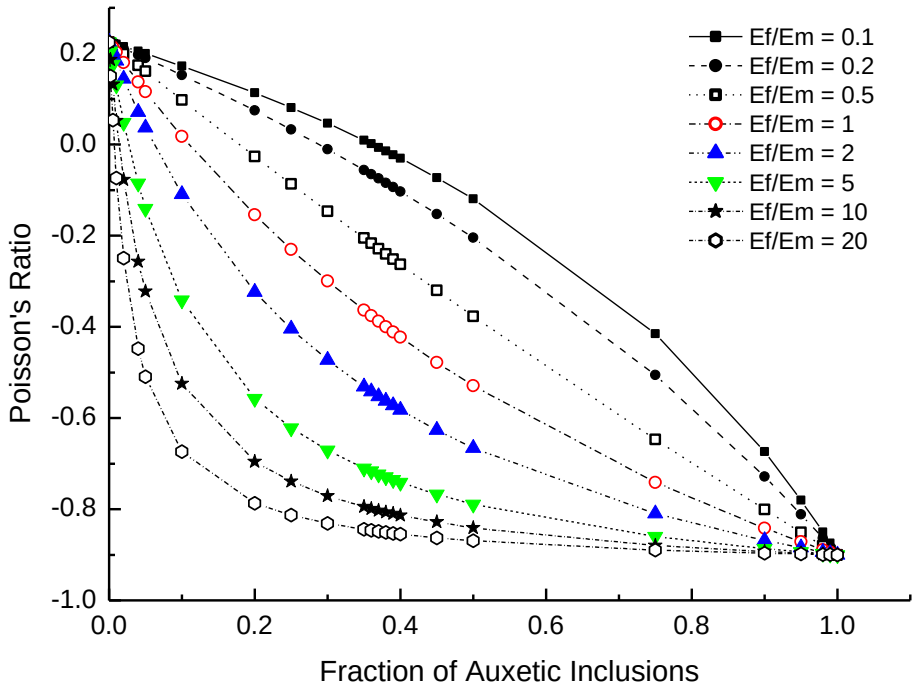

Fig 8.13 Predicted Poisson's ratio of the filled system versus volume fraction of auxetic inclusions for $E_f/E_m = 0.1 - 20$ in a conventional matrix; [υ_m= +0.225 and $\upsilon_f = -0.9$].

The effect of adding conventional fillers to an auxetic matrix follow similar trends (not shown) i.e. the effective Poisson's ratio of the composite varies smoothly with increase in filler volume fraction from the matrix value at zero filler to the filler value at a filler volume fraction of 1. The rate of change in Poisson's ratio with filler volume fraction increases as the E_f/E_m ratio increases, and the transition from negative to positive effective Poisson's ratio occurs at lower filler volume fraction as E_f/E_m increases for the conventional filler and auxetic matrix systems.

The effect of varying the Poisson's ratio of fillers on the overall Poisson's ratio of the composite was also investigated, Figs 8.14 and 8.15.

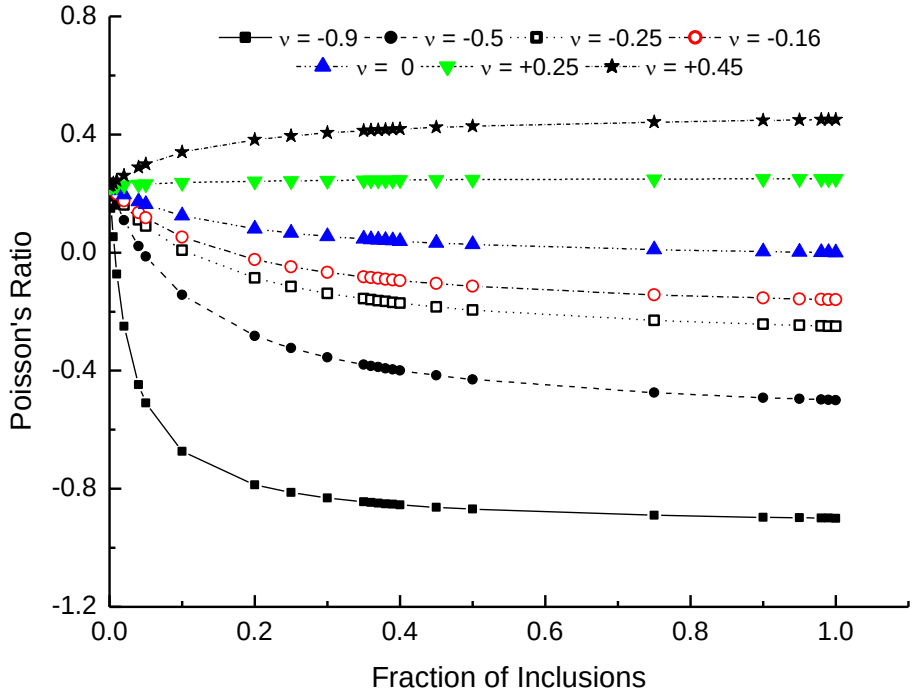

Fig 8.14 Predicted Poisson's ratio versus volume fraction of inclusions with $\upsilon_f = -0.9$ to +0.45 in a conventional matrix with $\upsilon_m = +0.225$; [$E_f/E_m = 20$].

The results plotted in Fig 8.14 show that a high modulus filler ($E_f/E_m = 20$) would require a small volume fraction (below 10%) to result in a composite having overall auxetic properties when $\upsilon_f < -0.25$. For a low negative Poisson's ratio high modulus filler such as polycrystalline α-cristobalite (i.e. $\upsilon_f = -0.16$), a filler content of approximately 20% may be needed to realise auxetic behaviour in the composite, although this will also depend on the matrix Poisson's ratio and the ratio of filler-to-matrix Young's modulus – the critical filler volume fraction for the transition from positive to negative effective Poisson's ratio decreasing as E_f/E_m increases (Fig 8.13).

Results for composites with $E_f/E_m = 0.2$ are shown in Fig 8.15.

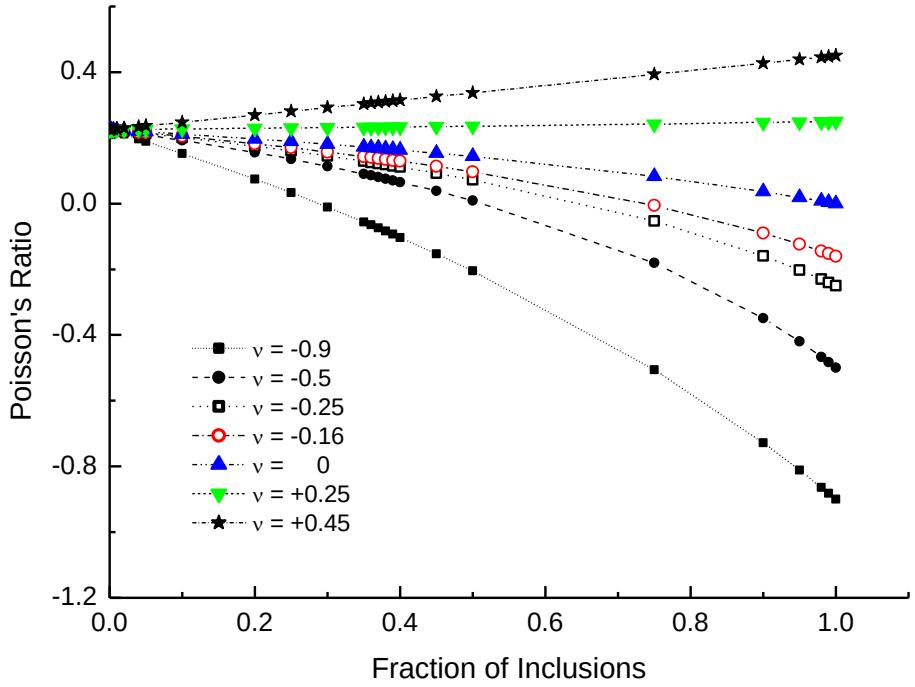

Fig 8.15 Predicted Poisson's ratio versus volume fraction of inclusions with $\upsilon_f = -0.9$ to +0.45 in a conventional matrix with $\upsilon_m = +0.225$; [$E_f/E_m = 0.2$].

Low modulus auxetic fillers require higher filler volume fractions than high modulus fillers of equivalent Poisson's ratio to transform the positive Poisson's ratio behaviour of a conventional matrix into a negative effective Poisson's ratio of the filled system. However, even for the filler with the most negative Poisson's ratio ($\upsilon_f = -0.9$), the filler volume fraction required to achieve the conventional-auxetic transition is high (approximately 30%). This may not be easy to achieve practically due to poor particulate dispersion and particle agglomeration at such filler volume fractions. From this study it can be concluded that the magnitude of the Young's modulus and Poisson's ratio of the filler material play a crucial part in modifying the mechanical properties (the Poisson's ratio, Young's modulus and shear moduli) of the filled composite system.

8.5 Summary

In this chapter, both FE and analytical models predicted improvements in the Young's

modulus when low modulus auxetic fillers were added to a high modulus conventional matrix. Conventional fillers showed improvements when the Young modulus of the filler was higher than that of the matrix. It was shown that the Poisson's ratio of the matrix could be modified by the addition of auxetic fillers.

8.5.1 Low Young's Modulus Particulate Fillers (E_f/E_m = 0.2)

The SCF theory was used to predict the effective Young's modulus of the filled composites employing low Young's modulus auxetic and conventional particulate fillers. In the SCF predictions, low modulus conventional particulate-filled composites showed little sensitivity to the variation of Poisson's ratio, with the effective Young's modulus of the composite decreasing with conventional filler content. On the other hand, the low modulus auxetic particulate-filled composites were predicted to show a Poisson's ratio-dependent decrease in the composite effective Young's modulus for filler Poisson's ratios > -0.8 and an increase in effective Young's modulus for filler Poisson's ratio ≤ -0.9.

8.5.2 High Young's Modulus Particulate Fillers (E_f/E_m = 20)

The SCF predictions show a reduction in Poisson's ratio when high modulus filler is added to the matrix when the filler Poisson's ratio is lower than the matrix Poisson's ratio. The reduction is more pronounced for the largest negative Poisson's ratio filler. The effective Young's modulus data showed the expected upward trend with an increase in the volume fraction of high modulus particulate filler, with the greatest increase again observed for the largest negative Poisson's ratio filler.

CHAPTER 9: DETAILS AND RESULTS OF EXPERIMENTAL TESTS TO VERIFY ASPECTS OF MULTI-LAYER (FLEXURAL MODULUS) AND PARTICLE-FILLED MODELS

9.0 Introduction

Experimental validation of the FE and analytical theories included the fabrication of multi-layer interfaces for the 3/4 point bending tests, tensile testing of particulate filled composites including polymeric chopped fibre – polymer matrix composites (low modulus auxetic and conventional fillers in a high modulus matrix) and alpha-cristobalite particulate - polymer matrix composites (high modulus auxetic filler in a low modulus matrix).

9.1 Flexural Stiffness of Layered Adhesive Interfaces

In this section, the fabrication of multi-layer interfaces incorporating films from the PP film processing study in Chapter 3 is reported. In addition to showing that the theoretically modelled layered interface systems can be fabricated, the results obtained from material property testing procedures provide a first attempt to verify experimentally the validity of the models. It is important to note that the modelled material behaviour may not match the experimentally observed behaviour due to the inherent variability in film properties reported in Chapter 3 as a result of micro-structural inhomogeneity in the films. The level of control over the processing parameters achieved on the extruder may also introduce variability, especially considering the tight extrusion temperature window for auxetic behaviour. The potential for the multi-layer interface fabrication process to alter the properties of individual layers must also be recognised. However, the observed trends in material behaviour as one varies the lay-up and/or the geometrical configuration of the interfaces are expected to be similar in the through-thickness tension and flexural modes, employed in the models and experimental tests, respectively.

9.1.1 Experimental Work -Materials

Polypropylene films were produced via the specially adapted melt extrusion process using polypropylene powder, as discussed in Chapter 3. The polypropylene powder used was Coathylene PB0580, supplied by Univar Plc, which is the same powder that was used in the previous production of auxetic polypropylene fibres [67, 69, 71]. A polyolefin adhesive (Polyolefin 6218) which can bond to polypropylene films was supplied by Bemis Inc. [146], for the production of the multi-layer interface. The properties of the polyolefin adhesive used in the fabrication of multi-layer interfaces are given in Table 9.1.

Table 9.1. Adhesive properties of Polyolefin 6218 [146].

Glue line temperature[1] (°C)	79 - 150
Softening point[2] (°C)	66
MFI at 150 °C /2.16Kg	6
MFI at 175 °C /2.16Kg	22
MFI at 190 °C /2.16Kg	35

[1]Glue line temperature is the actual temperature range to which the adhesive should be exposed. The optimum glue line depends on the applied pressure and the substrate permeability.

[2]Measured by Thermo-mechanical analysis (TMA).

Prior to the fabrication of the multi-layer film adhesive interface, the Young's modulus and Poisson's ratio of the films and the Polyolefin 6218 adhesive were determined using the same methodology (MESSPHYSIK ME 46 [138] video- extensometer and the Deben Micro-tensile testing machine) described in Chapter 3. Cyclic tests using travel limits maintained up to 1% strain levels were performed at a loading strain rate of 0.1 mm min^{-1}. The length, width and thickness of the test specimens were 50 mm, 10 mm and 0.8 mm respectively of which the gauge length for strain calculations is 10 mm. Conventional films extruded at a temperature of 230 °C, a screw speed of 1.05 $rads^{-1}$ and a take-up speed of 0.03ms^{-1} and auxetic films extruded at a temperature of 159 °C, a screw speed of 1.05 rads^{-}

[1] and a take-up speed of 0.0225 ms^{-1} were used in the fabrication of multi-layered interfaces. The Poisson's ratio and Young's modulus of Polyolefin 6218 were calculated from the gradient of the third extension cycle of the transverse true strain versus longitudinal true strain data (Fig 9.1) and longitudinal engineering stress versus longitudinal engineering strain data (Fig 9.2), respectively.

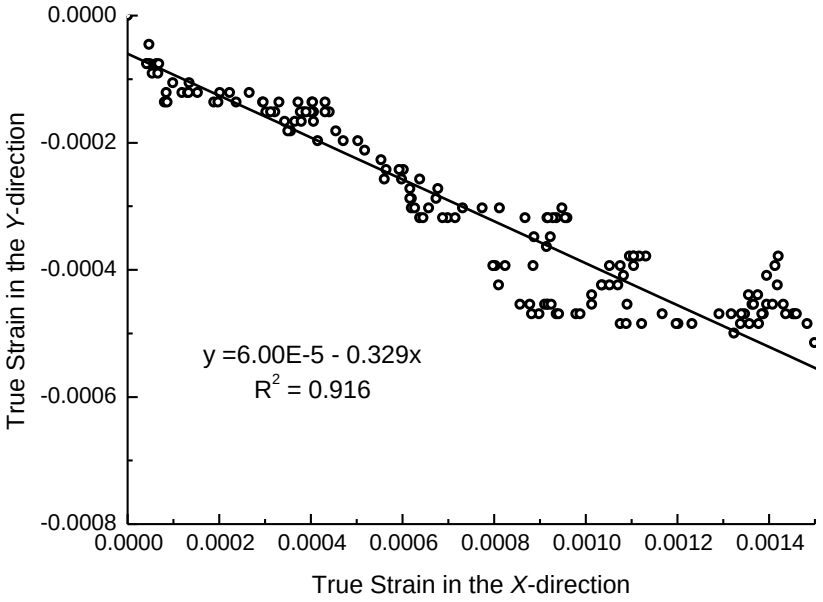

Fig 9.1 Average true strain in the (transverse) *Y*-direction versus true strain in the (longitudinal) *X*-direction for Polyolefin 6218.

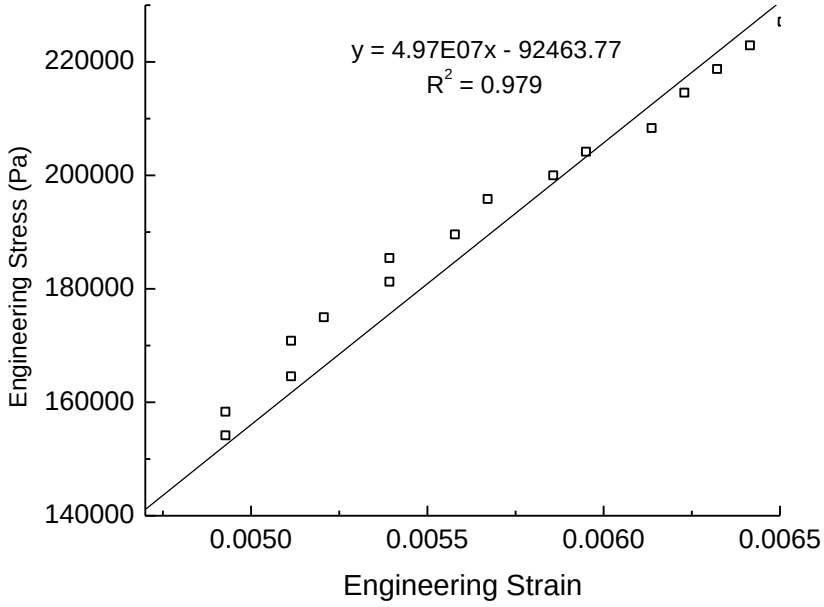

Fig 9.2 Engineering stress versus engineering strain of Polyolefin 6218.

The measured properties of the materials are as shown in Table 9.2. Average thickness values were taken from 3 different measurements per sample using a vernier calipers and a SKE Fabric Thickness Tester.

Table 9.2 Measured properties of the polyolefin adhesive and PP films.

Materials	Young's Modulus (MPa)	Poisson's Ratio	Average Thickness (mm)
Polyolefin 6218	50.0±5.5	+0.33	0.08±0.01
Conventional PP film	340±90	+0.34 to +0.43	0.17±0.05
Auxetic PP film	340±50	-0.95 to -0.40	0.20±0.06

9.1.2 Fabrication of the Multi-Layer Film Adhesive System

The films and polyolefin adhesive layers were alternately stacked on top of a steel block (100 mm x 50 mm x 50 mm, weighing 1000 g) covered with a release film. A second steel block also wrapped in release film was placed on top of the lay-up in order to provide a compressive pressure and minimise air bubbles from forming within the laminate (Fig 9.3). It was also ensured that the films were flat as they were added in order to avoid wrinkling of the cured multi-layer film/adhesive system. The mould was placed in a fan-assisted oven for curing. The oven temperature was steadily raised to 110 °C and held constant for an hour. Interface samples were on average 50 mm × 10 mm × 0.5 mm (length, width and thickness). An average length of 50 mm was determined by the size of the steel block used. Production of laminates with longer lengths was tried, however, it was discovered that the shorter laminates were of better quality; i.e. wrinkle and air bubble free. The thickness of the nine-layer film/adhesive interface (five PP films and four adhesive layers) was approximately 0.5 mm after curing.

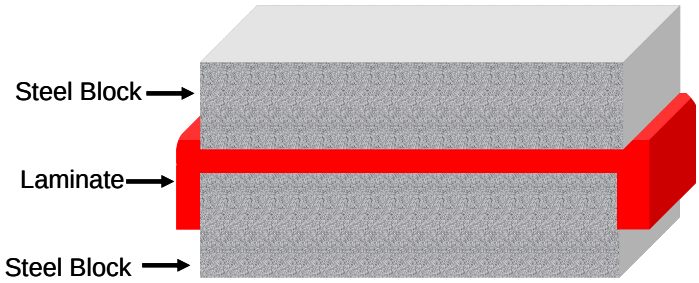

Fig 9.3 Schematic of the stacked laminate in between two steel blocks.

In the trial stages of laminate production, no axial strain was applied during lay-up and curing. However, the absence of pre-strain resulted in a wrinkled interface containing air bubbles, as shown in Fig 9.4.

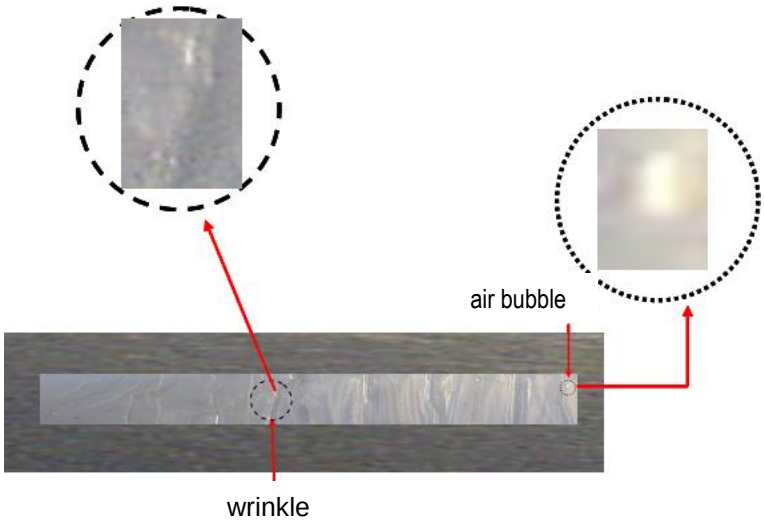

Fig 9.4 Wrinkled multi-layer film/adhesive system.

In order to avoid wrinkling, the interfaces were pre-strained during lay-up. A strain just enough to make the film flat was applied by hand. Care was taken not to over-stretch the films in order to preserve their mechanical properties. Following completion of the interface lay-up, a load was placed on top of it to maintain flatness. The interface lay-up was then placed in an oven to cure.

Following the improvements in the lay-up process, a wrinkle-free multi-layered

film/adhesive interface, shown in Fig 9.5, was obtained. Included is a photo of an actual multi-layer interface cross-section of the consolidated layered structure.

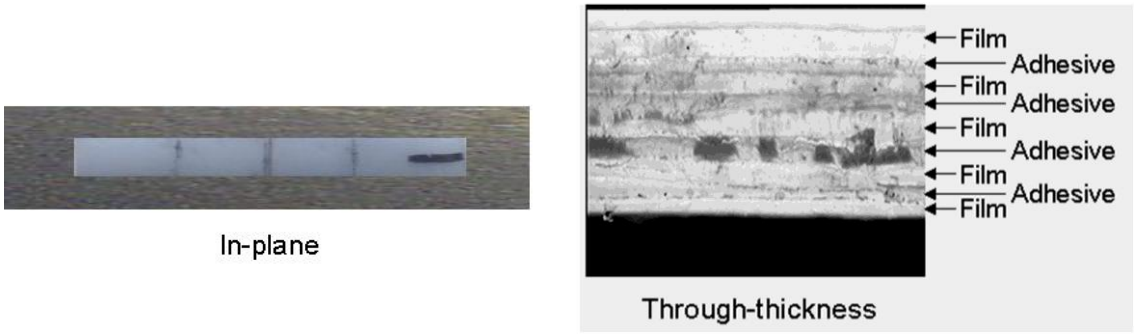

(a) (b)

Fig 9.5 (a) Multi-layer film/adhesive interface without wrinkles; (b) photo of multi-layer interface cross-section, (X40 magnification).

In the multi-layer interfaces fabricated and presented in this chapter, the adhesive thickness is the same throughout, so is the film thickness in order to simulate a CCLT model. Unlike in the models presented in Chapter 4 - Figs 4.8 and 4.9, the experimental multi-layer interfaces were produced so that the films formed the outer layers. This was done in order to prevent the adhesive from melting onto the mould otherwise it would have been very difficult to separate the bonded multi-layer interface from the steel rig. In this context, a nine-layer interface would comprise five films and four layers of adhesive. The stacking sequences of films in the multi-layer interfaces were as follows; (A—A—A—A—A), (C—C—C—C—C), (A—C—C—C—A), and (C—A—A—A—C) where C denotes a conventional film, A an auxetic film and — an adhesive layer. Following fabrication of the layered interfaces their dimensions were measured. The average interface dimensions are given in the Tables 9.3 and 9.4.

Table 9.3: All-auxetic interfaces (A—A—A—A—A) dimensions.

Specimen	Length (mm)	Width (mm)	Thickness (mm)
1	50.10	10.53±0.37	0.52±0.04
2	49.26	12.85±0.15	0.51±0.02
3	50.36	9.90±0.16	0.51±0.03

Table 9.4: All-conventional interfaces (C—C—C—C—C) dimensions.

Specimen	Length (mm)	Width (mm)	Thickness (mm)
1	48.05	12.02±0.27	0.47±0.02
2	49.00	9.74±0.17	0.51±0.04
3	48.60	8.97±0.12	0.50±0.02

The masses of the fabricated and trimmed interfaces were also measured and recorded. Approximate mass fractions were then estimated assuming no voids. Mass fractions of the films and adhesive layers in the laminates were calculated by determining the average mass of a film with the same length and width dimensions as those of the interface and then multiplying that value by the number of films in the lay-up. The mass of the films was subtracted from the total mass of the interface to determine the mass fraction of the adhesive. The mass fractions of films to adhesive in the auxetic and conventional interfaces were approximately 1:1. These values are shown in Tables 9.5 and 9.6 for (A—A—A—A—A) and (C—C—C—C—C) interfaces, respectively.

Table 9.5: Mass fractions of all-auxetic film/adhesive interfaces.

Specimen	Mass of Interface (g)	Mass of 5 Films (g)	Film Mass Fraction (%)	Adhesive Mass Fraction (%)
1	0.267	0.129	48.09	51.90
2	0.296	0.146	49.20	50.79
3	0.219	0.117	53.44	46.55

Table 9.6: Mass fractions of all-conventional film/adhesive interfaces.

Specimen	Mass of Interface (g)	Mass of 5 Films (g)	Film mass Fraction (%)	Adhesive Mass Fraction (%)
1	0.273	0.097	35.56	64.44
2	0.198	0.088	44.24	55.76
3	0.182	0.088	48.00	52.00

9.1.3 Three-Point Bending Tests

The flexural moduli of the laminates (50 mm × 10 mm × nominal thickness in mm) were measured in three-point bending tests using an Instron tensometer 3369. The cross-head speed was 1 mm/min and the load cell capacity was 100 N. A span length of 42 mm was used. A schematic diagram of the test set-up is shown in Fig 9.6.

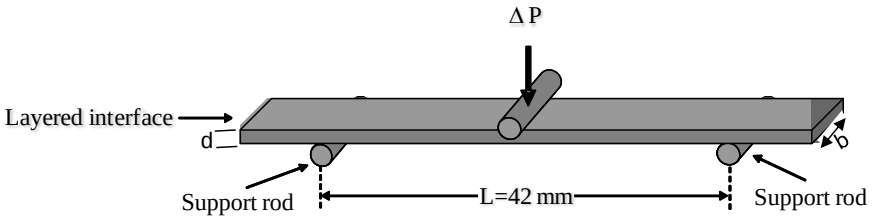

Fig 9.6 Three-point bending test set-up for multi-layer interfaces.

The flexural stress, σ_f, of the interface was calculated using Eq. (9.1) [148]:

$$\sigma_f = \frac{3PL}{2bd^2} \tag{9.1}$$

where σ_f is the stress at the midpoint of the layered interface, P is the applied load, L is the span length, b is the width and d is the thickness of the layered interface.

The flexural strain of the layered interface was calculated using Eq. (9.2) [148]:

$$\varepsilon_f = \frac{6Dd}{L^2} \tag{9.2}$$

where ε_f, is the flexural strain and D is the maximum deflection at the centre of the beam. The flexural modulus, E_f, was then calculated by diving Eq. (9.1) by Eq. (9.2) to yield:

$$E_f = \frac{L^3 m}{4bd^3} \tag{9.3}$$

where m is the slope of the load versus extension curve.

9.1.4 Four-Point Bending Tests

A test rig was developed for four-point bending tests using the Instron machine in accordance to specifications reported by Kawasaki *et al* [149] as shown in Fig 9.7. The video extensometer was set up (as described in Chapter 3) and the four-point bending tests were carried out. The load-deflection data were recorded by the Instron and deflection at mid-span was measured using the video extensometer.

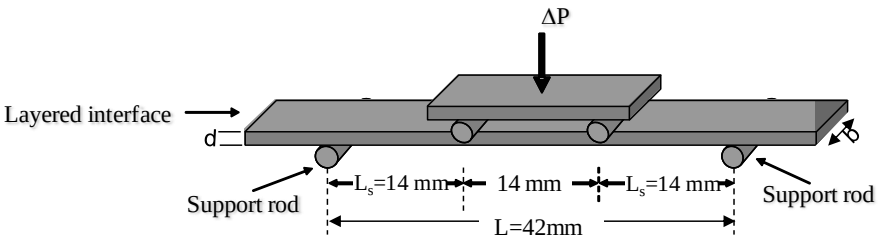

Fig 9.7 Four-point bending test set-up for multi-layer interfaces.

Deflections at the mid-point were measured using the video extensometer in order to determine the apparent elastic modulus (E_L). These values were calculated using Eq. (9.4) [149].

$$E_L = \frac{PL_S}{\Delta\delta_L}\left(\frac{3L^2 - 4L_S{}^2}{48I}\right) \tag{9.4}$$

where L_s is the span subjected to the shear deformation (i.e. distance between inner and outer roller), $\Delta\delta_L$ is the deflection at mid-point and I $\left(I = \frac{bd^3}{12}\right)$ is the second moment of area for a rectangular cross-section beam.

The slope $\frac{P}{\Delta\delta_L}$ is determined from the linear portion of plots between the load, P, and the deflection, $\Delta\delta_L$. These tests were performed in order to investigate the effect of shearing on the bending stiffness of the laminated beams.

9.1.5 Results and Discussion

9.1.5.1 Three-Point Bending Test Results

The flexural moduli of specimens 1-3 were calculated for both conventional and auxetic laminated beams using Eq. (9.3). The load-deflection graphs obtained from the tests on auxetic and conventional laminated beams are shown in Fig 9.8 and 9.9, respectively. The slopes of the curves are determined and then used to calculate the three-point bending flexural modulus. These values are given in Tables 9.7 and 9.8 for the all-auxetic and all-conventional laminate beams, respectively. Also shown in the tables are the average values for the flexural modulus of the specimen together with standard deviation.

Table 9.7: Flexural moduli for all-auxetic film/adhesive (A—A—A—A—A) laminates.

Specimen	Slope (N/mm)	Width (mm)	Thickness (mm)	Flexural modulus (MPa)
1	0.085	10.53	0.52	1063
2	0.100	12.85	0.51	1087
3	0.074	9.90	0.51	1044
Average				1064 ± 22

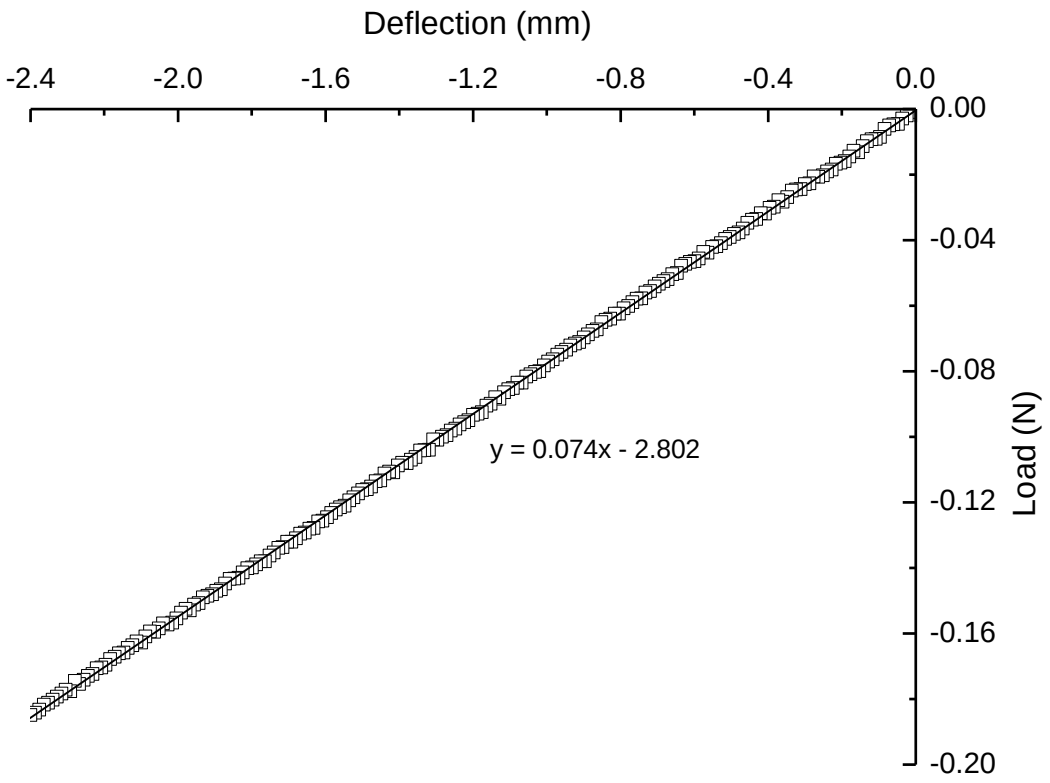

Fig 9.8 Experimental load-deflection response for the all-auxetic layered beam (specimen 3).

Table 9.8: Flexural moduli for all-conventional film/adhesive (C—C—C—C—C) laminates.

Specimen	Slope (N/mm)	Width (mm)	Thickness (mm)	Flexural modulus (MPa)
1	0.066	12.02	0.47	980
2	0.060	9.74	0.51	860
3	0.050	8.97	0.50	826
Average				889 ± 81

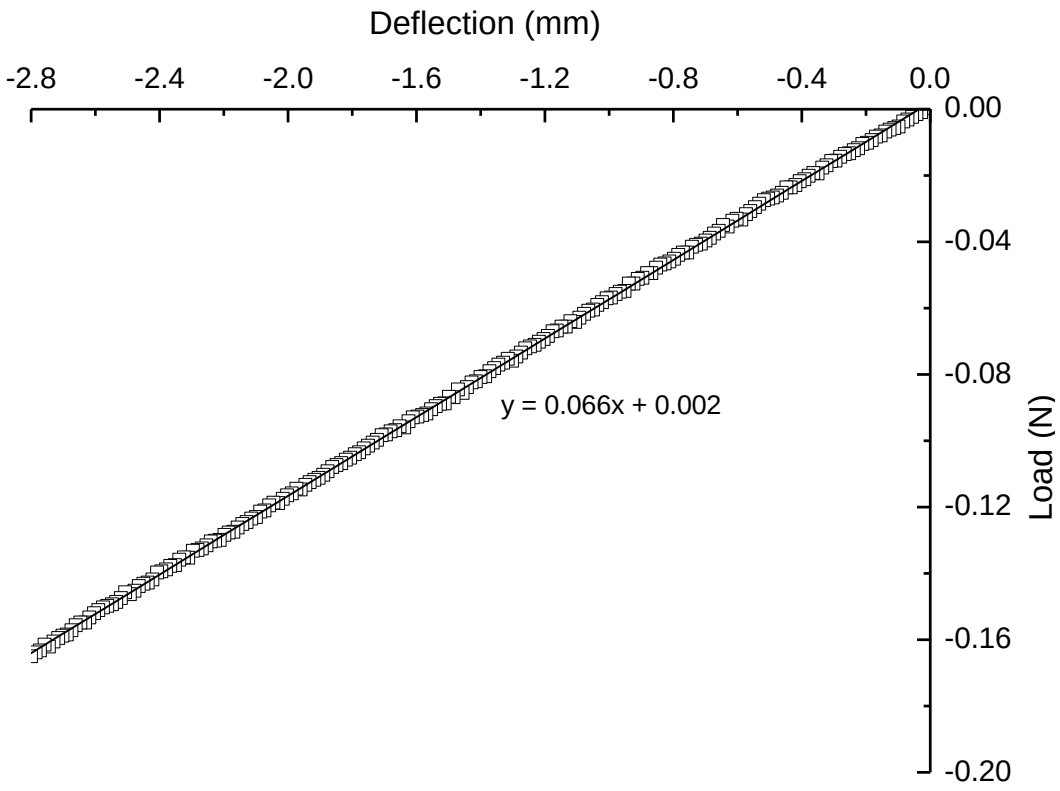

Fig 9.9 Experimental load-deflection response for all-conventional layered beam (specimen 1).

Following three-point bending tests, the average flexural modulus of the all-auxetic laminated beam (A—A—A—A—A) was found to be higher than that for an all-conventional laminated beam (C—C—C—C—C). Since the type and amount of adhesive used in both beams is the same, the differences in average flexural moduli can be attributed to the differences in the properties of the polypropylene films. The adhesive has a Young's modulus of 50 MPa while that of the PP films is nearly seven times larger with an average value of 340 MPa. From these values of Young's modulus, it is obvious that the addition of a polypropylene film regardless of it being auxetic or conventional will result in improved flexural stiffness. However, from the observed results, the flexural stiffness is not the same for the two types of laminated beams. The auxetic laminated beam has an approx 20% higher flexural modulus (1064 ± 22 MPa) compared to that of the conventional laminated beam (889 ± 81 MPa).

In addition to all-auxetic and all-conventional layered laminates, interfaces that contained a mixture of conventional and auxetic films were also fabricated and tested. These interfaces are identified as (A—C—C—C—A) and (C—A—A—A—C) in which the theoretical percentages of auxetic films relative to the total volume fraction of films (V_{aux}/V_{films}) are 40 and 60%, respectively. The data for (A—C—C—C—A) and (C—A—A—A—C) are shown Tables 9.9 and 9.10.

Table 9.9: Flexural moduli for the A—C—C—C—A interfaces.

Specimen	Slope (N/mm)	Width (mm)	Thickness (mm)	Flexural modulus (MPa)
1	0.080	10.2	0.53	976
2	0.085	12.6	0.51	942
3	0.087	11.9	0.53	910
Average				943 ± 33

Table 9.10: Flexural moduli for the C—A—A—A—C interfaces.

Specimen	Slope (N/mm)	Width (mm)	Thickness (mm)	Flexural modulus (MPa)
1	0.090	10.8	0.54	980
2	0.089	11.7	0.52	1002
3	0.090	10.5	0.56	904
Average				962 ± 51

The average flexural moduli for all the different stacking sequences are shown in Fig 9.10, as a function of V_{aux}/V_{films}.

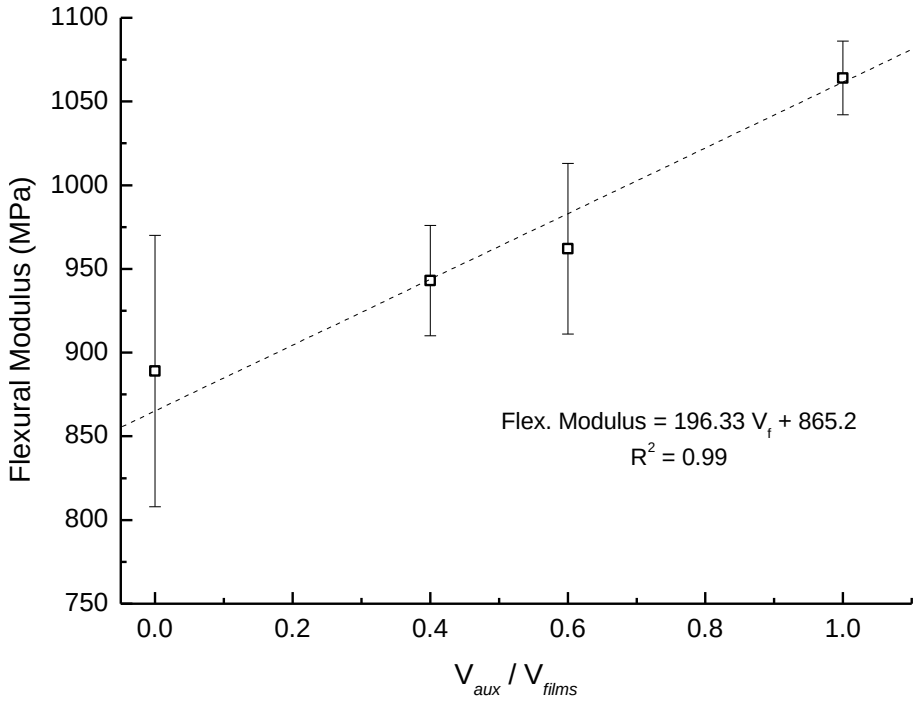

Fig 9.10 Average flexural modulus versus V_{aux}/V_{films} in the laminate. Dashed line corresponds to the least squares best fit straight line to the data.

Fig 9.10 shows that the flexural modulus increases linearly (gradient of least squares best fit straight line = 196.3) with the volume fraction of auxetic films relative to the total number of films. This is consistent with the increase in through-thickness modulus with the incorporation of auxetic films predicted from the FEM analysis in Chapters 6 and 7. From the linear relationships it is possible to predict the flexural modulus of any laminate provided the volume fraction of auxetic film is known.

9.1.5.2 Four-Point Bending Test Results

Laminate specimens of (A—A—A—A—A) and (C—C—C—C—C) were tested in four-point flexural bending mode. Four specimens produced using the same method described in Section 9.1.2 were tested for each sample. The load-deflection curves were obtained from the mid-span of the laminate beam. The gradients of these curves were used in the determination of E_L (Eq. (9.4)). Representative plots for both auxetic and conventional

layered interface samples are shown in Figs 9.11 and 9.12. The calculated equivalent elastic moduli, E_L, values together with the dimensions of A-A-A-A-A and C-C-C-C-C specimens are given in Tables 9.11 and 9.12, respectively. Specimens tested in the four-point bending mode are expected to yield stiffness results higher than those observed in the three-point bending mode. This is due to the fact that the four-point bending experiments include shear deformation effects.

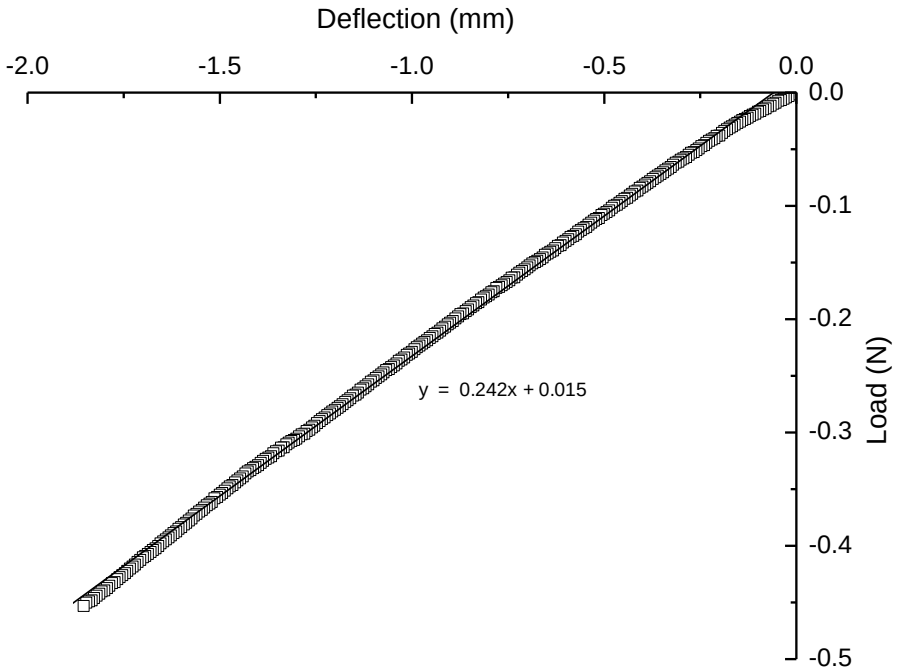

Fig 9.11 Load-deflection response for mid-span of the all-auxetic laminate beam (specimen 1).

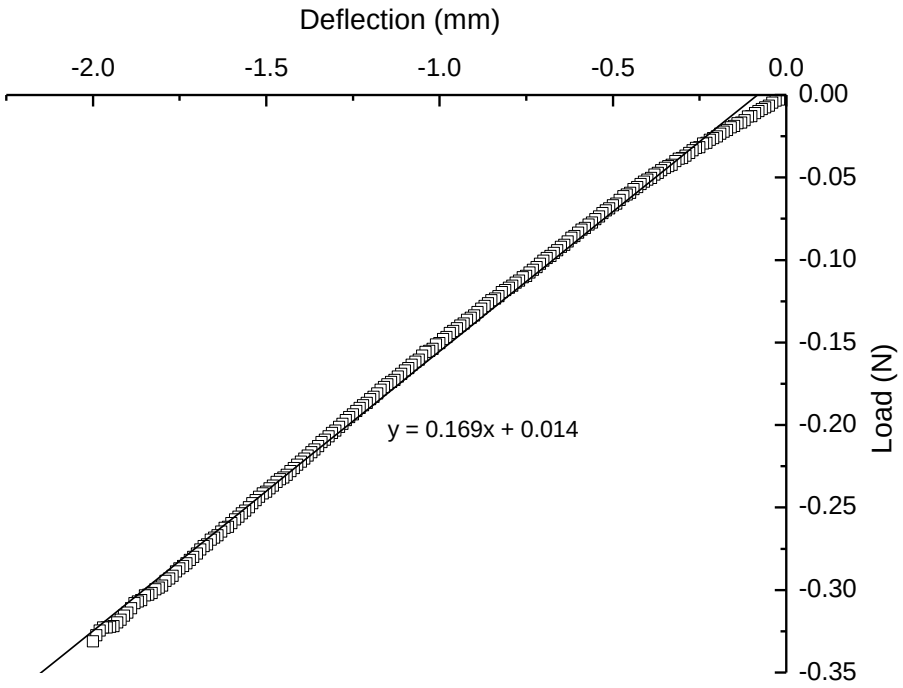

Fig 9.12 Load-deflection response for mid-span of the all-conventional laminate beam (specimen 2).

Table 9.11: Flexural moduli for the all-auxetic specimens.

Specimen	Slope (N/mm)	Width (mm)	Thickness (mm)	Second Moment of Area (mm^4)	Flexural Modulus (MPa)
1	0.242	10.53	0.52	0.123	2580.26
2	0.281	12.85	0.51	0.142	2601.28
3	0.200	9.90	0.51	0.107	2457.96
4	0.214	10.42	0.54	0.137	2031.41
Average					2420 ± 270

Table 9.12: Flexural moduli for the all-conventional specimens.

Specimen	Slope (N/mm)	Width (mm)	Thickness (mm)	Second Moment of Area (mm^4)	Flexural Modulus (MPa)
1	0.157	10.42	0.51	0.115	1792.15
2	0.169	10.53	0.52	0.123	1800.94
3	0.130	9.90	0.51	0.109	1561.90
4	0.133	12.85	0.51	0.142	1231.09
Average					1600 ± 270

The flexural modulus, E_L, for the all-auxetic laminate (A—A—A—A—A) is approximately 52% higher than that of the all-conventional laminate (C—C—C—C—C) laminate. The adhesive used is the same in both laminates; hence the difference in the measured moduli properties is due to the presence of either conventional or auxetic films. Given that the auxetic and conventional films were produced using parameters shown to lead to similar film Young's modulus (approx. 340 MPa) then these results show that the inclusion of auxetic films tends to increase the flexural modulus relative to conventional films, consistent with the 3 point bend test experimental results and the FEM through-thickness Young's modulus predictions.

9.1.6 FEM Results: Three-Point Bending Tests

FE analysis was used to model three-point flexural bending of the laminates as described in Section 4.6, Chapter 4. Table 9.13 gives the flexural modulus of laminates with varying volume fractions of the adhesive.

Table 9.13 Summary of three-point bending FEM results.

V_{aux}/V_{films}	Force (N)	Max Displacement (mm)	Flexural modulus (MPa)
0	1	25.32	585.26
0.4	1	17.26	858.44
0.6	1	11.96	1238.62
1	1	8.48	1747.99

A plot of the FE and experimental 3-point bending test results is shown in Fig 9.13.

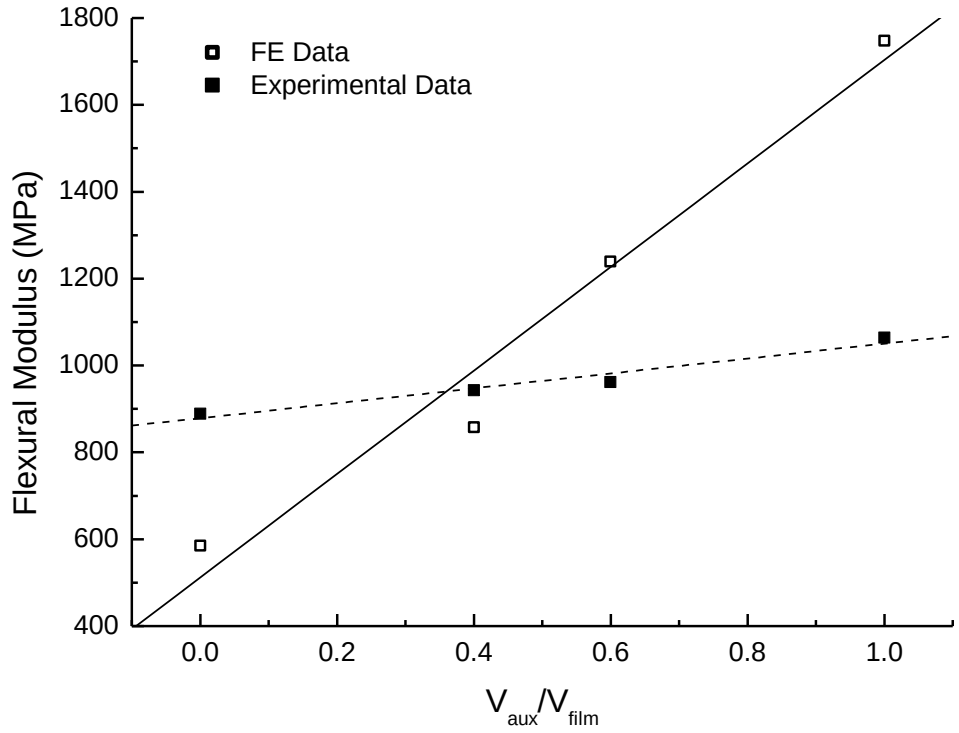

Fig 9.13 Comparison of FE and experimental flexural modulus as a function of the ratio of volume fraction of auxetic films to the total volume fraction of films in the laminate.

An increase in the flexural modulus is observed with increase in auxetic volume fraction from the FE analyses. This is consistent with increases observed in the experimental 3-point (and 4-point) bending test results, and also the observations made in Chapters 6 and 7 where all-auxetic film interfaces showed the highest through-thickness modulus.

The FE analysis tends to over-estimate the experimental flexural modulus. This is seen by the all-auxetic interface showing a 20% increase in the experimental flexural modulus

relative to the all-conventional film, whereas the increase rises to approx 200% in the FE analyses. The discrepancies between the FE analysis and experimental results may be attributed to the assumptions made in the FE analyses such as perfect bonding and uniform film properties which may not be the case in practice. The interfacial interactions between the layers are expected to play a major role in determining the properties of the multi-layered beam.

9.1.7 Conclusions – Flexural Tests

The results from both the three-point and four-point bending tests suggest that there is a systematic increase in flexural modulus as auxetic films are added into the multi-layered beam, Tables 9.7-9.12 and Fig 9.13. This is consistent with the FE results for the three-point bending test (Table 9.13) and those predicted for the through-thickness Young's and shear modulus in Chapters 6 and 7, respectively. Imperfections in the structural integrity of the fabricated laminate, and non-uniform film properties may lead to differences in the observed mechanical property improvements when compared to theoretical simulations (Fig 9.13) wherein interlayer bonding of uniform films is assumed to be perfect. The FE model employed uniform Poisson's ratios of -0.9 and +0.43 for the auxetic and conventional films, respectively, (Table 4.1) whereas in reality a spread of Poisson's ratios is measured (Table 9.2). In particular, as the auxetic film Poisson's ratio approaches the upper limit of -0.40 measured experimentally, a decrease in the enhanced stiffness would be expected relative to that predicted for the value of -0.9 used in the model calculations in Fig 9.13. It can be concluded that the inclusion of auxetic layers into laminated beams results in higher increases in flexural modulus compared to conventional films of similar Young's moduli. The observations from experiments and theoretical calculations suggest that there are benefits in using auxetic materials to achieve increased modulus of multi-layer interfaces.

9.2 Experimental Fabrication and Testing of Particulate Filled Composites

The testing of particulate filled composites was performed for both low and high modulus auxetic fillers relative to the matrix.

9.2.1 Low Modulus Auxetic Fillers

9.2.1.1 Materials – Chopped PP Fibres

Auxetic and conventional PP fibres (Coathylene PB0580 PP powder precursor supplied by Univar plc) were extruded at 159 °C, a screw speed of 1.05 rad/s, and a take-up speed of 0.03 m/s, and 230 °C, a screw speed of 1.05 rad/s and a take-up speed of 0.03 m/s, respectively [67]. These conditions have been previously established to produce auxetic and conventional comparator fibres having similar Young's moduli and diameters [67]. The fibres were chopped using a guillotine to lengths ranging from 2 – 6 mm.

9.2.1.2 Chopped Fibre Composites Sample Fabrication

A cold curing epoxy based on Araldite LY 5052 / Aradur HY 5052 supplied by Huntsman, was used to cast the chopped fibre filled polymeric composites. The weight ratio of resin to hardener used was 72%: 28 %. Preparation of chopped fibre filled composites included rigorously mixing the mixture so as to achieve good dispersion of the fibres. The mixture was then degassed to eliminate bubbles using a vacuum oven prior to curing. The following composites were fabricated: control (unfilled), 5% and 8% (by weight) filled chopped fibre composites. The mould used for casting the composites had a glass base with silicone rubber raised edges forming a rectangular cavity of dimensions 250 x 200 x 3 mm. The schematic of the mould is shown in Fig 9.14. The resin mixture was poured onto the glass mould and then left to cure at room temperature and pressure for 24 h.

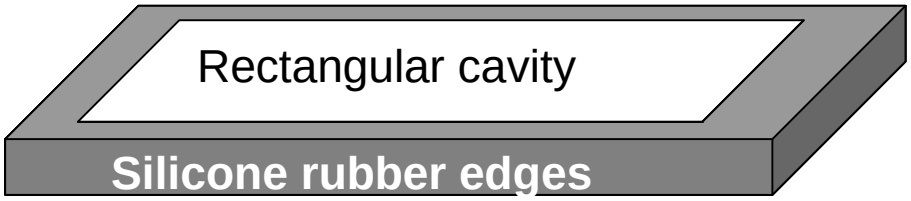

Fig 9.14. Schematic of the mould used for the preparation of the filled composites.

Post-curing was carried out in the oven at 100 °C for 4 h after which the sample was cooled and then removed from the mould. Dog bone specimens were prepared using a Computer Numerically Controlled (CNC) machine according to the British Standard [150]. The specifications of the specimen are shown in Fig 9.15.

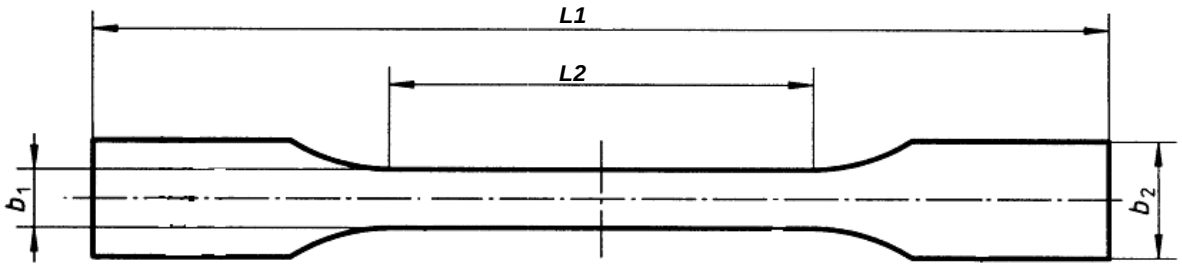

Fig 9.15. Specimen specification for tensile testing according to the British Standard [150].

The following parameters were used for the dog bone samples, overall length (L1) = 150 mm; length of narrow parallel-sided portion (L2) = 60.0±0.5; widths at ends (b_2) =20.00±0.002mm; width at narrow section (b_1)= 10.00±0.02; thickness (h) = 3 mm.

9.2.1.3 Chopped Fibre Composites Sample Characterisation

Micrographs of the filled composites were obtained using optical microscopy. Mechanical properties characterisation was performed in uniaxial tension. The tensile test set up is as shown in Fig 9.16, comprising an Instron 3369 fitted with a 50KN load cell. A displacement rate of 1mm/min was employed.

Fig 9.16. Tensile tests set-up.

9.2.1.4. Results and Discussion

9.2.1.4.1 Microscopy

Figures 9.17 and 9.18 show typical optical micrographs of the initial and bubble-free unfilled resin samples and demonstrate that good quality samples were produced following improvements to the original casting process.

Fig 9.17. Optical micrograph of the initial trial fabrication of cast resin (X40 magnification).

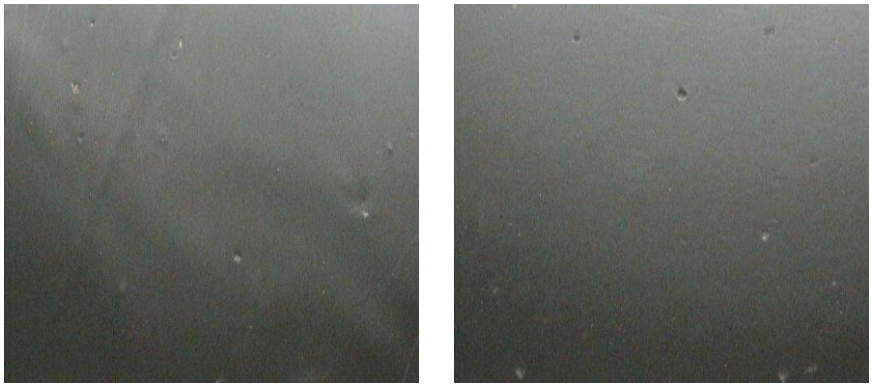

Fig 9.18. Optical micrograph of bubble-free cast resin (X40 magnification).

Micrographs of the cast fibre-filled samples are shown in Fig 9.19.

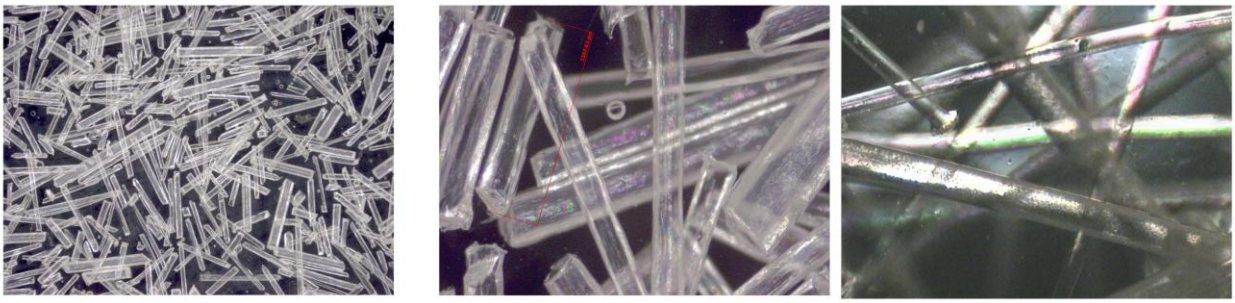

Fig 9.19. Micrographs of the 5 % chopped fibre-filled resin ((a), (b) and (c) at X5, X20 and X15 magnification, respectively).

From Fig 9.19 it is clear that the fibres are randomly and evenly distributed within the composite.

9.2.1.4.2 Tensile tests

The mechanical properties of the fibres were taken from the work done by Alderson *et al* [67] and are shown in Table 9.14.

Table 9.14. Mechanical properties of the auxetic and conventional fibres [67].

	Young's modulus (MPa)	Poisson's ratio
Auxetic fibres	340	-0.6
Conventional fibres	340	0.34

A minimum of five specimens were tested for each fibre-loading condition. Examples of typical load-extension graphs of the control, auxetic and conventional chopped fibre filled composites are shown in Fig 9.20.

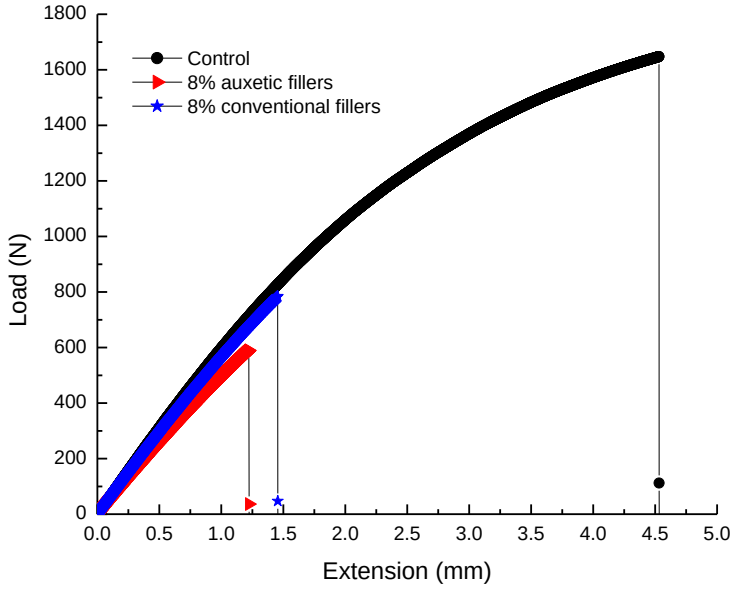

Fig 9.20 Graph showing the load–extension behaviour of the control (unfilled) specimen, and 8% chopped conventional and auxetic fibre filled composites.

The load extension curves of the filled composites show lower maximum load to failure, and lower extension to failure accompanied with brittle failure when compared to the control. The results, averaged over all specimens tested, for conventional and auxetic chopped fibre filled composites are shown in Tables 9.15 and 9.16 respectively.

Table 9.15. Results for chopped conventional fibre composites.

% chopped fibres (conventional)	Young's Modulus (MPa)	Maximum load to failure (N)	Maximum extension (mm)	Work done (Nmm)
0 (control)	1361 ± 66	1557 ± 295	4.07 ± 0.95	3172
5	1362 ± 20	637 ± 146	1.24 ± 0.32	396
8	1145 ± 31	780 ± 117	1.58 ± 0.13	616

Table 9.16. Results for chopped auxetic fibre composites.

% chopped fibres (auxetic)	Young's Modulus (MPa)	Maximum load to failure (N)	Maximum extension (mm)	Work done (Nmm)
0 (control)	1361 ± 66	1557 ± 295	4.07 ± 0.95	3172
5	1139 ± 100	656 ± 172	1.94 ± 0.33	635
8	1247 ± 69	640 ± 104	1.33 ± 0.24	427

Figures 9.21 and 9.22 show how the experimental Young's modulus data compare to the SCF predicted trends for composites containing auxetic and conventional fillers, respectively, having fibre Young's moduli given by Table 9.14, and an adhesive Young's modulus corresponding to that of the unfilled control sample (Tables 9.15 and 9.16). SCF predicted trends are shown for fibre Poisson's ratio ranges of $-0.9 \leq \nu \leq -0.1$ and $0.05 \leq \nu \leq 0.43$ in Figures 9.21 and 9.22, respectively, and an adhesive Poisson's ratio of +0.3 was assumed in the calculations.

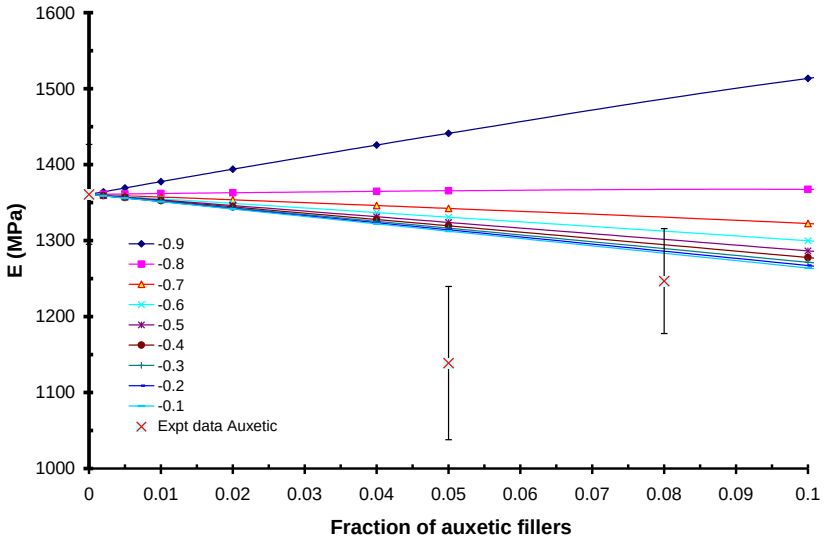

Fig 9.21. Comparison of experimental and SCF results for chopped auxetic fibre filled composites.

The SCF predictions for the low modulus auxetic filler show an increase in the composite Young's modulus with filler only for the lowest value of fibre Poisson's ratio, i.e. -0.9. When the filler Poisson's ratio is increased from -0.9 to -0.8, the SCF trends show that the effective Young's modulus of the composite decreases as the filler fraction increases. Hence the effective Young's modulus of the composite is very sensitive to slight variations in Poisson's ratio when the fibre Poisson's ratio is in the vicinity of -0.8 to -0.9. Further increases in fibre Poisson's ratio towards -0.1 have progressively less of an effect on the effective Young's modulus of the composite, and the trends are almost overlapping when $\nu \geq -0.3$. This was also observed in the parametric studies; Fig 8.9, when a low modulus auxetic filler was added to a high modulus conventional matrix. The experimental data show a decrease in effective Young's modulus of the composite for the filled composites, generally consistent with the decrease predicted by the SCF predictions for fibre Poisson's ratios of $\nu \geq -0.8$.

The predicted SCF model effective Young's modulus trends for the conventional fibre-

filled composites are not as sensitive to the magnitude of Poisson's ratio as is the case when auxetic fillers are used, tending to overlap for all positive values of fibre Poisson's ratio considered, Fig 9.22. All the predicted trends for low modulus positive Poisson's ratio fillers show a decrease in the effective Young's modulus of the composite as the filler fraction is increased. The experimental data for the chopped conventional fibre-filled composites show general agreement with the trend from the SCF predictions.

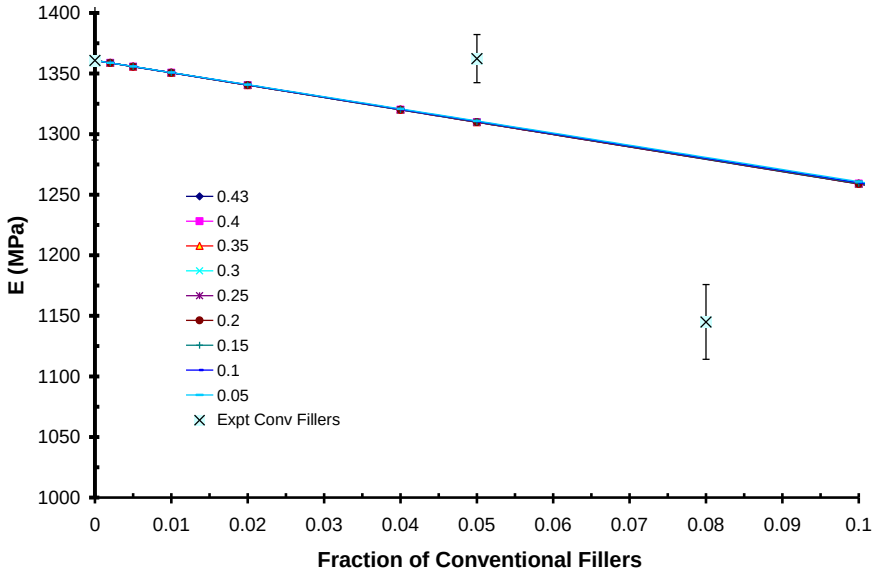

Fig 9.22. Comparison of experimental and SCF results for conventional filled composites.

Comparing the experimental values for the two systems at 5% filler concentration, the conventional fibre-filled samples appear to have a higher effective Young's modulus than the auxetic fibre-filled systems. However at the higher 8% filler concentration, where it might be expected the higher level of filler content should lead to more pronounced/detectable differences, the auxetic samples show a higher effective Young's modulus. With the exception of the 5% auxetic filler value, the experimental errors quoted for the effective Young's moduli (determined from the standard deviation from all samples tested) are of the order of 5% or less. The 5% auxetic filler value has an error of around 9%. This level of uncertainty is generally acceptable [151]. However, it is clear that in this

case the level of experimental accuracy is insufficient to enable a conclusive experimental verification of the predicted enhancement in effective Young's modulus for auxetic fibre-containing samples compared to their conventional fibre-containing counterparts.

It is likely that auxetic fibres having lower Poisson's ratios (i.e. $\nu < -0.8$) will be required in order to detect experimentally differences between the effective Young's moduli of the conventional and auxetic low modulus fibre-filled systems.

Recalling also that the auxetic fibres employed in this work generally show inhomogeneous mechanical properties along the fibre length, then it is possible that the average value of the Poisson's ratio of the chopped fibres within the composite may be higher than the value of -0.6 quoted in Table 9.14. This would diminish further the predicted difference in the effective Young's modulus for the auxetic and conventional systems, making experimental verification even more difficult. Hence, in addition to producing auxetic fibres having lower Poisson's ratios than currently available, fibres displaying increased homogeneity would also be desirable to confirm the model predictions via experimentation.

The chopped fibre filled composites showed a lower strain and load to failure accompanied by brittle failure. The addition of short fibres within a continuous resin introduces defects within the resin, thus weakening the interface. The chopped fibres in the epoxy resin are not perfectly aligned thereby restricting an efficient stress transfer mechanism when the composite is loaded [152], resulting in reduced composite stiffness. Aligned fibres offer maximum stiffness and strength in the direction of alignment, and in the case of auxetic fibres would tend to retain the fibre-matrix interface to higher loads than equivalent conventional fibres [69].

The compatibility of the fibre and resin components is also important. Polypropylene fibres have a low surface energy and hence are difficult to bond well to the resin. Gonzalez-Chi [153] and others used Raman Spectroscopy to monitor the loading and failure of a thermoplastic/thermoset interphase. Their work proved that untreated thermoplastic fibres formed a weaker interface due to the low reactivity of the polyethylene fibres. Bader *et al* [154] investigated the effect of silane coupling on short glass fibre reinforced nylon 6 composites. The poorly coupled fibre composites showed reduction in stiffness accompanied with a brittle failure.

Future studies should, therefore, also focus on the improvement of the surface energy through chemical or plasma treatments of the fibres so that a better bond between fibres and resin can be attained. A broader experimental test matrix which includes higher fractions of fillers should be performed to observe the trend of the composite effective Young's modulus. Different matrices giving a range of E_f/E_m ratios may also be investigated to show the effect of low modulus negative Poisson's ratio fillers.

9.3. High Modulus Auxetic Filler

9.3.1 Materials - α-Cristobalite

α-cristobalite was selected as a high modulus filler exhibiting auxetic behaviour and was supplied by Minerals Marketing Limited. From the material data sheet, the average particle size of the α-cristobalite used was 15 μm. Care was taken when handling α-cristobalite because of associated health risks that include respiratory complications and cancer. A room temperature curing epoxy resin system (Epon E828/D400) and silicone polycarbonate urethane (CarboSil®) viscosity modifier were supplied by AkzoNobel.

9.3.2 Sample Fabrication

Resin mixing was performed at Intertek, Wilton, in an air-controlled reaction chamber. α-cristobalite was added to the resin at mass fractions of 5, 10, 15, 20 and 25 wt.%. The mixture was vigorously stirred for 1 h after which the homogeneous slurry was transferred to AkzoNobel (Wilton) in a rotating sealed compartment and poured into pre-formed aluminium dishes and cured at room temperature. When α-cristobalite was added to the epoxy resin alone, it settled at the bottom of the aluminium dish due to its relatively high density compared to the resin resulting in a distorted plaque, Fig 9.23(a). In order to promote uniform dispersion of the α-cristobalite in the resin, a small amount (approx. 1% wt) of silicone polycarbonate urethane was added to the resin/α-cristobalite mixture. Samples of better quality displaying a flat rectangular plaque due to even distribution of the α-cristobalite particulates were obtained following the addition of CarboSil® (see Fig 9.23(b)).

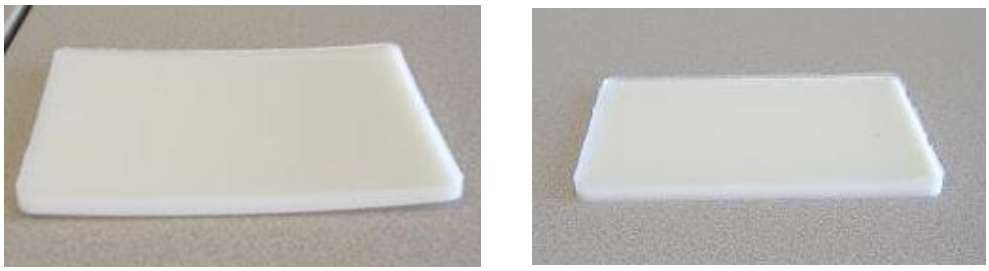

Without CarboSil® (a)

With CarboSil® (b)

Fig. 9.23 Photographic images of α-cristobalite-filled epoxy composites without (a) and with (b) CarboSil® viscosity modifier.

The samples were cut into specimens of dimensions 150 mm length, 15 mm width and 5 mm thickness for tensile testing, Fig 9.24.

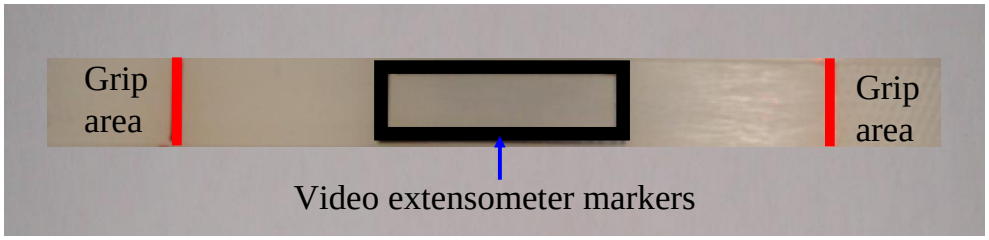

Fig 9.24 Tensile test specimens showing the grip areas and the video-extensometer markers.

9.3.3 Mechanical Tests

The tensile Young's moduli of the α-cristobalite composite specimens were measured using an Instron 3369 universal testing machine. A cross-head speed of 0.3 mm/min and load cell capacity of 50 kN were used. A schematic diagram of the test specimen and loading directions is shown in Fig 9.25.

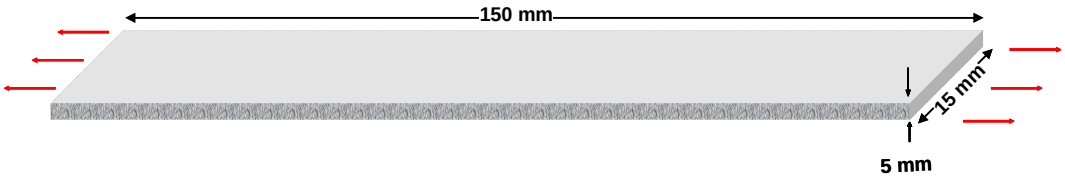

Fig 9.25 Schematic of the test specimen. Red arrows indicate the direction of applied force (i.e. tensile testing).

During tensile testing, a MESSPHYSIK ME 46 video-extensometer was used as described in Chapter 3 in order to determine the Poisson's ratio. Two rectangular sized markers providing targets on the specimen (40 mm × 10 mm and 10 mm x 10 mm) were used to determine the Poisson's ratios. Fig 9.24 shows the 40 x 10 mm markers in black on the specimen providing the targets for the video-extensometer to track the expansion and contraction of the test specimen.

9.3.4 Results and Discussion

9.3.4.1 Poisson's Ratio of α-Cristobalite Composites

Fig 9.26 shows the primary width and length data versus time from which the variation of the true strain in the transverse *Y* direction against the true strain in the longitudinal *X* loading direction of an unfilled epoxy specimen is determined, Fig 9.27.

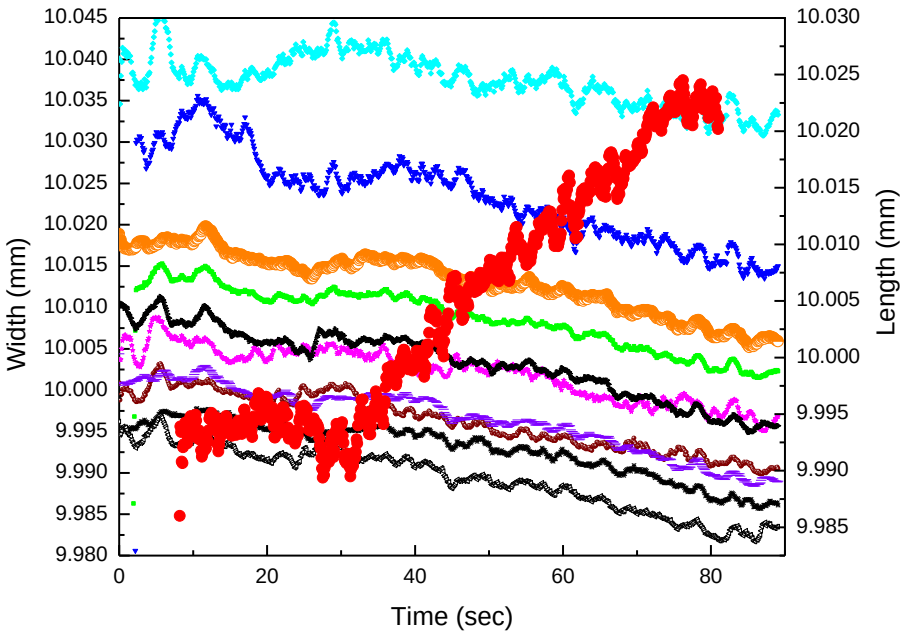

Fig 9.26 Video-extensometry displacement in length (bold red trend) and widths sections (all other traces) as a function of time for the control sample.

The Poisson's ratio, υ_{XY}, was calculated for the composite specimens with and without additives. The formulae for the calculation of true strains along the *X* and *Y*- directions are given in Chapter 3; Eqs (3.1) and (3.2), respectively. The Poisson's ratio calculated from the negative of the gradient of the best fit straight line in Fig 9.27 for this specimen is +0.32.

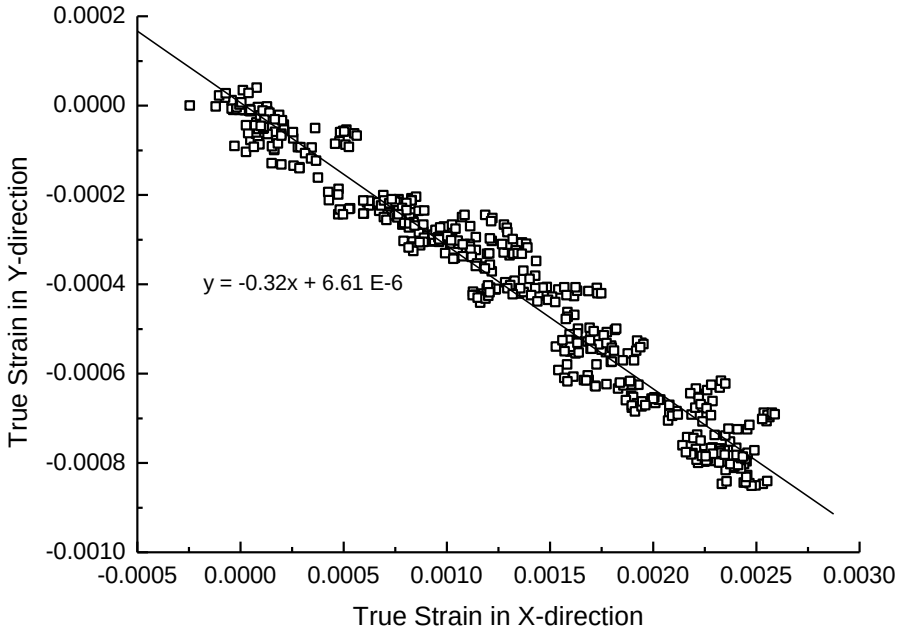

Fig 9.27 Average true strain in the *Y*-direction plotted against the true strain in the *X*-direction for the control (epoxy resin without additives).

In order to show the variation of the true strain in the *Y* -direction versus true strain in the *X*-direction when the composite contains α-cristobalite, data for a specimen containing 25% mass fraction of the additive is shown in Fig 9.28 (primary length and width versus time data) and 9.29 (true strain in *X* and *Y* directions).

The Poisson's ratio calculated for the specimen containing 25% mass fraction of α-cristobalite is +0.19 (Fig 9.29) and is thus lower than that calculated for the control specimen. The addition of auxetic fillers into a conventional resin leads to the reduction in the Poisson's ratio as discussed in Section 8.6.

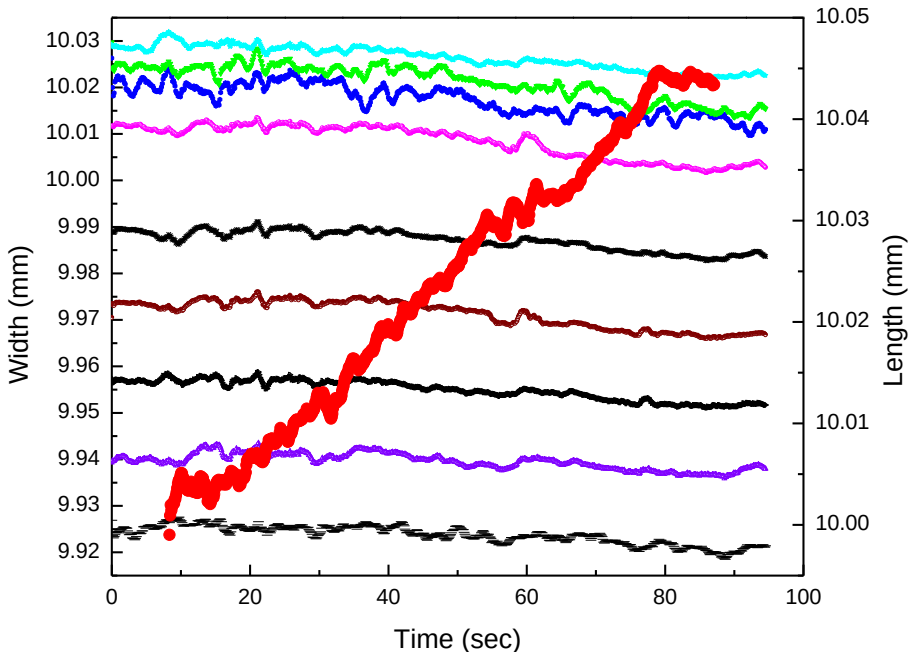

Fig 9.28 Video-extensometry displacement in length (bold red trend) and widths sections (all other traces) as a function of time for the control sample.

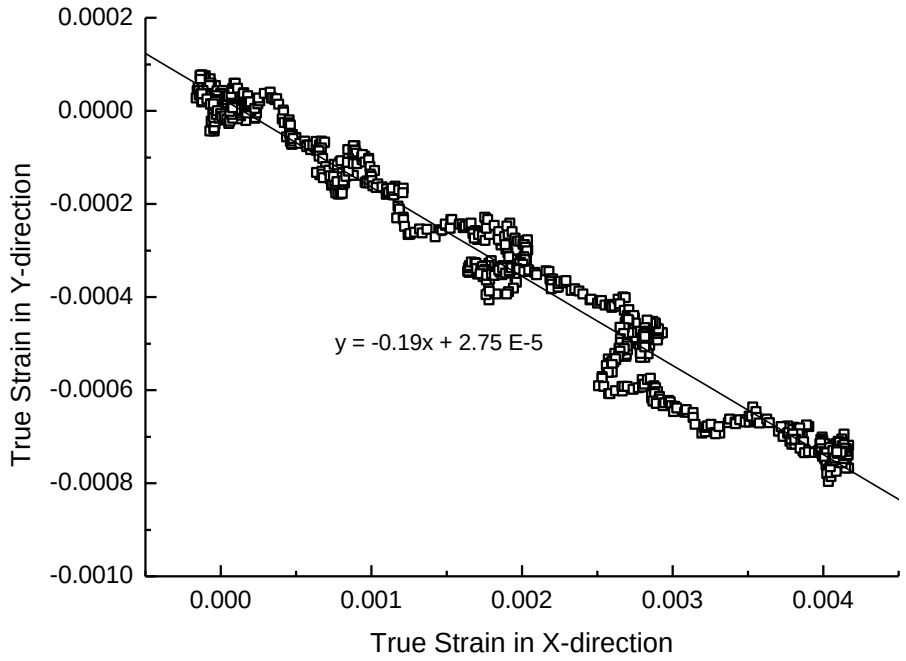

Fig 9.29 Average true strain in the *Y*-direction plotted against the true strain in the *X*-direction for the composite containing 25% mass fraction of α-cristobalite.

An average of six specimens for each percentage weight loading were tested in order to determine the average Poisson's ratio values for the composite sample tested, see Table

9.17. It can be clearly seen that the Poisson's ratios decrease with the increase in the weight fraction of auxetic fillers added to the conventional resin.

Table 9.17 Experimental Poisson's ratios for α-cristobalite-filled epoxy composites

Sample	Specimen Number						Average Poisson's Ratio	Standard Deviation
	1	2	3	4	5	6		
Resin	0.44	0.33	0.24	0.30	0.20	0.41	0.32	0.09
Resin + 5%	0.33	0.16	0.18	0.18	0.33	0.26	0.24	0.08
Resin + 10%	0.22	0.18	0.19	0.24	0.28	0.28	0.23	0.04
Resin + 15%	0.20	0.17	0.17	0.23	0.25	0.30	0.22	0.05
Resin + 20%	0.11	0.24	0.26	0.18	0.21	0.21	0.20	0.05
Resin + 25%	0.10	0.18	0.17	0.19	0.28	0.27	0.20	0.07

Theoretical predictions for the Poisson's ratio were determined using the SCF method discussed earlier in Section 8.6 and the FE model of Section 5.1.1. The Young's modulus used for the resin matrix was 2.75 GPa while that for α-cristobalite was 65.4 GPa. The Poisson's ratios for the resin (measured) and the α-cristobalite (polycrystalline aggregate value[132]) are +0.33 and −0.16, respectively. The mechanical properties of the matrix were provided by the supplier (AkzoNobel, Wilton). It is noted that the experimentally measured matrix Poisson's ratio of 0.32 ± 0.09 (Table 9.17) is in excellent agreement with the supplier value for the resin. The properties of α-cristobalite used in this study were taken from Yeganeh-Haeri et.al [132] and correspond to the polycrystalline aggregate values determined from averaging methods applied to the measured single-crystal properties. The E_f/E_m ratio for these two materials was thus calculated to be 24.

The average measured Poisson's ratios for all samples are plotted against the volume fraction of α-cristobalite together with the SCF predictions for E_f/E_m = 24 and 40 in Fig 9.30. The volume fractions were calculated using Eq. 9.5.

$$\frac{V_{\alpha-cristobalite}}{V_{total}} = \frac{V_{\alpha-cristobalite}}{(V_{\alpha-cristobalite}+V_{matrix})} = \left[\frac{m_{\alpha-cristobalite}}{\rho_{\alpha-cristobalite}}\right] / \left[\left(\frac{m_{\alpha-cristobalite}}{\rho_{\alpha-cristobalite}}\right)+\left(\frac{m_{matrix}}{\rho_{matrix}}\right)\right] \quad (9.5)$$

where $m_{\alpha\text{-}cristobalite}$ is the mass fraction (wt.%) of α-cristobalite, m_{matrix} is the mass fraction of the matrix, $\rho_{\alpha\text{-}cristobalite}$ is the density of α-cristobalite (2.33 g/cm^3) and ρ_{matrix} the density of the matrix (1.16g/cm^3).

The SCF predictions agree very well with the experimental values for α-cristobalite volume fractions up to 0.06. At volume fractions higher than 0.06, the SCF model and the FE analysis over predict the reduction in the Poisson's ratio as auxetic fillers are added to the conventional resin matrix. The experimental data show a reduced rate of decrease in Poisson's ratio at higher volume fractions than the analytical and FE model predictions.

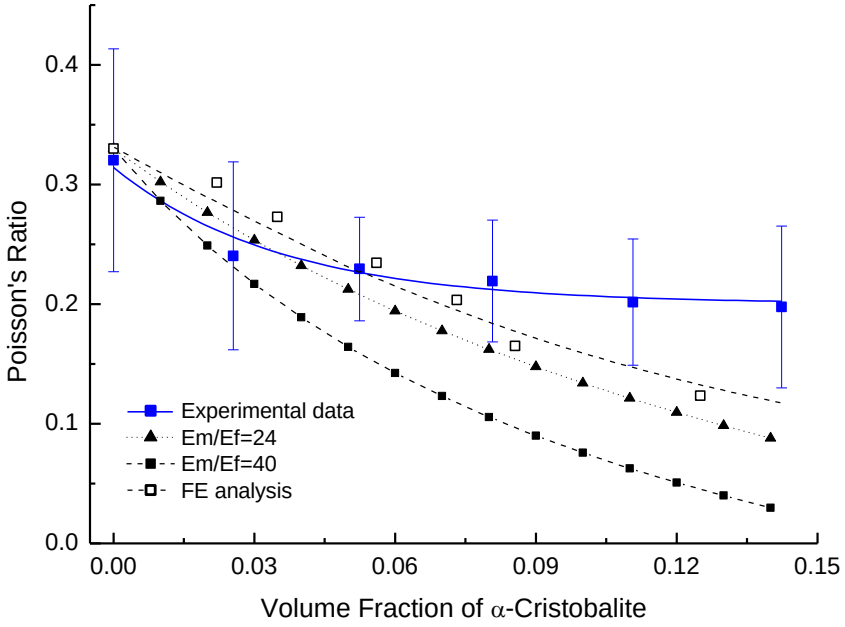

Fig 9.30 Poisson's ratio versus volume fraction of α-cristobalite inclusions for E_f/E_m of 24 (SCF and FE models) and 40 (SCF model) in a conventional resin; [υ_m = +0.33 and υ_f = −0.16]. Experimental values are also presented for comparison.

These results suggest that in practice, there is deviation from the theoretical model predictions. The theoretical models assume perfect bonding between the fillers and the matrix, and even distribution of non-contacting filler particulates. In practice, these assumptions may break down at the higher volume fractions in Fig 9.30, leading to the discrepancies between experimentally-determined values and model predictions

9.3.4.2 Young's modulus results - α-cristobalite composites

The Young's modulus data of the α-cristobalite-filled epoxy samples were obtained from the tensile tests. The Young's moduli trends obtained from experiments were compared to the trends calculated from the Self-Consistent Field theory and the Hashin Shtrikman upper and lower bounds using the same properties for the α-cristobalite and resin as for the above Poisson's ratio comparison. E_f/E_m = 24 was used in the models. A plot of the measured and predicted Young's modulus of the composite relative to that of the matrix (E_c/E_m) versus the volume fraction of the filler is shown in Fig 9.31.

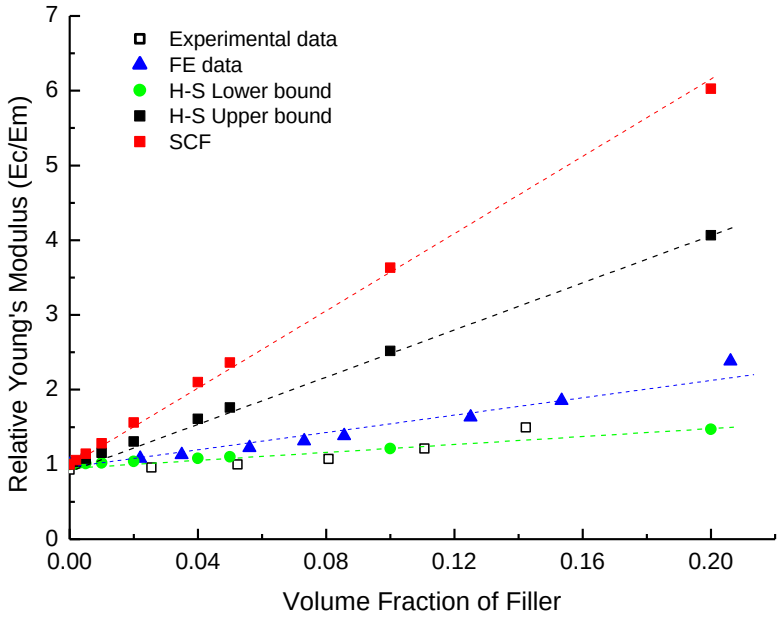

Fig 9.31 Comparison of the experimental relative Young's modulus of the α-cristobalite-filled epoxy composites with the theoretical (H-S Upper and Lower bounds and SCF model) and FEA predictions.

The addition of α-cristobalite into an epoxy-based resin matrix led to an increase in the Young's modulus of the composite. The experimental results are in good agreement with the Hashin Shtrikman lower bound and the FE analysis predictions. The Self-Consistent Field theory and the Hashin Shtrikman upper bound over predict the Young's modulus of the composites.

The theoretical analyses for predicting the Young's modulus of a particulate-filled composite indicate that the elastic modulus is dependent on the volume fraction of the filler. The theories used in this study do not take into account other factors such as particle size, shape, and imperfect adhesion between matrix and particles which may be responsible for the difference between experimental and theoretical results. Thus, theoretical models are expected to over predict the mechanical properties of composites. Spanoudakis and Young [155] investigated the effect of particle size on the modulus of particulate filled composites. Glass particles of sizes 4.5, 16, 32, 47 and 62 μm were used to fabricate particulate-filled epoxy composites. Their work revealed that there was a decrease in the Young's modulus of composites for a given volume fraction with an increase in particle size. The composites containing the smallest particle size tend to have higher Young's modulus values. This could be explained by the increased surface area as the particles become smaller hence providing a more effective interfacial bond. Coupling agents can be used to improve the matrix-particle interfacial bond. Further work by Spanoudakis and Young [156] used glass beads of sizes 4.5 and 62 μm with either improved or decreased adhesion properties. The adhesion of the particles was improved by using a silane adhesion promoter whilst the weak adhesion was achieved by mixing the particles with a release agent prior to adding them to the epoxy. Composites fabricated from particles which were treated by a silane coupling agent showed a higher Young's modulus for all volume fractions and particle sizes compared to those which were mixed with a release agent.

Studies done by Ahmad *et al* [157] showed that the Young's moduli of the composite depended on the shape of the particulate filler. In their work, they modified silica fillers to have three different shapes which are angular, cubical and elongated. The high aspect ratio elongated shaped fillers had the highest composite Young's modulus for any given volume fraction compared to the cubical and the angular shaped fillers. This is confirmed by the work done by Chow and co-workers [158, 159] who also concluded that the use of particles with high aspect ratios results in higher Young's moduli of the composite for a given volume fraction compared to particles with lower aspect ratios. Preliminary work on the effect of aspect ratios on the filled composite system (not shown in this thesis) also showed that the Young's modulus of the composite increased with an increase in the aspect ratio of fillers [160]. The packing of particles influences the load bearing capacity of the composite and also depends on the particle sizes and shapes. Mixtures of different particle sizes can pack more densely compared to mono-dispersed particles.

9.4 Summary – Particulate Filled Composites

In previous Chapters (Chapters 6,7,8) both FE and analytical models predicted improvements in the Young's modulus when low modulus auxetic fillers were added to a high modulus conventional matrix. Conventional fillers showed improvements when the Young modulus of the filler was higher than that of the matrix. It was shown that the Poisson's ratio of the matrix could be modified by the addition of auxetic fillers. Two possible auxetic fillers were identified; i.e. chopped auxetic PP fibres (low modulus filler) and α-cristobalite (high modulus filler). Filled epoxy samples were fabricated and the Poisson's ratios and Young's modulus of these composites were determined.

9.4.1 Chopped Auxetic Fibre Filled Composites

Low modulus auxetic and conventional fillers in the form of chopped extruded PP fibres were used to fabricate composites which were tested for tensile properties. The mechanical properties of the filled composites were compared to the cast resin (control). The SCF theory was used to predict the effective Young's modulus of the auxetic and conventional filled composites. Experimental results were compared to the SCF trends. In the SCF predictions, conventional fibre-filled composites showed little sensitivity to the variation of Poisson's ratio, with the effective Young's modulus of the composite decreasing with conventional fibre content. On the other hand, the auxetic fibre-filled composites were predicted to show a Poisson's ratio-dependent decrease in the composite effective Young's modulus for fibre Poisson's ratios > -0.8 and an increase in effective Young's modulus for fibre Poisson's ratio ≤ -0.9. Experimental results showed that both the conventional and auxetic fibre-filled composites showed a decrease in the effective Young's modulus with an increase in the volume fraction of the chopped fibres, consistent with the SCF trends for the fibre properties employed. The experimental results are in reasonable agreement with the SCF trends but the level of experimental accuracy, whilst generally acceptable, was not sufficient to conclusively confirm the enhancement in effective Young's modulus predicted by theory for auxetic fibre-filled systems relative to their conventional fibre counterparts.

9.4.2 α-Cristobalite Filled Composites

The experimental Poisson's ratio data compare well with the theoretical (SCF) and FE data. A reduction in Poisson's ratio (from 0.33 to 0.20) is observed when α-cristobalite is added to the matrix up to 0.14 filler volume fraction. The Young's modulus data showed the expected upward trend with an increase in the volume fraction of α-cristobalite. The Young's modulus data of the filled epoxy were found to be within the Hashin-Shtrikman

bounds. The Self-Consistent Field theory and the H-S upper bounds overestimated the Young's modulus data, which may be attributed to practical factors such as particle-matrix interactions, particle shape and size distribution. The H-S lower bound is close to the experimental Young's modulus data. The theoretical estimates (SCF, H-S theories) offer a reasonable estimate of the particulate-filled epoxy composites. Further work should focus on compatibility studies of filler and matrix in order to optimise the interfacial interactions in the samples.

CHAPTER 10: CONCLUSIONS AND SCOPE FOR FUTURE WORK

10.0 Conclusions

Conclusions drawn from the experimental, numerical and analytical studies carried out in this doctoral program are discussed in this chapter together with recommendations for possible improvements in further studies.

10.1 Polypropylene Film Extrusion: Parametric Studies

1. In Chapter 3, it was shown that the processing parameters of extrusion temperature, screw-speed and take-up speed are critical in the formation of PP films with conventional or auxetic properties. From the observations made in this thesis as well as previous studies [57, 60, 61], it appears that extrusion temperature is the most important parameter as observed by the tight processing window for auxetic PP films when extrusion is performed in the vicinity of the melting temperature of the polymer.

2. Polypropylene films produced at a temperature of 159 °C, a screw-speed of 1.05 $rads^{-1}$ and a take-up speed of 0.0225 ms^{-1} exhibited auxetic behaviour for every section tested along the extrusion direction; i.e. 100% auxetic properties were observed. While maintaining the same screw-speed and take-up speed but at a slightly lower temperature than the on-set melting temperature (at 157 °C extrusion temperature), 10 % of the films exhibited auxetic behaviour. Similarly, 75% of the films produced at a slightly higher temperature of 161 °C were conventional, confirming the tight temperature window for auxetic behaviour previously

established for the extrusion temperature in the vicinity of the melt on-set temperature of the polymer. As the temperature was increased (to 170-180 °C) the films produced showed 100% conventional behaviour. The occurrence of auxetic behaviour at low temperatures (159-161 °C) has previously [45, 67, 70] been suggested to be due to the fact that PP particles during processing are partially molten and form a fused particle micro-structure in the final product. Translation of fused particles in response to mechanical loading has been proposed to lead to auxetic behaviour.

3. Of the films produced at a screw-speed of 1.05 $rads^{-1}$ and a take-up speed of 0.0225 ms^{-1}, the ones produced at an extrusion temperature of 157 °C displayed the largest magnitude of negative and positive Poisson's ratios. This is consistent with previous research work on other auxetic systems [45, 141, 142] which shows that small changes in micro-structure can result in dramatic changes in Poisson's ratio, including flipping from very large negative to very large positive Poisson's ratios. The magnitude of the Poisson's ratios generally decreases as extrusion temperature increases in the range 157 to 165 °C, until a value in the vicinity of textbook values for polypropylene is reached for extrusion temperatures above 165 °C.

4. The effect of varying extrusion-screw speed was investigated at a constant extrusion temperature of 159 °C and take-up speed of 0.0225 ms^{-1}. Films produced at the lowest screw speed used (0.525 $rads^{-1}$) were conventional, and as the screw speed was increased, the films became completely auxetic (at 1.05 $rads^{-1}$). As the screw speed was further increased (above 1.05 $rads^{-1}$), the percent auxeticity within the films was reduced. The highest screw speed of 2.1 $rads^{-1}$ showed 40% auxetic behaviour in the films. Screw speed affects the residence time and induces

frictional heating of the polymer in the screw barrel. According to the translating fused particle microstructure model, auxetic behaviour will be observed in the final films when the residence time (determined by the screw speed) and the temperature in the polymer (due to the combined effects of the set extrusion temperature and frictional heating) produce surface melting of the particles during processing. Conventional films produced at the lowest screw speeds are then consistent with an increased residence time leading to full melting rather than partial melting of the particles. In which case the fused particle microstructure required for auxetic behaviour will not be produced in the final films. Conversely, the decrease in auxetic response at the highest screw speeds is consistent with an increase in frictional heating to once again lead to increased particle melting and a decrease in the required fused particle microstructure in the produced films. A detailed in situ study of the processing-microstructure relationships in PP films is now required to confirm or otherwise the suggested microstructural changes to explain the screw speed dependency of the auxetic property.

5. The effect of take-up speed was investigated by varying the take-up speed from from 0.0225 to 0.1500 ms^{-1} whilst keeping a constant extrusion temperature and screw-speed at 159 °C and 1.05 rad s^{-1}. Films with 100 % auxetic behaviour were observed at 0.0225 and 0.1500 ms^{-1} whilst at least 50% auxetic behaviour was observed for take-up speeds in between 0.0225 and 0.1500 ms^{-1}. The take-up speed gives a slight draw to the films whilst maintaining the micro-structure of the films.

6. The intrinsic variability, across the thickness of the film, of the fused-particle micro-structure leads to variation in the Poisson's ratio values of the film. Given the relationship between E and υ (e.g. from the isotropic expression $E \alpha (1+\upsilon)$), some variations in the Young's modulus values along the length of the films also

exists.

7. The possibility of producing auxetic PP films at higher processing temperatures than those established in the literature (159-161 °C) was investigated for the first time. It was found that auxetic PP films could be formed at a processing temperature of 180 °C when high screw-speeds (2.10 $rads^{-1}$) were used, and at the slightly higher temperature of 190 °C when using a lower screw speed of 1.05 $rads^{-1}$ (i.e. increased extrusion temperature/residence time and reduced frictional heating). The production of auxetic materials at higher temperatures, i.e. significantly above the melt temperature of the polymer, may have beneficial consequences for the viability of producing auxetic films on a commercial basis.

8. At the higher extrusion temperatures (180-190 °C), consideration of the melting of a spherical particle has been used in this work to show that the PP particles would have completely melted and a different micro-structure and mechanism must, therefore, be responsible for the occurrence of auxetic behaviour in the films. The determination of such micro-structure, and the deformation mechanisms involved, for the films produced at the higher extrusion temperature were beyond the scope of this study and will form the basis of future investigations.

10.2 The Effect of Auxetic Inclusions on the Through-Thickness Young's Modulus and Shear Modulus of Laminate Interfaces

When two materials having different Poisson's ratios are joined together in a layered arrangement, the transverse (in-plane) deformation of one material is constrained by the other (and vice versa) when a uni-axial stress is applied through the thickness of the multi-

layer system. The transverse constraints imposed by adjacent layers having different Poisson's ratios leads to an increase in the effective Young's modulus of the multi-layer system over that which would arise purely on a simple (unmodified) Rule of Mixtures (RM) basis. The increase in effective Young's modulus of the multi-layer system is most dramatically enhanced when one layer has a large negative Poisson's ratio and the adjacent layer has a positive Poisson's ratio. The Poisson's ratio mis-match between adjacent layers is responsible for the improvements in the Young's modulus of the multi-layer film adhesive/interfaces discussed in Chapter 6, and summarised below.

1. Increases in the through-thickness Young's modulus were observed for multi-layer film/adhesive interfaces even when the auxetic film had a lower Young's modulus (E_{film} = 340 MPa) than the adhesive (E_{adh} = 1700 MPa). Multi-layer interfaces with the highest number of auxetic layers showed the largest increase in the through-thickness Young's modulus.

2. Two different model types of the multi-layer film/adhesive interfaces (CIT and CCLT) were modelled. FE predictions showed that the through-thickness effective Young's modulus of the multi-layer system is dependent on the constituent Young's moduli values, Poisson's ratios and stacking sequence.

3. The RM expression was further modified in this work so that a 3-phase interface prediction could be made. Since the magnitude of the Young's moduli of the films and adhesive used in this study are closer together than those of the fibre and matrix in fibre-reinforced composites for which the RM is typically employed, a correction term was applied to the auxetic, conventional and adhesive layers, and the overall response calculated on a weighted basis. FE models were validated

against the Ramirez approach and the modified RM. Generally, good agreement between the FE and analytical models (Reuss bound configuration) was observed in all models. The FE analysis takes into account the geometry of the interfaces and influence of edge effects whereas the Rule of Mixtures and Ramirez approaches do not, and this is believed to be the main reason for discrepancies that exist, i.e. for the models where thin adhesive layers are employed.

4. For interfaces containing conventional films, the Rule of Mixtures-Voigt bound is higher than the transverse (Reuss) bound. However, for multi-layer film/adhesive interfaces containing auxetic films the modified transverse Rule of Mixtures (Reuss configuration) bound actually exceeds the Voigt bound.

Auxetic materials possess higher shear modulus than conventional materials when the two types of materials have the same Young's modulus according to Eq. (2.1). A negative Poisson's ratio reduces the magnitude of the denominator in Eq. (2.1) leading to an increase in the shear modulus. When multi-layer film/adhesive interfaces were modelled in the shear mode, Chapter 7, the following conclusions were made:

5. The addition of auxetic films (Poisson's ratio of -0.9 and Young's modulus of 340 MPa) to a multi-layer film/adhesive interface utilising a high modulus (1700 MPa) adhesive (Poisson's ratio of +0.3) increased the shear modulus of the interface by up to 85% for the CIT model. The addition of conventional films (Poisson's ratio of +0.43) with the same Young's modulus as auxetic films, led to reductions in the shear modulus of the interface. The 3-phase Rule of Mixtures predictions for shear modulus were in excellent agreement with the FE results since the transverse constraining effects under through-thickness loading of adjacent layers having mis-

matched Poisson's ratios are not present when loaded in shear. The shear response of the multi-layer system is simply a summation of the shear response of each layer.

10.3 Auxetic Particulate Filled Composites (FE Models)

FE predictions of the effect of auxetic particulate inclusions into a conventional matrix were performed (Chapter 8). The FE predictions were compared to predictions from the Self-Consistent Field (SCF) theory, the Hashin-Shtrikman (H-S) bounds and the Upper and Lower bounds. A parametric study using the SCF theory was performed for E_f/E_m (modular ratio of filler to matrix) ratios varying from 0.1-20 and Poisson's ratios varying from -0.9 to +0.45.

1. Modelling of the auxetic particulate filled polymeric matrix showed increases in Young's modulus of the composite system even when the auxetic fillers were of lower Young's modulus (340 MPa) than the matrix (1700 MPa) for low Poisson's ratio(-0.9). When the auxetic particles were replaced by conventional particles of the same Young's modulus, decreases in the Young's modulus were observed for the low modulus fillers. FE analysis results were found to be in good agreement with the Self-Consistent Field (SCF) and the Hashin Shtrikman (H-S) upper bound theories.

2. The addition of auxetic fillers to an auxetic matrix gave the same trends in the effective Young's modulus as those predicted when conventional fillers were added to a conventional matrix. High increases in effective Young's modulus were predicted when fillers and matrices had opposite signs of Poisson's ratio. Increased mis-match in the Poisson's ratios of the filler and matrix constituents leads to

increased constraint between the constituents, giving rise to an increase in effective Young's modulus.

3. Predictions from the Self-Consistent Field theory showed that the Poisson's ratio of a conventional matrix's can be reduced in a composite containing auxetic fillers. The reduction in the effective Poisson's ratio is enhanced by a high filler to matrix Young's modulus ratio (E_f/E_m ratio), and by a larger mis-match in the Poisson's ratios of the filler and matrix. Consequently, a naturally-occurring high modulus negative Poisson's ratio material, α-cristobalite, was then chosen as an additive in the production of particulate filled epoxy composites for experimental validation of the theoretical data. A readily available low modulus auxetic filler – chopped fibres - was also chosen in order to experimentally investigate the effect of a low modulus negative Poisson's ratio filler within a high modulus conventional matrix.

10.4 Experimental Validation-Flexural Stiffness of Layered Adhesive Interfaces and Particulate Filled Composites

In Chapter 9, multi-layer film/adhesive laminates were fabricated using a polyutherane-based adhesive. The multi-layer film/adhesive beams were tested in three and four-point bending modes. Three point flexure test simulations were carried out using FE analysis and the results were validated against experimental data. Experimental filled-systems (chopped PP fibre filled composites and α-cristobalite particulate filled composites) were also fabricated and their mechanical properties determined for comparison with the model predictions.

1. The flexural modulus of the laminate materials, as determined via experiments and FE analysis, increased with the increase in the volume fraction of auxetic material. Similar trends were observed from Chapters 6 and 7 for the through-thickness Young's and shear modulus, respectively. However, the increases in the flexural modulus as determined from experiments were lower than those predicted by FE analysis. Imperfections in the structural integrity of the fabricated laminates as well as the non-uniform film properties could explain why the numerical methods over predict the changes in material properties. Nevertheless, the study showed that there is an advantage in using auxetic materials to achieve increased flexural stiffness of the multi-layer interface.

2. The fabricating of an epoxy matrix filled with auxetic particulates was carried out using chopped fibres and α-cristobalite fillers. Tensile tests were carried out on the particulate-filled epoxy composites. The experimental data showed a decrease in effective Young's modulus of the chopped fibre filled composites (both conventional and auxetic) as the mass fraction of the filler was increased. The effective Young's modulus of the composite was found to be very sensitive to slight variations in Poisson's ratio when the fibre Poisson's ratio is in the vicinity of -0.8 to -0.9. The trends shown by the auxetic chopped fibres were generally consistent with the decrease predicted by the SCF predictions for fibre Poisson's ratios of $\nu \geq -0.8$. However, the level of experimental accuracy was insufficient to enable a conclusive experimental verification of the predicted enhancement in effective Young's modulus for auxetic fibre-containing samples compared to their conventional fibre-containing counterparts.

3. The α-cristobalite composites showed a reduction in the Poisson's ratio as the volume fraction of α-cristobalite was increased. The Poisson's ratio of the matrix

was reduced from 0.33 when no fillers were added to 0.20 when the filler content was 15% by volume. The trend in the Poisson's ratio reduction of the α-cristobalite filled epoxy was found to be consistent with the SCF and FE Poisson's ratio predictions.

4. Experimental data showed an increase in the Young's modulus of the composites with volume fraction of the α-cristobalite fillers. The relative modulus (E_c/E_m) of the α-cristobalite composites was compared to H-S and SCF theories. The experimental Young's modulus data lie in close proximity with the lower bounds. The theoretical approaches overlook some practical factors such as particle-matrix interaction, particle distribution, particle size and shape. However, the theoretical predictions serve as a useful tool in the predictions of mechanical properties of the particulate-filled composites in order to avoid large experimental test matrices.

10.5 Scope for Future Work

Further studies recommended following the experimental and theoretical investigations performed in this study are discussed in this section.

1. It is recommended that a mechanistic explanation of the occurrences of auxetic behaviour in PP films produced at extrusion temperatures in the range 180-190 °C be established. Microscopic analysis may be used to obtain the microstructure of the materials in order to develop an understanding of the structure responsible for the auxetic behaviour. It is possible this will require determination of the microstructure at lower length scale than reported in the literature for the films produced at extrusion temperatures in the vicinity of the melting temperature, since

the films at the higher temperature are likely to have been produced from fully molten polymer.

2. The non-uniformity of the films produced to date could be improved by using better control systems for extrusion parameters such as adaptive and multivariable control [161]. The adaptive and multi variable control is computer controlled with the ability to simultaneously regulate extrusion parameters such as temperature inside the barrel, screw speed and take-up speed, in order to maintain constant extrusion parameters, hence controlling the behaviour of the extrudate. In addition to improving control at extrusion temperatures around 159 °C, more work should focus on processing the polymer at the higher temperatures (180-190 °C), established here for the first time, and high screw speeds in order to study closely the occurrence of auxetic behaviour under these conditions.

3. An exploration of the extrusion of fibres at higher extrusion temperatures of 180-190 °C is of interest. The production process used to produce the PP films studied in this work was initially developed from the fibre extrusion process. The non-uniformity of the fibre properties is more pronounced than in films since fibre diameter is approximately 200 μm [45]. The particle size distribution of the starting polymer is between 50 to 300 μm with irregular shape and rough surfaces [45]. This means that a fibre can have up to four particles across the diameter. The non-uniform packing of the particles across the small fibre diameter results in high levels of inhomogeneous properties. The possibility of extruding auxetic fibres at high temperatures such as 180-190 °C may improve the uniformity of the fibres since the inhomogeneity introduced through particle size is removed for fibres produced from fully-molten polymer.

4. Microscopic studies of the interface region between the PP films and polyurethane adhesive should be performed in order to provide an indication of the degree of adhesion within the multi-layer film/adhesive interfaces.

5. Morphological studies including the fracture pattern of the particulate filled composites can also be performed to give an indication of the adhesion properties between the matrix and fillers. Compatibility studies for the particle and matrix may be required to improve the adhesion properties of the filler and matrix. This could improve the mechanical properties of the chopped fibre composites and the α-cristobalite filled composites towards the values predicted by the FE and theoretical models.

6. Fabrication of particulate filled composites with higher volume fractions of fillers as well as lower Poisson's ratios in order to observe the trend at high volume fractions is desirable. This could include the possibility of observing a conventional to auxetic transition of the filled system. In this latter respect the use of a lower Poisson's ratio unfilled matrix may also be explored.

7. A study of other alternative fillers apart from α-cristobalite and suitable resin systems can be explored. Particulates which have recently been shown to possess a negative Poisson's ratio include Nacre [162, 163] and Talc [164].

8. Studies of other property enhancement of the auxetic particulate filler other than those studied in this work (Young's modulus, Poisson's ratio, shear modulus) can be explored. These properties can include fracture toughness, tear resistance, impact tests, crack propagation, energy absorption and strain-stress fields of the particulate filled composites.

REFERENCES

1. Love A.E.H., A treatise on the mathematical theory of elasticity, 2nd Edition, Cambridge University Press, 1906.
2. Lakes, R., Foam structures with a negative Poisson's ratio., *J. Sci*., **235**, 1987, 1038-1040.
3. Gibson, L.J.; Ashby, M.F., Cellular solids: structure and properties, Pergamon Press, 1988.
4. Gibson, L.J.; Ashby, M.F.; Schajer, G.S.; Robertson, C.I., The mechanics of two dimensional cellular solids., *Proc. R. Soc. Lond*., **A382**, 1982, 25-42.
5. Wang, Y.C; Lakes, R; Butenhoff, A., Influence of cell size on re-entrant transformation of negative Poisson's ratio reticulated polyurethane foams., *Cellular Polym.*, **20**, (6), 2001, 373-385.
6. Lakes, R., Deformations in extreme matter., *The Amer. Asso. Adv. of Sci.*, **288**, (5473), 2000, 1976 -1977.
7. Alderson, A.; Evans, K.E., Rotation and dilation deformation mechanisms for auxetic behaviour in the α-cristobalite tetrahedral framework structure., *Phys. Chem. Minerals.*, **28**, (10), 2001, 711-718.
8. Williams, J.L.; Lewi, J.L., Properties and an anisotropic model of cancellous bone from the proximal tibial epiphysis., *Trans. ASME, J. Biomech. Eng.*, **104**, 1982, 50-56.
9. Lakes, R., Advances in negative Poisson's ratio materials., *J. Adv. Mat*., **5**, 1993, 293-296.
10. Choi, J.B., Lakes, R.S.; Fracture toughness of re-entrant foam materials with a negative Poisson's ratio: Experiment and analysis., *Int. J. Fracture*, 80, 1996,73-83.
11. Donescu, S.; Chiroiu, V.; Munteanu, L., On the Young's modulus of a auxetic

composite structure, *Mechanics Research Communications*, **36**, 2009, 294–301.

12. Kocer, C.; Mckenzie, D.R.; Bilek M.M.; Elastic properties of a material composed of alternating layers of negative and positive Poisson's ratio., *Mater. Sci. Eng. A.*, **505**,(1-2), 2009, 111-115.
13. Lim, T.C.; Rajendra Acharya U.; Counterintuitive modulus from semi-auxetic laminates, Phys Status Solidi B, **248**, 1, 2011, 60-65.
14. Evans, K. E., Auxetic polymers: a new range of materials, *Endeavour*., **15**, (4) 1991,170-174.
15. Evans, K.E; Nkansah, M.A; Hitchinson, I.J; Rogers, S.C., Molecular network design., *Nature*, **353**, 1991, 124-125.
16. Grima, J.N.; Gatt, R.; Alderson, A.; Evans, K.E., Negative Poisson's ratios in cellular foam materials., *Mat. Sci. Eng A.*, **423**, (1-2), 2006, 214-218.
17. Evans, K.E.; Nkansah, M.A.; Hutchinson, I.J., Modelling negative Poisson ratio effects in network-embedded composites., *Acta Metallurgica et Materialia*., **40,** (9), 1992, 2463-2469.
18. Alderson, K.L.; Simkins, V.R.; Coenen, V.L.; Davies, P.J.; Alderson, A.; Evans, K.E., How to make auxetic fibre reinforced composites., *Phys. Stat. Sol*, **242**, (3), 2005, 509-518.
19. Evans, K.E.; Nkansah, M.A.; Hutchinson, I.J., Auxetic foams: modelling negative Poisson's ratios., *Acta Metallurgica et Materialia*., **42**, (4), 1992, 1289-294.
20. Chen, C.P.; Lakes, R.S., Holographic study of conventional and negative Poisson's ratio metallic foams: elasticity, yield and micro-deformation., *J. Mater. Sci.*, **26**, 1991, 5397-5402.
21. Chen, C.P.; Lakes, R.S., Holographic study of non-affine deformation in copper foam with a negative Poisson's ratio -0.8., *Scripta. Metall et Mater.*, **29**, 1993, 395-

99.

22. Evans, K.E., Auxetic polymers., *Memb. Tech.*, **2001**, *(*137), 2001, 9.
23. Choi, J.B.; Lakes, R.S., Non-linear properties of polymer cellular materials with negative Poisson's ratio., *J. Mater. Sci.*, **27**, 1992, 4678-4684.
24. Pickles, A.P; Webber, R.S; Alderson, K.L.; Neale, P.J.; Evans, K.E., The effect of the processing parameters on the fabrication of auxetic polyethylene, Part 1: The effect of compaction conditions., *J. Mater. Sci.*, **30**, (16), 1995, 4059-4068.
25. Alderson, K.L.; Kettle, A.P.; Neale, P.J.; Pickles, A.P; Evans, K.E., The effect of the processing parameters on the fabrication of auxetic polyethylene, Part 2: The effect of sintering time and temperature., *J. Mater. Sci.*, **30**, (16), 1995, 4069-4075.
26. Alderson, A.; Rasburn, J.; Evans, K.E.; Grima, J.N., Auxetic polymeric filters display enhanced de-fouling and pressure compensation properties., *Memb. Tech.*, **2001**,*(*137**)**, 2001, 6-8.
27. Alderson, A; Alderson, K., Expanding materials and applications: exploiting auxetic textiles., *Text. Inter. Newsletters Ltd*, **29**, 2005.
28. Di Renzo, F.; Fajula, F., Introduction to molecular sieves: Trends of evolution of the zeolite community., *Studies in Surface Sci. Cat*., **157**, 2005, 1-12.
29. Grima, J.N., Jackson, R., Alderson, A., Evans K.E.; Do zeolites have a negative Poisson's ratio., *Adv. Mat.*, **12**, 24, 2000,1912-1918.
30. Grima, J.N.; Evans, K.E., Auxetic behaviour from rotating squares., *J. Mater. Sci. Lett*., **19,** 2000, 1563-1565.
31. Grima, J.N., Alderson, A., Evans K.E., Auxetic behaviour from rotating rigid units., *Phys. Stat. Sol. (b)*, **242**, 3, 2005, 561-575.
32. Wood, M.; Grima, J.N.; Evans, K.E.; Alderson, A., Molecular modelling of auxetic zeolites., *Xjenza*, **9**, 2004, 3-4.

33. Alderson, A.; Davies, P.J.; Evans, K.E.; Alderson, K.L.; Grima, J.N., Modelling of the mechanical and mass transport properties of auxetic molecular sieves: an idealised inorganic (zeolite) host-guest system., *Molecular Simulation.*, **31**, (13), 2005, 889-896.

34. Evans, K.E.; Alderson, K.L., Auxetic materials-The positive side of being negative., *Eng. Sci. and Educ. J.*, **9**, (4), 2000,148-154.

35. Choi, J.B.; Lakes, R.S., Design of a fastener based on negative Poisson's ratio foam., *Cellular Poly.*, **10**, 1991, 205-212.

36. Baughman, R.H.; Shacklette, J.M.; Zakhidov, A.A.; Strafstrom, S., Negative Poisson's ratios as a common feature of cubic metals., *Nature*, **392**, 1998, 362-365.

37. Lakes, R.S.; Design considerations for negative Poisson's ratio materials., *ASME, J. Mech. Design*., **115**, 1993, 696-700.

38. Scarpa, F.; Giacomin, J.; Zhang, Y.; Pastorino, P.; Mechanical performance of auxetic polyurethane foam for antivibration glove applications., *Cellular Polymers*, **24**, 5, 2005, 253-268.

39. Martz, E.O.; Lee, T.; Lakes, R.S.; Goel, V.K.; Park, J.B., Re-entrant transformation methods in closed cell foams., *Cellular Poly.*,**15**, (4), 1996, 229-249.

40. Friis, E.A.; Lakes, R.S.; Park, J.B., Negative Poisson's ratio polymeric and metallic materials., *J. Mater. Sci.*, **23**, 1998, 4406-4414.

41. Chan, N.; Evans, K.E., Indentation resilience of conventional and auxetic foams., *J. Cell. Plast.*, **34**, *1998*, 231-260.

42. Lakes, R.S.; Elms, K.J., Indentability of conventional and negative Poisson's ratio foams., *J. Comp. Mat*., **27**, 1993, 1193-1202.

43. Alderson, K.L.; Fitzgerald, A.F.; Evans, K.E., The strain depended indentation resilience of auxetic micro-porous polyethylene., *J. Mat. Sci.*, **35**, 2000, 4039-4047.

44. Alderson, A., A triumph of lateral thought., *Chem. and Ind.*, **1999**, 384-391.

45. Ravirala, N., PhD Thesis, Fabrication, characterisation and modelling of an expanded range of auxetic polymeric fibres and films., 2005.

46. Burke, M.; A stretch of imagination., *New Scientist.*, 154,(2085), 1997, 36-39.

47. Ravirala, N; Alderson, A; Alderson, K.L; Davies, P.J., Expanding the range of auxetic polymeric products using a novel melt-spinning route., *Physica Status Solidi (b)*, **242**, (3), 2005, 653-664.

48. Scarpa, F., Auxetic materials for bioprostheses., *Signal Processing Magazine, IEEE*., **25**, 2008, 126-128.

49. Lowe, A.; Lakes, R.S., Negative Poisson's ratio foam as seat cushion material., *Cellular Poly.*, **19**, (3) 2000, 157-167.

50. Wang, Y.C.; Lakes, R., Analytical parametric analysis of the contact problem of human buttocks and negative Poisson's ratio foam cushions**.,** *Inter. J. Solids and Struc.*, **39**, 2002, 4825-4838.

51. Theocaris, P.S.; Stavroulakis, G.E.; Panagiotopoulos, P.D., A numerical homogenization approach., *Arch. Appl. Mech*., **67**, 1997, 274-286.

52. Larsen, U.D.; Sigmund, O.; Bouwstra, S., Design and fabrication of compliant micro-mechanisms and structures with negative Poisson's ratio., *J. Microelectromech. Syst*., **6**, (1), 1997, 99-106.

53. Prall, D; Lakes, R.S., Properties of a chiral honeycomb with a Poisson's ratio of -1., *Int. J. of Mech. Sci.*, **39**, (3), 1997, 305-314.

54. Spadoni, A.; Ruzzene, M.; Scarpa, F., Global and local linear buckling behaviour of a chiral cellular structure., *Phys. Stat. Solidi B.*, **242**, (3), 2005, 695-709.

55. Paulhac, A.; Perrot, D.; Scarpa, F.; Yates, J.R., Flat-wise compressive behaviour of novel chiral honeycomb concept., DFC-7 Conference, Sheffield, 22-24 May, 2003.

56. Paulhac, A.; Scarpa, F.; Perrot, D.; Yates, J.R., Transverse shear strength of chiral cellular core., Conference Proceedings, ICEM12, Bari, Italy, 29 Aug-2 Sept, 2004.

57. Chan, N.; Evans, K.E., Fabrication methods for auxetic foams., *.J. Mater. Sci.,* **32**, 1997, 5725-5736.

58. Caddock, B. D.; Evans, K. E., Micro-porous materials with negative Poisson's ratios. I. Microstructure and mechanical properties., *J. Phys. D: Appl. Phys.,* **22**, 1989, 1877-1882.

59. Evans, K.E.; Caddock, B.D., Microporous materials with negative Poisson's ratios. II. Mechanisms and interpretation., *J. Phys. D: Appl.Phys*., **22**, 1989, 1883-1887.

60. Evans, K.E; Alderson, K.L., The static and dynamic moduli of auxetic micro-porous polyethylene., *J. Mater. Sci. Lett*., **11**, (24), 1992, 1721-1724.

61. Neale, P.J.; Pickles, A.P.; Alderson, K.L.; Evans, K.E., The effect of the processing parameters on the fabrication of auxetic polyethylene. Part III. The effect of extrusion conditions., *J. Mater. Sci*., **30**, 1995, 4087-4094.

62. Alderson, K.L.; Evans, K.E., The fabrication of micro-porous polyethylene having a negative Poisson's ratio., *Polym. Rep.,* **33**, 1992, 4435-4435.

63. Webber, R.S.; Alderson, K.L.; Evans, K.E., Novel variations in the microstructure of the auxetic micro-porous ultra-high molecular weight polyethylene. Part I: Processing and micro-structure., *Polym. Eng. Sci.,* **40**, (8), 2000, 1894-1905.

64. Alderson, K.L.; Webber, R.S.; Evans, K.E., Novel variations in the microstructure of the auxetic micro-porous ultra-high molecular weight polyethylene. Part II: Mechanical properties., *Poym. Eng. Sci.,* **40**, (8), 2000, 1906-1914.

65. Alderson, K.L.; Webber, R.S.; Mohammed, U.F.; Murphy, E.; Evans, K.E., An experimental study of ultrasonic attenuation in micro-porous polyethylene., *Appl. Acoustics.,* **50**, (1), 1997, 23-33.

66. Pickles, A.P.; Alderson, K.L.; Evans, K.E., The effects of powder morphology on the processing of auxetic polypropylene PP on negative Poisson's ratio., *Polym .Eng. Sci*., **36,** (5), 1996, 636-642.

67. Alderson, K.L.; Alderson, A.; Smart, G.; Simkins, V.R.; Davies, P.J., Auxetic polypropylene fibres: Part I- Manufacture and characterisation., *Plastics Rubber and Composites.*, **31**, (8), 2002, 344-349.

68. Ravirala, N.; Alderson, K.L.; Davies, P.J., Simkins, V.R.; Alderson, A., Negative Poisson's ratio polyester fibres., *Text. Res. J.*, **76**, (7), 2006, 540-546.

69. Simkins V.R.; Alderson, A.; Davies, P.J.; Alderson, K.L., Single fibre pullout tests on auxetic polymeric fibres., *J. Mater. Sci.*, **40**, (16), 2005, 4355-4364.

70. Ravirala, N.; Alderson, A.; Alderson, K.L.; Davies, P.J., Auxetic polypropylene films., *Polym. Eng. Sci.*, **45**, (4), 2005, 517-528.

71. Alderson. K.L.; Alderson, A.; Davies, P.J.; Smart, G.; Ravirala, N.; Simkins, V.R., The effect of processing parameters on the mechanical properties of auxetic polymeric fibres., *J. Mater. Sci*., **42**, 2007,7991-8000.

72. Ravirala, N.; Alderson, A.; Alderson, K.; Interlocking hexagons model for auxetic behaviour, *J. Mater.Sci.*, **42**, 2007, 7433-7445.

73. Herakovich, C. T., Composite laminates with negative through the thickness Poisson's ratios., *J. Comp. Mater.*, **18**, (5), 1984, 447-455.

74. Vlachopoulos, J.; Strut D., Polymer processing., *Mater. Sci. and Tech*.; **19**, (9), 2003, 1161-1169.

75. Wilcznski, K.; A computer model for single-screw plasticating extrusion., *Polymer-plastics Techn. Eng.*, **35**, (3), 1996, 449-477.

76. Thibault, F.; Tanguy, P.A.; Blouin, D., A numerical model for single screw extrusion with poly(vinyl chloride) (PVC) resins., *Polym. Eng. Sci*., **34**, (18), 1994,

1377-1386.

77. Chiruvella, R.V.; Jarulia, Y.; Sernas, V.; Esseghir, M., Extrusion of non-Newtonian fluids in a single-screw extruder with pressure back flow., *Polym. Eng. Sci*., **36**, (3), 1996, 358-367.

78. Gopalakrishna, S.; Jaluria, Y., Computational study of transport process in a single-screw extruder for a non Newtonian chemically reactive materials., *Sadhana*, **19**, (5), 1994, 817-832.

79. Chung, C.I., Plasticating single-screw extrusion theory., *Polym. Eng. Sci*, **11**, (2), 1971, 93-98.

80. Karwe, M.V.; Jaluria, Y., Numerical simulation of fluid flow and heat transfer in a single-screw extruder for non-Newtonian fluids., *Numerical heat transfer, Part A: Applications.*, **17**, (2), 1990, 167-190.

81. Fang, S.; Chen, L.; Zhu, F., Studies on the theory of single screw plasticating extrusion. Part II: Non-plug flow solid conveying., *Polym. Eng. Sci*., **31**, (15), 1991, 1117-1122.

82. Derezinski, S.J., Control volume analysis of feed flow in extruders., *J. Reinforced Plastics and Comp.*, **18**, (5), 1999, 437-453.

83. Chiew, L.M.; Gupta, M., Simultaneous simulation of solid conveying, melting and melt flow between parallel plates: An approximation to the flow in a screw extruder., *J. Reinforced plastics and Comp.*, **21**, (12), 2002, 1055-1078.

84. Ferretti, G.; Montanari, R., A finite-difference method for the prediction of velocity field in extrusion process., *J. Food Eng.*, **83**,(1), 2007, 84-92.

85. Weert, X.; Lawrence, C.J.; Adams, M.J.; Briscoe, B.J., Screw extrusion of food powders: prediction and performance., *Chem. Eng. Sci.*, **56**, (5), 2001, 1933-1949.

86. Tadmor, Z.; Lipshitz, S.D.; Lavie, R., Dynamic model of a plasticating extruder.,

Polym. Eng. Sci., **14**, (2), 1974, 112-119.

87. Darnell, W.H.; Mol, E.A.J., Solids conveying in extruders., *SPE Journal.*, **12**, 1956, 20-29.

88. Rauwendaal, C.J., Extruder apparatus., *United States Patent 4129386,* 1978.

89. Chung, I.C; Maximum pressure developed by solid conveying force in extruders., *Polym. Eng. Sci*., **15**, (1), 1975, 29-34.

90. Moysey, P.A., Thompson, M.R., Modelling the solids in-flow and conveying of single-screw extruder using the discrete element method., *Powder Tech.*, **153**, 2005, 95-107.

91. Janes, R.I.; Winch, P.J., Mixing and shear predictions for a single-screw extruder using computational simulation., *IMA J. Mathematics and Appl. in Business and Industry*, **5**, 1995, 399-415.

92. Croce, F.; Persi, L.; Scrosat, B.; Serraino-Fiory, F.; Plichta, E.; Henrickson, M.A., Role of the ceramic fillers in enhancing the transport properties of composite polymer electrolytes., *Electrochimica Acta,* **46**, 2001, 2457-2461.

93. Hornsby P.R., Fire retardant fillers for polymers., *Mater. Rev*., **46**, (4), 2001, 199-210.

94. Landon, G.; Lewis, G.; Boden, G.F., The influence of particle size on the tensile strength of particulate filled polymer., *J. Mater. Sci.*, **12**, 1977, 1605-1613.

95. Schwartz, C.J.; Bahadur, S., Studies on the tribological behaviour and transfer-film-counterface bond strength for polyphenylene sulfide filled with nanoscale alumina particles., *Wear*, **237**, 2000, 261-273.

96. Adams, R., Brain storming on carbon black: Houston, do we have a problem?, *Focus on Pigments.*, **2004,** (12), 2004, 1-4.

97. Pukanszky,B., Interfaces and interphases in multi-component materials: past, present,

future., *Europ. Polym. Journal*., **41**, (4), 2005, 645-662.

98. Liang, J.Z.; Li, R.K.Y., Rubber toughening in polypropylene: A review., *J. Appl. Polym. Sci*., **77**, (2), 1999, 409-417.
99. Alter, H., Filler particle size and mechanical properties of polymers., *J. Appl. Polym. Sci*, **9**, 1965, 1525-1531.
100. Zuiderduin, W.C.J.; Westzaan, C.; Huetink, J.; Gaymans, R.J., Toughening of polypropylene with calcium carbonate particles., *Polym*., **44**, (1), 2003, 261-275.
101. Wu, C.L.; Zhang, M.Q.; Rong, M.Z.; Friedrich, K., Tensile performance improvement of low nanoparticles filled-polypropylene composites., *J. Comp. Sci. Tech*., **62**, (10-11), 2002, 1327-1340.
102. Maiti, S.N.; Mahapatro, P.K., Mechanical properties of i-PP/$CaCo_3$ composites., *J. Appl. Polym. Sci.*, **42**, (12), 2003, 3101-3110.
103. Zhang, M.Q.; Rong, M.Z.; Yu, S.L.; Wetzel, B.; Friedrich, K., Effect of particle surface treatment on the tribology performance of epoxy based nanocomposites., *Wear.*, **253**, (9-10), 2002, 1086-1093.
104. Bigg, D.M., Mechanical properties of particulate filled polymers., *Polym. Comp*., **8**, (2), 1987, 115-122.
105. Pasternak, E.; Dyskin, A.V.; Multi-scale hybrid materials with negative Poisson's ratio., *IUTAM Symposium on scaling in Solid Mechanics*, **10**, 2009, 49-58.
106. Ashby, M.F.; Bre`chet, Y.J.M.; Designing hybrid materials, *Acta Materialla*, **51**, 2003, 5801 -5821.
107. Voigt, P.; Tarjus, G., Random sequential addition of un-oriented squares: Breakdown of Swendsen's conjecture., *Europhys. Lett.*, **13**, 1990, 295-300.
108. Khandkar, M.D.; Limaye, A.V.; Ogale, S.B., Shape effects in random sequential adsorption of zero-area angled objects on a continuum substrate., *Phy.Rev.Lett.*, **84**,

(3), 2000, 570-573.

109. Itoh, Y.; Solomon, H., Random sequential coding by hamming distance., *J. Appl. Prob.*, **23**, (3), 1986, 688-695.

110. Sherwood, J.D., Packing of spheroids in three- dimensional space by random sequential addition., *J. Phys. A: Math. Gen.*, **30,** (24), 1997, 839-843.

111. Yamamuro, S.; Simiyama, K., Why do cubic nanoparticles favor a square array? Mechanism of shape-dependent arrangement in nanocube self-assemblies., *Chem. Phy. Lett.*, **418**, (1-3), 2006, 166-169.

112. Yue, X.; Weinan, E., The local micro-scale problem in the multi-scale modelling of strongly heterogeneous media: Effects of boundary conditions and cell size., *J. Computational Physics.*, **222**, (2), 2007, 556-572.

113. Zorll, U., A simple theory of filler reinforcement in elastomers subjected to shear., *J. Appl. Polym. Sci*., **10**, (9), 2003, 1315-1322.

114. Tewari, A; Gokhale, A.M., Nearest neighbour distances in uniform-random poly-dispersed micro-structures., *Mater. Sci. Eng. A.*, **396**, (1-2), 2005, 22-27.

115. Jefferson, G.; Garmestani, H.; Tannenbaum, R.; Gokhale, A.; Tadd, E., Two-point probability distribution function analysis of co-polymer nano-composites., *Int. J. Plasticity.*, **21**, 2005, 185-198.

116. Voigt, W., Lehrbuch der Kristallphysik. Teubner, Leipizg, 1928.

117. Reuss, A., Berechnung der fliessgrenze von mishkristallen auf grund der plastizitatsbeding fur einkrustalle., *Z. Angew. Math. Mech.*, **9**, 1929, 49-58.

118. Jones, R.M., Mechanics of composite materials., 2nd edition, 1998, Taylor and Francis Inc.

119. Hashin, Z.; Shtrikman, S., A variational approach to the theory of the effective magnetic permeability of multi-phase materials., *J. Appl. Phys.*, **33**, 1962, 3125-

3131.

120. Hashin, Z.; Shtrikman, S., A variational approach to the theory of the elastic behaviour of multi-phase materials**.,** *J. Mech. Phys. Solids.*, **11**, 1963, 127-140.

121. Hashin, Z.; Rosen, B.W., The elastic moduli of fiber-reinforced composites., *Trans. ASME. Set. E: J. Appl. Mech*., **31**, 1964, 223-232.

122. Hill, R., A self-consistent mechanics of composite materials., *J. Mech. Phys. Solids.*, **13**, 1965, 213-222.

123. Ahmed, S.; Jones, F.R., A review of particulate reinforcement theories for polymer composites., *J. Mater. Sci*., **25**, 1990, 4933-4942.

124. Veldkamp, J.D.B., The elastic moduli of particle-filled materials., *J. Phys. D: Applied Phys.*, **6**, (17), 1973, 2012-2024.

125. Segurado, J.; Gonzalez, C.; Llorca, J., A numerical investigation of the effect of particle clustering on the mechanical properties of composites., *Acta Materialia.,* **51**, 2003, 2355-2369.

126. Hori, M.; Nemat- Nasser, S., On two micromechanics theories for determining micro-macro relations in heterogenous solids., *Mech. Mater*., **31,** 1999, 667-682.

127. Segurado, J.; Llorca, J., A computational micromechanics study of the effect of interface decohesion on the mechanical behavior of composites., *Acta Materilia*., **53**, 2005, 4931-4942.

128. Mishnaevsky, L., Three-dimensional numerical testing of microstructures of particle reinforced composites., *Acta Materilia.*, **52**, (14), 2004, 4177-4188.

129. Yan, W.; Lin, R.J.T.; Bhattacharyya, D., Particulate reinforced rotationally moulded polyethylene composites-Mixing methods and mechanical properties., *Comp. Sci. Tech*., **66**, (13), 2006, 2080-2088.

130. Frogley, M.D.; Ravich, D.; Wagner, H.D., Mechanical properties of carbon

nanoparticle-reinforced elastomers., *Comp. Sci. Tech*., **63**, (11), 2003, 1647-1654.

131. Nkansah, M.A.; Evans, K.E.; Hutchingson, I.J. Modelling the effects of negative Poisson's ratios in continuous-fibre composites., *J.Mater.Sci.*, **28**, (10), 1993, 2687-2692.

132. Yaganeh-Haeri, D.J.; Weidner, D.J.; Parise, J.B., Elasticity of α-cristobalite: a silicon dioxide with a negative Poisson's ratio., Sci., **257**, 1992, 650-652.

133. Keskar, N.R.; Chelikowsky, J.R., Negative Poisson's ratios in crystalline SiO_2 from first-principles calculations, Nature, **358**, 1992, 222-224.

134. Alderson, A.; Evans, K.E., Deformation mechanisms leading to auxetic behaviour in the α-cristobalite and α-quartz structures of both silica and germania., J. Phys: Condensed Matter., **21**, (2), 2009, 1-12.

135. He, C.; Liu, P.; Griffin, A.C., Towards negative Poisson's ratio polymers through molecular design., *Macromolecules.*, **31**, (9), 1998, 3145-3147.

136. Evans, K.E.; Alderson, A.; Christian, F.R., Auxetic 2-dimensional polymer networks-an example of tailoring geometry for specific mechanical properties., *J. Chem. Soc. Faraday Trans.*, **91**, 1995, 2671-2680.

137. Alderson, A.; Alderson **,** K.L. ; Evans K.E.; Grima, J.N.; Williams, M.R.; Davies, P.J., Modelling the deformation mechanisms, structure-property relationships and applications of auxetic nanomaterials., *Physica Status Solidi (b).*, **242**, (3), 2005, 499-508.

138. Messphysik video-extensometer package, Messphysik, Laborgerrite Ges, M.B.H., Furstenfeill, Austria.

139. Ileqbusi, O.J.; Iquchi, M.; Wahnsiedler, W.E., Mathematical and physical modelling of materials processing operations., Chapman and Hall/CRC, Florida, US, 2000.

140. Chirima, G.; Simkins, V.G.; Ravirala, N.; Rawal, A.; Alderson, K.; Alderson, A., The

effect of processing parameters on the fabrication of auxetic extruded polypropylene films., *Phys. Stat. Sol. (b),* **245**, (11), 2008, 2383 -2390.

141. Tadmor, Z.; Gogos, C.G., Principles of polymer processing., Wiley and Sons, New Jersey, US, 2006.

142. Masters, I.G.; Evans, K.E.; Models for the elastic deformations of honeycombs., *Comp.Struct.*, **35,** 1996, 403-422.

143. Horrigan, E.J.; Smith C.W.; Scarpa, F.L.; Gaspar, N.; Javadi A.A.; Berger M.A.;. Evans, K.E.; Simulated optimisation of disordered structures with negative Poisson's ratios., *Mech. of Mater.*, **41,** 2009, 919-927.

144. Daniel, I.M.; Ishai, O., Engineering Mechanics of composite materials, 2nd edition, 1994, Oxford University Press, Oxford New York.

145. Ramirez, M.; Nava-Gomez, G.C; Sabina, F.J.; Camacho-Montes, H.; Guinovart-Diaz, R.; Rodriguez-Ramos, R.; Bravo-Castellero, J.; Enhancement of Young's modulus and auxetic windows in laminates with istropic constituents., *Int. J. Eng. Scie*., **58**, 2012, 95-114.

146. Bemis Company Inc., www.bemisworldwide.com.

147. Gupta, N.; Gupta, S. K.; Mueller, B.J.; Analysis of a functionally graded particulate composite under flexural loading conditions, *Mat Scie. and Eng*.**485**, 1-2, 2008, 439 – 447.

148. Hosford, W.F., Solid Mechanics, Cambridge University Press, New York 2010.

149. Kawasaki, T.; Zhang, M.; Wang, Q.; Komatsu, K.; Kawai, S., Elastic moduli and stiffness optimization in four-point bending of wood based sandwich panel for use as structural insulated walls and floors, *J. Wood Sci.*, **52**, 2006, 302–310.

150. Plastics —Determination of tensile properties —Part 4: Test conditions for isotropic and orthotropic fibre-reinforced plastic composites, BS EN ISO 527-4:1997 BS 2782-3: Method 326F:1997.

151. Mills, A.F.; Chang, B.H.; Error Analysis of Experiments, A Manual for Engineering Students, University of California, 2004.

152. Yusoff, M.Z.M.; Salit, M.S.; Napsiah I.; Wirawan, R.; Mechanical Properties of Short Random Oil Palm Fibre Reinforced Epoxy Composites, *Sains Malaysiana*, **39**, 1, 2010, 87–92.

153. Gonzalez-chi, P. I.; Young, R. J.; Deformation micromechanics of a thermoplastic-thermoset interphase of epoxy composites reinforced with polyethylene fiber, *J. Mat. Scie.*, **39**, 2004, 7049 – 7059.

154. Bader, M. G. ; Collins J. F.; The Effect of Fibre-interface and Processing Variables on the Mechanical Properties of Glass-fibre Filled Nylon 6, *Fibre Science and Technology*, **18,** 1983, 217-231.

155. Spanoudakis; J., Young; R.J., Crack propagation in a glass particle-filled epoxy resin, Part 1 Effect of volume fraction and size, *J. Mat. Sci.*, **19**, 1984, 473-486.

156. Spanoudakis; J., Young; R.J., Crack propagation in a glass particle-filled epoxy resin, Part 2 Effect of particle-matrix adhesion , *J. Mat. Sci.*, **19**, 1984, 487-496.

157. Ahmad.; F.N., Jaafar.,M.; Palaniandy.,S.; Azizli., K.A.M.; Effect of particle shape of silica mineral on the properties of epoxy composites, *Comp. Sci. Tech.*, **68**, 2008, 346–353.

158. Chow, T.S.; The effect of particle shape on the mechanical properties of filled polymers, *J. Mat. Sci.*, **15**, 1980, 1873-1888.

159. Chow, T.S.; Elastic moduli of filled polymers: The effect of particle shape, *J. App. Phy.*, **48**, 10, 1977, 4072-4075.

160. Chirima, G.T.; Zied, K.; Ravirala, N.; Burgess, A.; Dooling, P.; Alderson, K.L.; Alderson, A.; Modelling of auxetic particulate-filled polymeric composites, In: ICCM 17 Conference Proceedings, Edinburgh, 2009.

161. Dennis-Germuska, D.; Taylor, P.A.; Wright, J.D.; Adaptive and multivariable control of a single screw extrusion system., *Canadian J. Chem. Eng*., **62**, 1984, 790−801.

162. Song; F., Zhou; J., Xu; X., Xu; Y., Bai;Y., Effect of negative Poisson's ratio in the tension of ceramics., *Phys. Rev. Lett.*, **100**, 2008, 245502-1 - 245502-4.

163. Li; X., Nanoscale structural and mechanical characterization of natural nanocomposites: Seashells, *JOM*, 2007, 71-74.

164. Mainprice; D., Page; Y.L., Rodgers; J., Jouanna; P., *Ab initio* elastic properties of talc from 0 to 12 GPa: Interpretation of seismic velocities at mantle pressures and prediction of auxetic behaviour at low pressure, *Earth and Planetary Science Letters*, 274, 2008, 327-338.

Appendix A

The Appendix contains a plot and derivation (Eq. 3.5) of the change in particle radius with time within a single screw extruder. A screw speed of 1.05 $rads^{-1}$ was used in the calculations.

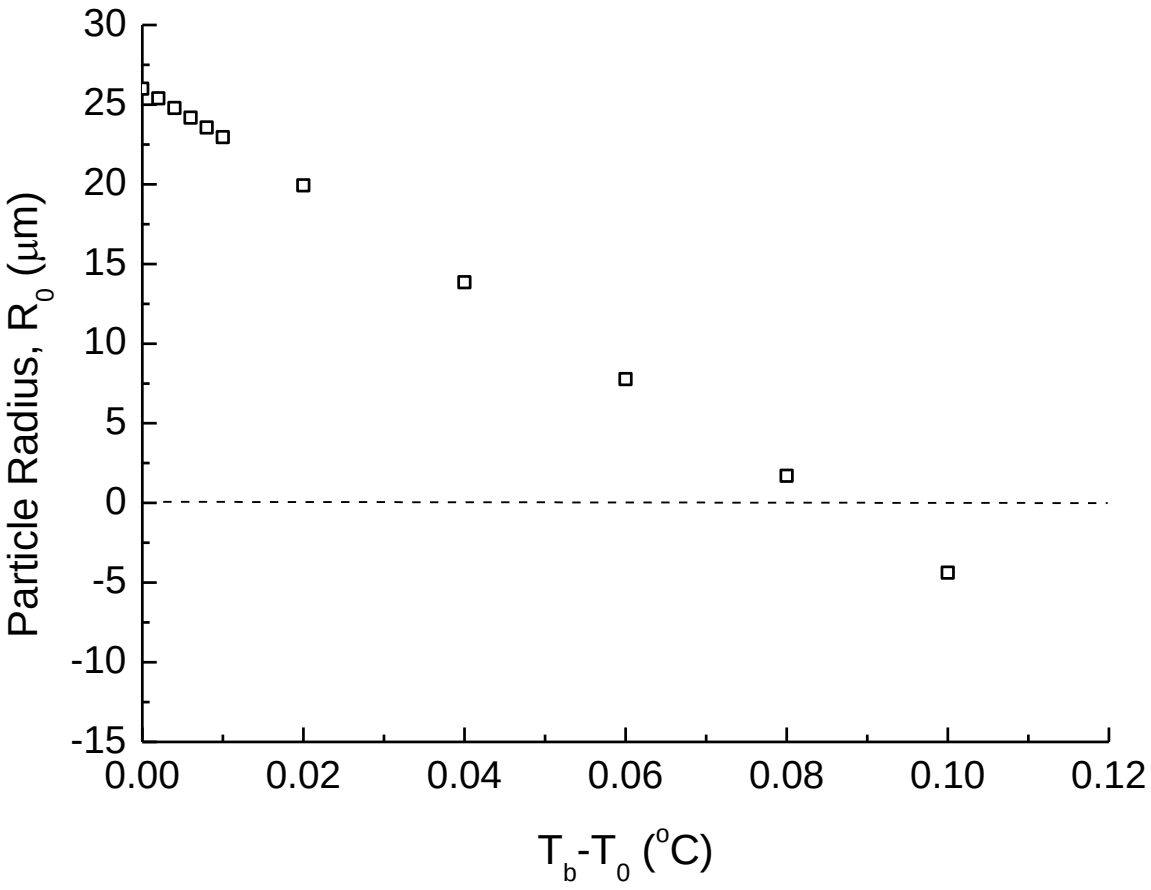

Fig 1. Plot of T_b-T_o vs. R_θ

Figure 1 shows that an increase of 0.1 °C in temperature is sufficient to ensure total melt of a polymer particle of 25μm radius within the extruder.

Derivation for Eqn 3.5

(methodology adapted from L. Ratke and C. Beckermann, Concurrent Growth And Coarsening of Spheres, *Acta Mater.*; **49** (2001) 4041–4054.)

The sphere grows when T_b (T_∞) is lower than T_0 (T_m), and shrinks (melts) when T_b (T_∞) is higher than T_0 (T_m). It is the latter condition which concerns the particle melting scenario considered in the thesis.

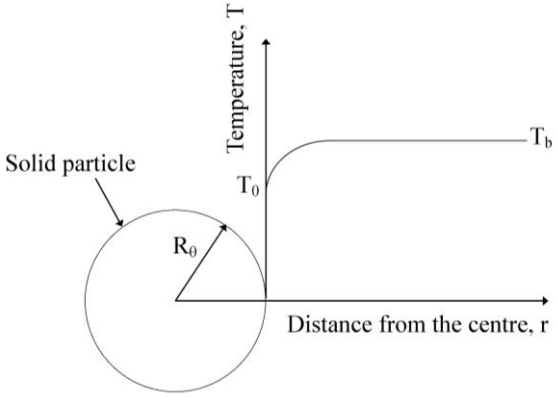

Figure 2. Melting of a sphere surrounded by a higher temperature medium

Referring to the spherically symmetric system in Figure 2, the temperature of the surrounding medium far from the surface of the sphere is T_b, which is higher than the melting temperature T_0 of the sphere. Assuming a stationary interface approximation is valid, the temperature T of the solid/melt/surrounding medium system as a function of distance r from the centre of the sphere is given by the steady state heat conduction equation in spherical coordinates:

$$\nabla^2 T = \frac{d^2 T}{dr^2} + \frac{2}{r}\frac{dT}{dr} = 0 \tag{1}$$

with the following boundary conditions:

$$T(r \to \infty) = T_b \tag{2}$$

$$T(r = R_\theta) = T_0 \tag{3}$$

The general solution of (1) is

$$T(r) = A + \frac{B}{r} \tag{4}$$

Substituting (2) into (4):

$$A = T_b \tag{5}$$

and (3) and (5) into (4):

$$B = R_\theta (T_0 - T_b) \tag{6}$$

From (4)-(6), the solution is

$$T(r) = T_b + (T_0 - T_b)\frac{R_\theta}{r} \tag{7}$$

The rate of melting is determined from the heat flow at the solid/melt interface (the heat balance equation):

$$-k\left(\frac{dT}{dr}\right)_{r=R_\theta} A = \rho_s \Delta H \frac{dV}{dt} \tag{8}$$

where k is the thermal conductivity, ΔH the latent heat, ρ_s the density, A_s the surface area ($= 4\pi R_\theta^2$), and V the volume ($= (4/3)\pi R_\theta^3$) of the sphere, and t is time.

Noting that

$$\frac{dV}{dR_\theta} = 4\pi R_\theta^2 = A_s \tag{9}$$

and differentiating (7):

$$\frac{dT}{dr} = -(T_0 - T_b)\frac{R_\theta}{r^2} \tag{10}$$

then substituting (9) and (10) into (8) yields:

$$\frac{k(T_0 - T_b)}{R_\theta} = \rho_s \Delta H \frac{dR_\theta}{dt} \tag{11}$$

Recalling that $h_\theta = k/R_\theta$ and rearranging (11):

$$\frac{dR_\theta}{dt} = -\frac{h_\theta (T_b - T_0)}{\rho_s \Delta H} \tag{12}$$

Eqn (12) is the same as Eqn (3.5) of the thesis. Note the equivalent symbols used in Ratke *et al.* and in the thesis.

Eqn 3.5 in thesis:

$$\frac{dR_\theta}{dt} = -\frac{h_\theta\left(T_b - T_0\right)}{\rho_s \Delta H} \qquad \text{Thesis (3.5)}$$

Eqn 7 of Ratke and Beckermann

$$\frac{dR}{dt} = \frac{k_L}{\rho L}\frac{T_m - T_\infty}{R} \qquad \text{Ref Eqn (7)}$$

Table of equivalence for symbols used in thesis and Ratke and Beckermann.

Property	Symbol (Thesis)	Symbol (Ref [3])
Particle radius (m)	R_θ	R
Time (s)	t	t
Local heat transfer coefficient (W/m^2K)	h_θ	-
Thermal conductivity (W/mK)	-	k_L
Bulk Temperature (K)	T_b	T_∞
Melting temperature (K)	T_0	T_m
Density (kg/m^3)	ρ_s	ρ
Latent heat (J/kg)	ΔH	L

From the table of equivalent symbols above, the growth/melt rates defined by the two above equations are the same when $h_\theta = k_L / R$ (this is correct in terms of the relationship between h_θ and k_L - http://en.wikipedia.org/wiki/Thermal_conductivity).

Appendix B

The Appendix contains the random number generator macro that was used in modelling the particulate filled composites. The Appendix also contains SCF plots of shear modulus predictions of the particulate filled composites.

Random Number Generator Macro

n= number of auxetic components in 25000

```
!random generation
*dim,RDM_NUM,array,n,2
*do,var,1,n,1
RDM_NUM(var)=nint(rand(0,(3**3*5*5*5)))+1
*enddo

*DO, var1,1,n,1
MPCHG,2,RDM_NUM(var1)
*ENDDO


!FILLER PERCENTAGE
esel,s,mat,,2
*GET, E_FILL, ELEM, 0,count
```

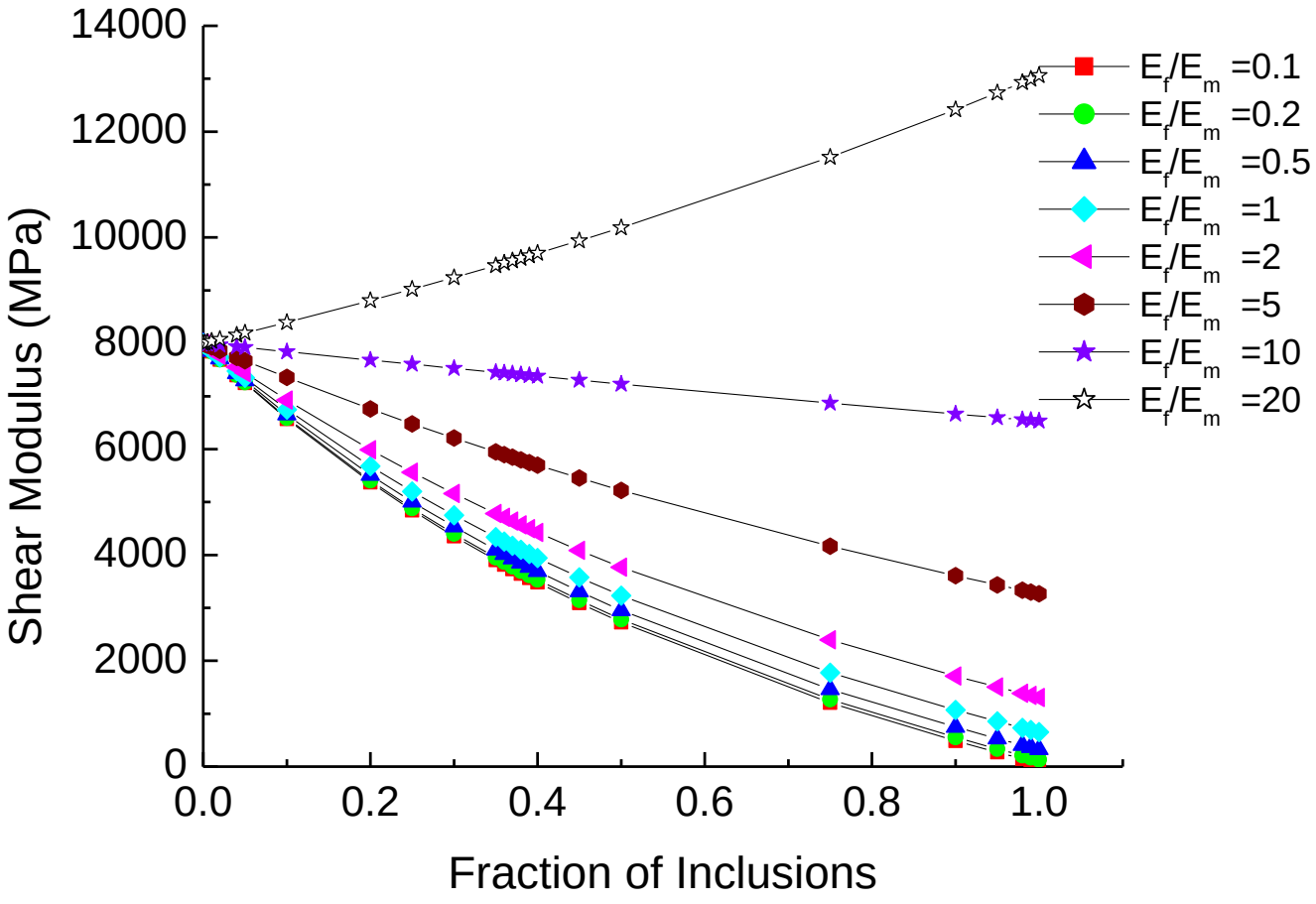

Fig 1. Predicted shear modulus vs. volume fraction of conventional inclusions for E_f/E_m = 0.1 – 20 in an auxetic matrix [υ_m = -0.9 and υ_f = +0.225]

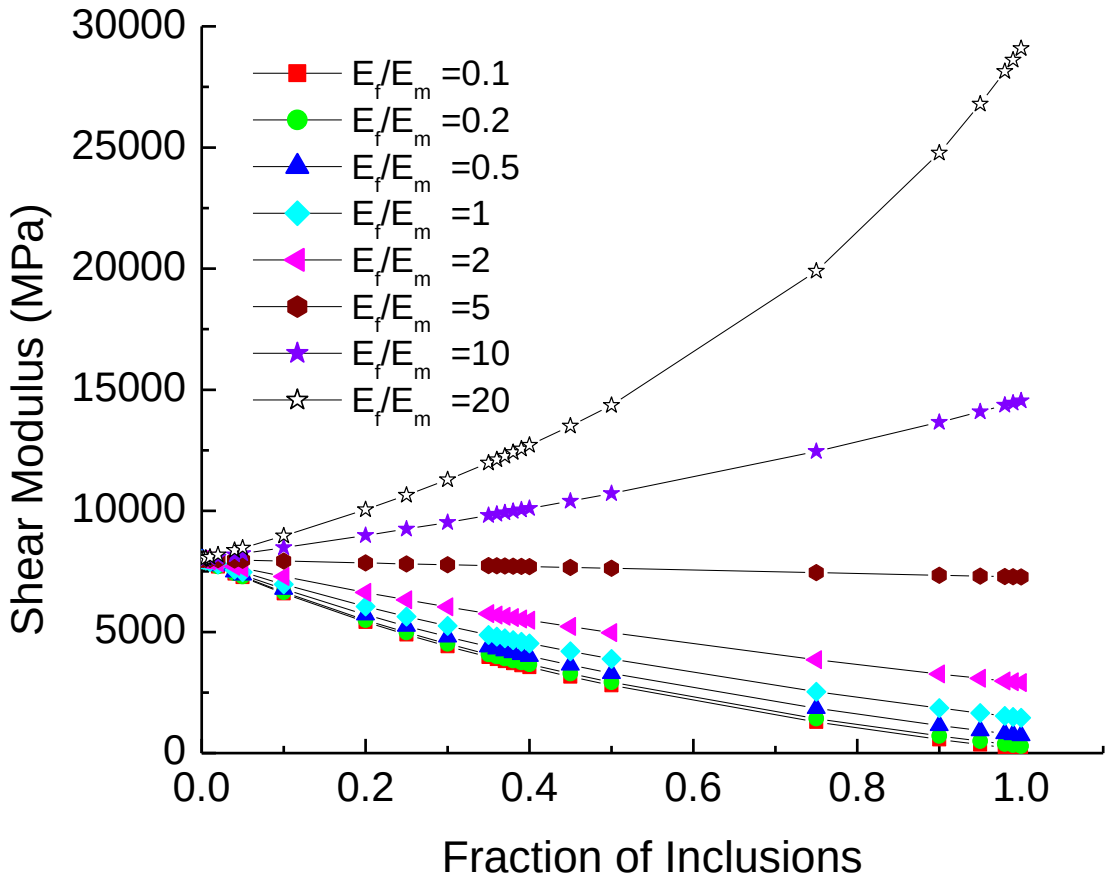

Fig 2. Predicted shear modulus vs. volume fraction of auxetic inclusions for E_f / E_m = 0.1 – 20 in an auxetic matrix [υ_m = -0.45 and υ_f = -0.9]

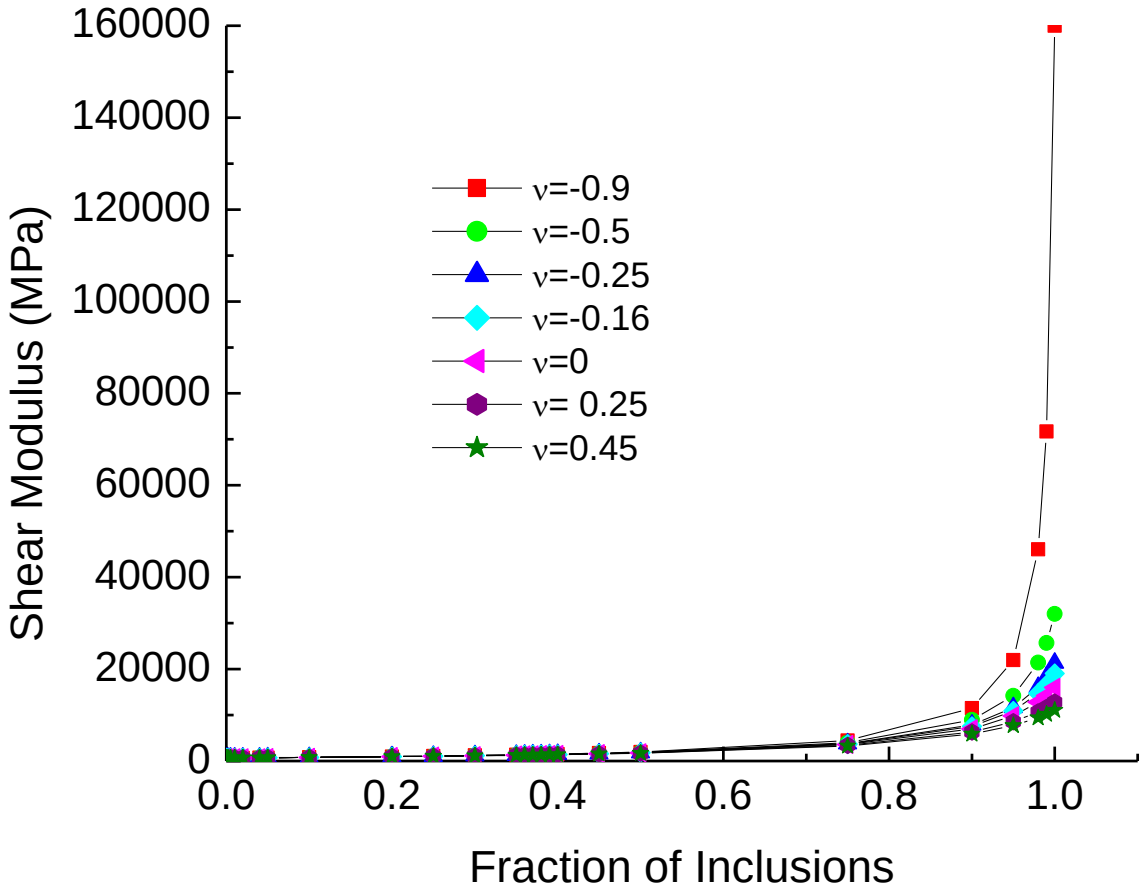

Fig 3. Predicted shear modulus vs. volume fraction of inclusions for υ_f = -0.9 to +0.45 in an conventional matrix [$E_f / E_m = 20$, $\upsilon_m = + 0.225$]

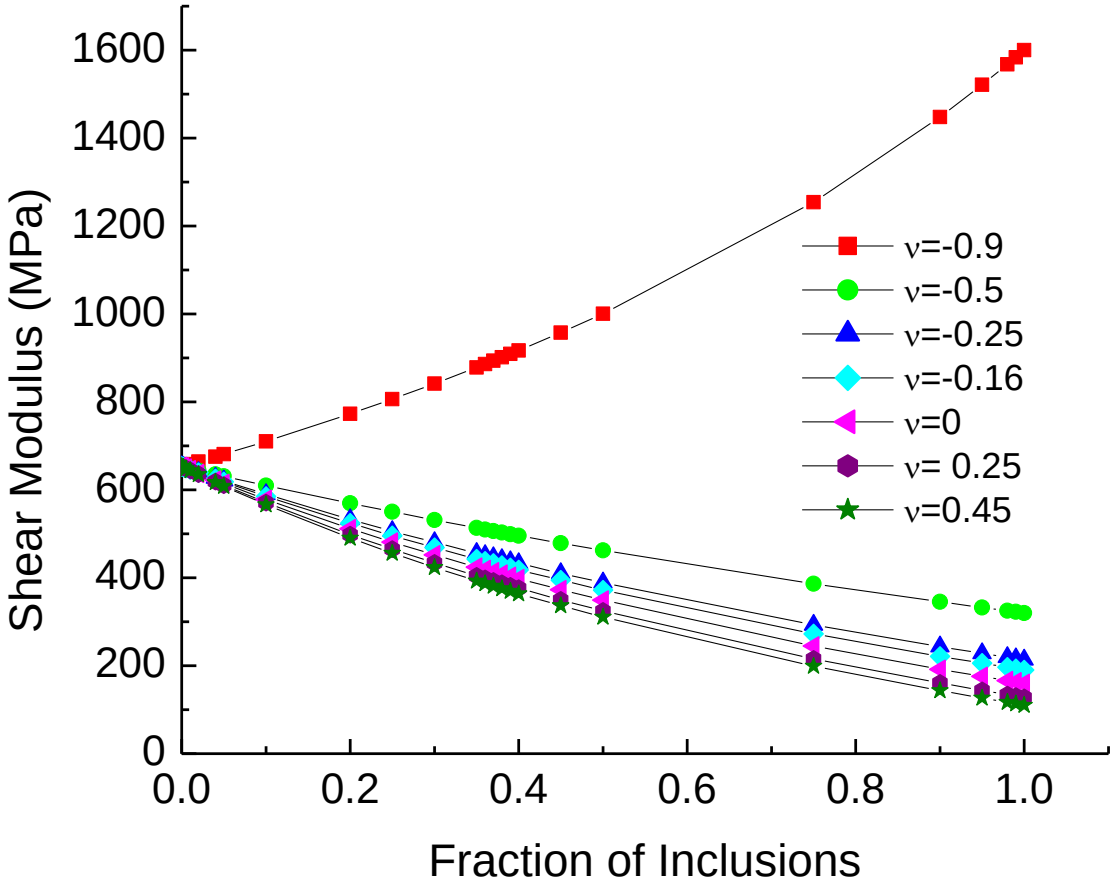

Fig 3. Predicted shear modulus vs. volume fraction of inclusions for υ_f = -0.9 to +0.45 in an conventional matrix [$E_f / E_m = 0.2$, $\upsilon_m = +0.225$]